uOttawa

Frequency Domain Analysis of Composite Long-span Cable-stayed Bridges by Finite Strip Method

By

Haoran Li

Thesis submitted to the
Faculty of Graduate and Postdoctoral Studies
in partial fulfillment of the requirements for the degree of
Master of Applied Science
in Civil Engineering

Department of Civil Engineering
Faculty of Engineering
University of Ottawa

ACKNOWLEDGEMENTS

I would like to take this opportunity to express my gratitude to all my friends, colleagues, my university, and family members who supported me throughout the period of this project.

In particular, I would like to thank my thesis supervisor, Professor Elena Dragomirescu, for offering her meticulous support and knowledge, while guiding me patiently and carefully through my research. I appreciate all her help indeed, and I feel so lucky to be supervised by her. I would also like to thank Hamidreza Naderian for his prior works and offering the basic codes for running parts of the current analysis, and last but not the least I would like to thank friends and colleagues for their suggestions, ideas, and help during my research period. I would like to thank my fellow friends and colleagues: Yang Li, Ahmad Shahroodi, Haisam Yakoub, Zhe Xiao, and Edgar Michel Pierre.

Finally, thanks also go to my family and my girlfriend, Xuan Chu who always encouraged me to do my best and never give up.

ABSTRACT

The finite strip method (FSM) is a very efficient numerical method employed for performing the structural analysis of slender structures, such as cable-stayed bridges; the strip discretization of the model allows for the usage of a lower number of degrees of freedom, in comparison with the finite element method (FEM), while, as it will be discussed in the current research, the results obtained from both methods are in relatively good agreement. Moreover, to address the latest developments in the area of smart construction materials used for long-span bridges, the fiber reinforced polymer (FRP) composites were implemented for the bridge deck modeling, as part of a hybrid composite FRP cable-stayed bridge, and an extend laminate integrated finite strip method (LFSM) was applied for estimating the static structural performance of the hybrid composite FRP long-span cable-stayed bridge under several concentrated and uniformly distributed loadings. The free vibrations analysis was conducted for the Kap Shui Mun Cable-stayed Bridge model, and the natural frequencies were compared with the ones obtained from an FE model of the same bridge. One of the advantages of using the integrated finite strip method is that number of vibration modes, which can be included in the dynamic analysis when the effect of a sweeping sinus and a seismic loading are investigated when a conventional FE analysis would fail to converge. The outcomes of this research will set the stage for the hybrid long-span cable-stayed bridges modeling by the laminate integrated finite strip method (LFSM) which is more efficient and straightforward than the finite element analysis, for performing the static, free vibration, time domain, and frequency domain analyses.

NOTATIONS

Symbol	Definition
A	Laminate Extensional Stiffness Matrix
$[A_d]$	Aerodynamic Damping Matrix
$[A_s]$	Aerodynamic Stiffness Matrix
B_3	Spline Function
B	Laminate Coupling Stiffness Matrix
b	Width of Strip
$[C]$	Damping Matrix of The Bridge Deck
$[D]$	Structural Damping Matrix
D	Logarithmic Decrement
D	Laminate Bending Stiffness Matrix
$[f]$	Mode Shape Matrix
$g(t)$	Envelope or Uniformly Modulating Function
$h(t)$	System Impulse Response Function
$I(x, t)$	Evolutionary Frequency Response Function
$[j]$	Vector of Generalized Coordinates
$[K]$	Stiffness Matrix
K	Reduced Frequency
$[M]$	Mass Matrix
M_x, M_y, M_{xy}	Bending and Twisting Moments Per Unit Length
N_x, N_y, N_{xy}	Membrane and Shear Forces Per Unit Length
N	The Number of Laminas
$\{p\}$	External Force Vector
P	Complex Variable
Q_{ij}	Components Of The Lamina Stiffness Matrix
r	Total Number Of Longitudinal Sections On A Nodal Line
U	Wind Velocity
$\{u\}$	Relative Displacement Vector
u	Transverse Displacement
v	Longitudinal Displacement
w	Vertical Displacement
$[n]$	Window Function
$\kappa_x, \kappa_y, \kappa_z$	Bending Curvature
y_m	Spline Function Center
$\tilde{y}(t,\omega)$	Pseudo Response
α&β	Rayleigh Damping Factors
ρ	Density of The Strip
$\delta(t)$	Function of Time

ω	Natural Frequency
$\{\delta\}$	Mode Shapes
Δt	Time Increment
$\Delta\delta_i$	The Displacement Increment
γ & λ	Newmark's Parameters

ACRONYMS

Acronym	Definition
AFRP	Aramid Fiber Reinforced Polymer
BFRP	Basalt Fiber Reinforced Polymer
CHBDC	Canadian Highway Bridge Design Code
CFRP	Carbon Fiber Reinforced Polymer
CQC	Complete Quadratic Combination
CRC	Compact Reinforced Composite
CS	Column Strip
DFT	Discrete Fourier Transform
FEA	Finite Element Approach
FEM	Finite Element Method
FFT	Fast Fourier Transform
FRP	Fibre Reinforced Polymer
FSE	Finite Strip Environment
FSM	Finite Strip Method
FT	Fourier Transform
GFRP	Glass Fiber Reinforced Polymer
GFVM	E-Glass Fiber and Vinylester Matrix
IFSM	Integrated Finite Strip Method
KSM	Kap Shui Mun Bridge
LFSM	Laminated Finite Strip Method
MDOF	Multi-Degree of Freedom
NPSD	Normalized Power Spectrum Density
PEM	Pseudo Excitation Method
PSD	Power Spectrum Density
SDOF	Single Degree of Freedom
SFSM	Spline Finite Strip Method
SFRC	Steel Fiber Reinforced Concrete
SMART	Strong Motion Arrary in Taiwan
SRSS	Square Root of the Sum of the Squares
WVB	Wind Vehicle Bridge
2D	Two Dimension
3D	Three Dimension

CONTENTS

Lists of Figures

Lists of Tables

CHAPTER 1. INTRODUCTION

1.1. BACKGROUND INTRODUCTION

Recent development shows that long-span bridges have rapidly spread in many urban areas as well as many rural and mountainous areas, especially in countries with a highly increasing traffic. Long-span bridges play a vital role for the traffic networks they can easily link, thus releasing the overwhelmingly congested transportation routes. In the meantime, the increasing dimensions and traffic requirements led to momentous changes in the types and characteristics of the bridges structures, and along with them an expansion of analytical methods has been registered. Typically, there are two primary analytical means to investigate the bridge models: Finite Element Method (FEM) and Finite Strip Method (FSM); the latter is a newly recommended method, which initially was applied only for simple and slender structures. However, several studies reported in the past decade have adopted the FS method for the long-span cable-stayed bridges. The cable-stayed bridges are relatively easier to build than the suspension bridges and thus have a lower construction cost. Therefore, these have been preferred by design and manufacturing companies, when distances of around 1000 m must be spanned. For longer span requirements, suspension bridges would become an efficient design solution.

1.2. RESEARCH MOTIVATION

The development of the cable-stayed bridges brought several innovative construction methods, and the usage of smart materials has expanded. For example, using the advanced composite FRP materials for building different components of the cable-stayed bridges, such as a deck, cables, and even towers and piers is one of the solutions would allow the increase in the span length and the towers' heights. However, the characteristics of the FRP materials differ very much from the standard steel and concrete construction materials. Thus structural analysis should be conducted to diligently check the stability problems, which might arise from the seismic and wind loading. Moreover, with the increase in the span length, the height of the tower should increase, and it may lead to the buckling phenomena in towers.

The structural response of complex structures such as cable-stayed bridges under dynamic earthquake loading become difficult to estimate due to the high number of degrees of freedom. Even if simplified taut strip and lumped mass bridge models are used still very powerful computational techniques are required to determine the dynamic response of such massive structures. Most of the long-span cable-stayed bridges are modeled by finite element method, which implies the use of thousands of degrees of freedom, while for the seismic analysis the finite element method often fails to converge when ordinary computers are used. Therefore, new

analytical methods must be tackled to verify the stability of multi-degrees of freedom long-span bridges in the light of using novel construction materials such as FRPs. For decreasing the number of degrees of freedom, increasing the size of the finite element can be considered by adopting longer strips with knots along their edges. An efficient and accurate solution can be achieved only if finite strip methodology would be implemented for slender structural elements, such as bridge decks, cables, towers, and piers. Thus, all the components of cable-stayed bridges are prone to achieve an acceptable design solution if modeled by FSM. Recent studies showed that the finite strip method could be efficiently used for modeling long-span bridges and for determining their response under the seismic time history loading. However, the introduction of FRPs for the bridge deck would significantly affect the weight, the damping and the natural frequencies of the bridge structure. Thus, a frequency domain analysis is required to be performed by FSM for FRP cable-stayed bridges. More recent developments of the FS formulation involve the adoption of the transition sections, which can model the interaction between the cables and deck, deck and towers, cables and towers within the newly formed Integrated Finite Strip Method.

1.3. PROJECT OBJECTIVES

The main objective of the current research is to propose a bridge model which involves the use of advanced composite materials, specifically the fiber-reinforced polymer (FRP) was explored as a new material for long-span cable-stayed bridges. Initially, a lamina model for a plate developed in the FSM was applied to a slab-girder bridge modeled with FRP deck. To validate the FSM model of the FRP Slab-girded bridge, the FEM model is adopted for simulating the FRP deck and for comparing the deflection under different static and dynamic loading conditions. Once the lamina model of the plate is validated for a simple slab-girder bridge, extending it to a cable-stayed bridge is sought. A case study can be performed by selecting the Kap Shui Mun Cable-stayed Bridge for analyzing the response to several earthquake signals, for different FRP deck thicknesses; performing the frequency domain analysis for all the investigations is set as the primary objective of this thesis. Based on the recently developed Integrated Finite Strip Method (IFSM) by Naderian et al. (2015) and Naderian et al. (2016), a new method for modeling the FRPs characteristics for different structural elements, called Laminate Finite Strip Method (LFSM) will be introduced.

By using the proposed laminate finite strip solution, one slab-girder bridge, and one long-span cable-stayed bridge are modeled, and the necessary studies will be performed regarding static analysis, free vibration analysis, and dynamic analysis. The dynamic analysis carried out in this thesis mainly concentrated on the seismic analysis by the frequency domain method, which is employed in the framework of the laminated integrated finite strip method. The results will show that the methodology can be successfully used for investigating simple short-span bridges and

long-span cable-stayed bridges. Frequency domain analysis is firstly applied by the finite strip method on the long-span cable-stayed bridges especially with the composite materials.

1.4. THESIS LAYOUT

This current thesis contains seven chapters divided as listed below:

Chapter 1 - Introduction:

- Introduces the significance of the current research, describes the main objectives and defines the scope of the work.

Chapter 2 - Literature review:

- Provides the background information related to the thesis topic and summarizes previous research on the finite strip method and its application for girder-slab bridges and cable-stayed bridges. In addition, some examples of bridges built with composite materials, GFRPs, CFRPs, and the laminated composites are introduced in this chapter.

Chapter 3 - Theoretical basis:

- Describes the static and dynamic theoretical basis and necessary programs, including the application of FSM on bridges, material parameters, the applied approaches, programs setups and multi-programs protocols.

Chapter 4 – Modeling and results of an FRP multi-span continuous slab-girder bridge:

- A case study is set as an example for the application of FSM for composite materials applied to bridges. This chapter summarizes the modeling of a continuous slab-girder bridge by the FSM derived from the C++ and MATLAB programs and discusses the effects of the laminated FRPs. The validation of the LFSM method will be presented by comparing the results obtained by FEM and FSM methods for both static and dynamic analyses.

Chapter 5 – Modeling and results of composite long-span cable-stayed bridges:

- Summarizes the modeling of Kap Shui Mun cable-stayed bridge by the FSM from the C++ and MATLAB programs, and discusses the effects of the laminated FRPs applied to the bridge deck. The results comparison based on the FEM and FSM models is discussed for both static and dynamic analyses.

Chapter 6 – Frequency domain analysis for the composite long-span cable-stayed bridges:

- Summarizes the frequency domain results and various observations related to the effects of the layout of laminated FRPs, the thickness of deck, the direction of waves, and the types of seismic excitations by comparing the power response of acceleration and displacement.

Chapter 7 – Conclusions and future work:

- Presents final remarks and highlights the findings from this research, and proposes recommendation for further studies.

CHAPTER 2. LITERATURE REVIEW

2.1. CHAPTER OVERVIEW

This chapter provides a literature review of the most pertinent studies related to the thesis research topic. The chapter begins with an introduction to the Finite Strip Method (FSM) followed by a review of previous research focussing on the analysis process of the long-span bridges by using FSM, where both the static analysis method and the dynamic analysis method are included. The chapter concludes with a review of previous experimental and theoretical research on composite FRP materials employed for the bridges, with a focus on the FRPs as well as on the studies, which investigated the performance of the structural members built with composites for the common bridges and hybrid cable-stayed bridges. In last part, frequency domain analysis that is the core of this thesis is introduced and developed by reviewing previous necessary studies related to long-span cable-stayed bridges.

2.2. DEVELOPMENT OF FINITE STRIP METHOD

This section provides a brief introduction to the Finite Strip Method used in the research study which includes: Classical Finite Strip Method, Spline Finite Strip Method, and an Integrated Finite Strip Method. The section ends with an introduction of the transit section for the Integrated Finite Strip Method.

2.2.1. CLASSICAL FINITE STRIP METHOD

The finite strip method was first proposed and created by Cheung (1968) to investigate the elastic plates with simply supported end conditions. However, the original idea to use FSM was to reduce the dimensions of long span structures via the implementation of an analytical solution along the longitudinal direction. The finite strip method can model the rectangular slab bridges, as proved by Powell et al. (1969). Therefore, engineers found out that there was a broad prospect to develop and put into the application for a considerable study on extending the theoretical new finite strip methodology, which has been proposed for a variety of structures including plates, shells, plates, bridges, and buildings. The main adventure of the FSM is that it is more reliable and has reasonable response under the applied loading, both in a harmonic and deterministic environment. The first applications were conducted by Cheung (1970) who studied the rectangular slabs with general end boundary conditions and a box girder bridge (Cheung, 1988).

After solving buckling bending problems, and the vibration conditions, the FS Method was pushed forward to analyze the linear-elastic, nonlinear and dynamic behavior of bridge structures. When it comes to the requirement for an alternative approach to developing the dynamic analysis,

Cheung et al. (1988) firstly proposed the finite strip solution for free vibration analysis of thin-walled structures with different boundary conditions. They proposed a method combines the finite strip method with another numerical method to increase the capability of the analysis in the FS environment. Moreover, Cheung et al. (1989) combined the FS with the finite element and boundary element methods and applied the combined method to several irregular plates and slab-girder bridges. Furthermore, Zhong et al. (1998) proposed a precise finite strip solution in which the precise integration method along with the space coordinate are combined with the semi-analytical analysis of prismatic domain structures. Valuable works had been done by Cheung (1989) and Zienkiewicz et al. (2016), they had shown that the application of the classic FSM is not enough to analyze the thick slabs and thick bridge boxes, in this case, they developed both the finite layer and finite prism methods for these special structures.

However, engineers and researchers were not content with the status quo; they wanted to create a completely new alternative method of FEM that can realize every analysis that FEM can currently perform. The pioneer in this research, Prezemieniecki (1973), showed how this new technique could be used to predict the initial elastic local buckling of plates and sections made of plates under biaxial compression. Typically, he used the finite strip method to work on predicting the structural stabilities into their applications. A similar case was reported by Plank and Wittrick (1974), who investigated the buckling under combined loading of thin-walled structures by applying a complex finite strip method. The advantage of their method over the formulations of the conventional finite strip method was the characteristics of the simplicity in handling shear forces. Furtherly, Wittrick (1968) developed a buckling analysis of stiffened panels in compression according to a proposed exact finite strip method. Schafer et al. (2013) derived the decomposing for the buckling modes of thin-walled open cross-section members by generalized beam theory based on a constrained finite strip method.

2.2.2. SPLINE FINITE STRIP METHOD

In the conventional (classic) finite strip method, the structure is subdivided into longitudinal strips, where the displacements field is defined by simple polynomials in the transverse direction and continuous harmonic functions in the longitudinal direction. It yields fewer degrees of freedom than the finite element method. However, it has the disadvantage that it usually allows only simple boundary conditions, simple structural geometries, and simple loading types to be analyzed. Even though there were several exact FSM, constrained FSM, etc., efforts were made to develop the conventional finite strip method much more capable of modeling different boundary end conditions (1995). Otherwise, these methods will not be suitable to investigate a large variety of problems.

To overcome the shortcomings of the semi-analytical finite strip method with boundary conditions, concentrated loads, and continuous spans, the spline finite strip method is now more universal and acceptable than the semi-analytical finite strip method, because of the work was done by Tham (1990) and Cheung et al. (1992) for firstly creating the spline finite strip method. The spline finite strip method (SFSM) can be considered as a unique form of the finite element method and at the same time an evolved version of the finite strip method. In this new technique, the displacement functions in the longitudinal directions are modeled as a B_3 spline involving, however, with more degrees of freedom in comparison with conventional finite strip method. The advantage of the new finite strip method is the stronger ability to handle more complex types of loadings, geometries, and boundary conditions.

The spline FSM has been successfully applied to the analyses of various kinds of structural problems such as circular plates, skew plates, arbitrary-shape plates, and box girder bridges. Fan and Cheung (1983) applied the spline finite strip method for analyzing several shallow shells. Regarding to the flat-walled structures, with the rapid development of the spline finite strip method, after the investigation of natural vibrations by Cheung (1971), Hancock et al. (1974) were the first researchers who applied SFSM for elastic and inelastic buckling of thin flat-walled structures subjected to longitudinal compression and bending, transverse compression as well as shear. The significant character of buckling of flat-walled structures was produced by Lau et al. (1986) by using the specified SFSM.

There were several signs of progress for different flat-walled structures; the isoparametric spline FSM was introduced in modeling structures of customized geometry for the plane structures (Au et al. 1993) and extended it to the thin-walled structures recently by Yao et al. (2010). Chen et al. (1991) introduced the unequally spaced B_3-spline functions in the analysis of stiffened plates and folded plate structures with intermediate supports.

The method can describe the accurate response in the region of high-stress gradients, or at the locations of abrupt geometric changes by spacing knots more closely. Wang et al. (2004) started to develop the dynamic analysis of the vibration based on composite laminated plates by a *B*-spline FSM. According to their research, the composite laminated plates are divided into some numerical layers that were more convenient to model the deflections.

Regarding nonlinear analysis which usually happened in dynamic analysis, Cheung (1968) and Zhu (1988, 1989, 1996) studied the elastic geometric nonlinear and post-buckling analysis of arbitrarily shaped thin plates and shells. Naderian (2010) and Naderian (2011) used the finite strip method for a number of applications in the field of buckling of plates and plate assemblies with

torsional and flexural buckling of the composite FRP structural plates and buckling analysis of cold-formed steel structures.

2.2.3. INTEGRATED FINITE STRIP METHOD

Based on the Spline Finite Strip Method, a new method named integrated spline finite strip method (ISFSM) was developed. The current practice of using conventional and spline finite strip methods are limited to analysis of the bridge superstructure subjected to simulated boundary conditions over the pier supports. Consequently, the interactions between the bridge deck (superstructure) and the piers (sub-structure) cannot be modeled using the conventional SFSM methods. Among a vast number of publications in this field of finite strip method, the following are worth to highlight.

Firstly, Cheung et al. (2009) have introduced a new method named integrated finite strip method (IFSM) for analyzing continuous multi-span slab-girder bridges and box girder bridges by modeling the bridge deck, the piers, and the bearings together by an assembling program, not existent in previous methods. This is due to the contribution of an individual transition section that is designed to combine the deck and the piers in the finite strip environment, while the bearings are modeled as special boundary conditions for the transition section. Also, the Column Strip (CS) was developed to model the cantilever-like piers as strip elements.

When modeling by a continuously differentiable smooth series in the longitudinal direction in the conventional finite strip method, difficulties are encountered in combining diverse types of structural components in various directions. Therefore, the analytical model developed using the finite strip method is still limited to super-structures without piers (Naderian, 2014). In the beginning, the proposed IFSM was realized in FORTRAN programs to analyze the bridges. However, Shen (2009) had modified and transferred them to the current C++ environment that is a relatively better program. The piers of the bridge are frequently replaced by certain assumed boundary conditions, and this assumption is reasonable only when the stress distribution along the girders and slab of the bridge superstructures is required. An alternative solution in considering the pier effect is to combine the finite strip bridge deck with piers modeled by other types of elements, such as the boundary element, and the interactions between the bridge deck and the piers which can be obtained via an iterative process. Nevertheless, this approach can be valid only for static and quasi-static analysis. In this regard, a cantilever type pier spline strip called Column Strip was formulated which is compatible with the well-developed spline finite strip bridge deck (Cheung et al. 2009). The integrated finite strip method was firstly applied to model a whole cable-stayed bridge by Shen (2009), which opened a new trend to apply the FSM into an integrated model same as FEM did.

In conclusion, the proposed IFSM is regarded as a tandem function that makes the separated structures into a reasonable integration. A bridge may have different structural components such as bridge deck, piers, towers, and cables. In this case, diverse types of the strip are developed to model the entire bridge as an integrated system with a flat shell spline finite strip used for modeling the deck. A column strip has been applied for modeling the piers as well as towers and based on the column strip; the cable strip has been proposed for modeling the cables. Finally, the transition section has been established so that different structural components can be linked.

In general, the displacement of a strip in the integrated finite strip method is obtained by applying B_3-spline functions in the longitudinal direction (Prenter, 1975). For the transverse direction, the idea is adopted from the finite element method in which the cubic polynomials are used to represent the transverse shape function of the strip that is the same as the spline finite strip method.

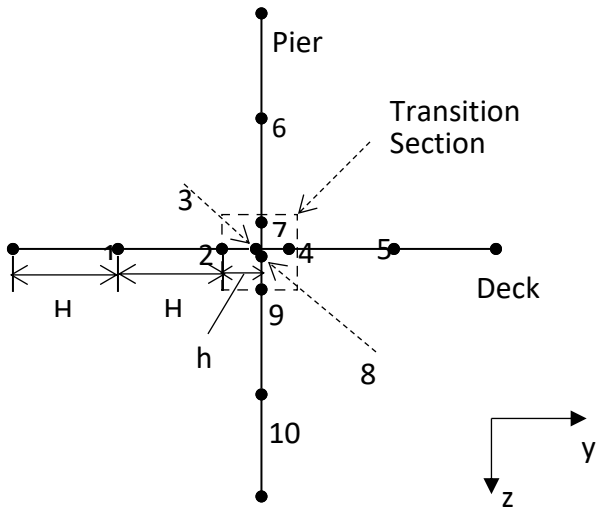

Figure 2-1 Transition Section between Deck and Pier (Shen et al. 2013)

The integrated FSM was developed for modeling the bridges to transfer the displacement and rotations of the connection parts (Shen et al. 2013). A typical transition section is shown in Figure 2-1where it is assumed that the width of standard sections is H, and the width of transition sections is h. The vertical line is one nodal line on the pier strip, while the horizontal line is one nodal line on the deck strip.

2.3. APPLICATION OF FINITE STRIP METHOD TO BRIDGES

2.3.1. FINITE STRIP MODELING OF BRIDGES

The analysis of bridge systems by using FSM has developed rapidly because of the typical slender characters of bridges which make them an acceptable fit for FSM modeling. The field of finite strip analysis in bridge engineering has extended to bridges with different geometric and boundary conditions including cylindrical orthotropic slab-girder bridge (Cheung, 1969) curved box girder bridges (Cheung, 1969), continuous slab and girder bridge (Cheung, 1969), skew slab bridge (Brown 1972), semi-analytic solution to box girder bridges (Brown, 1975), multi-span box girder bridges (Loo, 1975), haunched bridges (Cheung, 1988), and continuous haunched box girder bridges (Cheung, 1992). Static analysis of right box girder bridges with several types of the end and interior supports by spline finite strip method were first carried out by Cheung et al. (1983).

All the literature about the application of finite strip method on bridge engineering is limited to modeling the bridge deck. Other components like towers, piers, cables and bearing are modeled by applying special boundary conditions. It is a real disadvantage of the finite strip method in bridge modeling. Fortunately, this problem has been recently overcome by introducing the integrated finite strip method by Cheung et al. (2009). It makes the numerical analysis of bridges possible, especially for complicated ones, like long-span suspension and cable-stayed bridges.

Shen et al. (2013) provided a precise definition of general FSM modeling of the bridges in modern FSM analysis for bridges. Two types of strips were used to model bridges as shown in Figure 2-2, and Figure 2-3 below. Beyond that, one-dimensional spline strip is proposed for modeling the cables (Shen et al. 2013). By representing the entire bridge as a single integrated system, the actual static and dynamic behavior of the bridge can be studied.

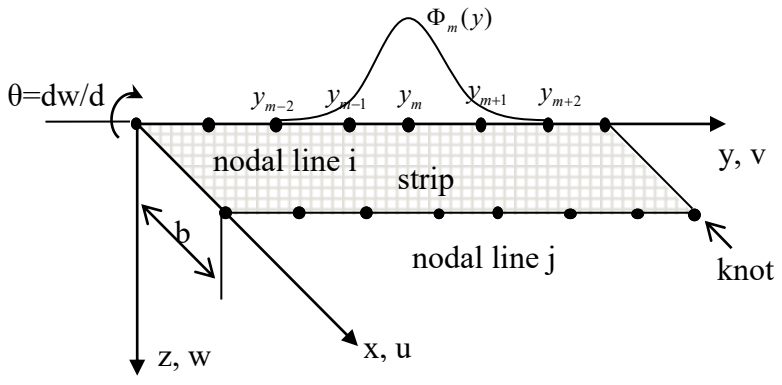

Figure 2-2 Flat shell spline finite strip for deck modeling (Shen et al. 2013)

When a complicated dynamic analysis like nonuniform seismic analysis is being considered, the ground excitations are transmitted from the piers to the super-structure, and the dynamic characteristics of the piers play a major role in the prediction of the bridge responses.

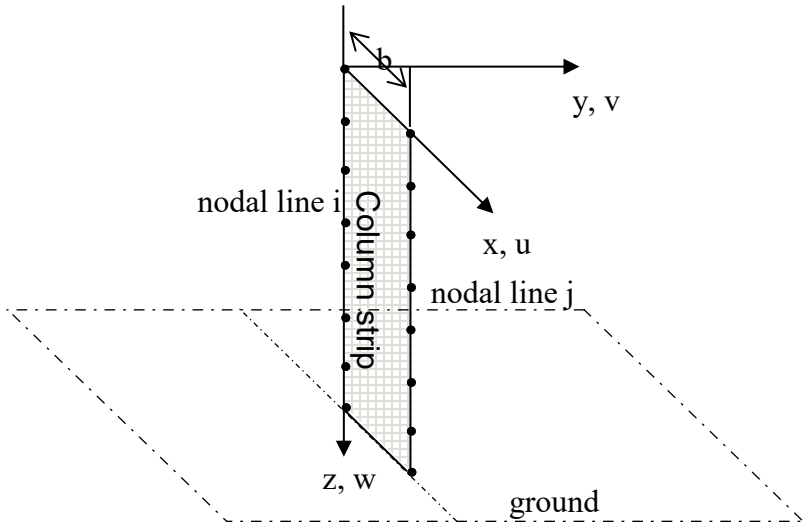

Figure 2-3 Column strip in local coordinate system (CS) (Shen et al. 2013)

The finite strip method requires the discretization of the continuous elements; thus, the strips are divided by shared nodal lines; on each line, there are knots which are shared between the adjacent strips. Therefore, the strips are connected to each other along a discrete number of nodal lines which coincide with the longitudinal boundaries of the strip. Due to the use of continuous functions in the longitudinal direction, the number of DOF on a strip nodal line is usually lower than that used in the finite element method when modeling the same element (Cheung, 1976). For example, for estimating the plate bending, w and θ_x are defined at each strip nodal line of the FS method, while w θ_x and θ_y, exist at each element node for FEM. However, the knots on the nodal lines used in FS are only the points employed for the spline interpolation, and are used to insert the internal supports and point loads, in contrast with the nodes in the finite element method (Shen et al. 2013). Another difference is that the knots are also shared between the adjacent strips, and this decreases significantly the number of DOF when compared with FEM.

2.3.2. STATIC ANALYSIS OF BRIDGES

The finite strip method has widely been used for the real beginning development on bridges, in particular for the simple bridges. Cheung et al. (1969) used the spline finite strip method for application analysis of the curved slab-girder bridge, which became the theoretical foundation for the spline FSM applied on the bridges regarding the static analysis. After that, several bridges were modeled and analyzed by the finite strip method that had been mentioned before. Among them,

Dey (1980) firstly developed the bending and deflection analysis for orthotropic curved bridge decks by the FSM. With the rapid development of FEM on bridges by the development of commercial software, ideas also came from the current FSM codes.

Regarding the static analysis of the simple support bridges, Shen et al. (2013) applied concentrated loads on a multi-span continuous concrete slab-girder bridge by using the spline finite strip method, as shown in Figure 2-4. Table 2-1 to Table 2-4 show the displacement response under four combinations of concentrated loads. It is obvious that the proposed FSM has a very closed estimation for the displacement under those concentrated loads.

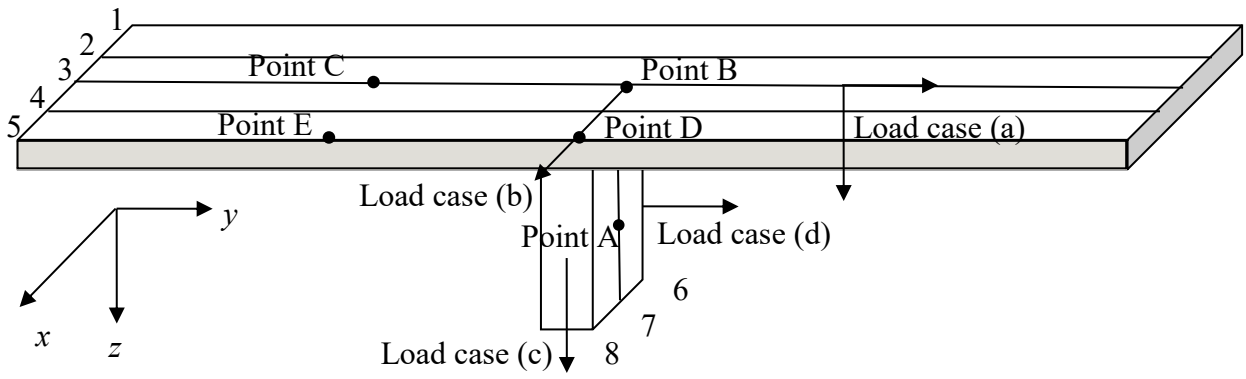

Figure 2-4 A Simple Slab Bridge: Structural Layout (Shen et al. 2013)

Table 2-1 Load Case (a) (Shen et al. 2013)

		Deck: nodal line 3					Pier: nodal line 7		
	y (m)	0 (left)	8	16	24	32 (right)	**z (m)**	0 (top)	2
v (m)	SFSM	0.000065	0.000125	0.000205	0.000343	0.000150	SFSM	0.000205	0.000066
	FEM	0.000063	0.000123	0.000203	0.000355	0.000145	FEM	0.000203	0.000064
w (m)	SFSM	-0.000799	-0.153012	0.000101	0.388455	0.003541	SFSM	0.000101	0.000046
	FEM	-0.000757	-0.152888	0.000095	0.388016	0.003352	FEM	0.000095	0.000045

Table 2-2 Load Case (b) (Shen et al. 2013)

		Deck: nodal line 3			Pier: nodal line 7		
	y (m)	0 (left)	8	16 (middle)	**z (m)**	0 (top)	2
u (m)	SFSM	-0.000021	0.000865	0.001695	SFSM	0.001695	0.000558
	FEM	-0.000016	0.000856	0.001671	FEM	0.001671	0.000548

Table 2-3 Load Case (c) (Shen et al. 2013)

		Deck: nodal line 4			Pier: nodal line 8		
	y (m)	0 (left)	8	16 (middle)	**z (m)**	0 (top)	2
w (m)	SFSM	0.00000005	0.000117	0.000203	SFSM	0.000203	0.000223
	FEM	0.00000005	0.000117	0.000202	FEM	0.000202	0.000240

Table 2-4 Load Case (d) (Shen et al. 2013)

		Deck: nodal line 2				Pier: nodal line 6	
	y (m)	0 (left)	8	16 (middle)	**z (m)**	0 (top)	2
v (m)	SFSM	0.000028	0.000062	0.000149	SFSM	0.000149	0.001838
	FEM	0.000026	0.000059	0.000144	FEM	0.000144	0.001743

When it came to the cable-stayed bridges, Shen (2009) extended the FSM to the cable-stayed bridges by nonlinear analysis method, where the finite strip method is employed to model the girder of a cable-stayed bridge. He applied specified concentrated load on the deck to determine the stiffness matrix and the mass matrix to develop the deflections and moment of the deck. Naderian et al. (2015) used the Integrated Finite Strip Method to analyze the static results for the Kap Shui Mun Bridge. They showed that the proposed solution proves to be very efficient in yielding accurate results, in a minimum amount of time with high convergence. They applied several concentrated loads both on the deck and towers, which corresponding displacements were considered for the static analysis. Figure 2-5 and Figure 2-6 show the critical locations and the specific loads that applied on the bridge.

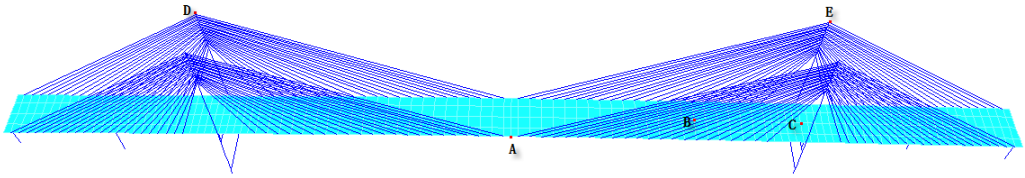

Figure 2-5 Critical locations (Naderian et al. 2015)

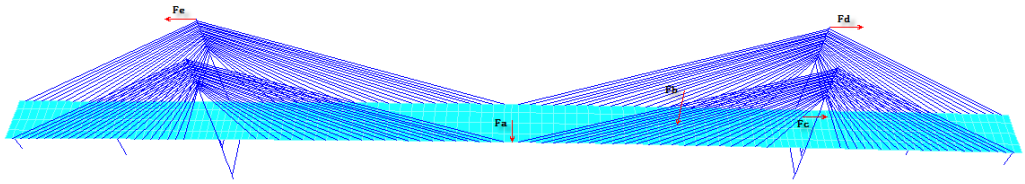

Figure 2-6 Applied concentrated loads (Naderian et al. 2015)

As the test locations and the specified loads applied as below, they summarized the displacements responds in Table 2-5 to Table 2-9 as follows. It is also indicated that the proposed FSM (IFSM) estimates a similar displacement response under those concentrated loads for the concrete cable-stayed bridge. Moreover, these corresponding displacement responses will be compared when

considering the displacement behavior for the composite cable-stayed bridge in Chapter 5 produced by the laminated finite strip method.

Table 2-5 Displacement under static load ''Fa''. (Naderian et al. 2015)

		Location	A (375 m)	B (493.4 m)	C (590 m)	D (Tower 1 left – top)	E (Tower 2 left – top)
Load "Fa"	*u* (mm)	IFSM	61.4	42.4	16.2	93.3	79.2
		FEM	61.3	42.6	16.4	92.4	76.8
	v (mm)	IFSM	2.7	1.2	1.1	69.7	66.8
		FEM	2.7	1.2	1.1	69.7	66.7
	w (mm)	IFSM	320.4	170.9	1.1	4.3	4.5
		FEM	318.1	169.9	1.1	4.2	4.4

Table 2-6 Displacement under static loads ''Fa'' and ''Fb''. (Naderian et al. 2015)

		Location	A (375 m)	B (493.4 m)	C (590 m)	D (Tower 1 left – top)
Load "Fa + Fb"	*u* (mm)	IFSM	61.4	42.4	16.2	93.2
		FEM	61.3	42.6	16.4	92.4
	v (mm)	IFSM	2.0	0.4	1.3	59.0
		FEM	1.9	0.4	1.3	59.1
	w (mm)	IFSM	260.2	108.7	0.3	4.7
		FEM	260.6	108.8	0.3	4.6

Table 2-7 Displacement under static loads ''Fa'', ''Fb'' and ''Fc''. (Naderian et al. 2015)

		Location	A (375 m)	B (493.4 m)	C (590 m)	D (Tower 1 left – top)	E (Tower 2 left – top)
Load "Fa + Fb + Fc"	*u* (mm)	IFSM	59.0	40.2	15.2	90.3	72.2
		FEM	58.9	40.3	15.4	89.4	74.4
	v (mm)	IFSM	4.5	3.0	1.3	56.7	46.2
		FEM	4.5	3.0	1.3	56.7	46.1
	w (mm)	IFSM	259.9	108.9	0.3	4.7	5.3
		FEM	260.2	109.0	0.3	4.6	5.4

Table 2-8 Displacement under static loads ''Fa'', ''Fb'', ''Fc'' and ''Fd''. (Naderian et al. 2015)

		Location	A (375 m)	B (493.4 m)	C (590 m)	D (Tower 1 left – top)	E (Tower 2 left – top)
Load "Fa + Fb + Fc + Fd"	*u* (mm)	IFSM	58.3	39.6	14.1	79.9	54.0
		FEM	58.1	39.7	14.3	79.2	56.0
	v (mm)	IFSM	7.2	5.7	3.7	65.9	138.7
		FEM	7.1	5.7	3.7	65.7	138.3
	w (mm)	IFSM	263.1	131.8	0.6	4.0	3.9
		FEM	264.6	131.9	0.6	3.9	4.0

Table 2-9 Displacement values under static load ''Fe''. (Naderian et al. 2015)

		Location	A (375 m)	B (493.4 m)	C (590 m)	D (Tower 1 left – top)	E (Tower 2 left – top)
Load "Fe"	u (mm)	IFSM	0.9	1.2	0.9	21.6	9.2
		FEM	1.0	1.3	0.9	21.3	9.4
	v (mm)	IFSM	0.3	1.3	3.5	162.6	76.7
		FEM	0.3	1.3	3.6	162.2	76.5
	w (mm)	IFSM	324.1	181.6	1.2	0.4	1.6
		FEM	325.4	181.5	1.2	0.4	1.6

2.3.3. DYNAMIC ANALYSIS OF BRIDGES

For a long time, engineers just used the finite strip method to conduct the static analysis both to the short-span bridges and long-span bridges. This is because the widespread use of the basic C++ programs had their limits due to the development when extended to the dynamic analysis. Moreover, the analysis of the bridges by FSM was usually divided by several sub-programs: deck, pier and so on. In this case, these separate programs comparatively independent before the generalizing of the IFSM.

When it comes to the dynamic analysis of bridges, initially it is easy to divide it into two main parts: bridge aerodynamics under wind loads, and earthquake excitations. The finite strip method is also capable of investigating aerodynamics of bridges; the finite strip method has been extended to flutter analysis by Lau et al. (2000). The firstly introduced a 3D flutter analysis of bridges by spline finite-strip method by simulation by numerical simulations, which provided a fundamental theory for the dynamic analysis for aerodynamics. A 3D self-excited vibration equation of the finite-strip model can be established through the dynamic equilibrium condition as follows:

$$[M]\{\ddot{X}\} + [D]\{\dot{X}\} + [K]\{X\} = \frac{1}{2}\rho U^2 \left([A_s]\{X\} + \frac{1}{U}[A_d]\{\dot{X}\}\right) \tag{2-1}$$

where $[M]$ is the mass matrix; $[D]$ is the structural damping matrix; $[K]$ is the stiffness matrix; $[A_s]$ represents the aerodynamic stiffness matrix, and $[A_d]$ is the aerodynamic damping matrix. It is noted that the effective stiffness of the bridge system during wind response is related to the structural stiffness and the aerodynamic stiffness. Similarly, the aerodynamic damping term contributes to the overall damping behavior of the bridge.

Considering the displacement transformation relationship $\{X\} = [\phi]\{\xi\}$, where $[\phi]$ is the mode shape matrix that involves all of the participating modes, $\{j\}$ is the vector of generalized coordinates, and assuming the generalized coordinates have a damped harmonic form, the dynamic equation of motion can be expressed as follows:

$$\left[[M]^g\left(\frac{U}{B}\right)^2 P^2+[D]^g\left(\frac{U}{B}\right)P+[K]^g-\frac{1}{2}\rho U^2\left([A_s]^g+\frac{1}{B}\right)[A_d]^g P\right]\{R\}\exp\left(\frac{U}{B}Pt\right)=0 \quad (2\text{-}2)$$

$$[M]^g=[\phi]^T[M][\phi];[D]^g=[\phi]^T[D][\phi];[K]^g=[\phi]^T[K][\phi] \quad (2\text{-}3)$$

where U is the wind velocity; P is the complex variable defined as $P=K(\delta+i)$; K is the reduced frequency, and d is regarded as logarithmic decrement. However, the aerodynamic extension is not a pure finite strip solution but combined with finite element method.

As a necessary sub-step, natural frequencies were always produced as a reference for the dynamic analysis. Table 2-10 shows the natural frequencies for the first ten modes for Nanpu Bridge. And as the following studies, Table 2-11 shows critical flutter frequency of simple support plate divided by different strips and nodal line, which is just a simple support plate that was put into the analysis by FSM for wind loads.

Table 2-10 Natural Frequency of Nanpu Bridge (Lau et al. 2000)

Mode number (1)	Frequency (Hz) (2)	Mode Shape (3)
1	0.1294	Floating antisymmetrical
2	0.3309	Heave (girder) symmetrical
3	0.3786	Sway (girder) symmetrical
4	0.4030	Heave (girder) antisymmetrical
5	0.4995	Torsion (girder) symmetrical
6	0.5138	Bending (pylon) antisymmetrical
7	0.5579	Bending (pylon) symmetrical
8	0.5581	Heave (girder) symmetrical
9	0.6097	Torsion (girder) antisymmetrical
10	0.6268	Heave (girder) antisymmetrical

Table 2-11 Critical Flutter Frequency of Simple Support Plate (Hz) (Lau et al. 2000)

Number of strips (1)	Number of nodal lines (2)	Number of Sections in Y-Direction					
		4 (3)	8 (4)	10 (5)	12 (6)	16 (7)	20 (8)
1	2	0.1056	0.1047	0.1048	0.1046	0.1045	0.1046
2	3	0.1053	0.1045	0.1045	0.1042	0.1044	0.1045
4	5	0.1053	0.1044	0.1045	0.1043	0.1044	0.1045
8	9	0.1053	0.1044	0.1045	0.1043	0.1044	0.1045

Naderian et al. (2015) analyzed the free vibrations of the cable-stayed bridges by using FSM. Table 2-12 shows the natural frequencies developed by the IFSM for Kap Shui Mun Bridge.

Table 2-12 Comparison of natural frequencies with updating FEM results. (Naderian et al. 2015)

Mode	Measured frequencies $f_{exp}(Hz)$	FE frequencies $f_{FEM}(Hz)$	Updated FE frequencies (Hz)	FS frequencies $f_{FSM}(Hz)$
V1	0.39	0.41	0.40	0.42
V2	0.66	0.58	0.66	0.85
V3	1.07	0.93	0.97	1.00
V4	1.54	1.51	1.53	1.65
V5	1.81	1.74	1.82	1.90
L1	0.49	0.49	0.48	0.52
L2	1.25	1.15	1.21	0.93
L3	2.12	2.45	2.26	1.35
T1	0.83	0.77	0.81	0.75
T2	1.39	1.62	1.50	1.34
T3	1.90	2.18	1.91	1.89

Shen et al. (2013) firstly developed the dynamic analysis of a continuous multi-span bridge by the integrated FSM. Also, with the characteristic property matrices well defined in the FSM environment, the conventional characteristic equation of motion can be constructed. They mainly used MATLAB programs develop the free vibration analysis, which frequency domain analysis was determined by using the Pseudo Excitation Method (PEM). To determine the accuracy of the IFSM for dynamic analysis in the frequency domain, Figure 2-7 and Figure 2-8 show the Log (PSD) curves that compare the FEM and IFSM regarding the power spectrum density. Also, the computer times required by different methods are compared in Table 2-13.

Table 2-13 Computational times (Shen et al. 2013)

Method	Static Analysis	Dynamic Analysis	
		262144 sampling freq.	524288 sampling freq.
SFSM	4.717s	8043.539s	16442.297s
FEM	5.296s	8817.141s	17874.802s

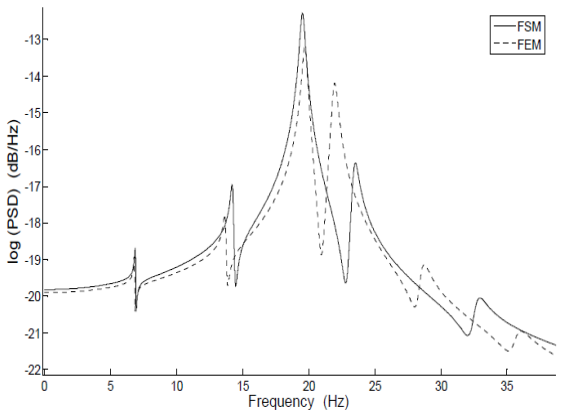

(a) at point A in the x direction

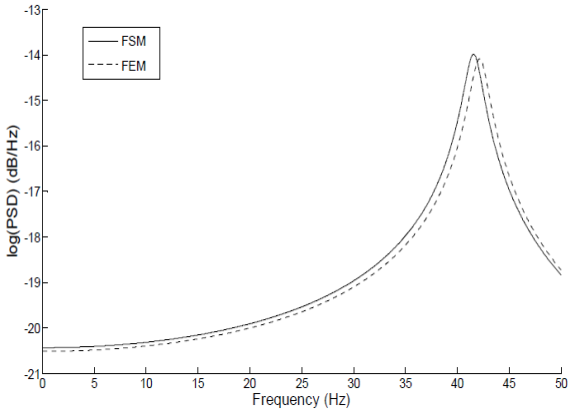

(b) at point B in the y direction

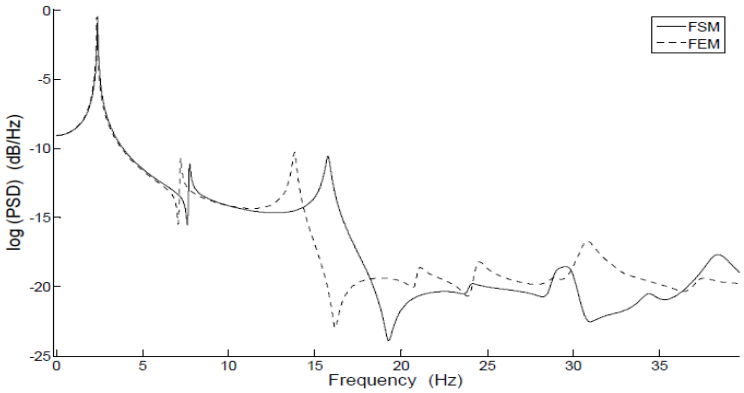

(c) at point C in the z direction

Figure 2-7 PSD of displacement response applied ground motion: white noise (Shen et al. 2013)

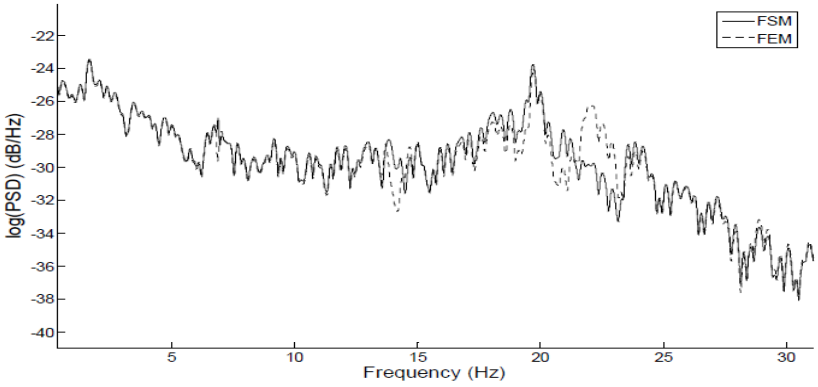

(a) at point D in the x direction

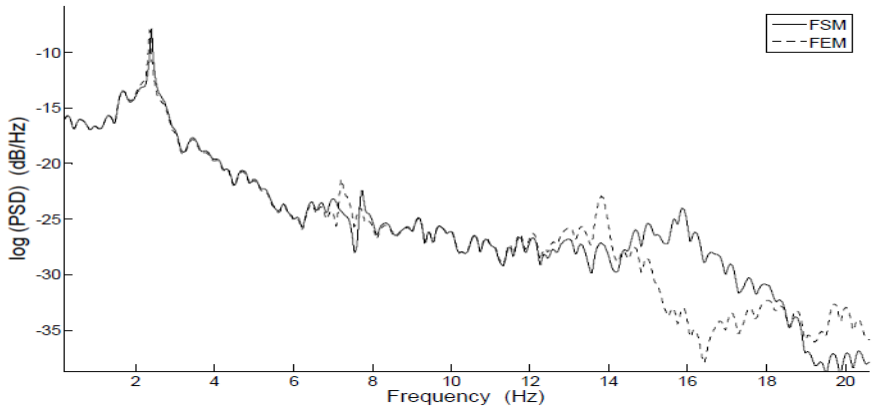

(b) at point E in the z direction

Figure 2-8 PSD of displacement response applied ground motion: Chichi earthquake (Shen et al. 2013)

Furthermore, Naderian et al. (2016) extended the dynamic analysis by FSM to the long-span cable-stayed bridges. They provided a very efficient, integrated framework for seismic studies of long-span cable-stayed bridges, which is concentrated on the time history analysis under real earthquake waving by FSM. Figure 2-9 shows the critical points to receive the seismic time history response investigation by applied seismic excitations. The dynamic time history analysis, both the FEM developed by SAP 2000 and FSM developed by MATLAB programs can be used to determine dynamic response under seismic excitations. Figure 2-10 gives the relative time domain response under Chichi earthquake excitation, which has a significant agreement between FEM and FSM both for acceleration and corresponding displacement.

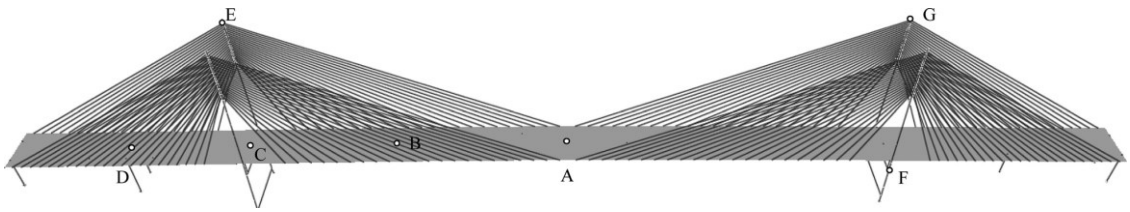

Figure 2-9 Some critical points for seismic response investigation (Naderian et al. 2016)

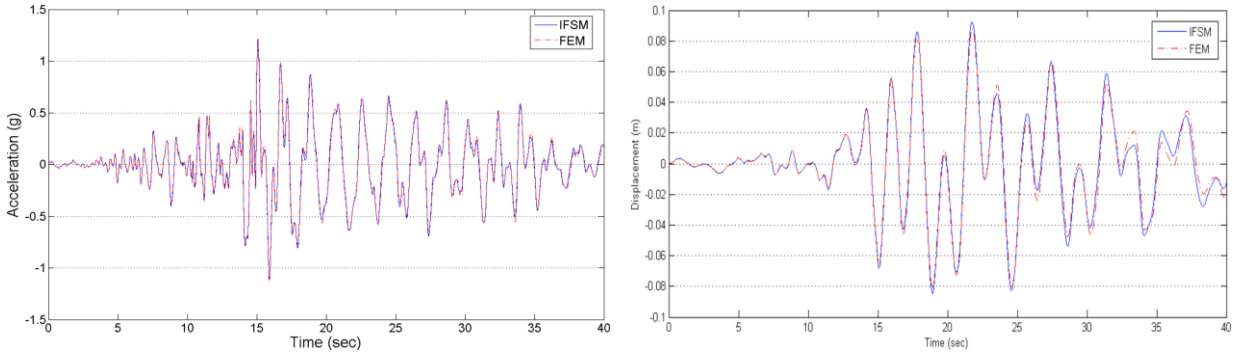

(a) Transverse acceleration responses (b) Transverse displacement responses

Figure 2-10 Responses under uniform Chichi earthquake excitation at Point B on the deck (Naderian et al. 2016)

By reviewing of previous work, inclusion, Shen et al. (2009) built the basic FS method using the C++ environment for both a typical slab-girder bridge model and the Kap Shui Mun Cable-stayed Bridge. Also, Shen et al. (2013) investigated the dynamic analysis for that slab-girder bridge by the Pseudo Excitation Method produced by the MATLAB programs.

Furthermore, Naderian et al. (2015) further developed the IFSM method and determined the accuracy of the results by investigating the response of the Kap Shui Mun Cable-stayed Bridge to concentrated static loads and seismic time history excitations (Naderian et al. 2016). Both the displacement results at critical locations and the time history responses had demonstrated the correctness of their models. Moreover, Naderian et al. (2017) built a MATLAB program to model a composite FRP plate element with different material properties. He also investigated a typical laminated FRP plate for static displacement analysis and the mesh sensitivity analysis by using the finite strip method through a C++ program.

The current research expands the previous researches on FSM, to a new milestone, by integrating the laminated FRP plate model into the typical slab-girder bridge model and the Kap Shui Mun Cable-stayed Bridge, thus proving the applicability of a new method named laminated finite strip method (LFSM) to model and analyse the composite slab-girder bridge and the composite cable-stayed bridge. More specifically, different laminates with various layout configurations (FRP deck thickness; distribution of layers; layer orientations; etc.) had been designed and applied to model the composite deck for both bridges. The comparison has been made between the concrete bridges and composite bridges modeled by both the FEM and the LFSM under static analysis and dynamic analysis, thus validating the applicability of LFSM to composite bridges. A major contribution of the current research was the frequency domain analysis which was developed for the composite cable-stayed bridges and continuous composite bridges, using the LFSM, for the first time.

2.4. ADVANCED COMPOSITE MATERIALS IN CIVIL ENGINEERING

2.4.1. INTRODUCTION AND GENERAL PROPERTIES OF COMPOSITE MATEIRLAS

The total cost of repairing structures in Canada affected by corrosion deterioration is estimated at $74 billion (Noël, 2016). FRP reinforcement provides a corrosion resistant alternative to steel rebar that can increase the service lives of concrete structures and reduce maintenance costs. They were originally developed for use in the automotive and aerospace sectors. Moreover, FRPs have recently been increasing in use in civil engineering projects due to reductions in costs, which are available in a wide range of types and shapes for various applications. FRP materials are a composite material made of high strength fibers and a polymer matrix, where fibers provide strength and stiffness, while the polymer matrix binds the fibers, protects them, and transfers forces between fibers. Typically, there are mainly four types of FRPs (AFRP, BFRP, CFRP, and GFRP), among which are primarily used to bridges: glass fiber-reinforced polymer (GFRP) and carbon fiber-reinforced polymer (CFRP).

Nowadays, there are many capable characteristics that FRPs can reach, in summary, Table 2-14 shows the comparison of the two types of FRPs.

Table 2-14 Comparisons of the material characteristics (Adapted from Noël, 2016)

Materials	Glass FRP	Carbon FRP
Costs	Lower cost	Higher cost
Usage	Most widely used	Limited used
Characteristics	Lowest strength and stiffness	Higher strength and stiffness

To distinguish the Figure 2-11 gives a comparison of the material characteristics of various kinds of FRP composites with the concrete and steel.

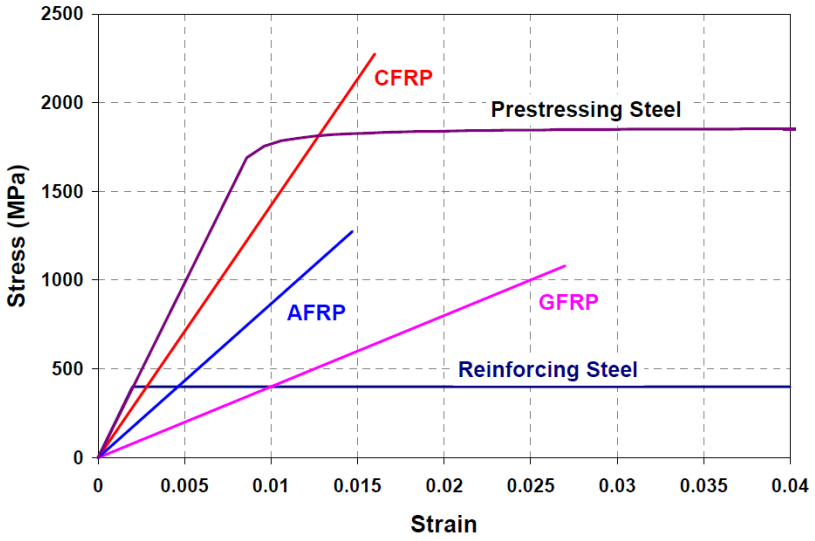

Figure 2-11 Strain-stress comparison between composites with concrete and steel materials (Noël, 2016)

Compared with the traditional materials like concrete and the steel structures, FRPs have their characteristics that attracted many research and practice in the engineering construction. As a conclusion, Table 2-15 shows the advantages and disadvantages of the FRP materials.

Table 2-15 The advantages and disadvantages of the FRP materials (Adapted from Noël, 2016)

COMPARISON	ADVANTAGES	DISADVANTAGES
STRENGTH	High strength to weight ratio	Low compression and shear strength and lower elastic modulus
DURABILITY	Excellent durability (GFRP)	Lower fire resistance
RESISTANCE	Excellent fatigue characteristics (CFRP)	Lower alkaline resistance and prone to creep and creep rupture (GFRP)
CONSTRUCTION	Ease the speed of installation	Must be formed and bent during manufacture and properties vary by manufacturer
SPECIAL CHARACTERS	Electromagnetically neutral	Linear elastic to failure
COST	Ability to tailor mechanical properties	High initial cost compared to steel

2.4.2. DEVELOPMENT OF COMPOSITE MATERIALS IN ENGINEERING APPLICATION

Fiber-reinforced polymer (FRP) materials have shown tremendous potential as an alternative reinforcement for reinforced and prestressed concrete structures. Many reinforced concrete structures are showing extensive signs of deterioration due to corrosion of steel reinforcement.

Mohammed et al. (2001) developed constitutive modeling, and failure criteria of carbon-fiber reinforced polymers. He firstly analyzed the failure criteria of the CFRP under the high strain rates for CRFP as what was usually done on the bridges. In further research, Mohammed et al. (2006) gave the detailed explanation of how to determine the rate-dependent constitutive equations for the CFRP materials. They applied the CFRP which is much more recommended than the GFRP when regardless the cost. In the meantime, the CFRP named IM6G carbon fiber and 3501–6 epoxy matrix were tested by their approaches.

With the rapid development of the advanced composite materials, the building structures were firstly applied such as beams and columns of buildings. Fang et al. (2009) applied the FRP on the concrete beams with hybrid FRP and stainless-steel reinforcements in a theoretical model, which is concentrated on the nonlinear behavior under failure modes. Consequently, engineers adopt the composite beams and columns with the steel materials by the advanced FRP because of its high stiffness capacity. Ilker et al. (2015) theoretically modeled the hybrid FRP/steel reinforced concrete beams and compared the static results with the experimental data.

2.4.3. APPLIED COMPOSITE MATERIALS TO BRIDGES

With the wide used of composite materials in structural engineering, specifically, the FRPs have been employed in a wide variety of structural bridges applications, from reinforced concrete deck slabs to post-tensioned parking garages. Manalo et al. (2012) had developed an experimental investigation into the composite behavior of a hybrid FRP bridge girder with an overlying concrete deck, which is an early experimental application of FRPs on the bridges that applied the full composite materials (CFRP and GFRP) on girders of the bridge supporting a concrete slab. Noël and Soudki (2016) firstly tested the effect of pre-stressing on the performance of a GFRP-reinforced concrete slab bridge strips.

Overall, regarding the bridges, several main parts such as a deck, cables, and girders have been designed and tested by composite materials.

2.4.4. HYBRID COMPOSITE CABLE-STAYED BRIDGES

Dawe et al. (2002) carried out extensive research on the utilization of both conventional and spline finite strip method in determining the behavior of composite laminated, prismatic plate, and shell structures based on the thin plate theory introduced previously, that was the basis for modeling the laminated FRP decks by the current FSM. They used the method for analyzing a variety of problems like buckling stresses and natural frequencies of the single span, and the multi-span bridges, the post-buckling response of plate structures, thermal buckling and the transient response

to dynamic loading of flat plates. The nonlinear analysis of thick and laminated plates was also developed by Kong and Cheung (1995).

As the cable-stayed bridges can only reach the second position among long-span bridges compared with the suspension bridges, engineers try to develop hybrid composite cable-stayed bridges to extend the strain-stress capacity of the cable-stayed bridges. Moreover, some researchers tried to apply only composite FRPs to the deck for the long-span bridges that can reduce the self-weight of bridges effectively. Almansour and Cheung (2010) firstly analyzed the structural performance of laminated FRP box girder bridge deck and developed the comparison to slab on pre-stressed concrete girder bridge. Figure 2-12 is the configurations of layout and the structural design of the FRP box girder deck. In the same time, they developed a critical procedure to design the composite decks for multi-scale analysis.

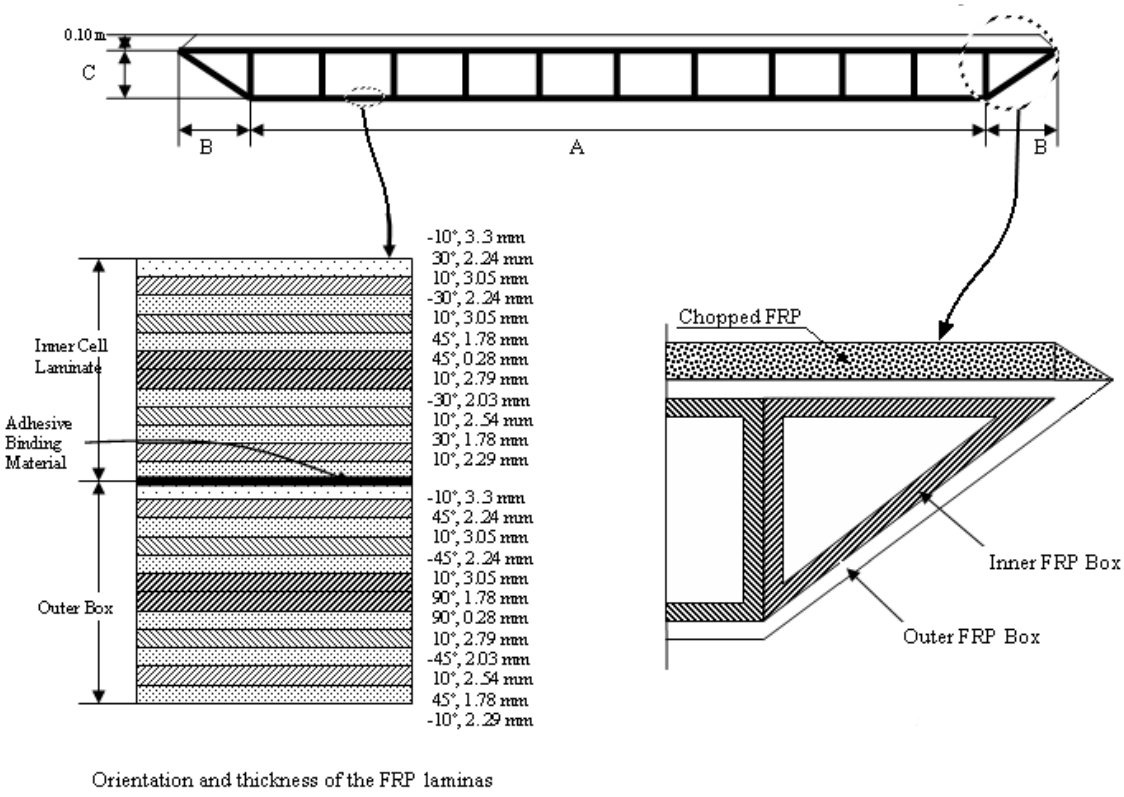

Figure 2-12 Plate orientated box-girder FRP deck system (Almansour et al. 2010)

By following the research of Almansour and Cheung (2010), Peng et al. (2015) improved the theoretical procedure which was more efficient in the real design process. As the laminated FRP material involved in the proposed deck sections has anisotropic properties, the procedure should include proper material failure criteria that must be examined in various stages of the procedure.

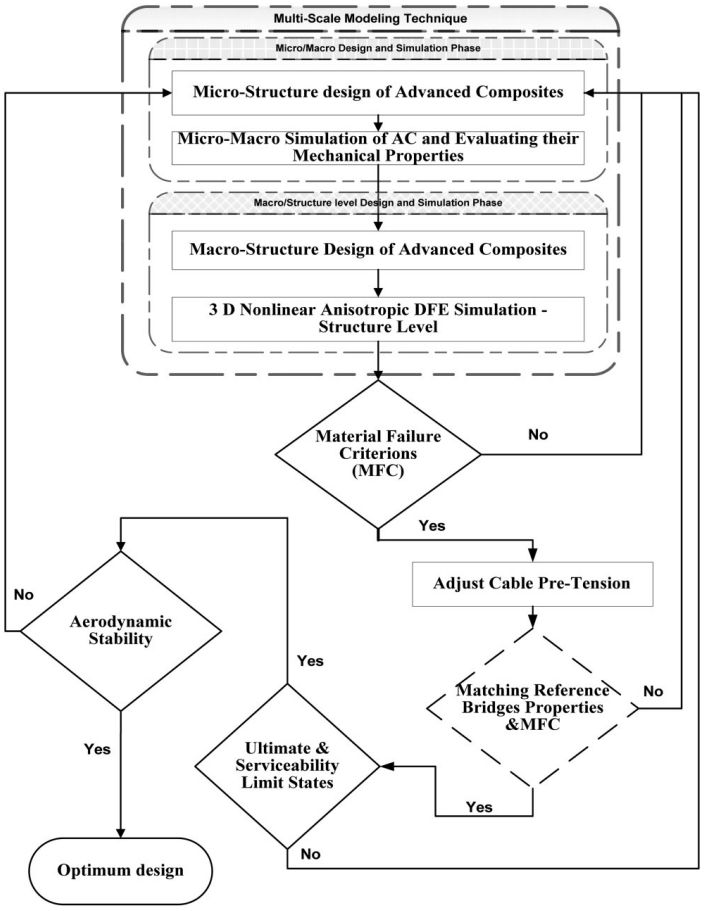

Figure 2-13 Analysis and design procedure of hybrid long span cable-stayed bridges. (Almansour et al. 2010)

Figure 2-13 provides the detailed improved design procedure, which was designed according to Canadian Highway Bridge Design Code 2001 (CHBDC-01) using CL-625-ONT truck and lane loading. Typically, they developed three types of models for the composite FRP box girders in Figure 2-14. In detail, Table 2-16 gives the three laminas alignment angle designs and the three thickness designs for the three reference bridges using GFVM advanced composite laminas, which gives an excellent and improved idea of the layout of laminas.

Table 2-16 Laminates macro design of E-glass fiber and vinylester matrix (GFVM) advanced composite with different laminas alignment and thickness sets-Annacis Island bridge and second Chang River bridge. (Almansour et al. 2010)

	Laminate thickness (m)			Laminas alignment angle (with respect to the bridge longitudinal direction) (degree)					
				LAa		LAb		LAc	
Lamina NO	LTha	LThb	LThc	Inner laminate	Outter laminate	Inner laminate	Outter laminate	Inner laminate	Outter laminate
1	0.0033	0.0066	0.0099	–10	–10	–20	–20	–30	–30
2	0.00224	0.00448	0.00672	30	45	40	55	50	65
3	0.00305	0.0061	0.00915	10	10	20	20	30	30
4	0.00224	0.00448	0.00672	–30	–45	–40	–55	–50	–65
5	0.00305	0.0061	0.00915	10	10	20	20	30	30
6	0.00178	0.00356	0.00534	45	90	55	–80	65	–70
7	0.00178	0.00356	0.00534	45	90	55	–80	65	–70
8	0.00279	0.00558	0.00837	10	10	20	20	30	30
9	0.00203	0.00406	0.00609	–30	–45	–40	–55	–50	–65
10	0.00254	0.00508	0.00762	10	10	20	20	30	30
11	0.00178	0.00356	0.00534	30	45	40	55	50	65
12	0.00229	0.00458	0.00687	–10	–10	–20	–20	–30	–30

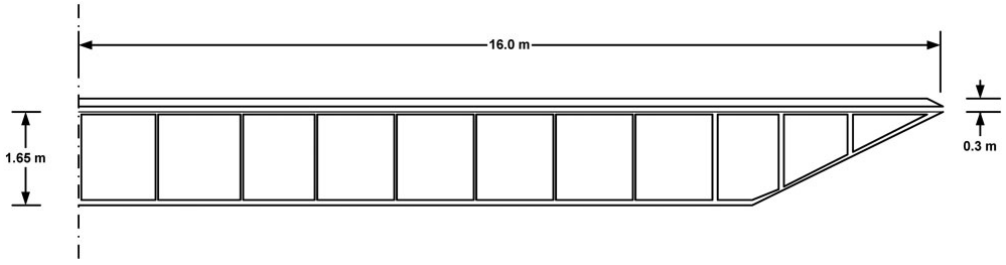

(a) Model I dimensioned for second Chang River cable-stayed bridge

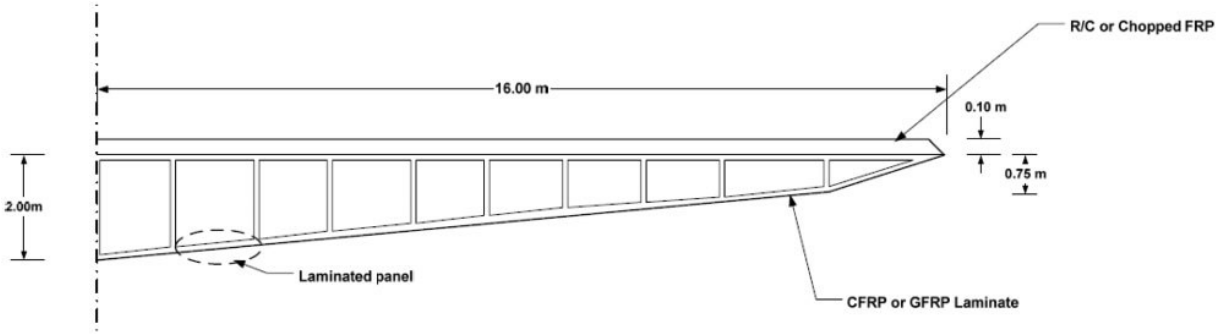

(b) Model II dimensioned for second Chang River cable-stayed bridge

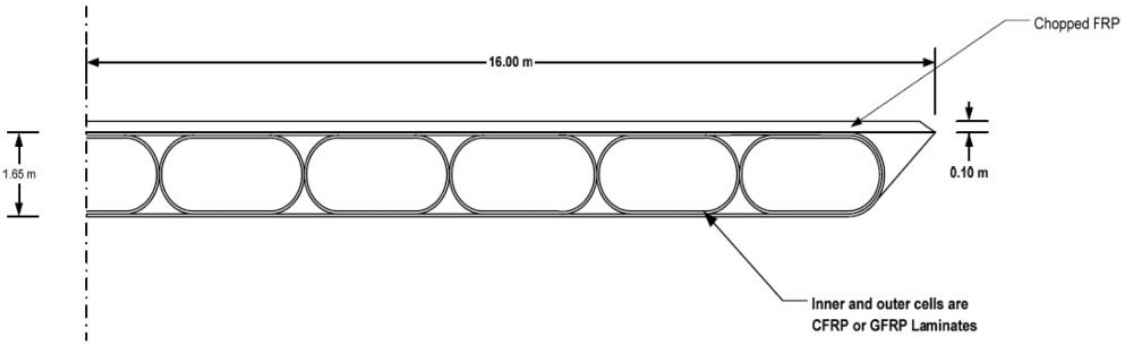

(c) Model III dimensioned for second Chang River cable-stayed bridge

Figure 2-14 Three models dimensioned for second Chang River cable-stayed bridge. (Almansour et al. 2010)

In the same time, Chan et al. (2013) tried to use only one FRP material to design the box girders for Kap Shui Mun Bridge. Figure 2-15 is the layout of the FRP bridge deck system for the Kap Shui Mun Bridge, which had been applied in the lab environment. Table 2-17 shows the specific section properties of the proposed box girder.

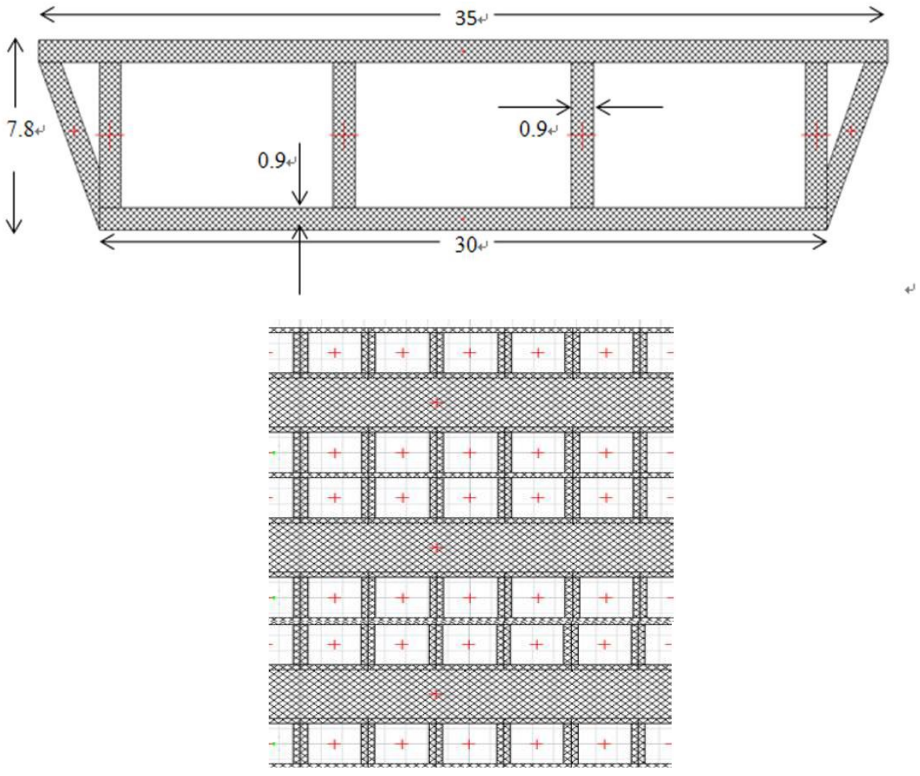

Figure 2-15 The design of the FRP bridge deck system and the tube's orientation. (Chan et al. 2013)

Table 2-17 Sectional properties of the FRP deck system (Chan et al. 2013)

Property	Value
Cross section area/m^2	12.7
Torsional constant/m^4	247.4
Moment of Inertia about 3 axis/m^4	105.1
Moment of Inertia about 2 axis/m^4	1240
Shear area in 2 direction/m^2	3.34
Shear area in 3 direction/m^2	7.19
Rotational mass / kg·m	4.616×10^6

Similarly, first, fifteen natural frequencies were developed by modes for both original Kap Shui Mun Bridge and the determined FRP bridge. Consequently, the mode shapes had changed with the natural frequencies that were described in Table 2-18.

Table 2-18 Natural modal frequencies of the bridge systems (Chan et al. 2013)

	Mode No.	Ori. Model	Mode Shape	FRP Model	Mode Shape
FREQUENCY / s^{-1}	1	0.40902	B	0.46053	B
	2	0.49862	P	0.50152	P
	3	0.59413	B	0.65015	P
	4	0.659	P	0.69357	L
	5	0.72181	L	0.73535	B
	6	0.83962	T	1.0222	B
	7	0.93887	B	1.1387	T
	8	1.2509	P	1.2646	B
	9	1.2527	L	1.3466	L
	10	1.3673	P	1.3789	P
	11	1.3771	P	1.3867	P
	12	1.5224	T	1.5205	T
	13	1.7022	T	1.6882	B
	14	1.7305	B	1.8154	L
	15	1.809	P	1.9654	T

*B-deck vertical bending; L-deck lateral bending; T-deck torsion; P-pylon swaying.

2.5. FREQUENCY DOMAIN ANALYSIS FOR BRIDGES

Until present, the FEA was always a trustable method that was used for the frequency domain analysis no matter for a seismic response or aerodynamic response. For a long-time history, frequency domain was produced from Fourier Transform (FT) or Fast Fourier Transform (FFT), which were a mathematical transformation from the time domain response. This method had been improved by Welch (1967) who developed an improved new method based on FT. This can

achieve a reduction in the number of computations and the required storage and is a more convenient application in non-stationarity tests. This so-called P Welch's method which was widely used in FEA for bridges in the past several decades.

Mohammed et al. (2001) analyzed the frequency domain of long-span suspension bridges subjected to nonuniform seismic motions, which was developed by FEM. Figure 2-16 shows the displacement PSD for different cases at mid-span on the suspension bridge.

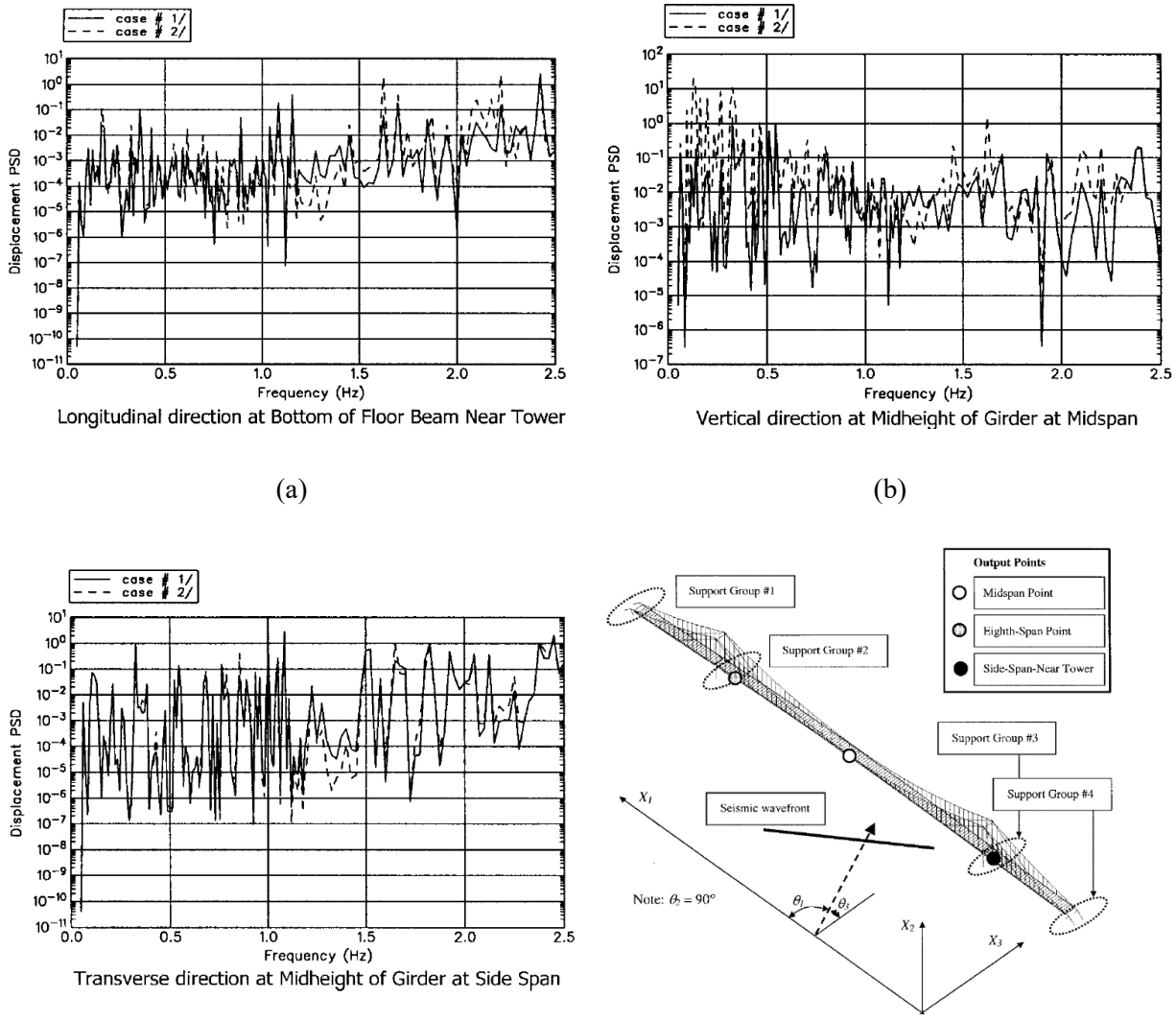

(a) (b)

(c) (d) Geometry of Suspension Bridge Problem

Figure 2-16 PSD at various locations (Mohammed et al. 2001)

Also, Carassale et al. (2012) used the frequency domain approach to distributing nonlinear aerodynamic and aeroelastic analysis of bridges, which was following a time domain analysis model. When it comes to the hybrid composite bridges, Chan et al. (2013) had developed both the FEA and laboratory tests for the frequency analysis under earthquake ground motion excitation. Figure 2-17 is the entire experimental model of the FRP cable-stayed bridge and the detailed structural analysis distribution. Figure 2-18 is the PSD of the acceleration on the FRP box girder for two separate locations.

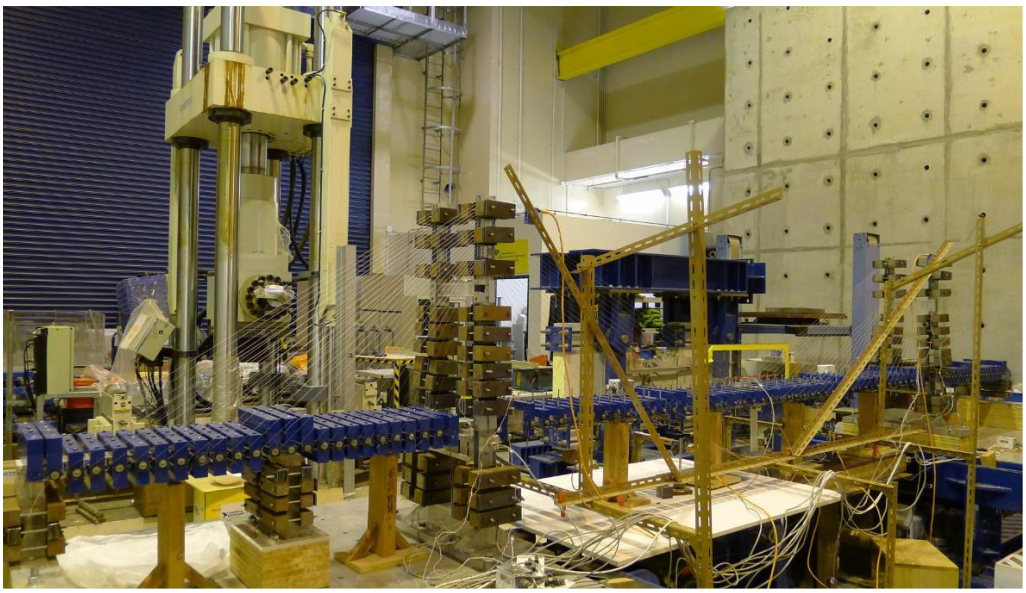

Figure 2-17 The whole model of FRP bridge (Chan et al. 2013)

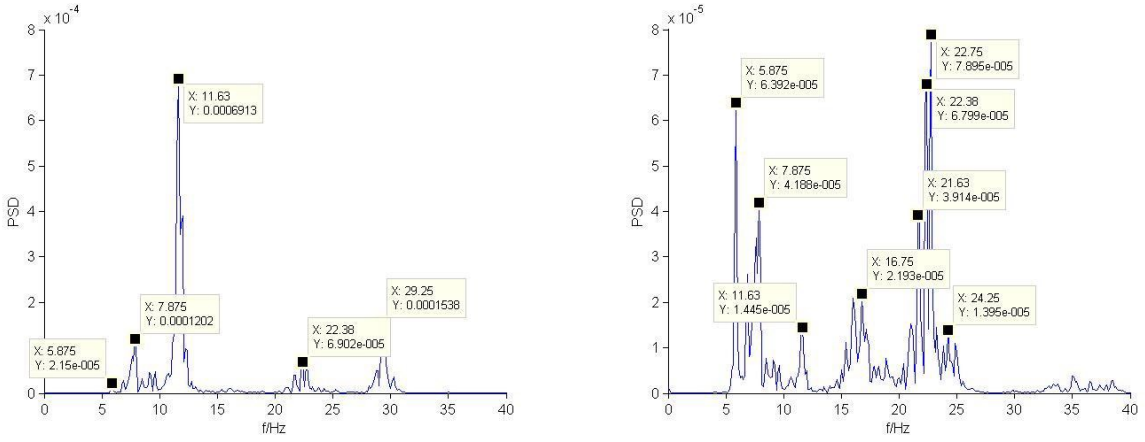

(a) 1/4 location of the mid girder (b) 1/2 location of the mid girder

Figure 2-18 The power spectrum density of the acceleration (Chan et al. 2013)

2.6. SUMMARY

This chapter presented a literature review related to the finite strip method and the effects of the high-strain-rate loading on material properties. The composite materials are also examined from previous studies, and the application of FRPs applied on the bridges especially for the cable-stayed bridges under static and dynamic loading test for numerical methods. Some conclusions can be summarized below:

- Previous research on FSM is more concentrated on beams and plates under flexural static loading shows that increasing the reinforcement ratio improves load resistance, although it reduces maximum displacement and ductility. Because of the limitations of primary software development environment that are C++ no matter for essential programs or bridges, it is more difficult to extend the application of FSM to a wider area. Lau et al. (2000) had firstly tried the 3D flutter analysis of bridges by spline finite strip method for the first time, which represents an important milestone study between the previous FSM and current updated FSM.
- However, the current research on FSM is more focused on the demonstration and comparison of the FEM, which was considered as an alternative method for FEM. It was effective in time control under service loads due to the rapid development of computing technologies for computers. Shen et al. (2013), Naderian et al. (2015) and Naderian et al. (2016) investigated the effects of several concentered loads and seismic excitations. It concluded that the use of FSM could be an approach meeting an acceptable agreement with FEM both for static results and dynamic results, and the errors of accuracy are reasonable, (approximately within 10%).
- In static analysis, regardless of the method of applying the loads on the bridges, all the static loads are concentrated loads, since previous studies for static analysis for bridges by FSM was just an alternative method compared with FEM. It means that all the bridges were pre-designed by FEM within several finite element software or experimental results. FSM had never been regarded as a priority method in design of bridges because of the several limitations of previous studies: only concentrated loads can be applied that not enough to perform the critical loads in design codes; complicated numerical simulations that were easier to make mistakes; separated parts of bridges should be designed in different models; and so on.
- In dynamic analysis, current research is more concentrated on the natural frequency analysis, except for Lau et al. (2000) who developed the results of both natural frequencies and flutter frequencies. Shen et al. (2013) used the pseudo-excitation method (PEM) to determine the accuracy of the IFSM to be used in seismic analysis by using the Log (PSD)

curves. Furthermore, Naderian et al. (2016) firstly developed time history analysis by IFSM for long-span cable-stayed bridges, which is the latest dynamic analytical method applied to bridges by FS method.

- Current studies indicated that application of composite materials for bridges had limit critical codes and standards, which was related to specific countries and practical applications. The application for FRPs in bridges was the cables, I-girders, box girders, and the partial decks (FRP-Reinforced Concrete decks), where the towers, as well as piers, are not been applied by FRPs because of the smaller compression capacity compared with concrete and reinforced concrete. Also, more studies are required to exam the FRP deck behavior if we would like to apply FRPs only when designing the decks.
- Limited research is available for bridge decks with composite materials only, even no published research for the slab-girders. Use of the high-strength FRPs could increase the shear strength, while the drift ratio at failure was less than the conventional concrete or steel girders. Further investigations are required.
- Limited research exists on the uniform loads and distributed loads applied by FSM, as well as dynamic analysis of the seismic and aerodynamic response of bridges by FSM. Recent studies investigated that use hybrid composite bridges resulted in a higher stiffness capacity but also decreased the ductility of the cables and decks.
- No research or studies have investigated the structural response of hybrid bridges by the FSM because of a large amount of program build up works and numerical simulations. Current research on hybrid composite bridges under static loads as well as dynamic behavior is based on the FEM modeling and experimental simulations.

CHAPTER 3. THEORETICAL ANALYSIS

3.1. CHAPTER OVERVIEW

This simulation project examines the static and dynamic performance of long-span cable-stayed bridges constructed with composite materials with original concrete and steel. As part of the study, two types of bridges were tested under simulated static loading, free vibration, and seismic loading analysis was tested for both bridges. The parameters investigated include the effect of types of bridges, the effect of laminated FRPs, and the effect of the layout and thickness of the whole bridges.

This chapter outlines the theoretical details of the simulation program and provides information regarding the Finite Strip Modeling, material properties, basic formulas and the analyzing process.

3.2. LAMINATE INTEGRATED FINITE STRIP METHOD

3.2.1. DISCRETIZATION OF FLAT SHELL STRIP BY SPLINE STRIPS

The flat shell strip described in this section is developed particularly for the modeling of bridge decks. However, in the latter case study, a slab-girder bridge with flat plate strip is desired to be replaced by a laminated FRP deck in the so-called laminated finite strip method (LFSM). To maintain compatibility and uniqueness throughout the whole structure, the more general B_3 spline finite strip function in the longitudinal direction is adopted as the basis for the development of the column strip's displacement field. Regarding transverse direction, a cubic polynomial is adopted to represent the vertical displacement variation, while linear interpolation is applied for the in-plane displacements. A conventional B_3 spline finite strip is introduced to interpolate an arbitrary function $f(y)$ by the spline functions, $f(y)$ which is divided into several sections, by the predefined known as knots.

For an equally spaced spline function $\Phi_m(y)$ with the center at $y = y_m$, as shown in Figure 3-1, the B_3 spline function is defined as (Prenter,1975):

$$\Phi_m(y) = \frac{1}{6h^3}\begin{cases} (y - y_{m-2})^3, & y_{m-2} \le y \le y_{m-1} \\ h^3 + 3h^2(y - y_{m-1}) + 3h(y - y_{m-1})^2 - 3(y - y_{m-1})^3, & y_{m-1} \le y \le y_m \\ h^3 + 3h^2(y_{m+1} - y) + 3h(y_{m+1} - y)^2 - 3(y_{m+1} - y)^3, & y_m \le y \le y_{m+1} \\ (y_{m+2} - y)^3, & y_{m+1} \le y \le y_{m+2} \\ 0, & \text{otherwise} \end{cases} \tag{3-1}$$

in which h is the width of these equal sections.

It is a piecewise cubic polynomial with continuity over the entire interval up to the second derivative for the B_3-spline function. The spline functions centered at all the knots compose a series of functions, which could be applied to interpolate an arbitrary function expressed as follows:

$$s(y) = \sum_{m=-1}^{r+1} c_m \Phi_m(y) \tag{3-2}$$

where the c_m is coefficients determined by the required boundary conditions.

To meet a better solution for the connection problem, each section is controlled by four spline functions, which are the functions centered at the two ends of the section and the two knots next to those ends, respectively. Therefore, when it comes to the shape functions for each strip within flat plates/shells, considering the situation with the bridge deck resisting in-plan stresses and bending, two more knots are needed to complete the interpolation of the whole function which distributes r to r+3 sections in the so-called flat B_3 spline functions as shown in Figure 3-1.

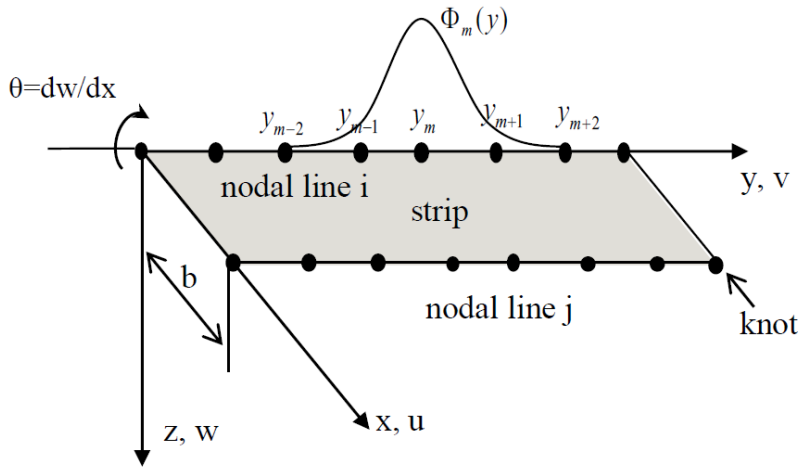

Figure 3-1 Flat shell spline finite strip for deck modeling (Shen, 2009)

To obtain a more accurate solution, it is intended to have the location of the supports and the concentrated load coinciding with the knots on the nodal lines in the formulation of SFSM. Therefore, unequally spaced knots is introduced and adopted that is much more capable to model irregular deformation, the spline function centered at y_m can be expressed as:

$$\Phi_m(y)=\begin{cases}0 & y<y_{m-2}\\ f_1 & y_{m-2}\le y<y_{m-1}\\ f_2 & y_{m-1}\le y<y_m\\ f_3 & y_m\le y<y_{m+1}\\ f_4 & y_{m+1}\le y<y_{m+2}\\ 0 & y_{m+2}\le y\end{cases} \tag{3-3}$$

where

$$\begin{aligned}
f_1&=\frac{\left(y-y_{m-2}\right)^3}{\left(y_{m+1}-y_{m-2}\right)\left(y_m-y_{m-2}\right)\left(y_{m-1}-y_{m-2}\right)}\\
f_2&=f_1-\frac{\left(y_{m+2}-y_{m-2}\right)\left(y-y_{m-1}\right)^3}{\left(y_{m+2}-y_{m-1}\right)\left(y_{m+1}-y_{m-1}\right)\left(y_m-y_{m-1}\right)\left(y_{m-1}-y_{m-2}\right)}\\
f_3&=f_4-\frac{\left(y_{m+2}-y_{m-2}\right)\left(y_{m+1}-y\right)^3}{\left(y_{m+1}-y_{m-2}\right)\left(y_{m+1}-y_{m-1}\right)\left(y_{m+1}-y_m\right)\left(y_{m+2}-y_{m+1}\right)}\\
f_4&=\frac{\left(y_{m+2}-y\right)^3}{\left(y_{m+2}-y_{m-1}\right)\left(y_{m+2}-y_m\right)\left(y_{m+2}-y_{m+1}\right)}
\end{aligned} \tag{3-4}$$

For each knot, three translational degrees-of-freedom (u, v, w) and one rotational degree-of-freedom ($\theta=dw/dx$), totally four degrees of freedom, were assigned respectively. Considering as an established habits, x, y, and z are considered as the transverse, longitudinal and vertical directions of the shell strip, respectively, which will be display latterly in the static analyses. All the following case studies obey this definition. Therefore, the corresponding displacements u, v and w were chosen to satisfy the pre-set boundary conditions as shown in Eq. (3-5) (Cheung and Li, 1990; Cheung et al. 1992). The in-plane displacements u and v are modeled by linear functions in the transverse direction, while the spline functions are assigned in the longitudinal direction. Similarly, the bending displacements and shapes are modeled by cubic Hermite polynomials in the transverse direction and by spline functions in the longitudinal direction.

$$\begin{aligned}
U&=\sum_{m=-1}^{r+1}\left(\left(1-X\right)u_{im}+Xu_{jm}\right)\Phi_m\left(y\right)\\
V&=\sum_{m=-1}^{r+1}\left(\left(1-X\right)v_{im}+Xv_{jm}\right)\Phi_m\left(y\right)\\
W&=\sum_{m=-1}^{r+1}\left(\left(1-3X^2+2X^3\right)w_{im}+x\left(1-2X+X^2\right)\theta_{im}+\left(3X^2-2X^3\right)w_{jm}+x\left(X^2-X\right)\theta_{jm}\right)\Phi_m\left(y\right)
\end{aligned} \tag{3-5}$$

where $X=x/b$, b is the width of the strip that may change along the longitudinal direction; $\Phi_m(y)$ is the B_3 spline function centered at y_m; r is the total number of longitudinal sections on a nodal line; u_{im}, v_{im}, w_{im} and θ_{im} are the displacement parameters of the knot m on nodal line i.

In this thesis, the basic integrated finite strip method was built and developed by several C++ programs by Cheung et al. (1992), which was regarded as a good reference.

3.2.2. STRAIN STRESS AND DISPLACEMENT RELATIONS

Regarding the static analysis for the LFSM, both the flat laminates no matter in LFSM or FEM, Kirchhoff-Love hypothesis is used to analyze all the in-plane bending loads. Kirchhoff hypothesis states that a line perpendicular to geometric mid-surface (reference plane) remains straight and does not change its length while the laminate is deforming under the applied loading when assuming that all layers are perfectly bonded (no slippage between the layers). This hypothesis results in a vanishing condition, as follows:

$$\varepsilon_{zz} = \gamma_{xz} = \gamma_{yz} = 0 \tag{3-6}$$

Then the strain distribution at a general point in the laminate is expressed by:

$$\begin{Bmatrix} \overline{\varepsilon}_x \\ \overline{\varepsilon}_y \\ \overline{\gamma}_{xy} \end{Bmatrix} = \begin{Bmatrix} \varepsilon_x \\ \varepsilon_y \\ \gamma_{xy} \end{Bmatrix} + z \begin{Bmatrix} \kappa_x \\ \kappa_y \\ \kappa_{xy} \end{Bmatrix} \tag{3-7}$$

in which ε_x, ε_y, γ_{xy} in the middle surface are written as:

$$\varepsilon_x = \frac{\partial u}{\partial x}, \varepsilon_y = \frac{\partial v}{\partial y}, \gamma_{xy} = \frac{\partial u}{\partial y} + \frac{\partial v}{\partial x} \tag{3-8}$$

And the three mid-surface strains and curvatures κ_x, κ_y, κ_{xy} are defined respectively as:

$$\kappa_x = -\frac{\partial^2 w}{\partial x^2}, \kappa_y = -\frac{\partial^2 w}{\partial y^2}, \kappa_{xy} = -2\frac{\partial^2 w}{\partial x \partial y} \tag{3-9}$$

where κ_x is a bending curvature associated with bending of the middle surface in the xz plane and κ_y is a bending curvature associated with bending of the middle surface in the yz plane. κ_{xy} is a twisting curvature associated with out-of-plane twisting of the middle surface, which lies in the xy plane before deformation.

3.2.3. LAMINATED COMPOSITE MATERIALS FOR DECK

With the strain-stress relationship shown above, the other resultants can be written in similar form. The following constitutive equations can relate the stresses to the strains in an arbitrary lay-up

laminate strip In Eq. (3-10) and (3-11), $(Q_{ij})_k$ are the components of the transformed k^{th} lamina stiffness matrix as below (Gibson 1994):

$$\bar{Q} = \begin{bmatrix} \bar{Q}_{11} & \bar{Q}_{12} & \bar{Q}_{16} \\ \bar{Q}_{12} & \bar{Q}_{22} & \bar{Q}_{26} \\ \bar{Q}_{16} & \bar{Q}_{26} & \bar{Q}_{66} \end{bmatrix} \tag{3-10}$$

$$\begin{aligned}
\bar{Q}_{11} &= Q_{11}\cos^4\theta + Q_{22}\sin^4\theta + 2\left(Q_{12}+2Q_{66}\right)\sin^2\theta\cos^2\theta \\
\bar{Q}_{12} &= \left(Q_{11}+Q_{22}-4Q_{66}\right)\sin^2\theta\cos^2\theta + Q_{12}\left(\cos^4\theta+\sin^4\theta\right) \\
\bar{Q}_{22} &= Q_{11}\sin^4\theta + Q_{22}\cos^4\theta + 2\left(Q_{12}+2Q_{66}\right)\sin^2\theta\cos^2\theta \\
\bar{Q}_{16} &= \left(Q_{11}-Q_{12}-2Q_{66}\right)\cos^3\theta\sin\theta - \left(Q_{22}-Q_{12}-2Q_{66}\right)\cos\theta\sin^3\theta \\
\bar{Q}_{26} &= \left(Q_{11}-Q_{12}-2Q_{66}\right)\cos\theta\sin^3\theta - \left(Q_{22}-Q_{12}-2Q_{66}\right)\cos^3\theta\sin\theta \\
\bar{Q}_{66} &= \left(Q_{11}+Q_{22}-2Q_{12}-2Q_{66}\right)\sin^2\theta\cos^2\theta - Q_{66}\left(\sin^4\theta+\cos^4\theta\right)
\end{aligned} \tag{3-11}$$

in which Q_{ij} are the components of the lamina stiffness matrix which are related to the engineering constants as below

$$Q_{11} = \frac{E_1}{1-\nu_{12}\nu_{21}}, Q_{12} = \frac{\nu_{12}E_2}{1-\nu_{12}\nu_{21}}, Q_{22} = \frac{E_2}{1-\nu_{12}\nu_{21}}, Q_{66} = G_{12} \tag{3-12}$$

Substitute the lamina stress-strain relationships from Eq. (3-11) and Eq. (3-12), respectively, the material properties can be expressed as following three types of stiffness.

The laminate extensional stiffnesses are given by:

$$A_{ij} = \int_{-t/2}^{t/2}\left(\bar{Q}_{ij}\right)_k dz = \sum_{k=1}^{N}\left(\bar{Q}_{ij}\right)_k\left(z_k - z_{k-1}\right) \tag{3-13}$$

The laminate coupling stiffnesses are given by:

$$B_{ij} = \int_{-t/2}^{t/2}\left(\bar{Q}_{ij}\right)_k dz = \frac{1}{2}\sum_{k=1}^{N}\left(\bar{Q}_{ij}\right)_k\left(z_k^2 - z_{k-1}^2\right) \tag{3-14}$$

And the laminate bending stiffnesses are given by:

$$D_{ij} = \int_{-t/2}^{t/2}\left(\bar{Q}_{ij}\right)_k dz = \frac{1}{3}\sum_{k=1}^{N}\left(\bar{Q}_{ij}\right)_k\left(z_k^3 - z_{k-1}^3\right) \tag{3-15}$$

where the subscripts *i, j*=1,2, or 6; N is the number of laminas; t is the laminate thickness; z_k and z_{k-1} are distances from the middle surface to inner and outer surfaces of the k^{th} lamina respectively as illustrated in Figure 3-2.

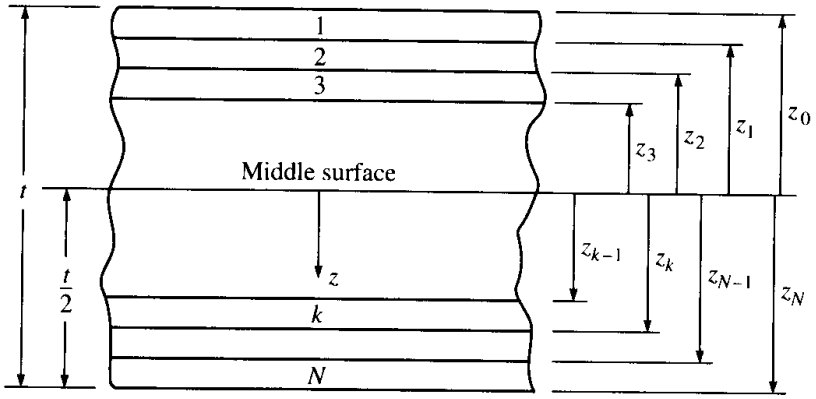

Figure 3-2 Laminated plate geometry and ply numbering system (Gibson, 1994)

Therefore, the other stress resultants can be written in similar form, and the complete set of equations can be expressed in matrix form as (Gibson, 1994):

$$\begin{Bmatrix} N_x \\ N_y \\ N_{xy} \\ M_x \\ M_y \\ M_{xy} \end{Bmatrix} = \begin{bmatrix} A_{11} & A_{12} & A_{16} & B_{11} & B_{12} & B_{16} \\ A_{12} & A_{22} & A_{26} & B_{12} & B_{22} & B_{26} \\ A_{16} & A_{26} & A_{66} & B_{16} & B_{26} & B_{66} \\ B_{11} & B_{12} & B_{16} & D_{11} & D_{12} & D_{16} \\ B_{12} & B_{22} & B_{26} & D_{12} & D_{22} & D_{26} \\ B_{16} & B_{26} & A_{66} & D_{16} & D_{26} & D_{66} \end{bmatrix} = \begin{Bmatrix} \varepsilon_x \\ \varepsilon_y \\ \varepsilon_{xy} \\ \kappa_x \\ \kappa_y \\ \kappa_{xy} \end{Bmatrix} \tag{3-16}$$

or in a partitioned form as:

$$\begin{Bmatrix} N \\ M \end{Bmatrix} = \begin{bmatrix} A & B \\ B & D \end{bmatrix} \begin{Bmatrix} \varepsilon^0 \\ \kappa \end{Bmatrix} = [E] \begin{Bmatrix} \varepsilon^0 \\ \kappa \end{Bmatrix} \tag{3-17}$$

where N_x, N_y, N_{xy} are membrane and shear forces per unit length while M_x, M_y, M_{xy} are the bending and twisting moments per unit length in the middle surface of the laminate. A, B, and D are matrices of order 3 including laminate extensional stiffness, laminate-coupling stiffness, and laminate-bending stiffness matrices respectively and are obtained by the following integrations (Gibson, 1994).

The extensional stiffness matrix [A] relates the in-plane forces $\{N\}$ to the mid-plane strains $\{\varepsilon\}$, and the bending stiffness matrix [D] relates the moments $\{M\}$ to the curvatures $\{\kappa\}$. Moreover, the coupling stiffness matrix [B] couples the in-plane forces $\{N\}$ with the curvatures and the moments $\{M\}$ with the mid-plane strains. Having nonzero B_{ij} means that the laminate will bend or

twist under in-plane forces, and will also exhibit mid-plane stretching under bending or twisting moment forces. It is worth noting that for a symmetric laminate with respect to the middle surface in terms of geometry and material property, the matrix [*B*] will be zero. On the other hand, for the asymmetric laminate about the middle surface, the matrix [*B*] will have nonzero elements. In fact, the coupling at laminate is not related to material anisotropy but is due to geometric and/or material property asymmetry with respect to the middle surface (Gibson, 1994).

The above formulations provided the theoretical basis to combine the shell finite strip model with the laminated FPRs. To determine all the necessary parameters needed in the C++ programs of shell finite strip model, a MATLAB program was built by Naderian et al. (2013) and modified by the current author of the thesis in 2016. Next, the author assembled the MATLAB program with the new modified finite strip C++ programs to model and analyzed the laminated FRPs deck bridges.

3.3. STATIC PROCESS

A static analysis has been considered as the foremost analysis of engineering structures. The shape functions assembled as column strip [*N*], can be developed using traditional finite element concepts. The column strip and the transition section formed, together with the SFSM can be expressed in an effective and efficient FS environment as a total solution for bridge analysis.

All strip elements must come with the pre-set boundary conditions in the finite strip method, and in the case of the column strip, the fixed-free condition should be implemented in the formulation process. Once the shape functions are defined, the stiffness matrix ([K_c]) and the mass matrix ([M_c]) of the CS can be calculated using the following equation expressions:

$$\left[M_c\right]_{mn} = \int \rho h \left[N\right]_m^T \left[N\right]_n dA \tag{3-18}$$

$$\left[K_c\right]_{mn} = \int \left[B\right]_m^T \left[D\right] \left[B\right]_n dA \tag{3-19}$$

in which ρ is the density of the strip, and h is the thickness of the strip; [*D*] and [*B*] are the elastic matrix and the strain matrix respectively; [*N*] is the shape function matrix.

Like FEM, the SFSM properties are converted to nodal properties during the model formulation process, although the number of nodes required is significantly reduced due to the semi-analytical nature. Therefore, it is possible to model and construct the mass matrix $[M]_i$, stiffness matrix $[K]_i$ of the bridge deck, the piers and the bearings using the spline finite strip, the CS, and the transition section, respectively, using the Eq. (3-18) and (3-19). It is indicated that these two equations, where [K_c] is related to the material and section properties, and [M_c] is related to the density of materials

and thickness of the strips. In theory, that is the core concepts to display composite materials in the LFSM environment.

Shen et al. (2013) extended the static analysis of the finite strip method and modified the basic programs in 2009 to model several bridges. The current author modified the programs by extending the existing C++ laminated plate program to two composite FRP bridges. The programs are based on the C++ modules for the concrete slab-girder bridge and the C++ and MATLAB programs for the concrete Kap Shui Mun Bridge provided by Naderian et al. (2015) and Naderian et al. (2016).

3.4. DYNAMIC PROCESS

3.4.1. VIBRATION ANALYSIS

To realize the vibration analysis of the two bridges by FSM, a MATLAB program was built by Shen et al. (2009) by using the following approaches for bridges.

3.4.1.1. FREE VIBRATION

To evaluate the natural frequencies of the bridge, the free vibration analysis is performed. According to the structural dynamics, the overall matrix equation for a bridge structure in free vibration at any instant of time is defined as follows:

$$[K]\{\delta(t)\} + [M]\{\ddot{\delta}(t)\} = 0 \tag{3-20}$$

where δ (t) is the function of time, and [K] and [M] are the overall stiffness and mass matrices of the bridge which can be formed using an integrated finite strip method. It is assumed that the bridge structure has a sinusoidal vibration.

The following equation Eq. (3-21) is obtained from Eq. (3-20) which is a generalized eigenvalue problem where the natural frequency ω and displacement vector $\{\delta\}$ are referred as eigenvalue and eigenvector respectively. Also, both [K] and [M] are symmetrical and positive definite matrices that can be expressed in a convenient format.

$$\left[[K]-\omega^2[M]\right]\{\delta\}=0 \tag{3-21}$$

The natural frequencies of the bridge structure and corresponding mode shapes $\{\delta\}$ can be easily obtained by solving the eigenvalue problem of Eq. (3-21) using computer techniques. After determining the stiffness matrix [K] and the mass matrix [M] by the IFSM, for the damping matrix, classical Rayleigh damping is adopted in the present study.

3.4.1.2. CLASSIC RAYLEIGH DAMPING

Similar to FEM, the finite strip method is another kind of finite element method that all the structure components can be considered by stiffness and mass respectively. All the elements (strips) are re-assembled together regardless of the geometric distributions. Regarding vibration analysis, it starts from spline finite strip method, these properties are converted to nodal properties during the model formulation process, although a number of nodes required are significantly reduced due to the semi-analytical nature.

For the damping matrix, classical Rayleigh damping is adopted in the present study, whereby the damping matrix of the bridge [*C*] is a function of the stiffness matrix [*K*] and mass matrix [*M*] of the bridge:

$$[C] = \alpha[M] + \beta[K] \tag{3-22}$$

where α *and* β are the Rayleigh damping factors, which can be evaluated if two structural damping ratios associated with two distinct frequencies are given direcly. The coefficients can be determined from specified damping ratios for two different modes. Expressing the above equation for two different modes (i_{th} mode and j_{th} mode) in matrix form leads to:

$$\frac{1}{2}\begin{bmatrix} 1/\omega_i & \omega_i \\ 1/\omega_j & \omega_j \end{bmatrix}\begin{Bmatrix} \alpha \\ \beta \end{Bmatrix} = \begin{Bmatrix} \zeta_i \\ \zeta_j \end{Bmatrix} \tag{3-23}$$

If both modes are assumed to have the same damping ratio, the two parameters come to a similar expression:

$$\alpha = \zeta \frac{2\omega_i\omega_j}{\omega_i + \omega_j} \quad \beta = \zeta \frac{2}{\omega_i + \omega_j} \tag{3-24}$$

With the characteristic property matrices well defined in the FS environment, the conventional characteristic equation of motion can be constructed, and the dynamic analysis procedure, using the same approach as for FEM, can be applied by LFSM.

3.4.2. TIME HISTORY DOMAIN ANALYSIS

The moment, for focus on the seismic analysis of the both bridges. And to develop the time history analysis of the Kap Shui Mun Bridge, several MATLAB programs were built as the sub-programs of the FSM by Shen (2009) and Naderian et al. (2016) and verified by the thesis author regarding the time history results for the concrete cable-stayed bridge.

3.4.2.1. TIME HISTORY

When it comes to the time domain analysis, the dynamic motion equation of a discrete structure with multiple DOF can be written as:

$$[M]\{\ddot{u}\} + [C]\{\dot{u}\} + [K]\{u\} = \{p\} \tag{3-25}$$

where $\{u\}$ is the relative displacement vector and $\{p\}$ is the external force vector. When the structure is subjected to a uniform earthquake excitation, the Eq. (3-25) can be modified as :

$$[M]\{\ddot{u}\} + [C]\{\dot{u}\} + [K]\{u\} = -[M]\{r\}\ddot{u}_g(t) \tag{3-26}$$

in which $\{r\}$ is the vector indicating the DOFs influenced by the ground motion. $\ddot{u}_g(t)$ is the ground acceleration record of the excitation event.

By considering the multiple support excitations, some modifications in the formulation Eq. (3-25) and Eq. (3-26) are required to made to allow the above method be applied under FS environment. Then, knot displacement and knot displacement parameter can be written in the following relationships:

$$\{\bar{U}\} = [A]\{u\} \tag{3-27}$$

where $\{\bar{U}\} = \{u_{-1}\ U_0\ U_1 \ldots U_n\ u_{n+1}\}^T$, $\{u\} = \{u_{-1}\ u_0\ u_1 \ldots u_n\ u_{n+1}\}^T$ (3-28)

In the above equation, additional entries u_{-1} and u_{n+1} for each nodal line are added to the vector $\{\bar{U}\}$ to obtain a square transformation matrix [p].

$$\{u\} = [A]^{-1}\{\bar{U}\} = [B]\{\bar{U}\} \tag{3-29}$$

Thus, Eq. (3-29) can also be written as:

$$[B]^T[M][B]\{\ddot{\bar{U}}\} + [B]^T[C][B]\{\dot{\bar{U}}\} + [B]^T[K][B]\{\bar{U}\} = [B]^T\{p\} \tag{3-30}$$

$$[\bar{M}]\{\ddot{\bar{U}}\} + [C]\{\dot{\bar{U}}\} + [K]\{\bar{U}\} = \{\bar{p}\} \tag{3-31}$$

where

$$\begin{aligned}\left[\bar{M}\right] &= \left[B\right]^T \left[M\right]\left[B\right] \\ \left[\bar{C}\right] &= \left[B\right]^T \left[C\right]\left[B\right] \\ \left[\bar{K}\right] &= \left[B\right]^T \left[K\right]\left[B\right] \\ \left\{\bar{p}\right\} &= \left[B\right]^T \left\{p\right\}\end{aligned} \tag{3-32}$$

With the above modification, the conventional dynamic analysis in a FEM formulation can now be applied to the SFSM formulation. It discovered that FEM could be improved by the FSM not only in accuracy but also in computing time. It is desired to consider the effects of spatially varying earthquake ground motion, Eq. (3-32) can be re-formulated as:

$$\begin{bmatrix} M_s & M_c \\ M_c^T & M_b \end{bmatrix} \begin{Bmatrix} \ddot{U}_s \\ \ddot{U}_b \end{Bmatrix} + \begin{bmatrix} C_s & C_c \\ C_c^T & C_b \end{bmatrix} \begin{Bmatrix} \dot{U}_s \\ \dot{U}_b \end{Bmatrix} + \begin{bmatrix} K_s & K_c \\ K_c^T & K_b \end{bmatrix} \begin{Bmatrix} U_s \\ U_b \end{Bmatrix} = \begin{Bmatrix} 0 \\ F_b \end{Bmatrix} \tag{3-33}$$

where $[M_s]$, $[C_s]$, $[K_s]$ are the mass, damping and stiffness matrices respectively, which are associated with the unrestrained degree of freedom $\{U_s\}$. $[M_b]$, $[C_b]$, $[K_b]$ are the mass, damping and stiffness matrices respectively, which are associated with the restrained degree of freedom $\{U_b\}$; $[M_c]$, $[C_c]$, $[K_c]$ are the coupling mass, damping and stiffness matrices respectively. $\{U_s\}$, $\{\dot{U}_s\}$, $\{\ddot{U}_s\}$are absolute displacement, velocity and acceleration vectors of unrestrained DOF. $\{U_b\}$, $\{\dot{U}_b\}$, $\{\ddot{U}_b\}$ are absolute displacement, velocity and acceleration vectors of restrained (support) DOF; and $\{F_b\}$ is the reaction force vector.

3.4.2.2. NEWMARK'S METHOD

Since there are different methods for solving Eq. (3-26) like the Newmark method, the Wilson-u method, or the precise integration method (Zhong et al. 1998). The concept of time-stepping methods in the framework of Newmark's Method is described in the following section. It is worth noting that the stiffness and mass matrices and consequently damping matrices are derived from the integrated finite strip method.

Assuming that at $t = t_i$ and $t_i = t_{i+1}$, then the equation of motion can be obtained:

$$[M]\{\ddot{\delta}_i\} + [C]\{\dot{\delta}_i\} + [K]\{\delta_i\} = \{p_i\} \tag{3-34}$$

$$[M]\{\ddot{\delta}_{i+1}\} + [C]\{\dot{\delta}_{i+1}\} + [K]\{\delta_{i+1}\} = \{p_{i+1}\} \tag{3-35}$$

The other types of time-stepping methods the bridge responses at $t = t_{i+1}$ can be predicted under the condition when $t = t_i$ and the loading at both times are known by the Newmark's method. The responses at $t = t_{i+2}$, t_{i+3}, t_{i+4},... can be calculated using an iteration process (Chang, 2004). As a result, the time history response of the bridge can be conducted. Based on Eq. (3-34) and (3-35),

the number of equations are less than the number of unknowns. In this case, further assumptions must be introduced so that the responses can be solved (Naderian et al. 2016). There are some approximate methods, for instance, the excitation interpolation method, the central difference method, the Newmark's method, and Wilson's θ method are suggested.

The Newmark's method is regarded as the most popular method because it can be used to deal with nonlinear structures and multiple degrees of freedom structures. Assuming that $\dot{\delta}_{i+1}$and δ_{i+1} are related to $\ddot{\delta}_{i+1}$, δ_i, so that $\dot{\delta}_i$and $\ddot{\delta}_i$ can be written as:

$$\dot{\delta}_{i+1} = \dot{\delta}_i + [(1-\gamma)\Delta t]\ddot{\delta}_i + (\gamma \Delta t)\ddot{\delta}_{i+1} \tag{3-36}$$

$$\delta_{i+1} = \delta_i + \Delta t\dot{\delta}_i + \left[\left(\frac{1}{2} - \lambda\right)\Delta t^2\right]\ddot{\delta}_i + (\lambda \Delta t^2)\ddot{\delta}_{i+1} \tag{3-37}$$

where $\Delta t = t_{i+1} - t_i$ is the time increment which is normally assumed to be a constant from step to step. In addition, the time increment is assumed to be less than 1% of the period of the system. In Eq. (3-37), γ and λ are Newmark's parameters defining the variation of the acceleration over a time step, and they can be applied to determine the accuracy and stability of the proposed method (Chang, 2004). $\gamma = 1/2$ and $1/6 < \lambda < 1/4$ are the typical values for the Newmark's parameters. Mathematically, a distinct set of parameters is assigned depending on the various physical interpretations. In the case, the average acceleration is used, in which the acceleration between t_i and t_{i+1} is considered as an average of $\ddot{\delta}_i$ and $\ddot{\delta}_{i+1}$, the Newmark's parameters are $\gamma = 1/2$ and $\lambda = 1/4$. In the linear acceleration, the acceleration between t_i and t_{i+1} varies linearly between $\ddot{\delta}_i$ and $\ddot{\delta}_{i+1}$, the Newmark's parameters are $\gamma = 1/2$ and $\lambda = 1/6$ (Naderian et al. 2016). The Newmark's time history analysis therefore has the incremental form. Using the equations Eq. (3-36) from (3-35) leading to:

$$M\Delta\ddot{\delta}_i + C\Delta\dot{\delta}_i + K\Delta\delta_i = \Delta P_i \tag{3-38}$$

in which the response and the force increments are predicted as:

$$\begin{aligned} \Delta\delta_i &= \Delta\delta_{i+1} - \delta_i \\ \Delta\dot{\delta}_i &= \Delta\dot{\delta}_{i+1} - \dot{\delta}_i \\ \Delta\ddot{\delta}_i &= \Delta\ddot{\delta}_{i+1} - \ddot{\delta}_i \\ \Delta P_i &= \Delta P_{i+1} - P_i \end{aligned} \tag{3-39}$$

Subtracting the defined increments in Eq. (3-39), Eq. (3-37) can be rewritten as:

$$\Delta\ddot{\delta}_i = \frac{1}{\lambda\Delta t^2}\Delta\delta_i - \frac{1}{\lambda\Delta t}\Delta\dot{\delta}_i - \frac{1}{2\lambda}\ddot{\delta}_i$$
$$\Delta\dot{\delta}_i = \frac{1}{\lambda\Delta t}\Delta\delta_i - \frac{\gamma}{\lambda}\Delta\dot{\delta}_i + \Delta t\left(1 - \frac{\gamma}{2\lambda}\right)\ddot{\delta}_i \quad (3\text{-}40)$$

and substituting into the Eq. (3-38), one obtains:

$$\hat{K}\Delta\delta_i = \Delta\hat{P}_i \quad (3\text{-}41)$$

where

$$\widehat{K} = K + \frac{\gamma}{\lambda\Delta t}C + \frac{1}{\lambda\Delta t^2}M$$
$$\Delta\hat{P}_i = \Delta P_i + \left(\frac{M}{\lambda\Delta t} + \frac{\gamma C}{\lambda}\right)\dot{\delta}_i + \left[\frac{M}{2\lambda} + \Delta t\left(\frac{\gamma}{2\lambda} - 1\right)\right]\ddot{\delta}_i \quad (3\text{-}42)$$

The displacement increment $\Delta\delta_i$ can be produced from Eq. (3-41) while the acceleration and velocity increments can be obtained from Eq. (3-40) respectively. The time history response of the bridge by the Newmark's method can be programmed using programming languages or technical software (Chang, 2004). In the present research, MATLAB software is used for scientific computation including the current problem because of its many mathematical subroutines.

Not only the SDOF system but also the response of the MDOF system can be developed by the proposed Newmark's method. But the magnitude ranges of the Newmark's parameters γ and λ remain the same as they are in the SDOF system (Naderian et al. 2016).

3.4.3. PSEUDO EXCITATION METHOD

The pseudo-excitation method (PEM) was introduced and has been explained in some publications. It has several advantages over other methods. The computational advantage of the PEM has more traditional methods: the complete quadratic combination (CQC) and the square root of the sum of the squares (SRSS). For a system with N^2 modes, CQC requires N^2 complex multiplications; SRSS requires N^2 (but is less accurate for structures with closely spaced modes), while PEM requires one multiplication (Eq. (3-47)) and is exact. Therefore, PEM is ideally suited to systems with a large number of degrees of freedom with closely spaced frequencies, typical of real constructed bridges.

3.4.3.1. STATIONARY EXCITATION

For completeness, brief reviews of the PEM are given for stationary and non-stationary excitation. Following the reviews, the application of the PEM to determine the pedestrian-induced excitation of a bridge is described in detail (Caprani et al. 2013).

The basic principle of the pseudo-excitation method is presented as follows: considering a linear system subjected to a zero-mean stationary random excitation with a given $S_{XX}(\omega)$ and assuming

that for two arbitrarily selected responses $y(t)$ and $z(t)$, the auto-PSD $S_{YY}(\omega)$ and cross-PSD $S_{YZ}(\omega)$ are desired, then the $H_Y(\omega)$ and $H_Z(\omega)$ which are the corresponding frequency response functions are estimated. Therefore, the spectral density of the response of a linear system can be expressed as:

$$S_{YY}(\omega) = H_Y^*(\omega) H_Y(\omega) S_{XX}(\omega) = \left|H_Y(\omega)\right|^2 S_{XX}(\omega) \tag{3-43}$$

Further, the response, $y(t)$, of a linear system to a complex sinusoidal input, $x(t) = F_0 \exp(i\omega t)$ is:

$$y(t) = H(\omega) x(t) = H(\omega) F_0 \exp(i\omega t) \tag{3-44}$$

Therefore, if the sinusoidal excitation is replaced by a pseudo excitation:

$$\tilde{x}(t,\omega) = \sqrt{S_{XX}(\omega)} exp(i\omega t) \tag{3-45}$$

Then the pseudo-complex response is:

$$\tilde{y}(t,\omega) = H(\omega)\sqrt{S_{XX}(\omega)} exp(i\omega t) \tag{3-46}$$

Multiplying each side by its complex conjugate gives:

$$\tilde{y}(t,\omega)\tilde{y}^*(t,\omega) = |H(\omega)|^2 S_{XX}(\omega) \tag{3-47}$$

Therefore, by virtue of Eq. (3-42), we find the spectral density of the response to be given by:

$$S_{YY}(\omega) = \tilde{y}(t,\omega)\tilde{y}^*(t,\omega) \tag{3-48}$$

where the pseudo response is obtained by analyzing the structure when subjected to the pseudo excitation of Eq. (3-45). Thus, the spectral density of a structure's response, $S_{YY}(\omega)$, to an input spectral density, $S_{XX}(\omega)$, can be obtained by subjecting it to a range of pseudo excitations (Eq. (3-46)) covering the range of frequencies of interest, establishing its pseudo response at each of those frequencies, $\tilde{y}(t,\omega)$, and then using Eq. (3-48).

3.4.3.2. NON-STATIONARY EXCITATION

In the case of random loads traversing bridges, the response is non-stationary. PEM has been used to analyze such complicated problems (Cheung, 1969). Considering only one response (e.g. mid-span acceleration), $y(t)$, the 'force' causing this response can be thought of as a modulated version of the random moving load:

$$f(t) = g(t) x(t) \tag{3-49}$$

where $g(t)$ is the envelope or uniformly modulating function. It is assumed that variations in $g(t)$ occur at a lower frequency than the lowest of $x(t)$. If the modulated force is replaced by a pseudo excitation as follows:

$$\tilde{f}(t,\omega) = \sqrt{S_{XX}(\omega)}g(t)exp(i\omega t) \tag{3-50}$$

then the pseudo response is:

$$\tilde{y}(t,\omega) = \sqrt{S_{XX}(\omega)}I(\omega,t) \tag{3-51}$$

where the evolutionary frequency response function $I(x, t)$ is given regarding the system impulse response function $h(t)$ by (Cheung, 1969):

$$I(\omega,t)\int_{-\infty}^{\infty} h(t-\tau)g(\tau)\exp(-i\omega\tau)d\tau \tag{3-52}$$

From Eq. (3-51) and Eq. (3-52), the evolutionary PSD of the response, $S_{YY}(\omega,t)$, is found by multiplying each side by its complex conjugate:

$$\tilde{y}(t,\omega)\tilde{y}^*(t,\omega) = S_{XX}(\omega)I(\omega,t) = S_{YY}(\omega) \tag{3-53}$$

For moving load problems, the modulation is not explicit but is implicit due to the movement of the load. Thus, it suffices to pass a pseudo-excitation $\tilde{x}(t) = \sqrt{S_{XX}(\omega)}exp(i\omega t)$ across the beam and measure the pseudo-response, $\tilde{y}(t,\omega)$. Then, using equation, the non-stationary response can be found to describe moving seismic excitations.

3.4.4. FREQUENCY DOMAIN ANALYSIS

Regarding the slab-girder bridge, the current research determined the frequency results directly based on the pseudo-excitation method according to Shen et al. (2013). The stationary excitation program was built to analyze the stationary seismic excitations. However, the non-stationary excitation program was built to develop the non-stationary (moving) excitations analysis.

3.4.4.1. FOURIER TRANSFORM

The Fourier transform is named after the French mathematician Joseph Fourier. It is a mathematical transform used to express a function in the time domain as a function in the frequency domain. The Fourier transform of a continuous function can be represented as:

$$\hat{f}(\xi) = \int_{-\infty}^{\infty} f(x)e^{-2\pi ix\xi}dx \tag{3-54}$$

For every real number ξ, $f(x)$ is regarded as a function in the time domain, and $\hat{f}(\xi)$ is the corresponding function in the frequency domain. The inverse of a Fourier transform can be used

to transform a function from the frequency domain to the time domain, which can be represented as:

$$f(x) = \int_{-\infty}^{\infty} \hat{f}(\xi) e^{2\pi i \xi x} d\xi \tag{3-55}$$

For every real number x, if the function in question is not continuous, e.g. measured acceleration of a structure, the Discrete Fourier Transform (DFT) can be used. The DFT is the discrete counterpart of the Fourier transform of the continuous function. Considering a discrete function $f(t)$ where $t = k\Delta$ and $k = 0, ..., N-1$, the DFT is then defined as the sum:

$$\hat{f}(\xi) = \sum_{k=0}^{N-1} f(t) e^{-2\pi i k \xi / N} \tag{3-56}$$

3.4.4.2. FAST FOURIER TRANSFORM

The power spectrum measures the frequency content of a signal, and it shows which frequencies are dominating in the signal. This is widely used to determine the frequency patterns in measured signals. The FFT is a direct computation of the power spectral density (PSD). Different signal processing algorithms can be used to calculate the PSD, in order to reduce the amount of noise and to reduce computational effort.

The definition of PSD is nothing but the square of the magnitude of DTF and expressed as follows, in other words, ω is discretely and uniformly distributed (Peng et al. 2012):

$$S_x\left(e^{j\omega}\right) = \frac{1}{N}\left|\sum_{n=0}^{N-1} x[n] e^{-j\frac{2\pi kn}{N}}\right|^2 \tag{3-57}$$

where

$$\omega = \frac{2\pi k}{N}, k = 0,1,...,N-1 \tag{3-58}$$

The DFT can be computed very efficiently using the Fast Fourier Transform algorithm (Eq. 3-56, 3-57, 3-58). This reduces the number of computations needed for N points from $2N^2$ to $2N\,log_2(N)$. For example, if $N = 2^{10} = 1024$ the FFT algorithm only requires 0.5% of the computational operations necessary for the standard method (Welch, 1967). Regarding the MATLAB programs, the N is considered as parameter "nfft" which is the greater of default value 256 or the next power of 2 greater than the length of the segment.

3.4.4.3. WELCH'S METHOD

Welch's method is one of the methods used to obtain the power spectrum. In short Welch's method divides the data into short segments, applies a filtering window to each, then performs a Fourier transform on each segment and takes the average of each transform. The squared magnitude of the transforms is then used to construct the power spectrum.

The Welch's method is the application of the fast Fourier transform (FFT) in power spectrum analysis that was introduced and described by Welch (1967). This approach provided some principal advantages that there was a reduction in the number of computations and required core storage and a convenient application in the non-stationary tests. This method involved sectioning the record and averaging modified periodograms of sections.

Since a periodogram is a basic Fourier transform, it derived from the problem of reduced variance and bias behavior. When a windowing function is firstly applied to the data, a periodogram is called a modified periodogram and is defined as follows (Peng et al. 2012):

$$S_x\left(e^{j\omega}\right)=\frac{\frac{1}{N}\left|\sum_{n=0}^{N-1}w[n]x[n]e^{-j\omega n}\right|^2}{\frac{1}{N}\sum_{n=0}^{N-1}\left|w[n]\right|^2} \tag{3-59}$$

where $w[n]$ is the so-called window function, the use of which helps ease the problem of frequency leaking involved in DFT and reduce the variance in the estimation of PSD.

The Welch method is a common procedure and involves sectioning the time series into several overlapping shorter intervals. Each interval is treated with a window to limit the discontinuities between the intervals. An FFT is calculated for each windowed segment, and the total PSD is an averaged estimated spectrum. The averaging reduces the variance of the spectra, and the PSD is improved. The noise improvement is illustrated in Figure 3-3.

Eq. (3-59) follows the idea of a famous algorithm called the Welch's method, put forth in, which depends heavily on for our data analysis. In the Welch's method, we used one commonly used window function, the Hamming window, which is defined as follows (Hetland, 2015):

$$w[n]=0.54-0.46\cos\left(\frac{2\pi n}{N-1}\right),n=0,1,...,N \tag{3-60}$$

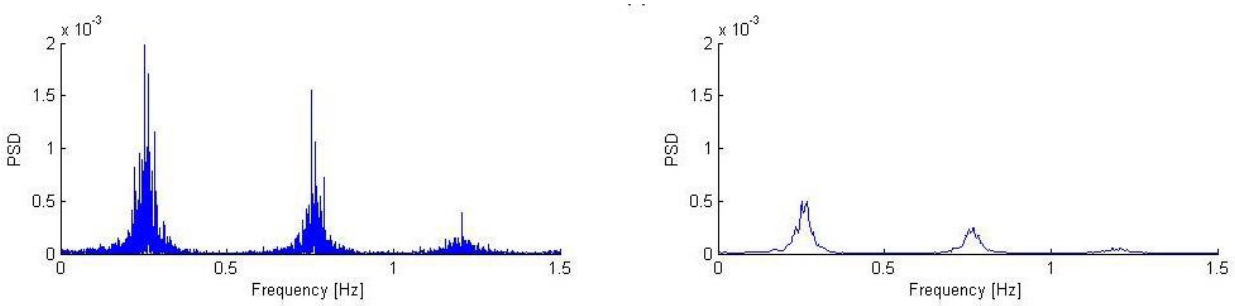

Figure 3-3 The PSD of a one-hour long time series, N sampling values is divided into segments with K=N/15 sampling values each with a 50% window overlap (Hetland, 2015)

In this thesis, the Welch's method is used to determine the power spectral density for acceleration and displacement measurements of the Kap Shui Mun Bridge; this was done using the built-in MATLAB function "pswelch" that the codes will be shown in detail in Appendix A. Moreover, this method transformed all the necessary time history analysis results to frequency domain analysis. The Welch method requires fewer computations and gives an improved result of the FFT calculations.

3.5. SUMMARY

This chapter provides a brief review of the necessary theoretical analysis and the process of calculation. To be specific, regarding finite strip method, all the bridge analysis is supposed to have several main steps: static analysis, natural frequency analysis, and dynamic analysis. The two bridges analyzed in this thesis have similar theoretical basis and procedure.

For the Slab-girder Bridge, firstly, all the static procedures are realized in C++ programs to conduct stiffness matrix [*K*]. In dynamic analysis, mass matrix [*M*] are produced upon to continue the natural frequency derived from the MATLAB programs. Finally, in dynamic analysis, the frequency domain results are developed directly from the MATLAB programs assembled for the Slab-girder Bridge.

For the Long-span Cable-stayed Bridge, firstly, the stiffness matrix [*K*] and mass matrix [*M*] are all produced from C++ programs only. However, the assembling matrix that is used to derive specified strain and stress value, as well as displacement response for each knot on strips, are built by the MATLAB programs. Then, these matrices are going to apply to the natural frequency MATLAB programs. Furthermore, time history domain analysis is also derived from MATLAB programs that were contributed to the frequency domain analysis in the last steps.

It is indicated that the C++ programs are produced both in VC++ 6.0 and Visual Studio 2013 in the PC with an Intel Core i7 CPU and 8GB physical memory. However, the MATLAB programs are operated in the in MATLAB with vision 2013a, and 2013b.

CHAPTER 4. FRP CONTINUOUS SLAB-GIRDER BRIDGE

4.1. BACKGROUND

The static and dynamic analyses of a medium span slab-girder bridge are presented in this chapter, as part of the first study case. The deflection of the slab under the static loadings was obtained using the laminate spline finite strip code, and then the deflection was verified and compared with the results reported by Shen et al. (2013). An acceptable agreement was noticed between the results. Typically, to compare the composite bridge with the concrete bridge efficiently, the same mesh dimensions and distributions are modeled as the ones used by Shen et al. (2013) for both approaches.

The laminate integrated finite strip method was applied for determining first the static analysis of the bridge as per the methodology developed by Shen et al. (2013). In conformity with the same study, the natural frequencies of the bridge response were illustrated, based on the analytical procedure developed by Shen et al. (2013). Finally, after validating the FRP bridge model, frequency domain analysis is conducted. In the following sections, first, the developed programs are briefly explained, and then the numerical results related to the FRP slab bridge are presented.

4.2. FINITE STRIP MODELING

4.2.1. GEOMETRIC DISTRIBUTION

The proposed laminate finite strip solution was based on the integrated finite strip methodology. Thus the dimensions and the geometry of the FRP slab bridge model were selected as per the model developed by Shen et al. (2013), as shown in Figure 4-1.

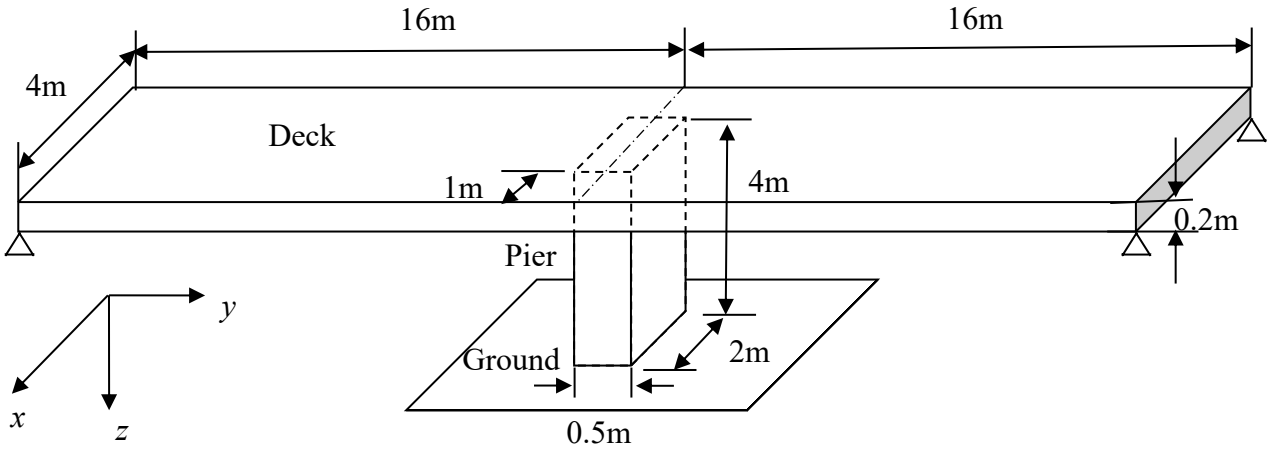

Figure 4-1 A simply support continuous FRP slab-girder bridge (Adapted from Shen et al. 2013)

The symmetric bridge with an equal length of 16 m for the two spans, was designed by two materials: concrete for the pier and FRPs for the bridge deck. For the concrete pier, the modulus of elasticity was $E = 3.0 \times 10^4$ MPa for all the concrete sections, the Poisson's ratio was 0.2, and the material density was 2,500 kg/m^3. The laminated FRP deck has a material density of 1,600 kg/m^3 and thickness of 0.2 m. Both LFSM and FEM are adopted to model the static and dynamic behavior of the structure, and the results obtained from different methods were compared.

4.2.2. LAMINATE FINITE STRIP MODELING AND LOAD CASES

For the integrated LFSM, a full bridge model is constructed using B_3 spline shell finite strip for the deck, column strip (CS) for the pier and transition elements for the bearings. The deck is divided into four equal strips, while the pier was divided into two CSs. Each deck strip is composed of 32 sections as well as two additional transition sections. Each pier strip is composed of four sections, as well as one transition section. The FEM was built by the SAP 2000 software, and the mass and stiffness of the bridge in FEM were constructed with five degrees-of-freedom (DOF) shell elements throughout the structure. In total, there are 827 DOF for the LFSM model, and 1041 DOF for the FEM model. A shell element was adopted from a combination of an in-plane element with translation in the *x* and *y* directions, and a bending element with translation in the *z* direction, plus bending above *x* and *y* (Shen et al. 2013).

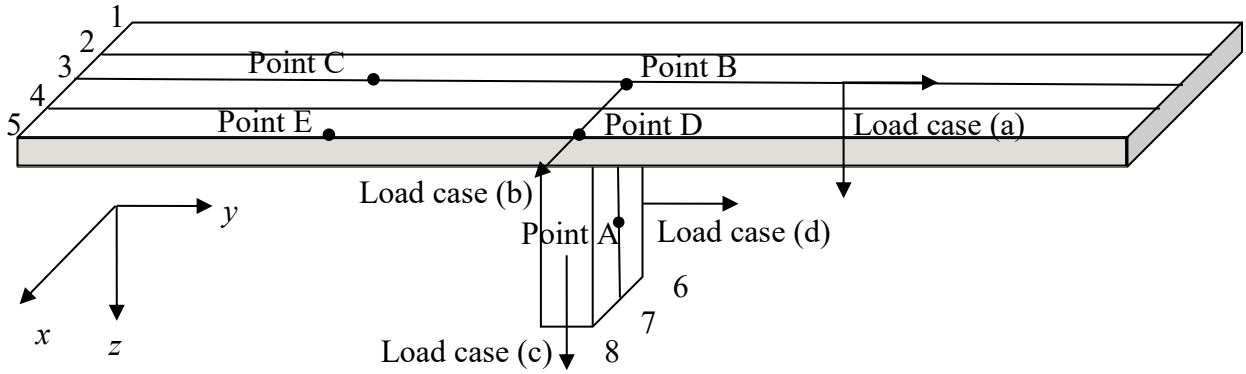

Figure 4-2 FSM model and load cases and test points of the slab-girder bridge (Adapted from Shen et al. 2013)

Several concentrated loads were applied at the middle of the bridge deck (points C and E) and on the deck, but at the pier location (points B and D) as presented in Figure 4-2. Also, one point on the pier (point A) was considered for conducting displacement behavior under concentrated load. Four loading cases combinations were considered as detailed in Table 4-1, where each

concentrated force was considered 1000 kN. The loading pattern was same to the one employed by Shen et al. (2013), such that the static analysis results can be compared and validated.

Table 4-1 Load cases combinations details

LOAD CASES	DESCRIPTION	LOCATION	DIRECTION
Load case (a)	Two concentrated loads	Deck y=24m, nodal line 3	Longitudinal (+y) Vertical (+z)
Load case (b)	One concentrated load	Deck y = 16m, nodal line 3	Transverse (+x)
Load case (c)	One concentrated load	Pier z = 2m, nodal line 8	Vertical (+z)
Load case (d)	One concentrated load	Pier z = 2m, nodal line 6	Longitudinal (+y)

As boundary conditions, the bridge deck was considered as simply supported at the four corners at the end of the deck, and the base of the pier was restrained for all the translations and rotations, to simulate the connection with the foundation better. The transition sections were employed between the deck and the piers and were modeled by the integrated FSM (Shen et al. 2013 and Naderian et al. 2015).

4.2.3. MATERIAL PROPERTIES

The properties of concrete were considered for the pier, and the laminate FRPs properties were used to model the deck. Table 4-2 details the material properties of the CFRP material including longitudinal modulus of elasticity (E_{11}), transverse modulus of elasticity (E_{22}), in-plane shear modulus (G_{12}), in-plane Poisson ratio (v_{12}), which are defined in particular for the composite materials. Also, the concrete deck material properties are described in the same table as a comparison.

Table 4-2 Basic material properties of FRP materials adopted in the design

Material	ρ (kg/m^3)	E_{11} (GPa)	E_{22} (GPa)	G_{12} (GPa)	v_{12}
CFRP (IM6G/3501-6)	1600	147	10	7	0.25
Concrete (Shen et al. 2013)	2500	30	30	10	0.2

4.2.4. MODELING ASSUMPTIONS

To derive the laminate properties of the FRP materials and to obtain the numerical simulation results from the computing codes, several relevant assumptions were made when modeling the slab-girder bridge by LFSM. Also, a FEM model of the same bridge was used for comparing the results, and Table 4-3 shows the detailed assumptions and the main differences between the LFSM and FEM approach. The FEM model was built by the aid of SAP 2000 version 15.0.0. Since most of the results were obtained by these two numerical simulation methods, it is always assumed that the FEM holds and derives the most accurate solution, and these results were used for validating the outcomes from the static analysis which is obtained by LFSM.

Table 4-3 Summary of modeling concepts and definitions for LFSM and FEM

ASSUMPTIONS	LAMINATE FSM	FEM (SAP 2000)
Orthotropic Laminae	The plate consists of orthotropic laminae bonded together, with the principal material axes of the orthotropic laminae oriented along arbitrary directions with respect to the *xy* axes	
Material Property	1) Extensional stiffnesses A_{ij} 2) Coupling stiffnesses B_{ij} 3) Bending stiffnesses D_{ij}	E_2=E_3, G_{12}=G_{13}, υ_{12}=υ_{13}=υ_{23}, $G_{23} = 4GPa$
Thickness	The thickness of the plate elements, *t*, is constant and is much smaller that the lengths of the plate edges, *a* and *b*	
In-plane Strain	ε_x, ε_y, and γ_{xy} are small compared with unity	
Transverse Shear Strain	γ_{xz} and γ_{yz} are negligible	The material component $S_{22} \neq 0, S_{23} = \infty$
Tangential displacement	*u* and *v* are linear functions of the *z* coordinate	
Transverse Normal Strain	ε_z is negligible	
Principal	Each ply obeys Hooke's law	
Transverse Shear Stress	τ_{xz} and τ_{yz} vanish on the plate surfaces defined by $z = \pm t/2$	
Deck types	Top flange plate strip	Shell-layered/nonlinear

4.2.5. SECTION PROPERTIES AND LAYOUT OF LAMINATE DECK

In general, a structure built out of composite materials should have high strength in the longitudinal direction and should prevent failure in the weaker direction. Chan et al. (2013) proposed two efficient layout patterns for laminates, one of them has a $[0/45/90/-45/0]_s$ orientation, exhibiting a much better performance than the $[0_{10}]$ and $[0/90/0/90/0]_s$ orientations. They had reported that when the deck was modeled with the $[0/45/90/-45/0]_s$ orientation; this failed because of the high bending moment has the highest stiffness capacity and stiffness. In one single loop simulation, the $[0_{10}]$ sample had higher strength, stiffness, and ductility under longitudinal loading than the other orientations. However, its properties decreased rapidly when the load direction changed to transversal. Therefore, the composite materials layout and properties should be carefully designed, according to the loading condition. Table 4-4 and Figure 4-3 provides the detailed configurations of those two laminas.

Table 4-4 Distinctive designs of laminates and the ply layout

LAMINA	LAMINA (1)		LAMINA (2)	
Ply Number	***Laminate Alignment***	***Thickness***	***Laminate Alignment***	***Thickness***
Top-Bottom	**Deg.**	**mm**	**Deg.**	**mm**
1	0	20	0	20
2	45	20	90	20
3	90	20	0	20
4	-45	20	90	20
5	0	20	0	20
6	0	20	0	20
7	-45	20	90	20
8	90	20	0	20
9	45	20	90	20
10	0	20	0	20
Total		200		200

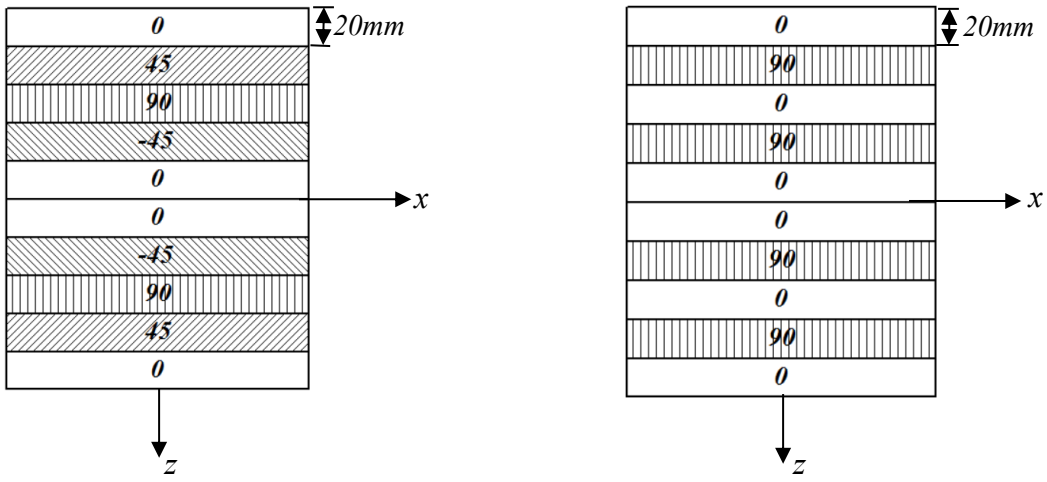

(a) Lamina (1): Configuration of layout (b) Lamina (2): Configuration of layout

Figure 4-3 Configurations of layout for two types of symmetric laminates

The corresponding lamina stiffnesses were calculated by the MATLAB programs developed by Naderian (2013) and modified by the thesis author in 2016 regarding the units. The material properties of the two layouts above corresponding to Lamina (1) and Lamina (2) are estimated as follows.

a) Lamina (1):

The laminate extensional stiffnesses A_{ij} (i, j=1, 2, or 6) are:

$$[A] = 10^{7} \times \begin{bmatrix} 1.6026 & 0.2995 & 0 \\ 0.2995 & 1.0522 & 0 \\ 0 & 0 & 0.3893 \end{bmatrix} kPa \cdot m \tag{4-1}$$

The laminate coupling stiffnesses B_{ij} (i, j=1, 2, or 6) are:

$$[B] = 10^{-9} \times \begin{bmatrix} -0.3576 & -0.0652 & -0.0075 \\ -0.0652 & -0.1863 & -0.0075 \\ -0.0075 & -0.0075 & -0.0838 \end{bmatrix} kPa \cdot m^{2} \tag{4-2}$$

The laminate bending stiffnesses D_{ij} (i, j=1, 2, or 6) are:

$$[D] = 10^{4} \times \begin{bmatrix} 6.1020 & 0.8987 & 0.5503 \\ 0.8987 & 2.9468 & 0.5503 \\ 0.5503 & 0.5503 & 1.1979 \end{bmatrix} kPa \cdot m^{3} \tag{4-3}$$

b) Lamina (2):

The laminate extensional stiffnesses A_{ij} (i, j=1, 2, or 6) are:

$$[A] = 10^7 \times \begin{bmatrix} 1.8519 & 0.0502 & 0 \\ 0.0502 & 1.3015 & 0 \\ 0 & 0 & 0.1400 \end{bmatrix} kPa \cdot m \tag{4-4}$$

The laminate coupling stiffnesses B_{ij} (i, j=1, 2, or 6) are:

$$[B] = 10^{-9} \times \begin{bmatrix} -0.3874 & -0.0084 & 0 \\ -0.0084 & -0.2906 & 0 \\ 0 & 0 & -0.0224 \end{bmatrix} kPa \cdot m^2 \tag{4-5}$$

The laminate bending stiffnesses D_{ij} (i, j=1, 2, or 6) are:

$$[D] = 10^4 \times \begin{bmatrix} 6.6132 & 0.1674 & 0 \\ 0.1674 & 3.8982 & 0 \\ 0 & 0 & 0.4667 \end{bmatrix} kPa \cdot m^3 \tag{4-6}$$

The geometric and material symmetry about the middle surface of the laminate material used for the current model is also reflected in the matrices above. Lamina (1) has symmetric angle-ply laminates, and the Lamina (2) has the symmetric cross-ply laminates as shown in Figure 4-3. Both laminae have the symmetric condition, according to the definition given by Eq. (3-14) and the numerical results of the current $[B]_{ij}$ matrix above, which leads to the major simplification that all the terms of this matrix are null $B_{ij} = 0$. It means that the bending-stretching coupling will not be present in such laminates. Consequently, in-plane loads will not generate bending and twisting curvatures which are the cause of out-of-plane warping, and bending or twisting moments; therefore, these will not cause a strain on the middle surface. For composite structures built in extreme environments and subjected to high thermal and hygrothermal forces, this assumption should be reconsidered by the new conditions.

For each lamina, after substituting the elastic modulus, shear strength modulus, and the Poison ratio, etc., a total of 18 components of stiffnesses were derived to describe the FRP material properties. Obviously, the magnitude of $[A]_{ij}$ and $[D]_{ij}$ for lamina (2) are larger compared with those for lamina (1) when both $[B]_{ij}$ is equal to 0, which means the lamina (2) deck model is more stiffer than the lamina (1) model. In the sam time, the stiffness matrix for the whole bridge models shows the same trend. Consequently, these components were assembled into the laminate FSM programs to calculate the strain and stress magnitudes.

4.3. STATIC ANALYSIS

4.3.1. STATIC ANALYSIS RESULTS

For the static analysis, the transition element of the IFS method was used to model the transfer of the loading between the deck strips and the column strips. The displacement response for the laminate FRP decks was investigated by determining the deflections obtained for the four load cases: (a), (b), (c), (d), with constant 1000 kN point forces acting on different structure components and in different directions, as shown in Figure 4-2. The deformed shapes for each load case are shown in Figure 4-4 for Lamina (1) and in Figure 4-13 for Lamina (2). The displacements are corresponding to the four loading cases were plotted along the analytical nodal line 3 for the deck and along the nodal line 7 for the pier. The results determined by LFSM were compared with those obtained from the FEM for the same bridge model and identical material properties and were represented in Figure 4-5 to Figure 4-12 for Lamina (1) and in Figures Figure 4-14 to Figure 4-21 for Lamina (2). It was noticed that the displacement calculated from the laminate FSM approach agrees well with the FEM results for all loading conditions, which indicates that the proposed LFSM approach can successfully model a hybrid composite bridge structure, taking the pier-bearing deck interaction into consideration.

4.3.1.1. LAMINA (1): SYMMETRIC ANGLE-PLY LAMINATES

The overall deformed shape of the bridge modeled by LFSM is represented for all four loading conditions in Figure 4-4. For the load case (a), when the concentrated force acted on the right span, the deck bears most of the deformation; similar deformation was noticed for load cases (b) and (c), in contrast with the load case (d), when the concentrated force was applied to the pier and it was obvious that the deformation of the pier is higher, while the deck doesn't exhibit significant deformations.

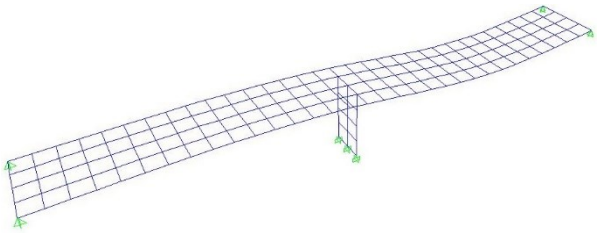

a) Deformed shape 1: Load case (a)

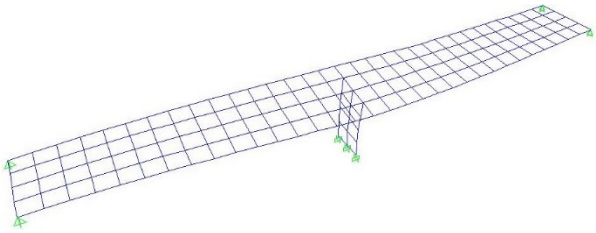

b) Deformed shape 2: Load case (b)

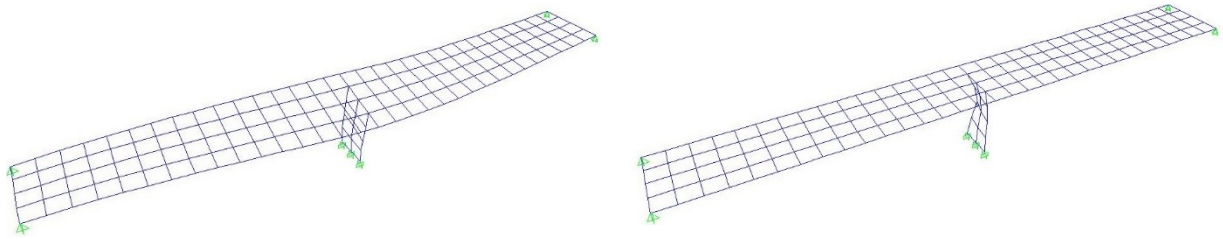

c) Deformed shape 3: Load case (c) d) Deformed shape 4: Load case (d)

Figure 4-4 Deformed shapes under four load cases for Lamina (1) by SAP 2000

1) Load case (a)

Load case (a), had the concentrated loads applied on nodal line 3 of the deck, as shown in Figure 4-2 above. From Figure 4-5 a) below was noticed that static displacements of nodal line 3 on the middle of the deck and of nodal line 7 on the pier, changed significantly, thus these two lines were chosen for comparing the results between the LFSM and FEM models. Figure 4-6 shows the global coordinate displacements distribution for the deck and the pier that was developed through the interaction on the transit sections as modeled by Shen et al. (2013).

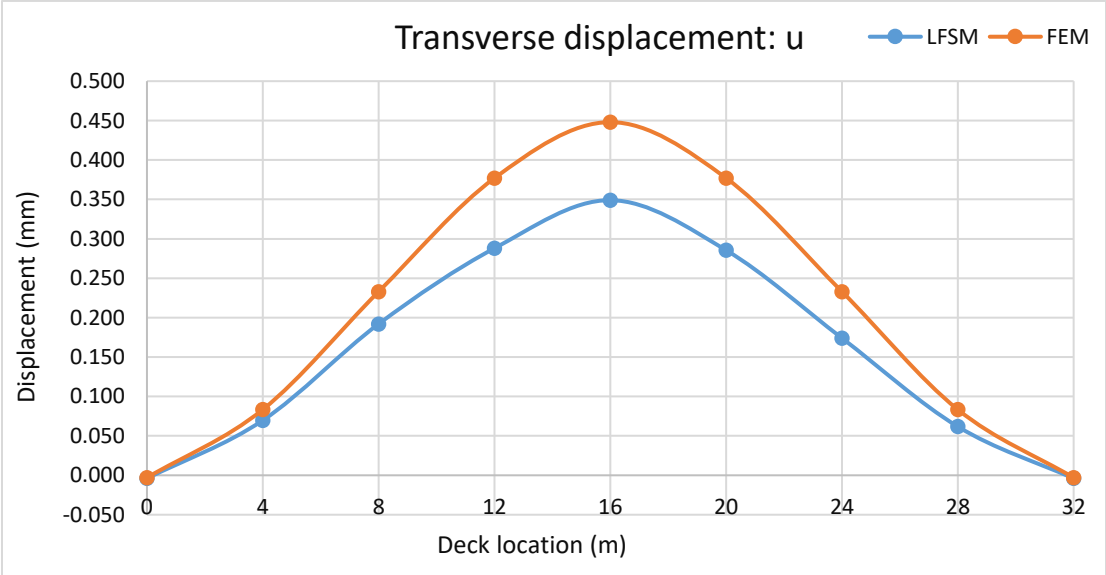

a) Transverse displacement *u* on the deck: Nodal line 3.

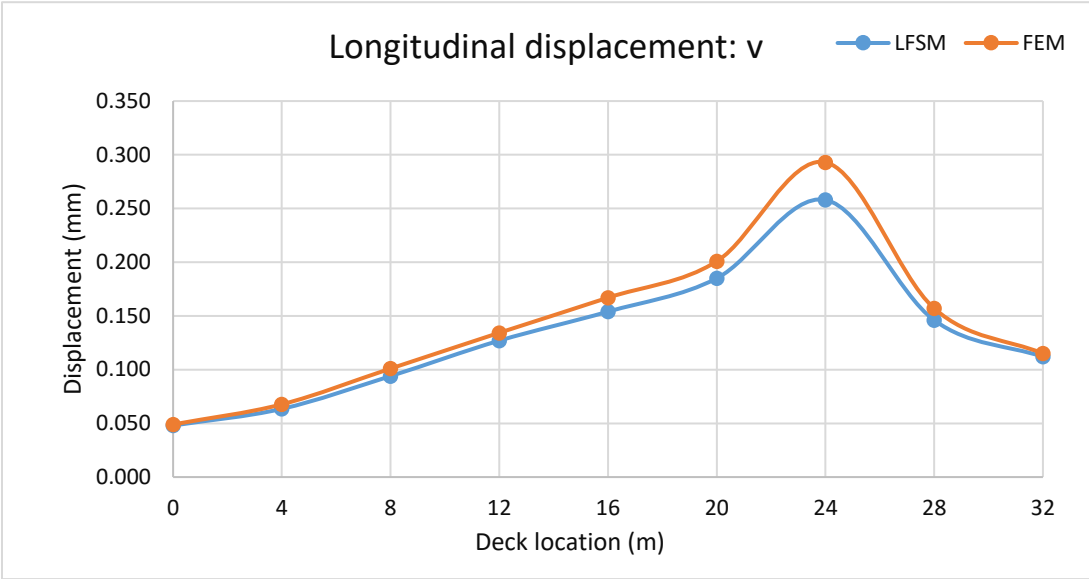

b) Longitudinal displacement *v* on the deck: Nodal line 3.

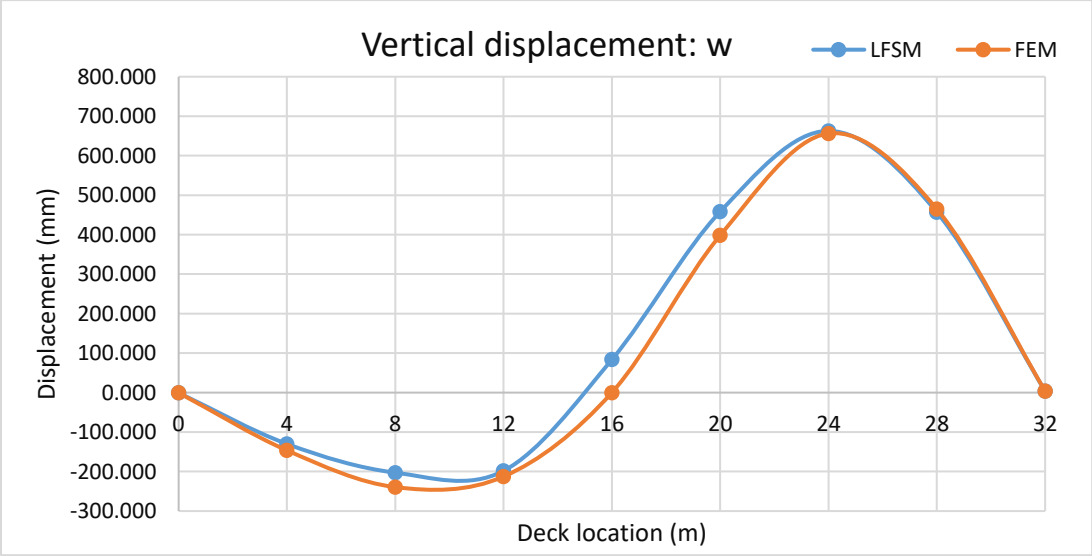

c) Vertical displacement *w* on the deck: Nodal line 3.

Figure 4-5 Deck displacements under load case (a) for Lamina (1)

The vertical displacement *w* had the best agreement, as it can be noticed in Figure 4-5 c), while the longitudinal displacement *v* was higher when estimated by the LFSM method, especially towards the middle of the right span (Figure 4-5 b)). The deck transverse displacement u had the highest difference at the pier location when compared with the FEM model (Figure 4-5 a)). This

might be due to the interaction between the lamina layers, which in the current model were considered as not having a perfect bond ($B_{ij} \neq 0$).

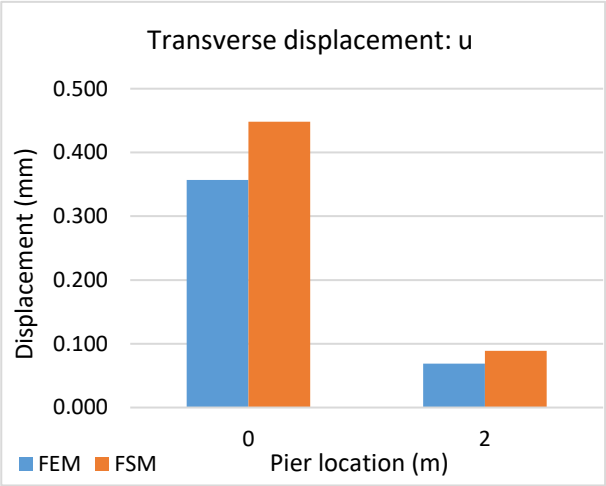

a) Transverse displacement *u* on the pier: Nodal line 7.

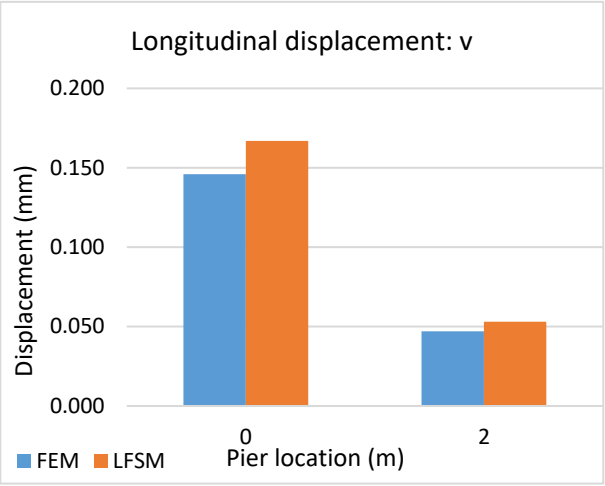

b) Longitudinal displacement *v* on the pier: Nodal line 7.

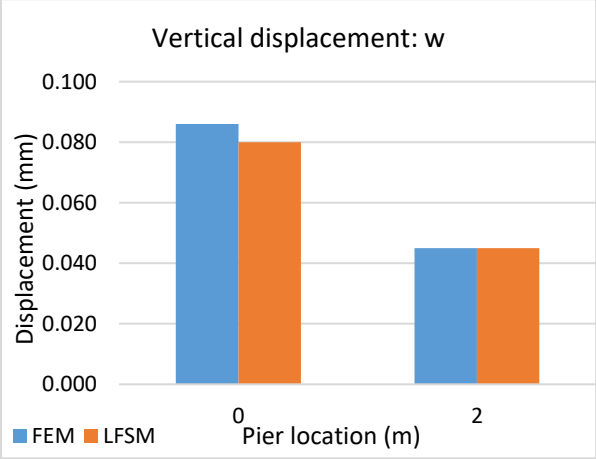

c) Vertical displacement *w* on the pier: Nodal line 7.

Figure 4-6 Pier displacements under load case (a) for Lamina (1)

Regarding the pier displacements on nodal line 7 (Figure 4-6), FEM always holds a higher displacement compared with the LFSM from 0 m on the top of the pier and 2 m on the middle point of the pier. However, regarding the vertical displacements, they are very similar.

2) Load case (b)

For the load case (b), when the concentrated load was applied on nodal line 3 on deck, but at the location of the pier and in the transverse direction, the same displacements were extracted on nodal line 3 for the deck and on nodal line 7 for the pier, for both LFSM and FEM approaches. In this

case, Figure 4-7 and Figure 4-8 show the global coordinate displacements distribution for the bridge deck and the pier respectively. It should be mentioned that the global longitudinal displacement was not plotted for the deck since the *v* displacements are negligible under load case (b) conditions. Similarly, the longitudinal displacements and the vertical displacements vanish for the pier.

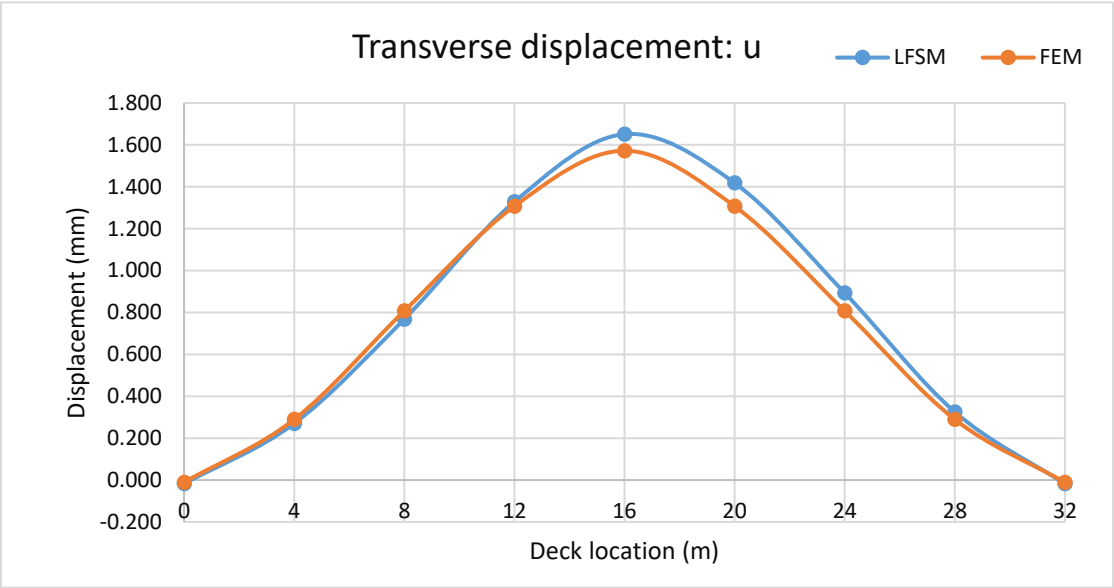

a) Transverse displacement *u* on the deck: Nodal line 3.

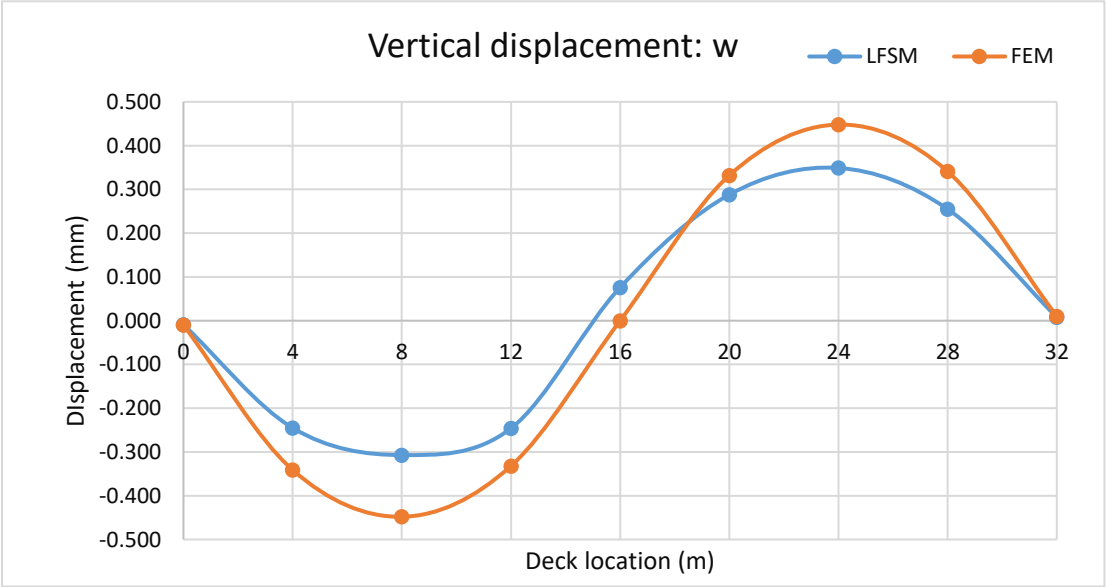

b) Vertical displacement *w* on the deck: Nodal line 3.

Figure 4-7 Deck displacements under load case (b) for Lamina (1)

The LFSM transverse displacement *u* for the deck, under loading case b) has reached a better agreement with the results plotted for the FEM model. However, the vertical displacement *w* shows a slight overestimation when the LFSM is used, especially towards the middle of the spans. However, the differences are smaller than 0.15 mm. Thus the two methods do not show significant discrepancies for the vertical response.

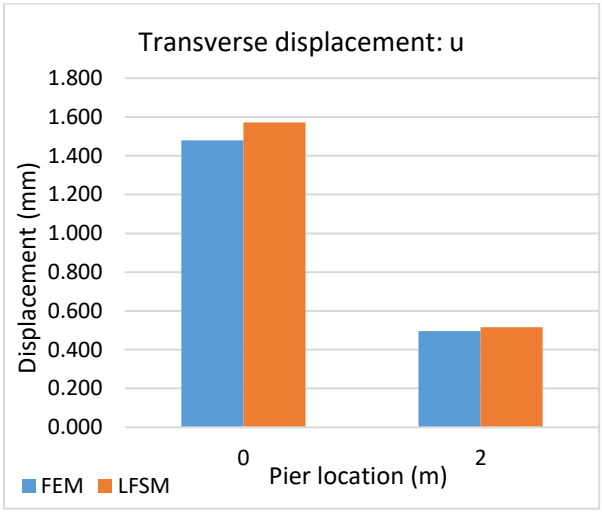

Figure 4-8 Pier displacements of nodal line 7 under load case (b) for Lamina (1)

Both LFSM and FEM have a negligible displacement response on the pier under load case (a) in the longitudinal and vertical directions, transverse displacements on each point have a little bit higher value developed by FEM.

3) Load case (c)

Regarding the load case (c), because the concentrated load is applied on nodal line 8 of the pier, the displacements registered on the nodal line 8 of the pier and the nodal line 4 of the deck were reported. In this case, Figure 4-9 and Figure 4-10 show the global coordinate displacements distribution for the deck and the pier respectively. For the current loading case, there are no global longitudinal displacements for the pier since the *v* displacements have vanished under the conditions of loading case (c).

The longitudinal displacement *v* of the deck, obtained by the LFSM model is in conformity with the FEM one, while for the transverse displacement *u*, is slightly overestimated by the LFSM model mainly at the location of the pier, as it can be noticed in Figure 4-9 b) and a) respectively. The vertical displacement *w* is higher when the LFSM approach is used, an evolution which is similar to the previous load case (b).

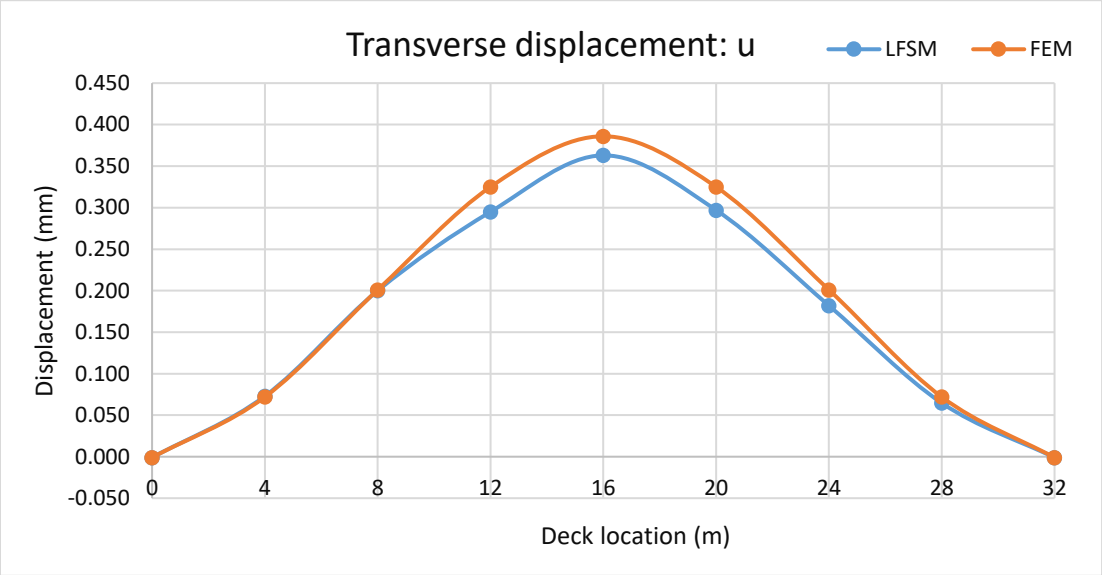

a) Transverse displacement *u* on the deck: Nodal line 3.

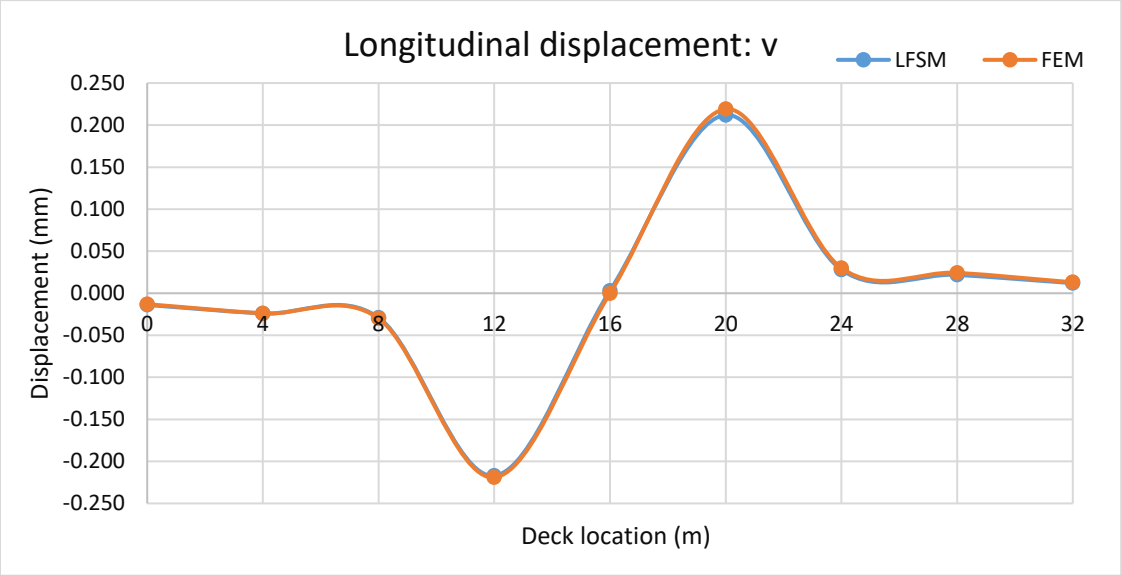

b) Longitudinal displacement *v* on the deck: Nodal line 4.

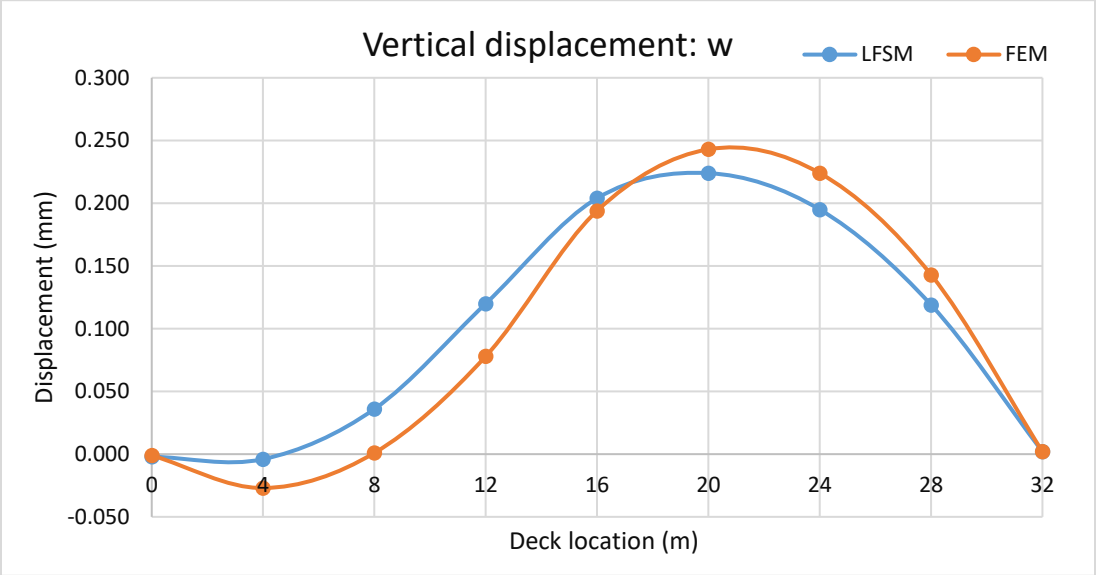

c) Vertical displacement *w* on the deck: Nodal line 4.

Figure 4-9 Deck displacements under load case (c) for Lamina (1)

Since the longitudinal displacements are too negligible to display, transverse and vertical displacements are compared as a result that LFSM is totally reliable to develop the pier displacement under load case (c) in an accurate way.

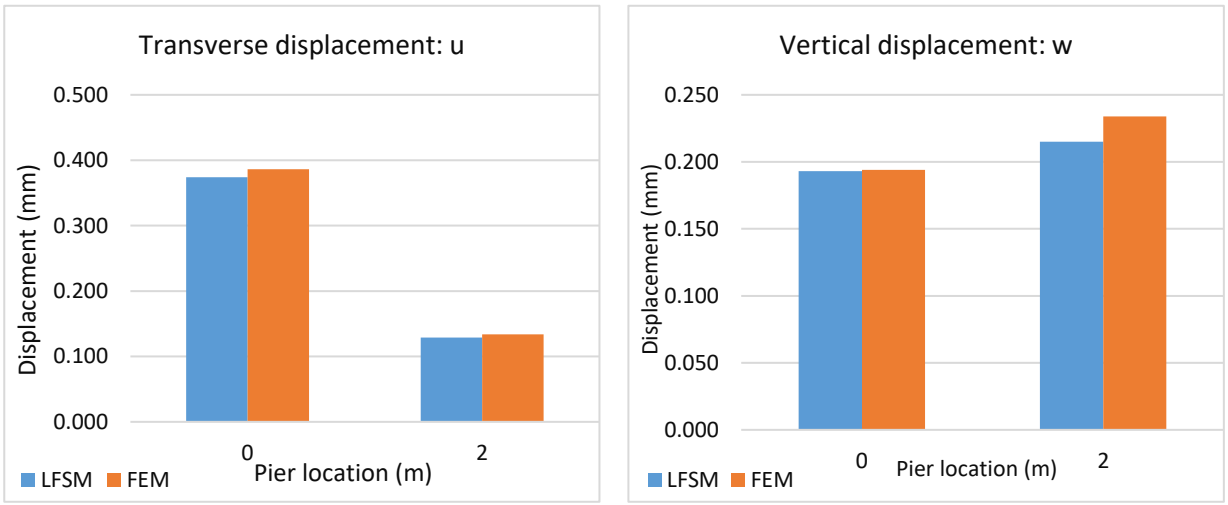

a) Transverse displacement *u* on the pier: Nodal line 8. b) Vertical displacement *w* on the pier: Nodal line 8.

Figure 4-10 Pier displacements under load case (c) for Lamina (1)

4) Load case (d)

For the load case (d), the concentrated force was applied on nodal line 6 of the pier in longitudinal direction, thus the displacements along the nodal line 6 on pier and the nodal line 2 on the deck, were extracted because these show a more significant change when compared with other nodal lines of the bridge model. In this case, Figure 4-11 and Figure 4-12 represent the global coordinate displacements distribution for both the deck and the pier, displacement that is developed from the interaction modeled by the transit sections (Shen et al. 2013). No global longitudinal displacement was registered for the deck since the *w* displacements vanished under the load case (d). Similarly, the transverse displacements and vertical displacements for the pier vanished as well.

The transverse and longitudinal displacements reported for the LFSM model were in acceptable agreement with the same displacements obtained from the FEM model, the differences registered for the middle spans and the deck at the pier location, for both displacements being lower than 0.02-0.03 mm (Figure 4-11 a) and b)). The longitudinal displacement *v* recorded for the tower is the only direction to display the displacements because of the relative larger magnitude. In this case, LFSM seems to hold higher but reasonable value compared with FEM.

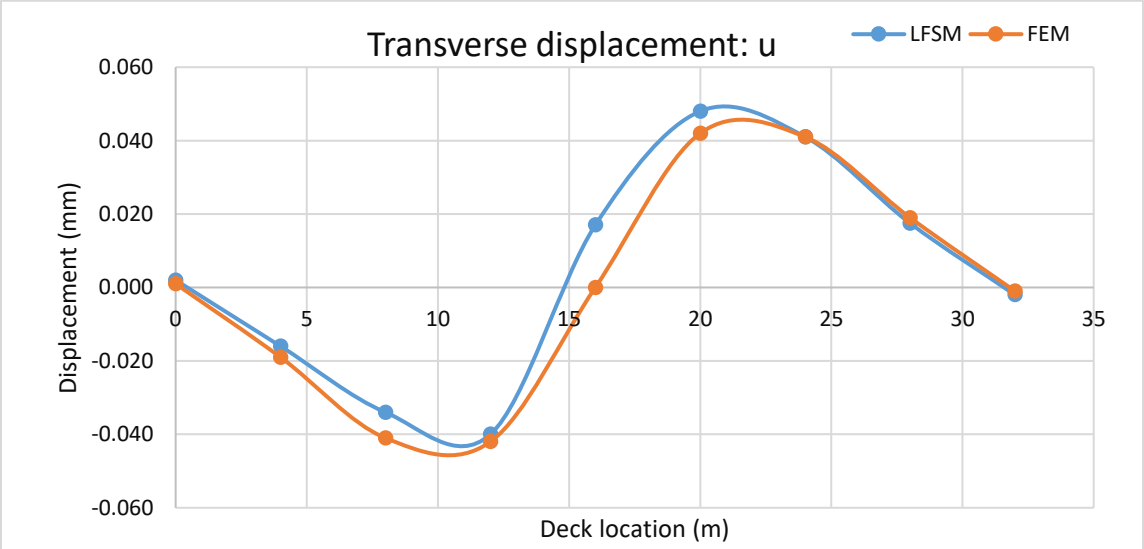

a) Transverse displacement *u* on the deck: Nodal line 2.

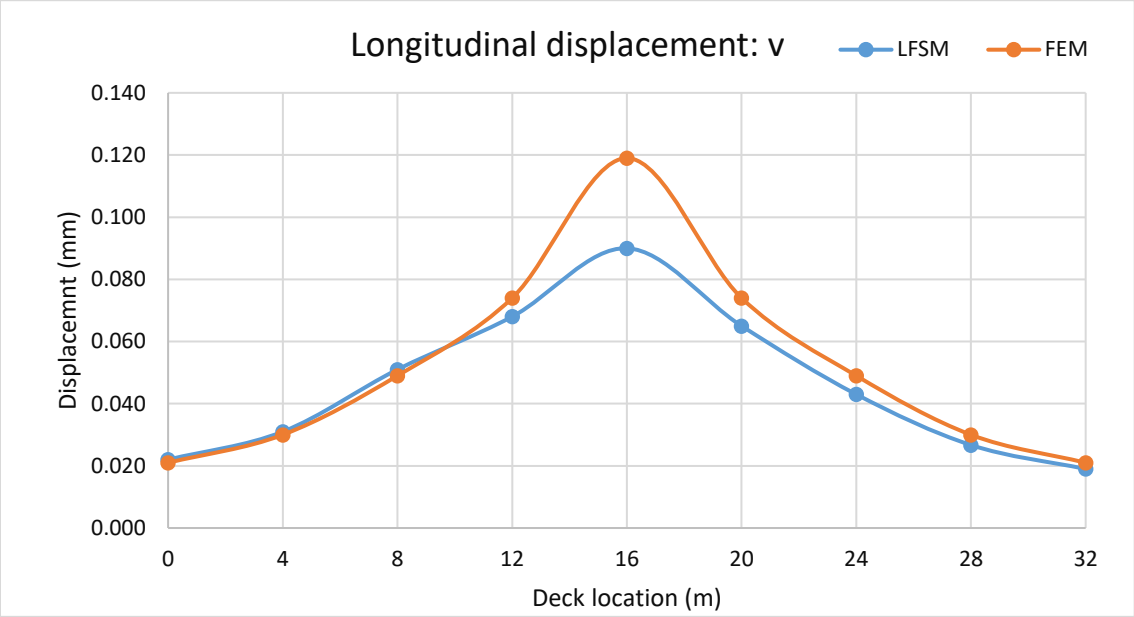

b) Longitudinal displacement *v* on the deck: Nodal line 2.

Figure 4-11 Deck displacements under load case (d) for Lamina (1)

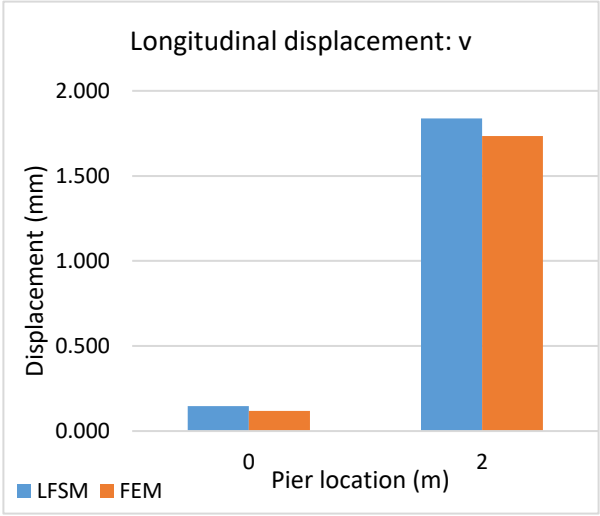

Figure 4-12 Pier displacements of nodal line 6 under load case (d) for Lamina (1)

4.3.1.2. LAMINA (2): SYMMETRIC CROSS-PLY LAMINATES

The deformed shape of the bridge deck modeled with Lamina (2) was represented in Figure 4-13, and it was noticed that, compared with the deformed shape of the Lamina (1) deck, plotted in Figure 4-4, no major difference between the two responses was noticed. This is because of the

single difference between the lamina (1) and lamina (2) models, is the layout of the laminates. However, the material properties were modeled the same. However, some differences in the displacement magnitudes can be determined under the same load cases, as it will be detailed below in the displacements plots and comparison tables.

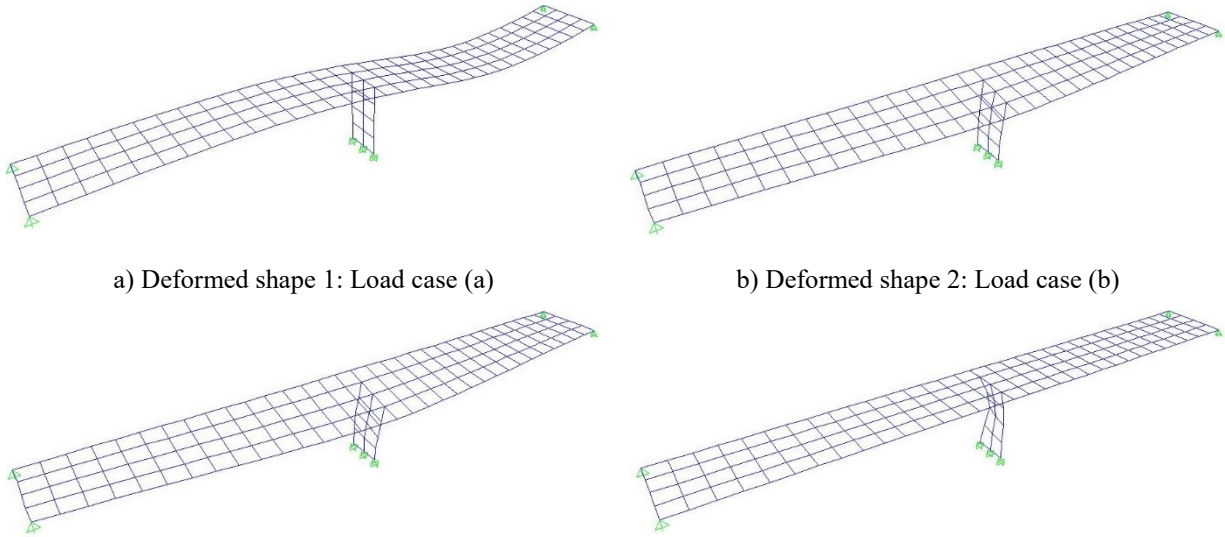

a) Deformed shape 1: Load case (a)

b) Deformed shape 2: Load case (b)

c) Deformed shape 3: Load case (c)

d) Deformed shape 4: Load case (d)

Figure 4-13 Deformed shapes under four load cases for lamina (2) by SAP 2000

1) Load case (a)

For the load case (a), as illustrated in Figure 4-14 and Figure 4-15, the LFSM global coordinate displacements distribution for both the deck and the pier that is developed based on the interaction of the transit section, were in acceptable agreement with those obtained from the FEM model. It should be mentioned that there is no global transverse displacement plot for the deck and the pier since *u* displacements vanish under conditions of load case (a). This might be due to the interaction between the lamina layers, which in the current lamina (2) were considered as having a perfect bond ($B_{ij} = 0$).

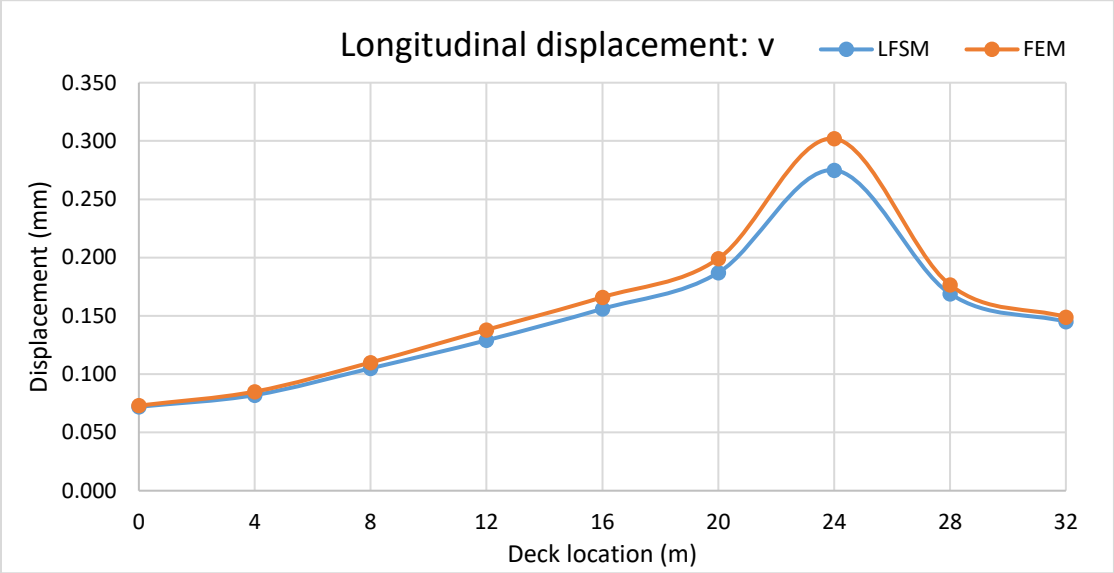

a) Longitudinal displacement *v* on the deck: Nodal line 3.

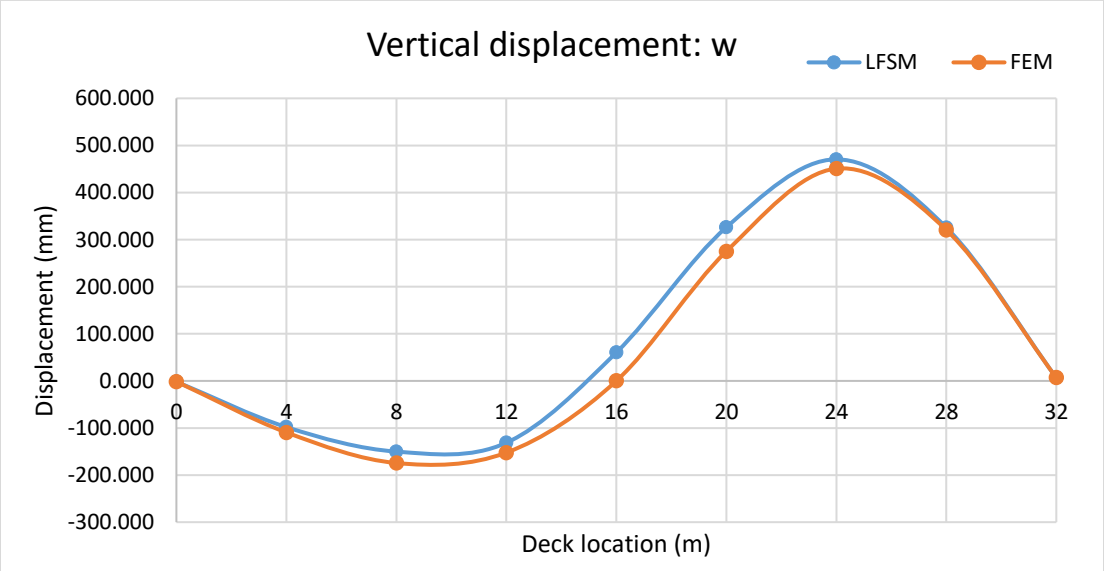

b) Vertical displacement *w* on the deck: Nodal line 3.

Figure 4-14 Deck displacements under load case (a) for lamina (2)

As shown in Figure 4-14, the longitudinal and vertical displacements obtained by the LFSM approach for the lamina (2) modeled deck was in exquisite agreement with the FEM model response, both registering a sudden increase for the middle of the right span, where the concentrated load was applied. Similarly, for the pier, the longitudinal and vertical displacements obtained by the LFSM approach were in acceptable agreement with the FEM model response, as shown in Figure 4-15.

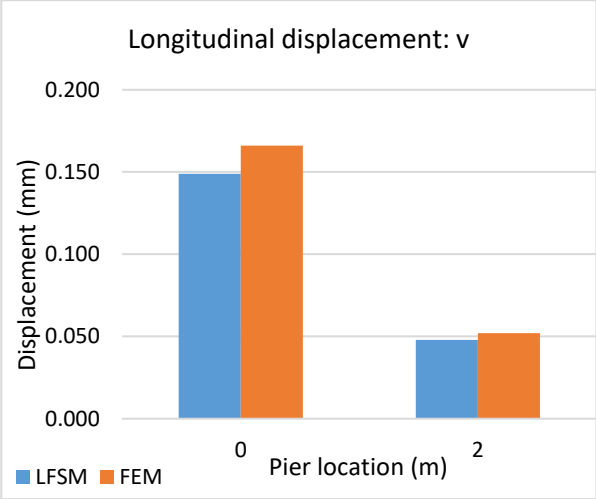

a) Longitudinal displacement *v* on the pier: Nodal line 7.

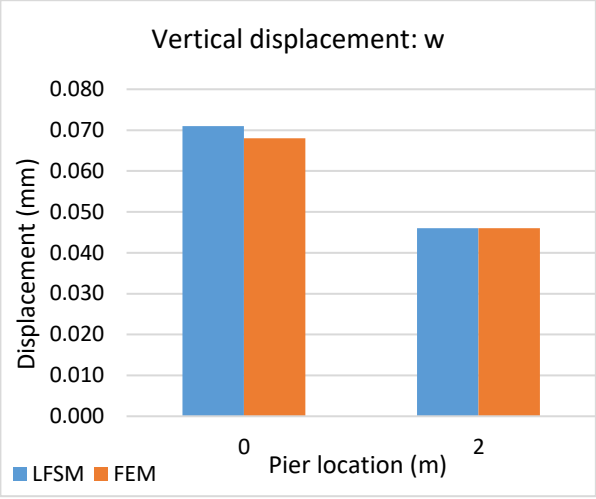

b) Vertical displacement *w* on the pier: Nodal line 7.

Figure 4-15 Pier displacements under load case (a) for lamina (2)

2) Load case (b)

In this case, as Figure 4-16 and Figure 4-17 show, the global coordinate displacements distribution for the deck and the pier that developed from the LFSM model are in acceptable agreement with the FEM model of the same bridge.

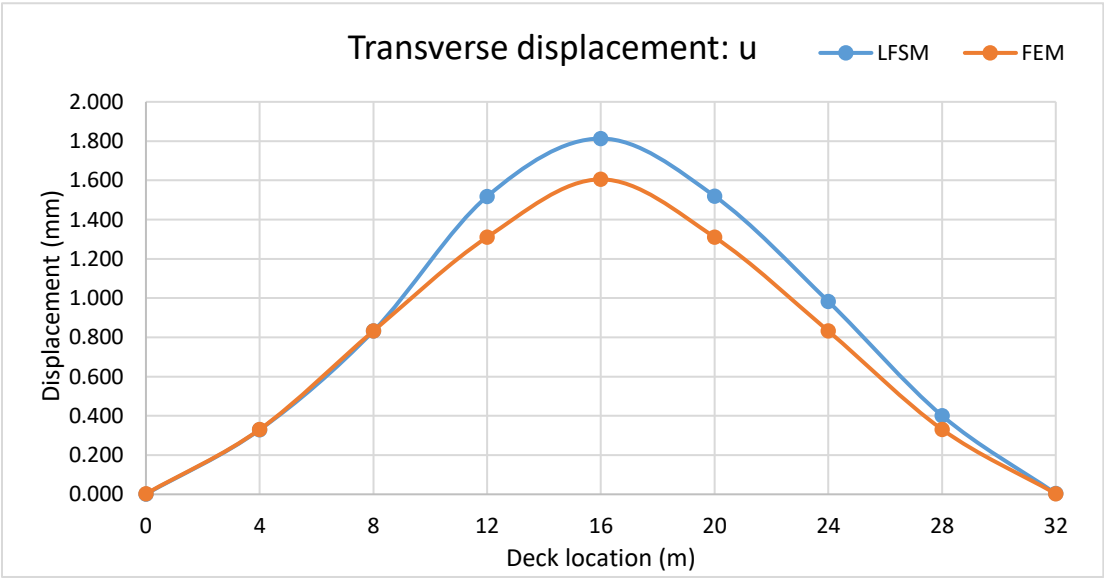

a) Transverse displacement *u* on the deck: Nodal line 3.

Figure 4-16 Deck displacements under load case (b) for lamina (2)

Also, similarly to lamina (1) model, for the current case, there are no global longitudinal, and vertical displacements plots for the deck and the pier since the *v* and *w* displacements vanish under the load case (b) for both of structural elements.

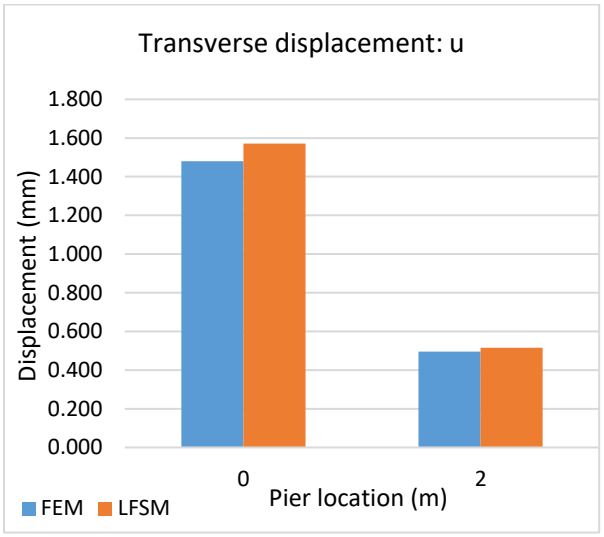

Figure 4-17 Pier displacements of nodal line 7 under load case (b) for lamina (2)

The lamina (2) deck displacement was higher at the location of the pier for both LFSM and FEM models, while an acceptable agreement was, with differences lower than 0.2 mm between the two approaches (Figure 4-16). Similarly, a very acceptable agreement was noticed for the pier displacement estimated through the LFSM and FEM methods (Figure 4-17).

3) Load case (c)

For the load case (c), for which one concentrated load was applied along the vertical direction on the nodal 6 of the pier, Figure 4-18 and Figure 4-19 show the global coordinate displacements distribution for both the deck and for the pier. No global longitudinal displacement for the pier, since the *v* displacements vanish under the load case (c) conditions.

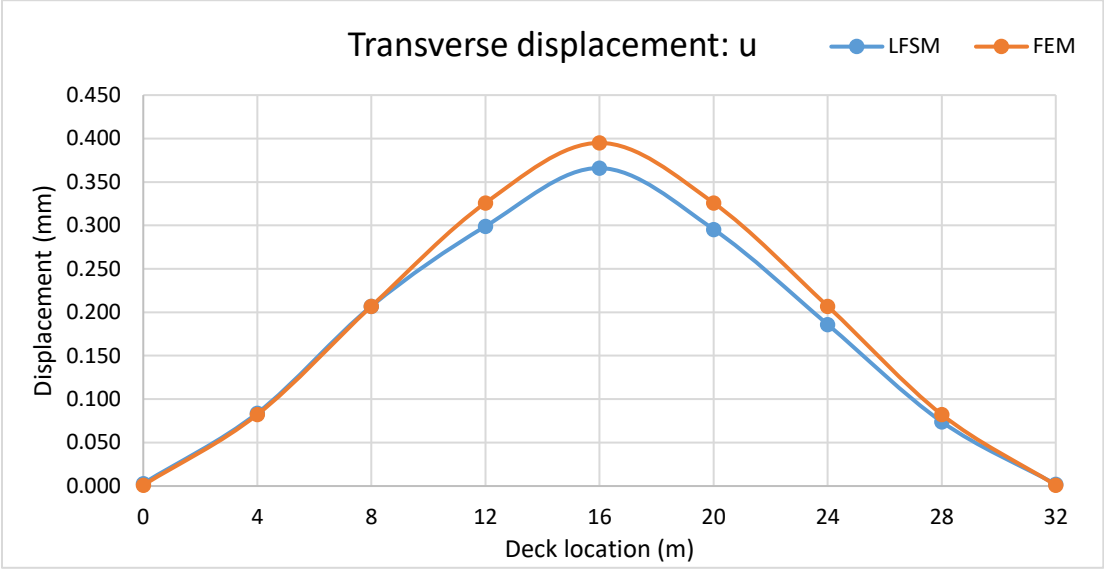

a) Transverse displacement *u* on the deck: Nodal line 3.

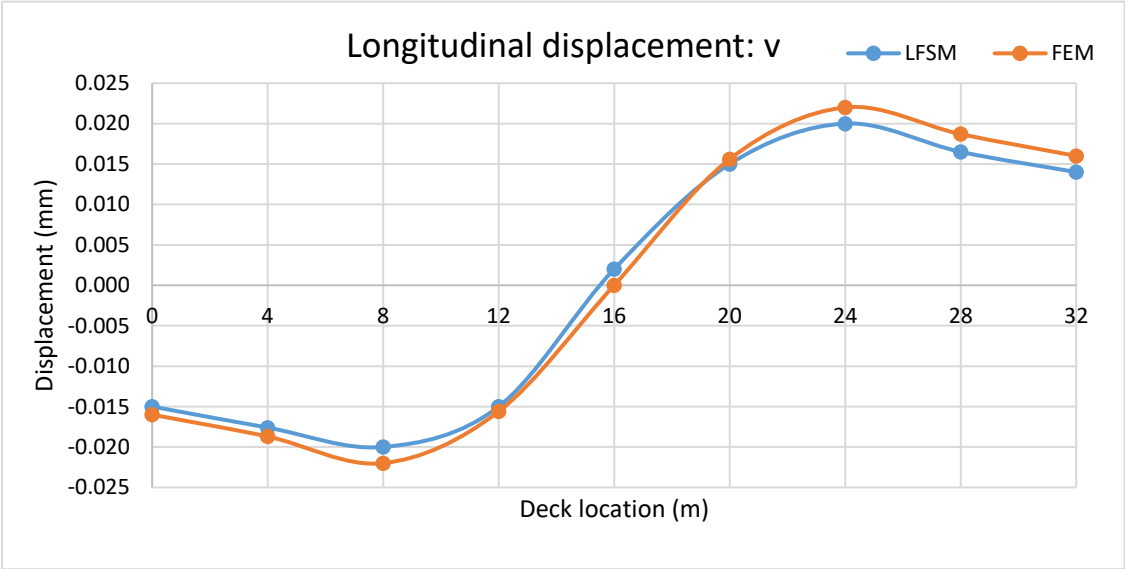

b) Longitudinal displacement *v* on the deck: Nodal line 4.

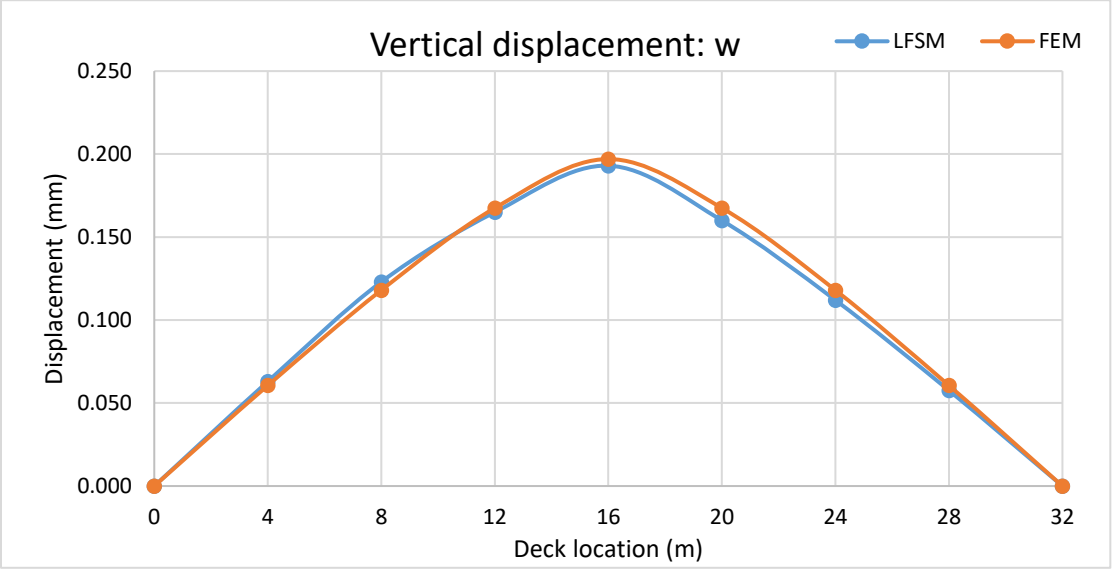

c) Vertical displacement *w* on the deck: Nodal line 4.

Figure 4-18 Deck displacements under load case (c) for lamina (2)

The displacements along the deck were not significantly affected by changing the location of the load, and thus very slight differences between the LFSM and the FEM extracted displacements were recorded as 0.03 mm for the transversal displacement, 0.002 mm for the longitudinal displacements and 0.004 mm for the vertical displacement (Figure 4-18).

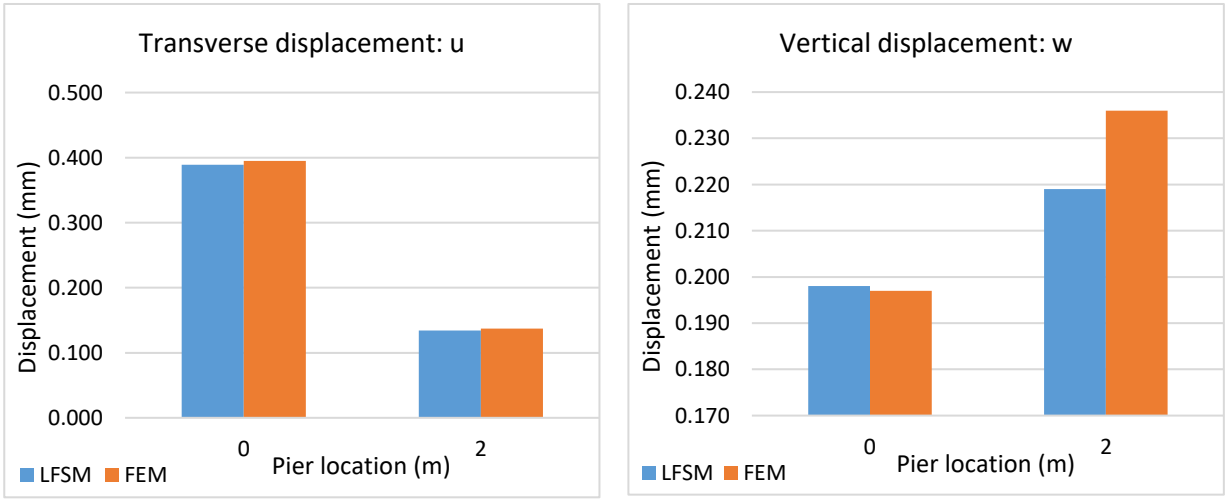

a) Transverse displacement *u* on the pier: Nodal line 8. b) Vertical displacement *u* on the pier: Nodal line 8.

Figure 4-19 Pier displacements under load case (c) for lamina (2)

Transverse displacements have a wonderful agreement in Figure 4-19 a), however, the FEM has a higher value in the vertical displacement on 2 m, which is due to the sensitive effects of the concentrated load on the same location.

4) Load case (d)

In this case, the concentrated load was applied to the pier, but in the longitudinal direction and the Figure 4-20 and Figure 4-21 show the global coordinate displacements distribution estimated by LFSM and by FEM, for both the deck and the pier of the Lamina (2) modeled bridge. Also for this case, there was no global vertical displacement for the deck because the *w* displacements are negligible under the load case (d). Similarly, the transverse displacements *u* and vertical displacements *w* of the pier vanish. Thus they do not need to be represented in a figure.

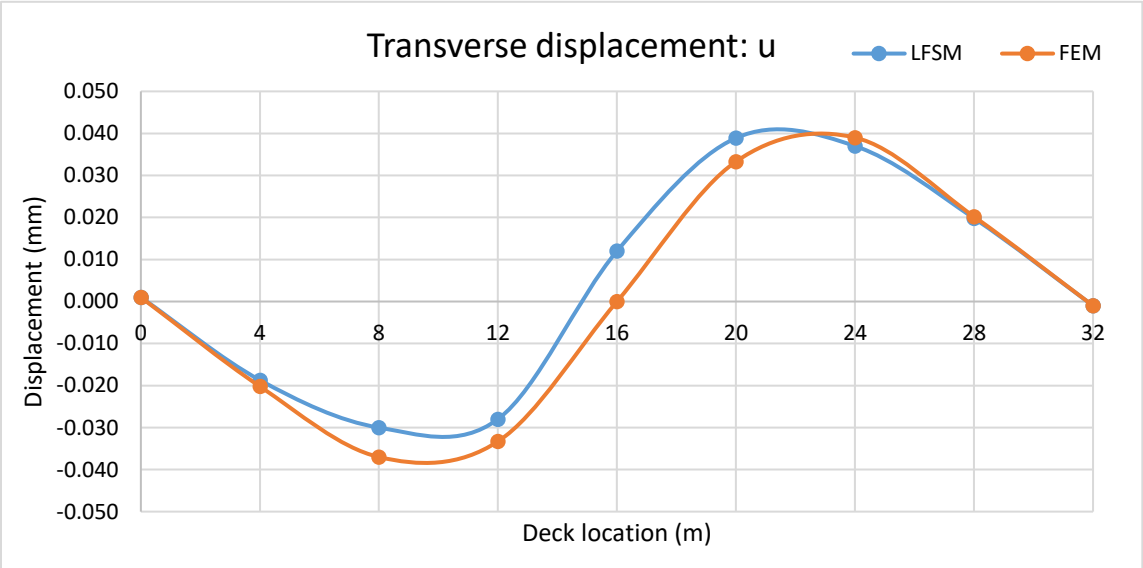

a) Transverse displacement *u* on the deck: Nodal line 2.

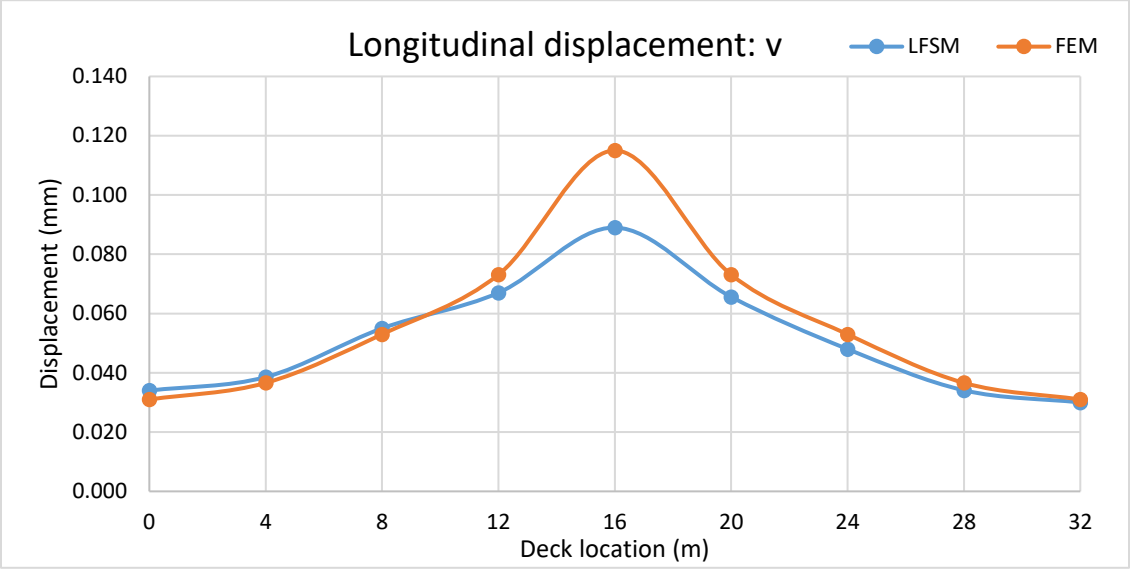

b) Longitudinal displacement *v* on the deck: Nodal line 2.

Figure 4-20 Deck displacements under load case (d) for lamina (2)

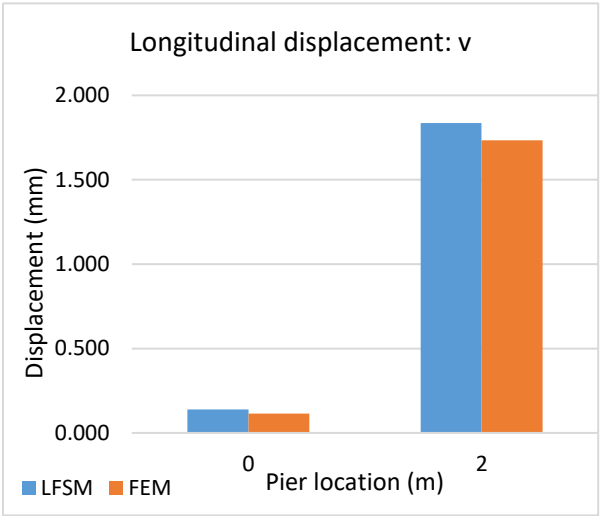

Figure 4-21 Pier displacements of nodal line 6 under load case (d) for lamina (2)

The differences between the LFSM and FEM obtained displacements are very small in the order of 0.1 mm to 0.002 mm for the transverse and longitudinal displacements of the bridge deck, however these show more discrepancy than the previous loading case (loading case (c)), especially around the pier location (Figure 4-20). The pier displacement, however, was in very acceptable agreement when comparing the LFSM and FEM models results, as it can be noticed in Figure 4-21.

4.3.2. COMPARISON OF STATIC RESULTS

Typically, all the static results for both laminae were derived from meeting a very acceptable agreement between the two methods employed: LFSM and FEM. The validation was performed against the results obtained through the FEM approach because it was considered that the FEM always has the most accurate values between these two methods. In this case, two types of laminae models were applied to the simply supported bridge. The static displacements at different nodal lines along the bridge deck and the pier were compared, and the results reported by Shen et al. (2013) for the original concrete simply supported bridge were compared.

Derived from meeting the requirement of strain, and the current author also verifies the results in this thesis that are used to compare the static results. And since both concrete bridge and hybrid composite bridge meet the acceptable agreement between the two methods, Table 4-5 compares the static results developed from the LFSM. All the values are maximum displacement magnitudes under each load cases for the specific nodal lines.

Table 4-5 Comparison of static displacements (mm) between the concrete bridge and the FRP bridge

	ORIENTATION	DECK			PIER		
Material	**Global Coordinate**	**Concrete (Shen et al. 2013)**	**Lamina (1)**	**Lamina (2)**	**Concrete (Shen et al. 2013)**	**Lamina (1)**	**Lamina (2)**
Load case (a)	***Longitudinal***	0.343	0.258	0.275	0.194	0.357	0.149
	Vertical	461	662	470	0.090	0.146	0.071
Load case (b)	***Transverse***	1.858	1.651	1.813	1.619	1.480	1.486
Load case (c)	***Vertical***	0.195	0.204	0.193	0.224	0.215	0.219
Load case (d)	***Longitudinal***	0.118	0.090	0.089	1.855	1.838	1.836

The maximum value of the displacements for both the original concrete bridge and the laminated composite bridge models are collected in Table 4-5, and it can be easily observed that the actual displacements of the deck and the pier are approaching to another. In order to select the best materials and lamina layout for the deck, the maximum, medium and maximum displacement cases among the loading cases investigated were discussed, and three colors were used in Table 4-5, red for maximum value, yellow for medium value, and green for minimum value, for an easier identification and discussion of the deck selected for the bridge modeling.

Obviously, the maximum displacements, as depicted by the red cells in Table 4-5, occurred for the concrete bridge model and the Lamina (1) bridge, for both the deck and the pier. Also, most of the maximum displacements were distributed mostly for the concrete bridge. As for the lamina (1) bridge model, there is a mix of maximum, medium, and minimum displacement values. The Lamina (2) bridge model only medium and minimum displacement values were encountered for this bridge deck and the piers, which means that this is the most capable material and layout to be used for bridge deck modeling. The most reasonable load scenario was the load case (a), which had the vertical concentrated load on the top of the bridge deck, and recorded the largest vertical displacement of the deck. Lamina (2) model had the thickness of deck t = 0.2m, which is smaller than the concrete bridge deck thickness but shows acceptable displacement under static loads.

4.4. FREE VIBRATION ANALYSIS

A good estimation of the frequency domain response of the bridge depends on the accuracy of the dynamic analysis, which relies on the free vibrations and the natural frequencies of the bridge model. Therefore, special attention was paid to estimating and comparing the mode shapes and natural frequencies of the LFSM bridge and the FEM bridge models. The visualization of the vibration mode shapes reported below was determined by using the modal analysis in FEM in SAP 2000. In general, the free vibration characteristics of a bridge are very sensitive to any geometry or material change. Thus minor differences are expected to be encountered when assessing the modal analysis results.

4.4.1. NATURAL FREQUENCIES

4.4.1.1. LAMINA (1): SYMMETRIC ANGLE-PLY LAMINATES

Regarding natural frequencies, Figure 4-22 compares the first fourteen natural frequencies of the lamina (1) modeled bridge, which is obtained from the FEM model built in SAP 2000 and the LFSM method adapted from the IFSM MATLAB developed codes (Shen et al. 2013). It can be noticed that the two numerical methods result in good agreement for the first fourteen natural frequencies.

It is obvious that the differences of frequencies between LFSM and FEM models are very small for most of the vibration modes investigated. However, the discrepancy was noticeable especially in modes 5, 9 and 14. When the vibration mode shapes were analyzed, it could be noticed that among the fourteen vibration modes, a total of seven bending modes of the deck, and seven torsional modes of the deck occurred for both models, LFSM and FEM. After identifying the vibration mode shapes, the two vibration types, the heave, and the torsion modes were compared in Figure 4-23.

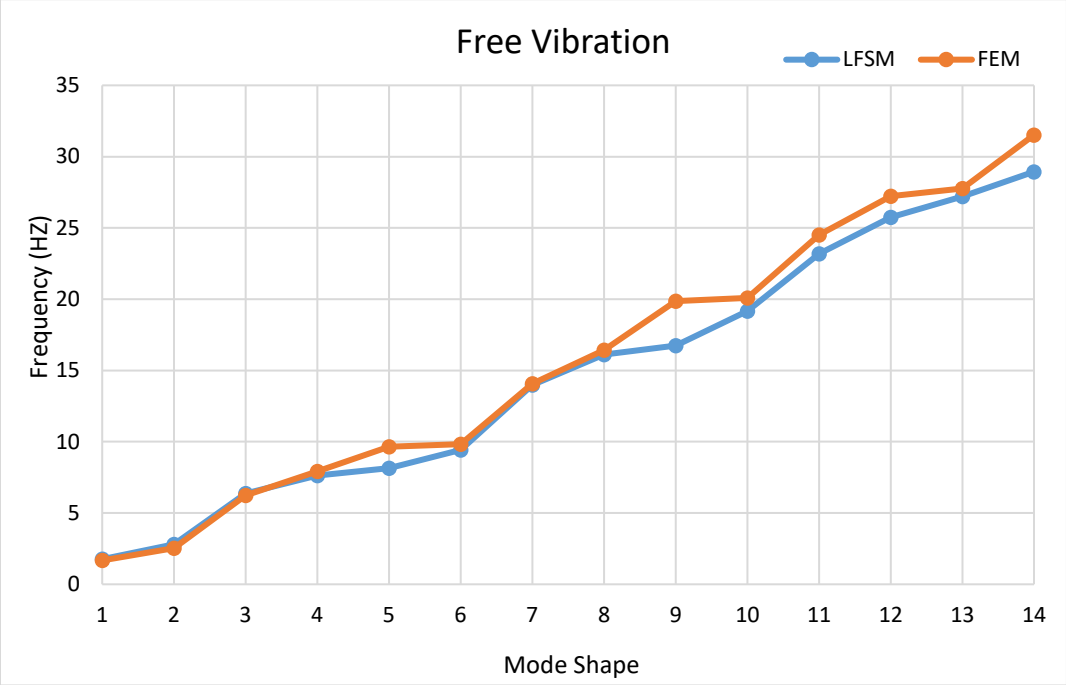

Figure 4-22 Natural frequencies for the first fourteen mode shapes for lamina (1)

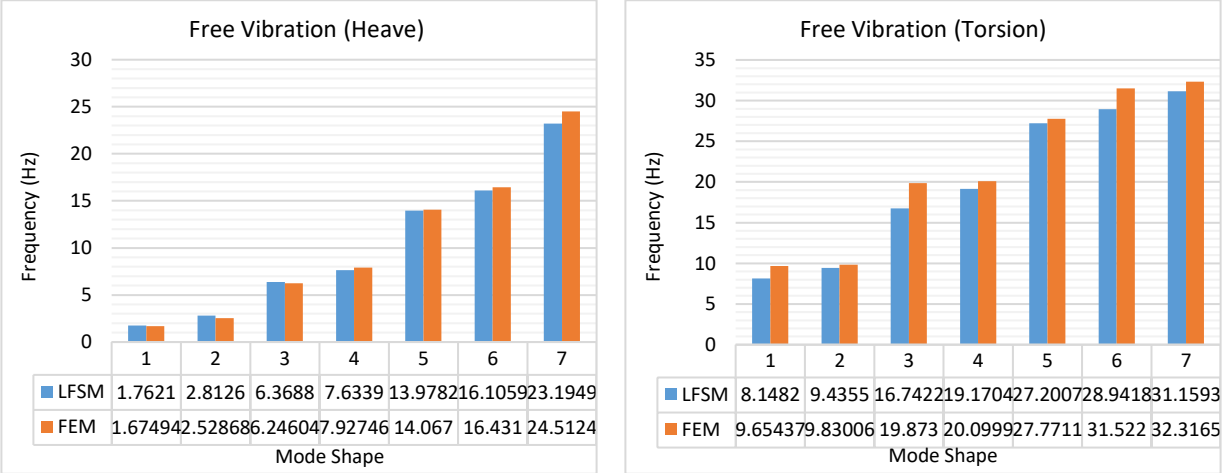

a) Heave (deck): First eight heave modes b) Torsion (deck): First eight torsional modes

Figure 4-23 Natural frequencies for the heave and torsion modes for Lamina (1)

It is evident that there are very slight differences in the natural bending frequencies for the two models LFSM and FEM. On the other hand, bigger differences were noticed for the natural frequencies of the torsional modes than those of the bending mode shapes. When the overall vibration mode shapes were plotted in Figure 4-24 and Figure 4-25 respectively, was noticed that the first bending modes have different shapes of vibration for both heave and torsion mode shapes

of the deck, which is most likely caused by the definition model of deck elements and the interactions between the laminae layers.

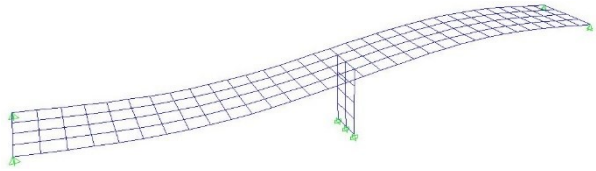

a) Mode shape 1: Heave (deck) antisymmetric

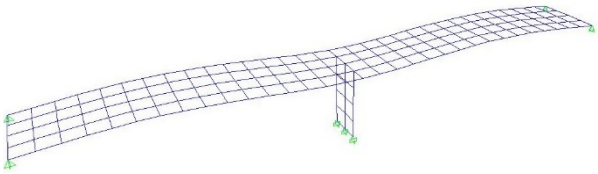

b) Mode shape 2: Heave (deck) symmetric

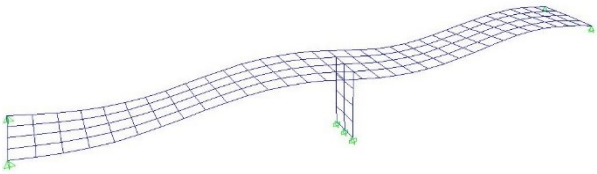

c) Mode shape 3: Heave (deck) antisymmetric

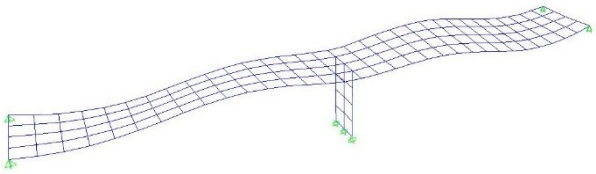

d) Mode shape 4: Heave (deck) symmetric

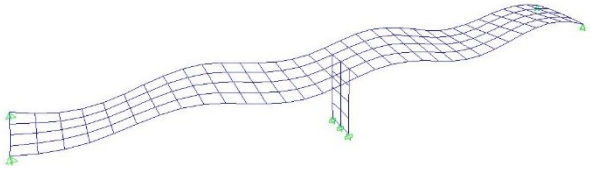

e) Mode shape 5: Heave (deck) antisymmetric

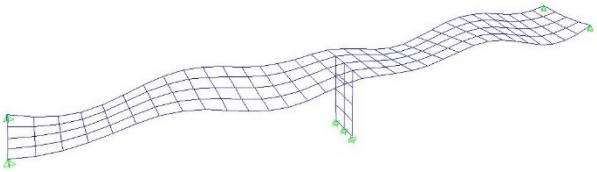

f) Mode shape 6: Heave (deck) symmetric

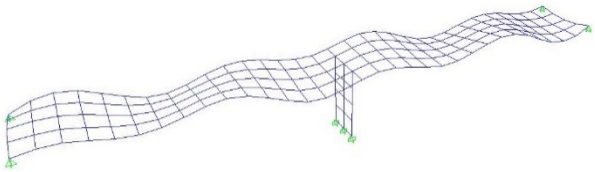

g) Mode shape 7: Heave (deck) antisymmetric

Figure 4-24 The heave deck mode shapes analysis for lamina (1)

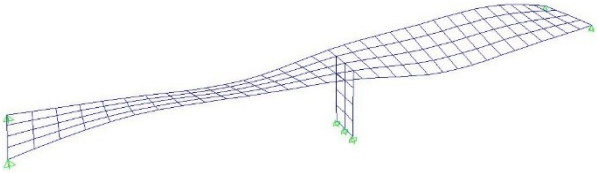

a) Mode shape 1: Torsion (deck) antisymmetric

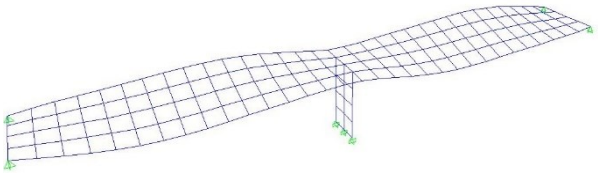

b) Mode shape 2: Torsion (deck) symmetric

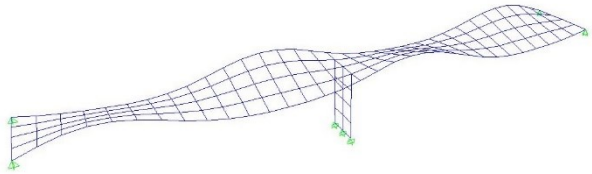

c) Mode shape 3: Torsion (deck) antisymmetric

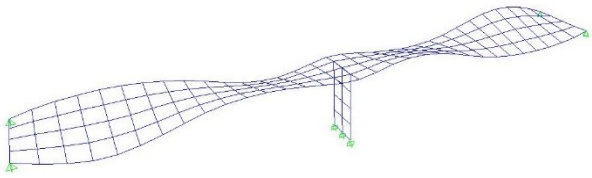

d) Mode shape 4: Torsion (deck) symmetric

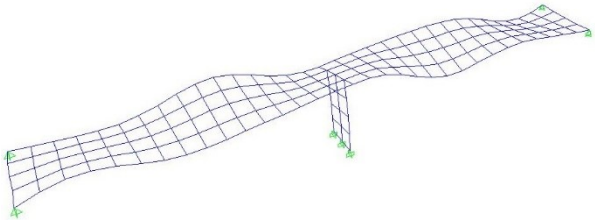

e) Mode shape 5: Torsion (deck) symmetrical

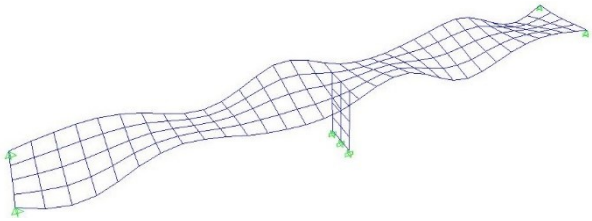

f) Mode shape 6: Torsion (deck) antisymmetrical

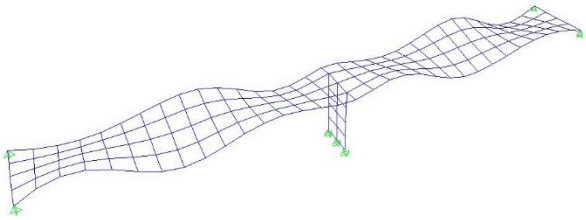

g) Mode shape 7: Torsion (deck) symmetric

Figure 4-25 The torsion deck mode shapes analysis for lamina (1)

4.4.1.2. LAMINA (2): SYMMETRIC CROSS-PLY LAMINATES

For the bridge modeled with lamina (2) deck model, the same good agreement was met by the natural frequencies estimated by LFSM and FEM approaches. In general, according to the comparison between the LFSM and the FEM outcomes for the laminated bridges investigated, the natural frequency results are in an acceptable agreement for the first vibration modes, which proves the validity of the laminated finite strip method and it enables it for performing the dynamic analysis of hybrid multi-span bridges under different loading conditions.

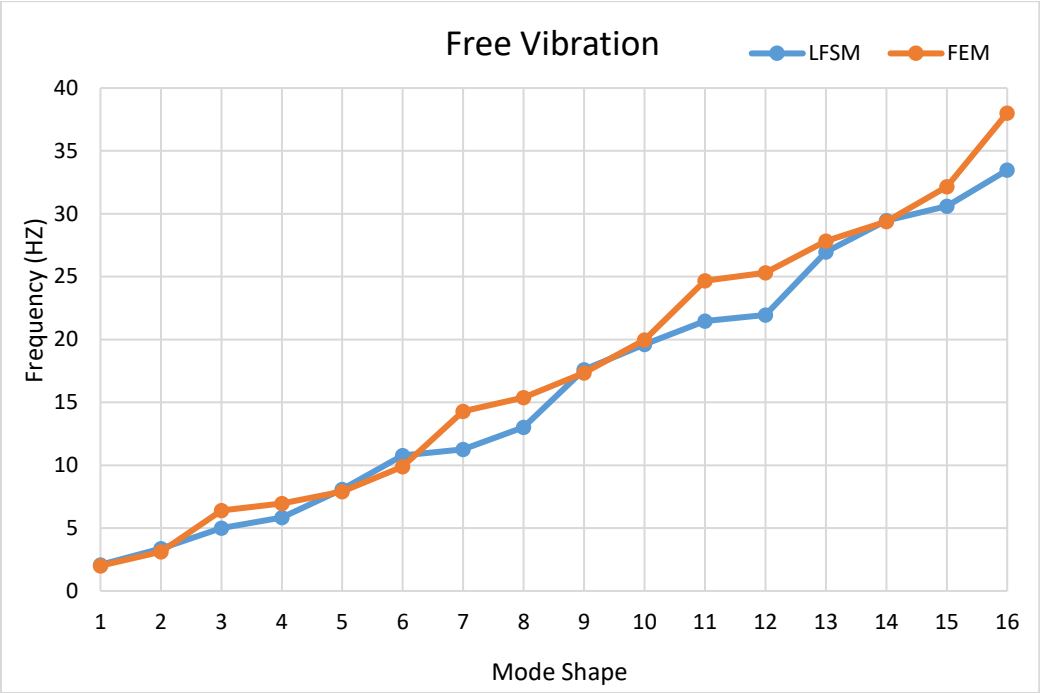

Figure 4-26 Natural frequencies for the first sixteen mode shapes for lamina (2)

Different from lamina (1) modeled bridge deck, for the lamina (2) deck model, the first sixteen vibration modes are obtained from analyzing the natural frequencies because the sixteen modes consist with eight heave and torsion modes. However, the same good agreement was noticed between the natural frequencies estimated by the LFSM method and those determined by FEM laminated bridge model, except for vibration modes 7, 8, 11, 12, and 16, for which the LFSM method yielded slightly higher vibration frequencies. Among the sixteen modes represented in Figure 4-26, eight were bending modes, and the other eight were torsional modes, according to the overall deformed shapes represented in Figure 4-27. The natural frequencies comparison for each type of vibration shape has shown that smaller discrepancies are observed for the natural bending frequencies, and larger differences occurred for the natural torsion frequencies when estimated by LFSM and FEM approaches (Figure 4-26).

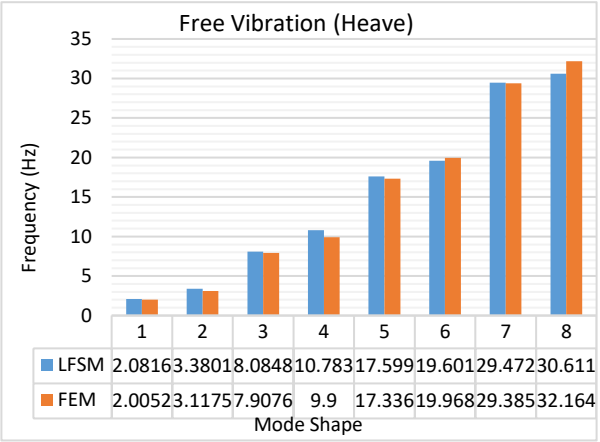

a) Heave (deck): First eight modes

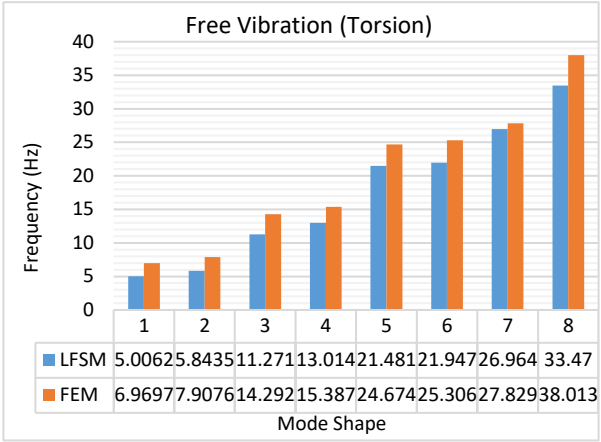

b) Torsion (deck): First eight modes

Figure 4-27 Natural frequencies for the heave modes and torsion modes for Lamina (2)

According to the natural frequencies presented in Figure 4-27, the detailed deformed shapes of the bridge structure for the first eight heave vibration modes and the first eight torsional modes are illustrated in Figure 4-28 and Figure 4-29 respectively.

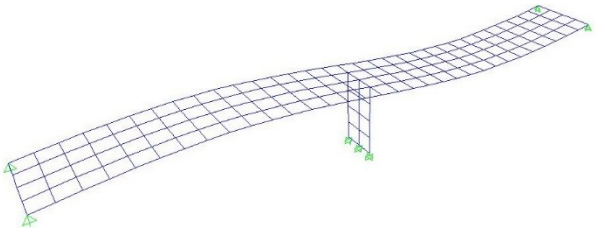

a) Mode shape 1: Heave (deck) antisymmetric

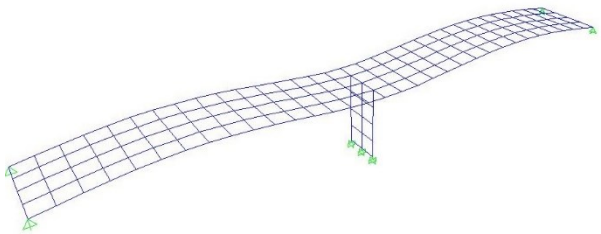

b) Mode shape 2: Heave (deck) symmetric

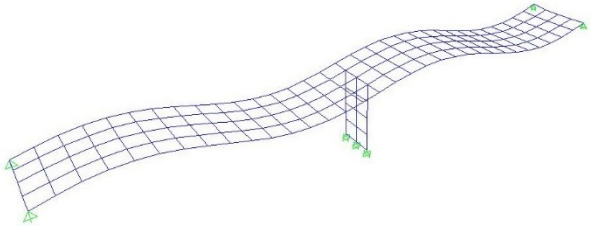

c) Mode shape 3: Heave (deck) antisymmetric

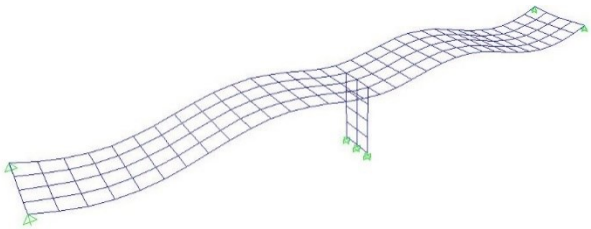

d) Mode shape 4: Heave (deck) symmetric

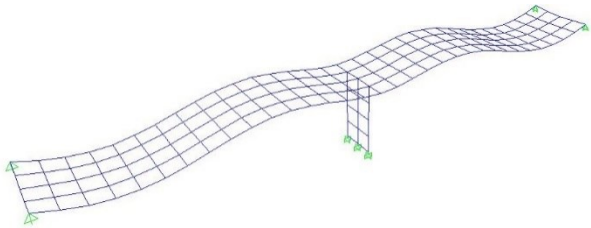

e) Mode shape 5: Heave (deck) symmetric

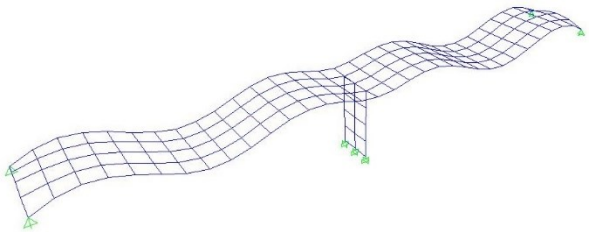

f) Mode shape 6: Heave (deck) symmetric

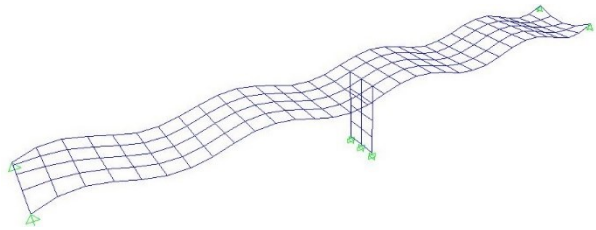

g) Mode shape 7: Heave (deck) antisymmetric

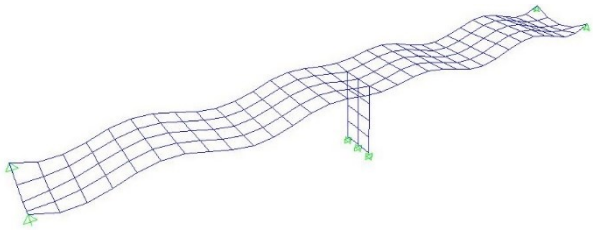

h) Mode shape 8: Heave (deck) symmetric

Figure 4-28 The heave deck mode shapes analysis for lamina (2)

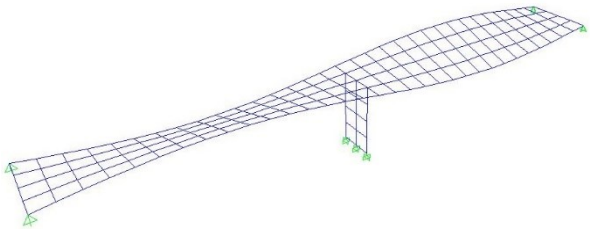

a) Mode shape 1: Torsion (deck) antisymmetric

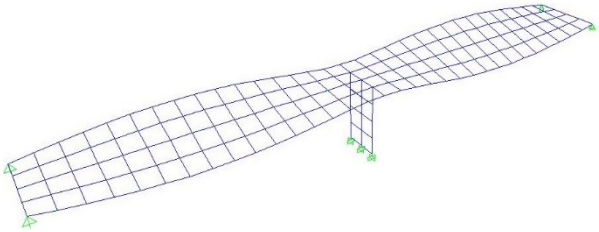

b) Mode shape 2: Torsion (deck) symmetric

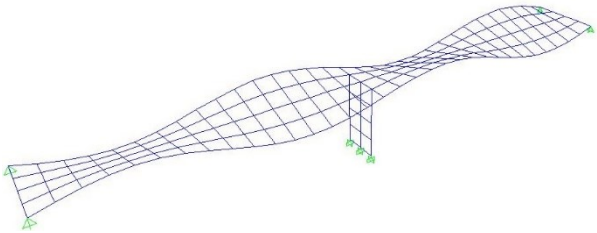

c) Mode shape 3: Torsion (deck) antisymmetric

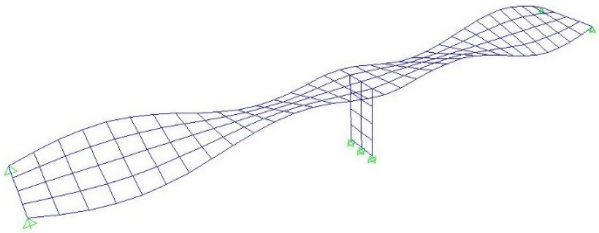

d) Mode shape 4: Torsion (deck) symmetric

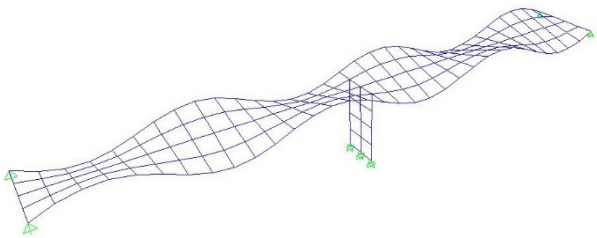

e) Mode shape 5: Torsion (deck) antisymmetric

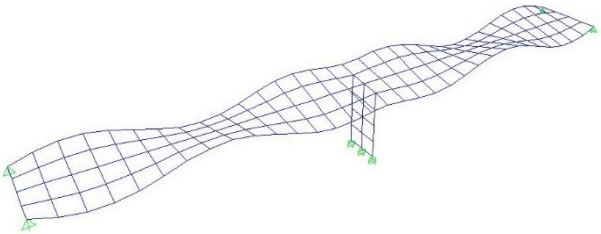

f) Mode shape 6: Torsion (deck) symmetric

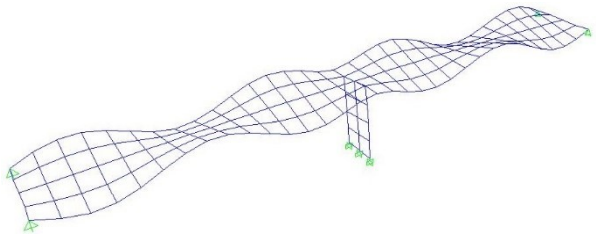

g) Mode shape 7: Torsion (deck) symmetric

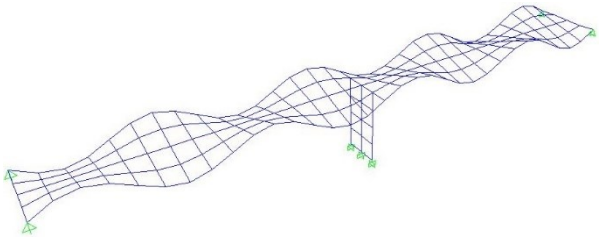

h) Mode shape 8: Torsion (deck) antisymmetric

Figure 4-29 The torsional deck mode shapes analysis for lamina (2)

4.4.2. COMPARISON OF NATURAL FREQUENCIES

For validating the results of the LFSM laminated bridge model, similarly to the static analysis, a results comparison was sought for the natural frequencies reported for the concrete bridge by Shen et al. (2013), and the two laminated composite bridges. In general, the natural frequencies developed of the laminated bridge by both LFSM and FEM models agree very well. However, the magnitudes of the frequencies have changed for certain vibration modes because of the change of materials and the laminae layouts of the bridge.

Shen et al. (2013) also calculated the natural frequencies of the concrete bridge, and they reported the first seven heave of vibration modes of the deck. The current author verified the results and extended the laminated deck model to the laminated composite bridges. Table 4-6 shows the comparison of the free vibration results between the concrete bridge and hybrid FRP bridges for the deck heave models. Because of the lower self-weight and the similar stiffness, the FRP bridges have higher natural frequencies compared with a concrete bridge. However, lamina (2) has a much higher stiffness than lamina (1), it seems to hold the largest natural frequencies.

Table 4-6 Comparison of natural frequencies between concrete bridge and hybrid FRP bridge

DECK HEAVE MODE	NATURAL FREQUENCIES (Hz)		
Mode Numbers	**Concrete (Shen et al. 2013)**	**Lamina (1)**	**Lamina (2)**
Mode 1	1.5338	1.7621	2.0816
Mode 2	2.4026	2.8126	3.3801
Mode 3	6.1169	6.3688	8.0848
Mode 4	7.7336	7.6339	10.7831
Mode 5	13.5770	13.9782	17.5989
Mode 6	15.7780	16.1059	19.6007
Mode 7	22.4560	23.1949	29.4719

It is well-known that the natural frequencies of a structural system do not depend on the structural damping, they only depend on the mass and stiffness of the overall bridge system. For the concrete bridge, the concrete material with a density of 2,500 kg/m^3 has been used by Shen et al. (2013) introduced above. As for the composite bridges, they have the same concrete pier, but the FPR material used for modeling the deck had a material density of 1,600 kg/m^3. Also, the deck of the concrete bridge was 0.25 m thick, which is 25% larger than the thickness of FRP bridge decks

which were 0.2 m, for both lamina models investigated. In this case, the total weight of the FRP bridges are equal but are lower than the original concrete bridge. Because the total weight is reduced, it is found that the FRP bridge has a higher frequency than the concrete bridge. This means that the FRP bridges would have a different dynamic response than the concrete bridge, as discussed below.

4.5. FREQUENCY DOMAIN ANALYSIS

To study the dynamic behavior of the slab bridge using the Pseudo Excitation Method (PEM), two ground motion inputs were assigned to the bridge models in different directions. The first input is a typical white noise wave with a PSD of 4.0 W/Hz. The second input is a recorded earthquake (Chichi Earthquake) wave record, as shown in Figure 4-34 (a). In this example, the ground motions are uniform, without considering the spatial variation of the earthquake excitations. The two loading conditions were chosen as per the study performed by Shen et al. (2013), to compare the conclusive results of the FRP bridge with the ones reported in the literature.

The power spectrum density (PSD) response spectra were determined at five critical positions on the bridge, as shown in Figure 4-2, were extracted from for both lamina FRP bridge models. Figure 4-30, 4-32, 4-35, and 4-37 compare the displacement response PSD spectra for a white noise loading and a recorded earthquake load. To better illustrate the result, the logarithmic scale was adopted for the PSD values on the vertical axis used to report the frequency domain results. Therefore, Figure 4-31, 4-33, 4-36, and 4-38 compare the Log(PSD) spectra of the displacement response obtained from the FEM bridge model and the proposed laminated FSM model.

4.5.1. WHITE NOISE

The white noise is a theoretical signal, which covers all frequencies, therefore when used as a loading scenario, this becomes a very important tool for verifying the critical dynamic responses of a structural system. The displacement results obtained from applying a white noise input were arranged regarding the response spectra for the proposed LFSM with PEM, which has the advantage that it can pick up the discrete frequency peaks that appear in the response spectra, as FEM does. Thus a direct comparison can be drawn between these two methods. As shown in Figure 4-30 and Figure 4-32, from the spectral response of the signals recorded by the FEA and LFSM at three points on the slab-girder bridge, the response frequencies under the white noise input occur at some of the natural frequencies for different vibration modes of the laminated bridge model, as identified above.

4.5.1.1. LAMINA (1)

As shown in Figure 4-30, the bridge model which used the lamina (1) for modeling the deck, the displacement PSD extracted at point A in the transverse direction *x*, showed that the dominant vibration frequency under the white noise loading scenario was dominated by the frequency of 27.77 Hz, which corresponds to the 13th natural vibration mode for the FEM model. For the LFSM model, the 14th natural vibration mode responded at the frequency of 29 Hz. Both were identified as torsional modes in Figure 4-23 above. Since the natural frequencies of the laminated bridge differ slightly depending on the method employed, the corresponding natural frequency for the FRP Bridge was determined as 28.94 Hz (mode 14) by LFSM accordingly. For location B, the PSD of the longitudinal displacement showed no dominant frequency for the first 50 Hz wiped by the white noise. It is also confirmed again that there are no longitudinal vibration mode shapes for the free vibrations within the investigated 50 Hz. The vertical response PSD for location C showed dominant vibration peaks for 2.528 Hz and 2.83 Hz, for the LFSM and FEM models respectively, which are very close to the frequencies of these correspond to the natural frequencies for the FRP Bridge of 1.7621 Hz (mode 1) and 2.8126 Hz (mode 2) by LFSM accordingly. A second vibration peak, much weaker than the dominant one, can be identified in the PSD of the response obtained by LFSM model, which corresponds to the first vibration mode of the structure. The FEM model did not estimate a second vibration peak for the vertical response PSD.

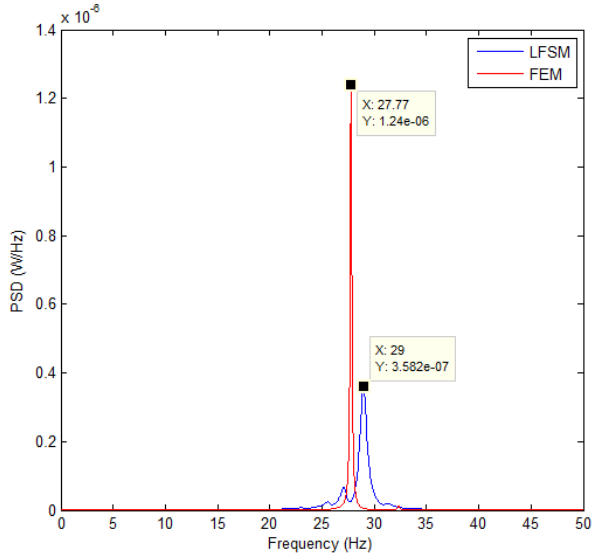

a) At point A in x direction

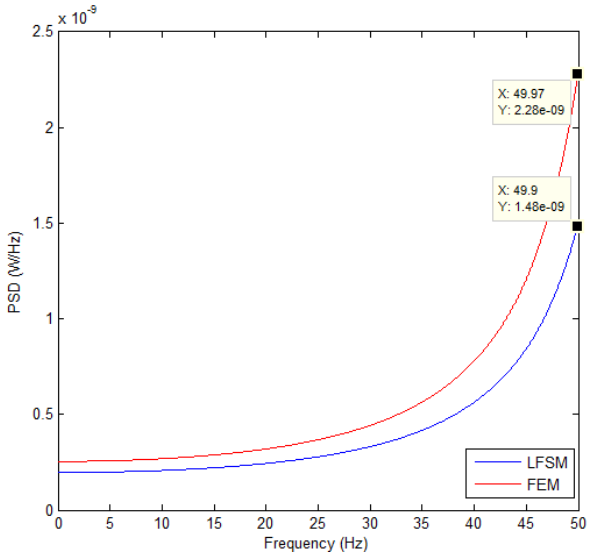

b) At point B in y direction

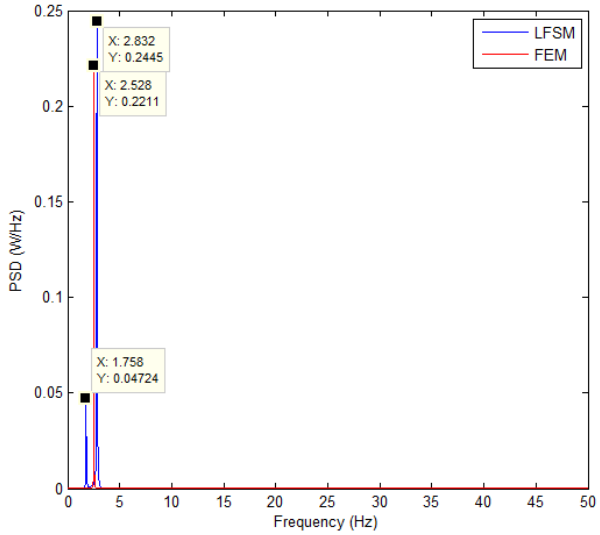

c) At point C in z direction

Figure 4-30 PSD of displacement response applied ground motion: white noise for lamina (1)

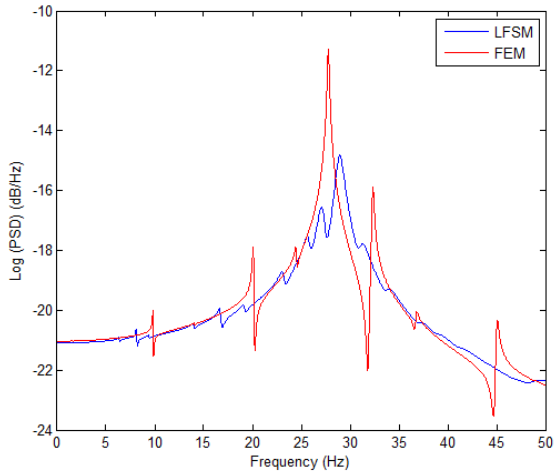

a) At point A in x direction

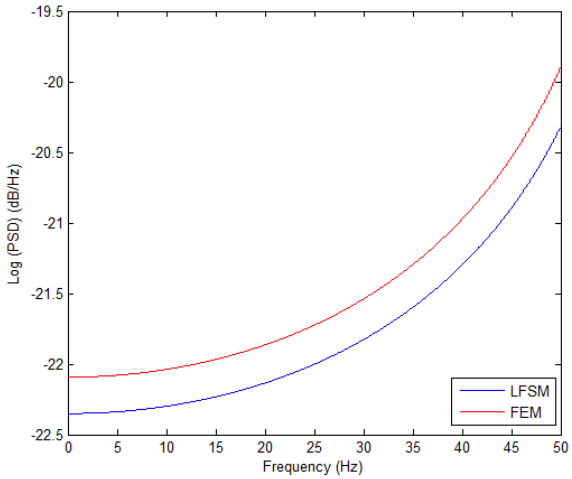

b) At point B in y direction

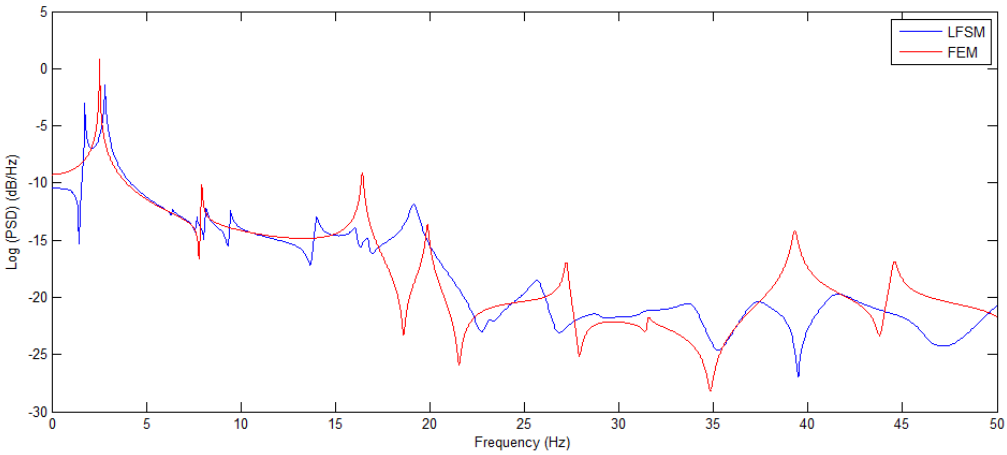

c) At point C in z direction

Figure 4-31 Log (PSD) of displacement response applied ground motion: white noise for lamina (1)

The Log (PSD) illustrates all the frequency windows that might appear in a signal, not only the dominant one for which the PSD estimate is determined. The Log (PSD) was represented as shown in Figure 4-31, to represent in more detail the frequency content of the response spectra at point A, it was noticed that besides the dominant 29 Hz and 27 Hz estimated by the LFSM and the FEM models respectively; for FEM, other weak frequency responses appear at 11 Hz, 22 Hz, 33 Hz and 44 Hz, which represent the multiples of the minimum frequency resolution. For the LFSM these windows occur at 7 Hz, 17 Hz, and 26 Hz, before the dominant frequency of 28 Hz. However, no distinguishable frequency component can be noticed after the peak of 29 Hz. As expected, for point B no specific frequency content was noticed in the longitudinal response of *y*-direction (Figure 4-31 b). For point C, the FEM shows more details in the frequency content of the response, both before and after the dominant frequencies of 2.5 Hz and 2.8 Hz estimated by the FEM and LFSM models respectively. The frequency-domain analysis is a very sensitive tool this the results obtained from different models would not achieve an identical distribution. However, it is very important to observe the tendency of identifying higher energy modes for the same or very similar frequencies. Thus, the Log PSD results based on the two methods, have identified similar windows of frequency components, which means that the dynamic response of the modeled laminated bridge is very well represented. Also, the FEM has higher PSD compared with the spectra derived by LFSM.

4.5.1.2. LAMINA (2)

In the previous sections, it is indicated that the lamina (2) hybrid bridge has a more capacity for static displacement and has larger natural frequencies. Figure 4-32 and Figure 4-33 show the PSD and Log(PSD) spectra of the lamina (2) FRP slab-girder bridge.

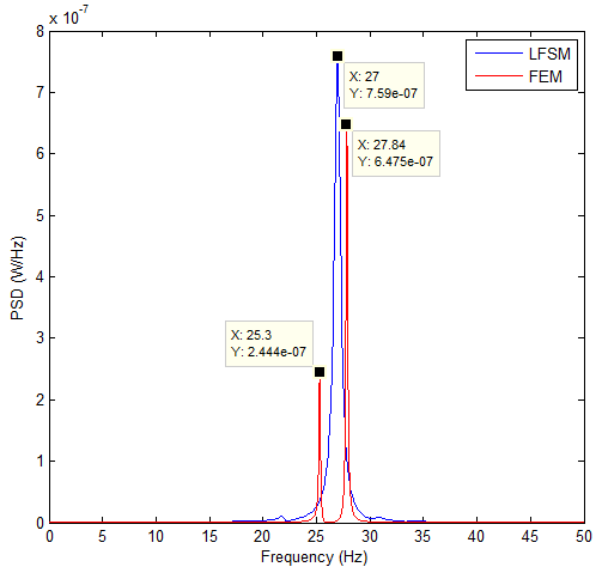

a) At point A in x direction

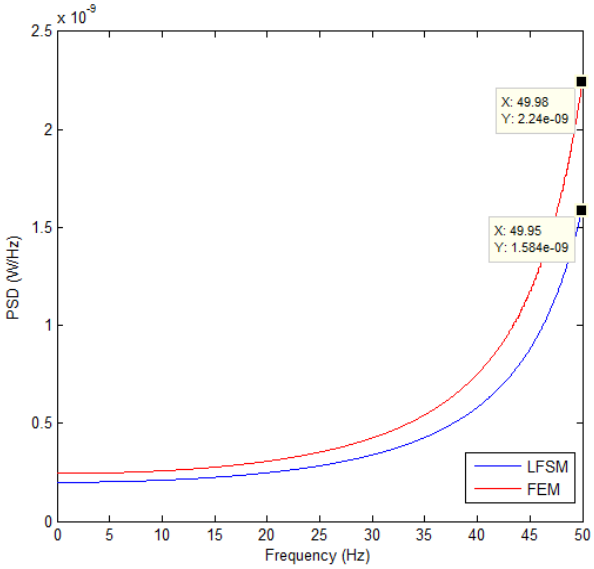

b) At point B in y direction

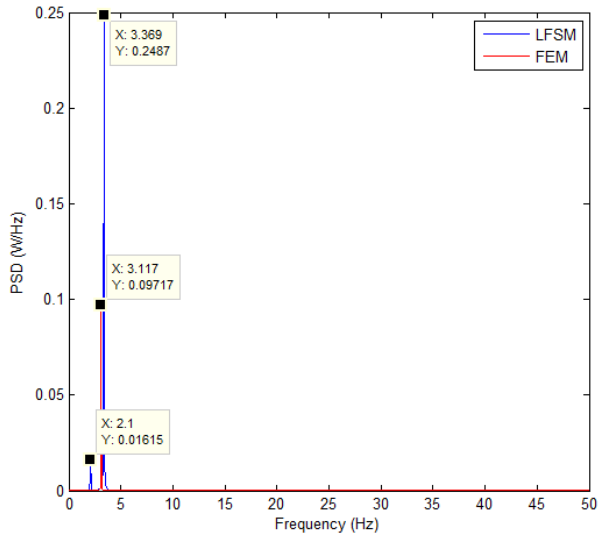

c) At point C in z direction

Figure 4-32 PSD of displacement response applied ground motion: white noise for lamina (2)

For a transverse response, as shown in Figure 4-32 (a), the dominant frequency of a white noise ground motion was 27 Hz as calculated by LFSM. This corresponds to the natural frequency of the FRP bridge of 26.96 Hz associated with vibration mode 14 determined by LFSM accordingly. The results from the FEM, are similar, however these registered two peaks of vibrations within the first 50 Hz, one at 25.3 Hz (corresponding to the mode 12 of vibration) and a second at 27.84 Hz (corresponding to mode 13 of vibration). This indicates that the first two deck heave mode shapes are derived in the frequency domain for FEM.

For longitudinal vibration, as shown in Figure 4-32 (b), it happens again that there is no peak within 50 Hz in the frequency domain for both FEM and LFSM. It is also confirmed again that there are no longitudinal mode shapes for the free vibrations within 50 Hz.

For a vertical response, as shown in Figure 4-32 (c), the first two natural frequencies are 2.1 Hz and 3.369 Hz when calculated by LFSM. Since the natural frequencies for the different methods vary slightly, the corresponding natural frequencies for the FRP Bridge are 2.08 Hz (mode 1) and 3.38 Hz (mode 2) estimated by LFSM accordingly. Compared with the results from the finite element analysis, which estimates only one dominant frequency of 3.117 Hz (mode 2), the LFSM has two peaks within the first50 Hz. This indicates that the first two deck heave mode shapes are derived in the frequency domain for LFSM.

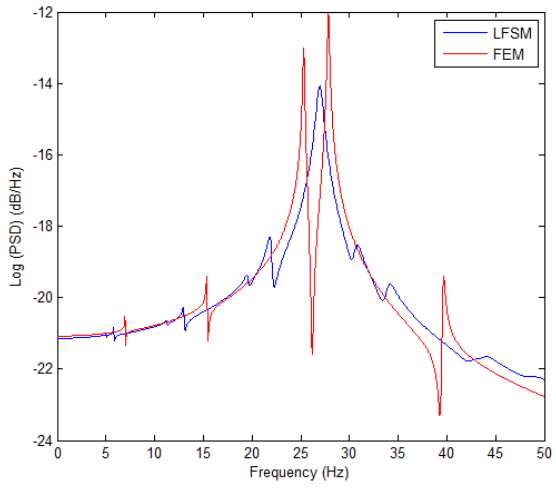

a) At point A in x direction

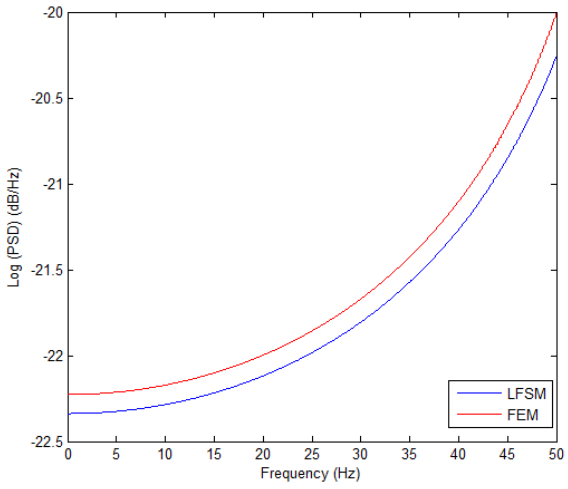

b) At point B in y direction

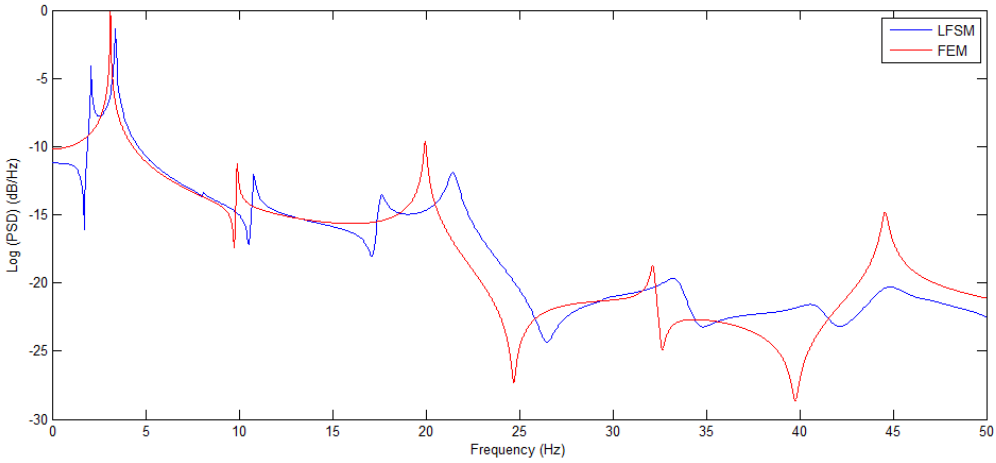

c) At point C in z direction

Figure 4-33 Log (PSD) of displacement response applied ground motion: white noise for lamina (2)

The Log (PSD) is used to capture the frequency content in detail, as shown in Figure 4-33. For location A, the Log PSD has shown good agreement between the FEM and the LFSM models, because the frequencies windows captured before the dominant frequency peak has similar trends, while after the peak the LFSM results show a slightly lower energy in the frequency content than the FEM model, as it can be noticed in Figure 4-33 b). for point B, as expected the Log PSD does not identify any additional frequency bins or windows. The agreement between log PSD for the responses derived from the LFSM and FEM models is remarkably good, showing similar dominant frequencies, but also a similar trend in the frequency windows until 50 Hz.

4.5.2. CHICHI EARTHQUAKE

In this case, the real earthquake record for the Chichi Earthquake which occurred in Taiwan in 1999, was used as shown in Figure 4-34. The acceleration time history was transformed into the equivalent PSD record in the frequency domain, as illustrated in Figure 4-34 (b), by using the Welch's method (Welch, 1967). For the real seismic loading case, better results agreement between the FEM and LFSM models was achieved, which further reinforces the conclusions formulated above; therefore, the proposed LFSM with transiting sections (Shen et al. 2013) is considered as a reliable numerical tool for performing seismic analysis of hybrid composite bridges. Since there is no dominant frequency peak in the longitudinal response, only the transverse and vertical vibrations were reported for the Chichi Earthquake.

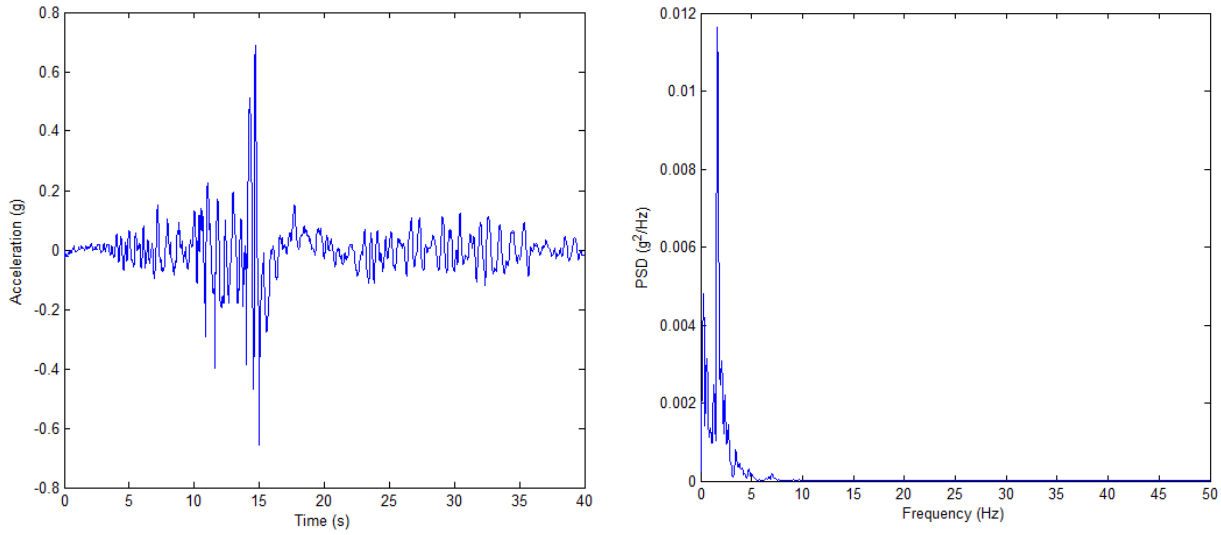

a) Acceleration of Chichi Earthquake b) PSD of Acceleration for Chichi Earthquake

Figure 4-34 Chichi Earthquake record (Adapted from Shen et al. 2013)

4.5.2.1. LAMINA (1)

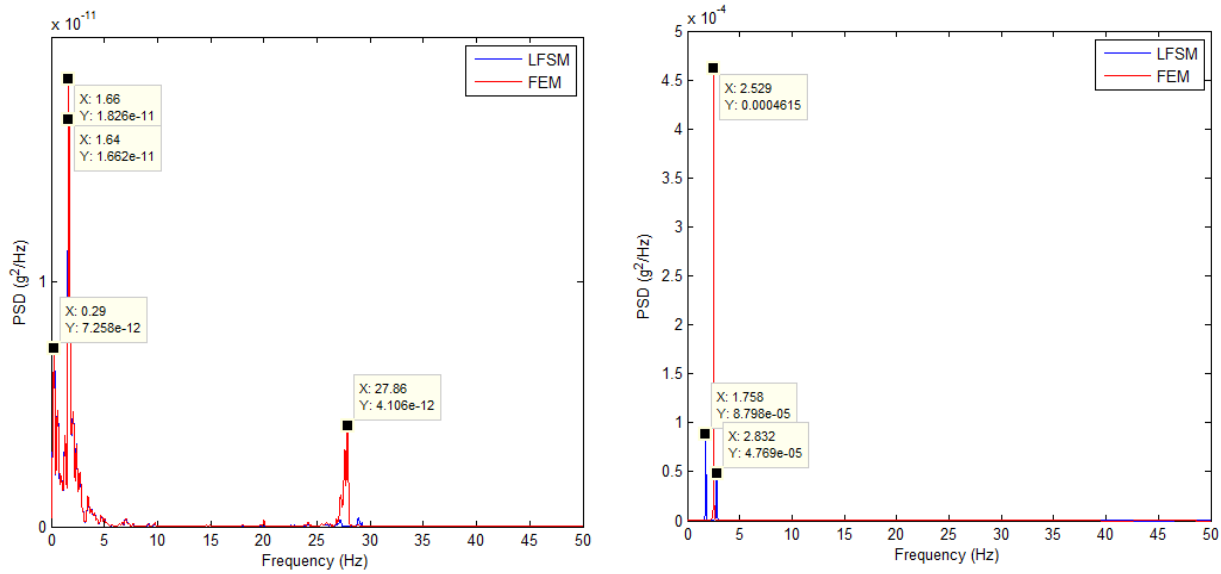

a) At point D in x direction b) At point E in z direction

Figure 4-35 PSD of displacement response applied ground motion: Chichi Earthquake for lamina (1)

For the transverse vibration shown in Figure 4-35 (a), the first two frequency peaks calculated by LFSM are 0.29 Hz and 1.64 Hz (1.66 Hz for FEM). These two peak frequencies are the simulation of the PSD response to Chichi Earthquake. The third peak corresponds to the dominant frequency of 27.86 Hz as estimated by FEM, for which the 27.83 Hz the natural frequency of the FRP Bridge was determined. This means that the FEM has estimated three frequency peaks within the 50 Hz,

which indicates that heave mode shapes are derived in the frequency domain for FEM. For vertical response as shown in Figure 4-35 (b), the two peak frequencies are 1.758 Hz and 2.832 Hz as calculated by LFSM. Compared with the results from the finite element analysis, which is represented only by one dominant peak at 2.529 Hz, the LFSM has two lower frequency peaks within 50 Hz.

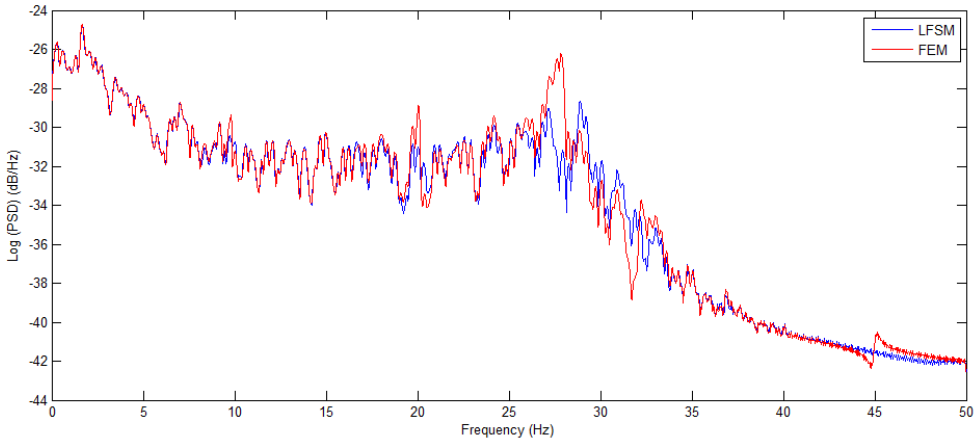

a) At point D in x direction

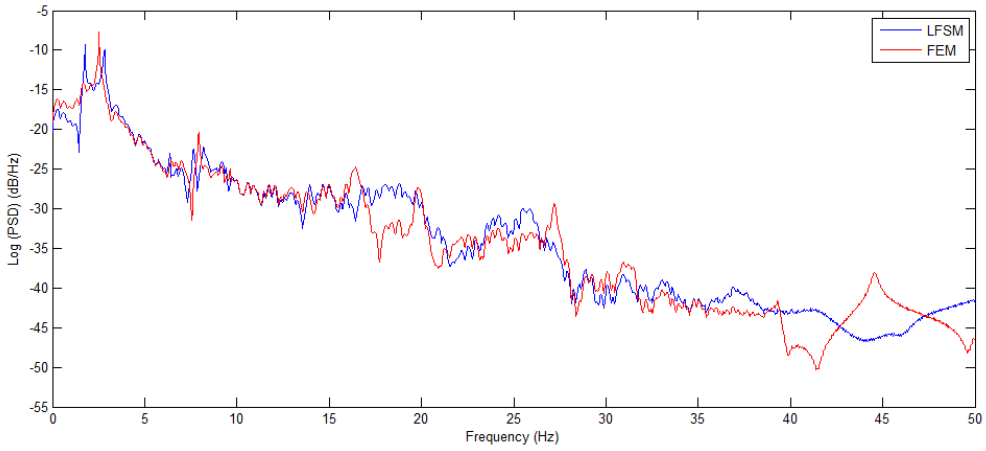

b) At point E in z direction

Figure 4-36 Log (PSD) of displacement response applied ground motion: Chichi Earthquake for lamina (1)

As shown in Figure 4-36, the log PSD for the real earthquake record shows a more complicated structure when compared with the response under a white noise. However, an exquisite agreement

can be noticed between the LFSM and FEM models, with very similar evolution until the dominant frequency peak, and a similar trend after this, for both responses at locations A and E.

4.5.2.2. LAMINA (2)

It is obvious that the lamina (2) has very similar PSD spectra distribution for the loading input of real earthquake wave as represented in Figure 4-37 and Figure 4-38.

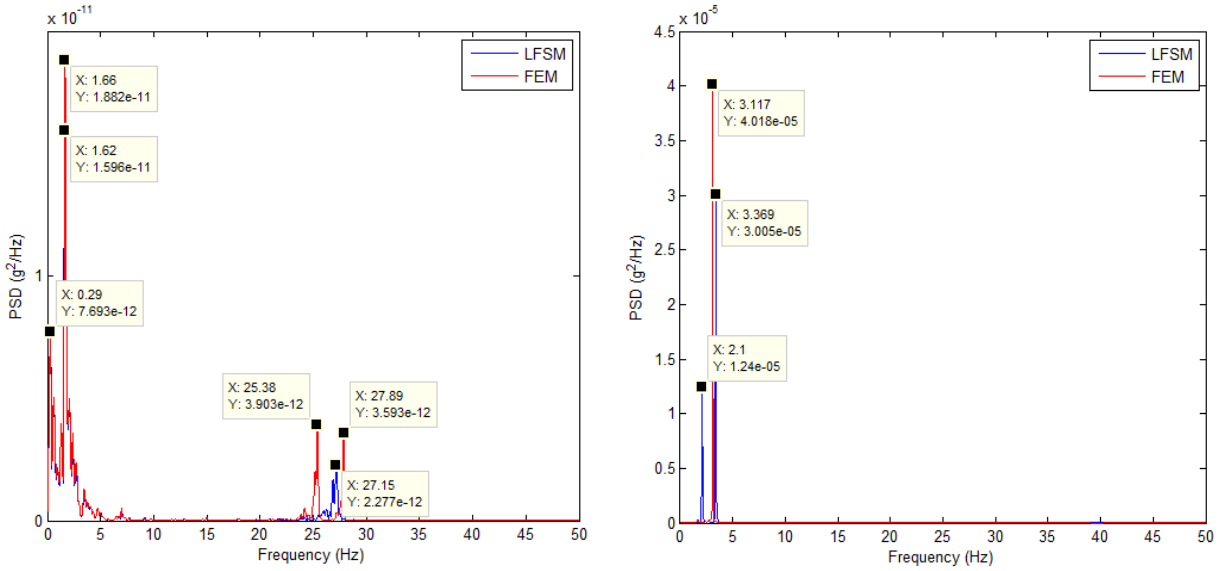

a) At point D in x direction

b) At point E in z direction

Figure 4-37 PSD of displacement response applied ground motion: Chichi Earthquake for lamina (2)

For the transverse response, as shown in Figure 4-37 (a), the first two peak frequencies calculated by LFSM were 0.29 Hz and 1.62 Hz, while for FEM this was 1.66 Hz. The third peak corresponds to the natural frequency of the FRP Bridge of 27.15 Hz as estimated by LFSM accordingly that is for 26.96 Hz (mode 13) for the natural frequency. However, there are two additional peaks calculated by FEM that is 25.38 Hz and 27.89 Hz corresponding to the 25.31 Hz (mode 13) and 29.39 Hz (mode 14) in natural frequency. It means that the FEM has one more peak within 50 Hz, compared with LFSM, which indicates that one more heave mode shape is derived in the frequency domain for FEM.

For vertical vibrations, as shown in Figure 4-37 (b), the two peak frequencies are 2.1 Hz and 3.369 Hz that were calculated by LFSM, which correspond to the natural frequencies 2.08 Hz (mode 1) and 3.38 Hz (mode 2). Compared with the results from the finite element analysis, which is only

one peak at exactly natural frequency 3.117 Hz (mode 2), the LFSM has two lower peaks within 50 Hz.

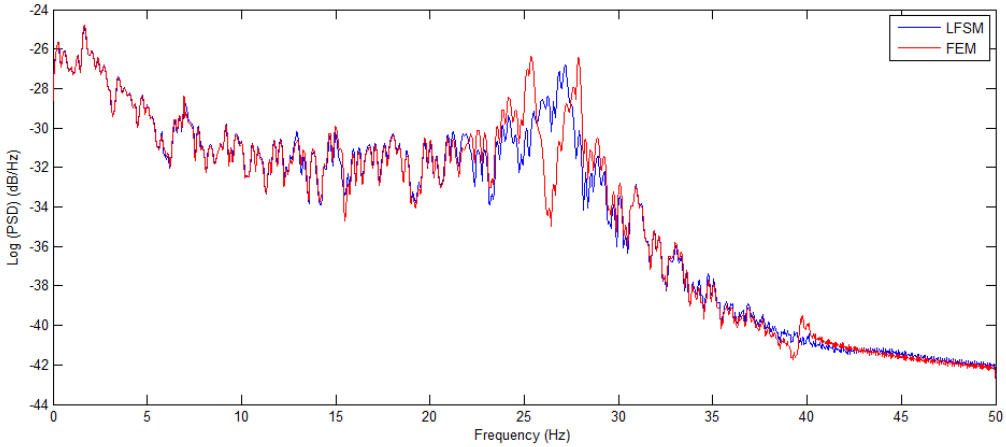

a) At point D in x direction

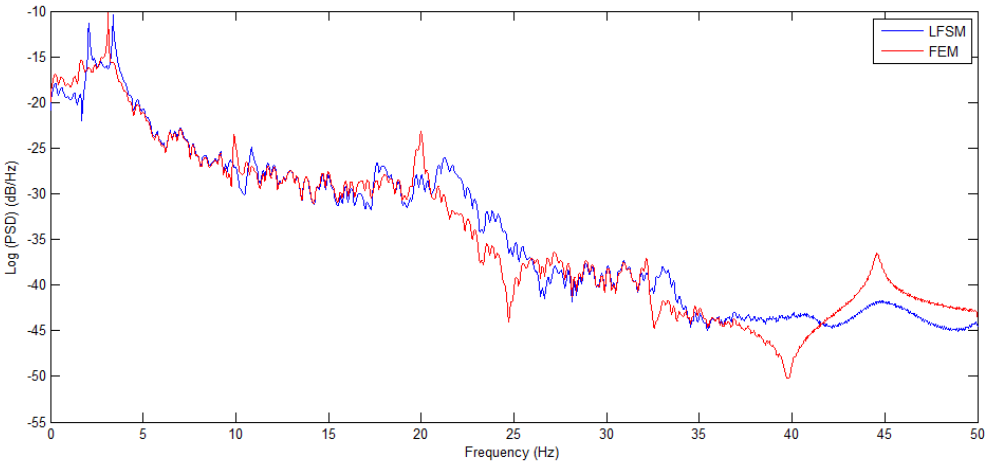

b) At point E in z direction

Figure 4-38 Log (PSD) of displacement response applied ground motion: Chichi Earthquake for lamina (2)

As shown in Figure 4-38, very like lamina (1), the Log(PSD) spectra for the real earthquake have met a great agreement between these two numerical simulation methods.

4.5.3. CONCLUSIONS

Regarding the study both for static analysis and dynamic analysis for the FRP slab-girder bridge, the [0/90/0/90/0] is considered as the proposed distribution of FRP laminates of decks. The current frequency-domain study developed a model for the static and dynamic analyses of a complete hybrid composite bridge mode, considering the piers and the bearing conditions. The semi-analytical finite strip approach reduces a 3D problem into a 2D problem and significantly reduces the degrees-of-freedom in formulating the solution, and hence the computational effort.

For the dynamic analysis, the efficient PEM is employed, and it has been successfully proven in this study that the PEM is applicable with the LFSM. Also, the response PSD from the two methods agree well, especially within the low-medium frequency range. These results indicate that PEM is functioning well in the spline finite strip environment, with high accuracy.

For the smaller difference between these two methods, it is considered that some noises and errors are induced by the torsional modes of the girder and some inaccuracy are introduced by the modification during the LFSM assembling process that shown in detail in the assumptions in Table 4-3. Since the vertical modes are more distinct to distinguish than the torsional modes, and the corresponding test locations A, B, and C are on the middle line of the deck and pier, the recorded signal may result in more accurate vertical frequencies. But D and E are on edge or the side of the deck, therefore, the recorded signal may contain the components of the torsional vibration of the composite bridge.

CHAPTER 5. COMPOSITE LONG-SPAN CABLE-STAYED BRIDGES

5.1. GENERAL

In the current chapter, the Finite Strip modeling, static analysis, free vibrations analysis of the selected composite cable-stayed bridge will be developed, while the time domain results are presented into Appendix D. The dynamic analysis by frequency domain, and the results from the seismic analysis performed for the same bridge are introduced in Chapter 6 and Appendix D, including the detailed outcomes and the comparison with the results reported by similar studies. A typical long-span cable-stayed bridge named Kap Shui Mun Bridge, shown in Figure 5-1 (Hui et al. 2011), was selected for developing the bridge modeling and the analyses reported in this chapter. The initial finite strip model of this bridge was developed by Naderian et al. (2015). Also by using similar programs and the analyses methods developed for the Slab-girder Bridge, the static analysis, and modal analysis were applied. The deflections of the tower elements and the deck were obtained for the Kap Shui Mun Bridge, by the incorporating the laminate model bridge characteristics in the C++ and MATLAB codes. A thorough validation of this model was performed by Naderian et al. (2015) and Naderian et al. (2016), by comparing the static and dynamic analyses results with the outcomes reported by FEM and site studies, carried out for the same bridge; an acceptable agreement between these results was reported.

Also, the complete details of the integrated finite strip method applied to the Kap Shui Mun Bridge were presented by Naderian et al. (2015), as well as the free vibration and time history analysis. For validating the results of the composite Kap Shui Mun Bridge, the same analysis steps were introduced in the previous chapters. In the following sections, first the parameters and methodologies required for the adapted computer codes are briefly explained, and the numerical results related to the FRP model of the Kap Shui Mun Bridge are presented.

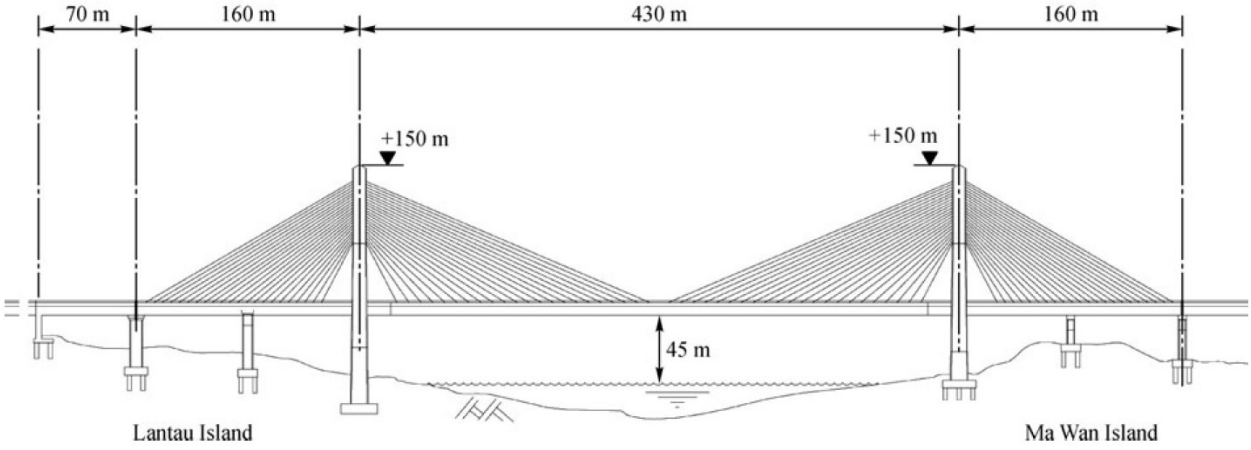

Figure 5-1 Kap Shui Mun Bridge (Hui et al. 2011)

5.2. MODELING OF KAP SHUI MUN BRIDGE

As shown in Figure 5-1, the Kap Shui Mun Bridge, a massive and complex long-span cable-stayed bridge structure, is selected for the current study. Kap Shui Mun Bridge has a total length of 820 m and is the world's second longest cable-stayed bridge carrying both road and rail traffic. The bridge is supported by two 150 m high concrete towers; the base of each tower was constructed by the jump-form process towers which were also post-tensioned to resist the forces caused by the stay cables anchorages. The total length of the all stay cables are 11 km, for the geometric distribution, they are located in 470 mm at mid-span in the lateral direction, 155 mm at mid-span in the longitudinal direction, and 320 mm near the piers. In total for modeling the FRP Kap Shui Mun Bridge, the number of DOF used for the LFSM model was is 9490, and for the FEM model, the number of DOF was 4242.

In the original finite element model, the bridge has been simplified with a number of assumptions (Yang et al. 2011). In this thesis, the author applied composite materials to the bridge deck, by adapting the plate laminate finite strip model developed by Naderian et al. (2013) and extending it to the composite Kap Shui Mun Bridge FSM programs. Also, the static and dynamic responses of the composite Kap Shui Mun Bridge were estimated based on the finite strip model of the same bridge with original materials developed by Naderian et al. (2015) and Naderian et al. (2016).

5.2.1. BRIDGE GEOMETRIC PROPERTIES

For comparison reasons, the FEM of the Kap Shui Mun Bridge developed by Shen et al. (2009), was used, as represented in Figure 5-2, which includes the two concrete towers, four concrete piers, 176 stay cables, bearings, as well as the bridge deck. Among these structural elements, the deck was adapted to introduce the composite FRP deck for both the main span and the side spans. For the FEM model, the deck was also replaced by the laminated FRP deck for the further results comparisons.

The overall model of the Kap Shui Mun Bridge is designed by three types of materials: concrete for towers and piers, steel for the pre-stressed cables, and FRPs materials for the deck. The laminated FRP deck has the material density of 1,600 kg/m^3. Both FSM and FEM are adapted to model and for estimating the static and dynamic behaviors of the structure, and the results from these two methods were compared. As it was already shown, the accuracy and efficiency of the proposed laminated finite strip solution for both static and dynamic analyses applied to the FRP Slab-girder Bridge in Chapter 4 were found to be acceptable. Therefore, the same laminated finite strip model was extended to the Laminated Finite Strip Method (LFSM) and FEM for the composite cable-stayed bridge model.

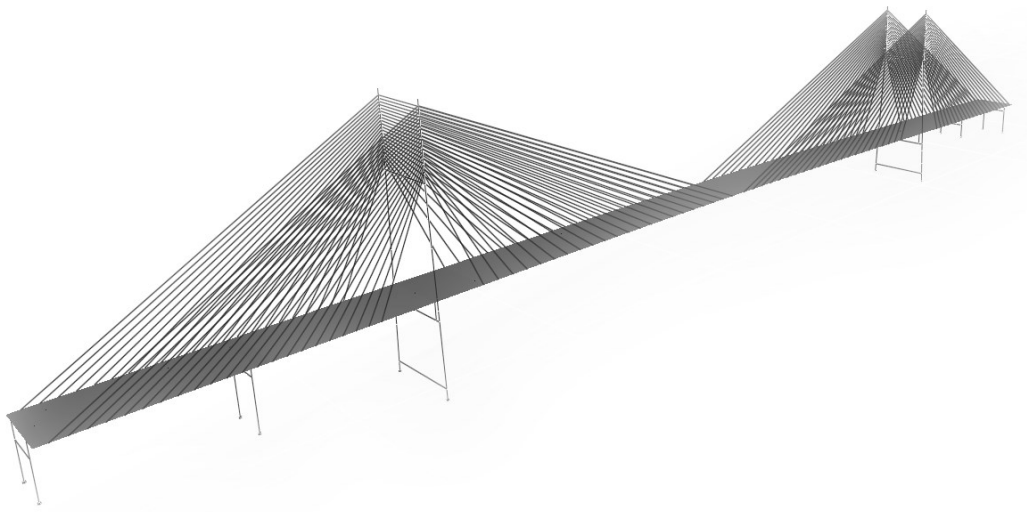

Figure 5-2 Three-dimensional FEM model of the FRP Kap Shui Mun Bridge (Adapted from Shen, 2009)

5.2.2. FINITE STRIP MODELING

A full bridge model was constructed by Shen (2009), using B_3 spline shell finite strip for the deck, column strip for the towers and piers, transition elements for the interaction between the deck and towers, towers and cables, and other components such as the bearings, and cables strip for modeling the axial force of the cables. The deck is divided into four equal strips, while the towers and piers are divided into two column strips. Each deck strip is composed of 32 sections. The FEM used for results comparison was built by the aid of SAP 2000 software which is based on the original Kap Shui Mun Bridge model built by Naderian et al. (2015), and it was modified by the current author in 2016 to model the hybrid bridge with a composite FRP deck. For the KSM Bridge FE model, the mass and stiffness of the bridges were constructed by five degrees-of-freedom shell elements, throughout the structure, and were modified by the current author to incorporate the laminated FRP model for the deck, in order to investigate the static and dynamic behavior for the FRP Kap Shui Mun Bridge. A shell element was used from a combination of in-plane elements with translation in the *x* and *y* directions, and bending elements with translation in the *z* direction, plus rotation capability above *x* and *y-axes*.

5.2.2.1. COMPOSITE DECK MODELING

The deck of the Kap Shui Mun Bridge consists of one main span and two side spans. The entire bridge deck, including the main span and the side spans, was modeled as a composite FRP structure, which had the FRP material properties same as the Slab-girder Bridge presented in the previous chapter. For the laminate finite strip modeling, the deck was modeled as shell strip

elements, with the geometrical properties are illustrated in Figure 5-3, which is modified from the original concrete and steel deck. The entire deck was divided into four shell strips from the beginning to the end, along with the entire length of the bridge spans for the finite strip method; also, all the strips were divided into 290 sections according to the Lagrange interpolation (Naderian et al. 2015). The lengths of the sections vary along the deck so that the locations of the knots could match the ends of the cables. To provide compatible results, the knots allocation was similar in both FEM and LFSM models. Also, the FEM model employed the same FRP material properties as the LFSM for the shell element used for simulating the bridge deck. The overall thickness of the deck was estimated at 1.02 m that are mainly according to the deflection behavior under live load as well as several verifications for the effects of thickness. A parametric study was performed by investigating the effect of the thicknesses of 0.38 m, and 0.76 m, the latest being described by Naderian (2017).

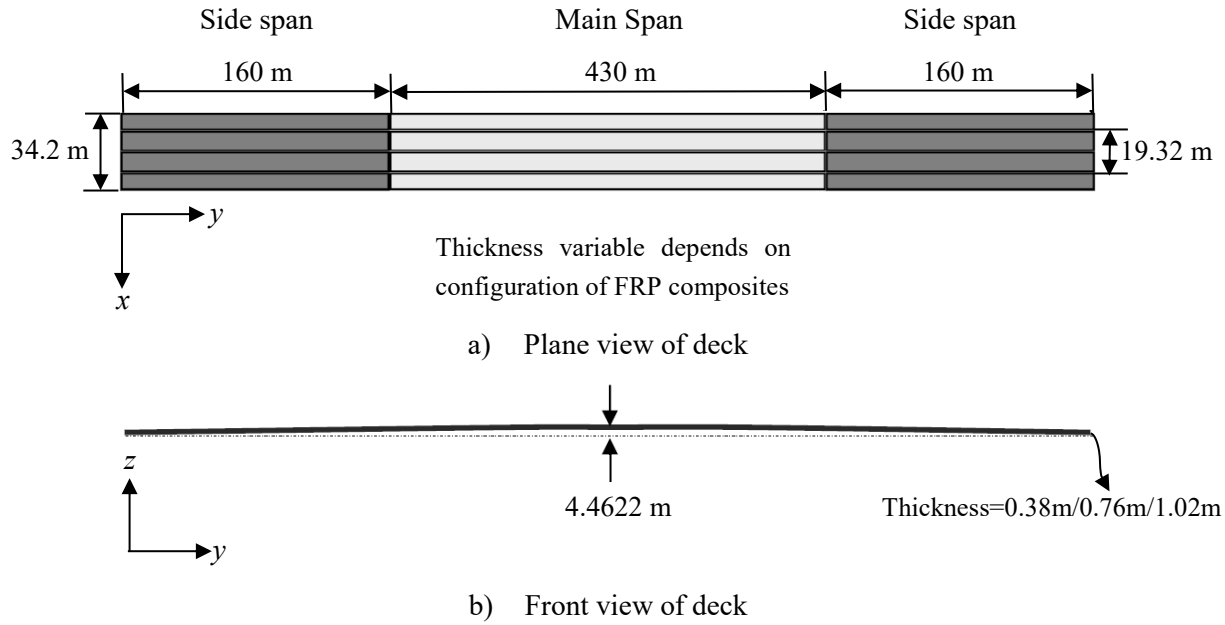

Figure 5-3 Modeling of Composite FRP deck (Adapted from Naderian et al. 2015)

5.2.2.2. MODELING THE TOWERS AND PIERS

Modeling the towers and the piers with FRP elements was not one of the objectives of the current study. Therefore, the towers strip meshing shown in Figure 5-4 was used as described by Naderian et al. (2015). The FSM model they developed is based on the one-dimensional Column Strip for the tower elements as well as for the piers in the finite strip model. In each tower, three struts were considered, linking the upper, intermediate and lower parts of the towers, respectively. The link beams were rigid, and all six degrees of freedom of the joints were restrained. For the one-

dimensional column strip, each knot has three translational degrees of freedom, while the rotational degrees of freedom were not taken into account. The four piers of the bridge were also modeled by one-dimensional column strip in the finite strip model. The boundary conditions of towers and piers were fixed at the ground level to account for a perfect connection with the foundation.

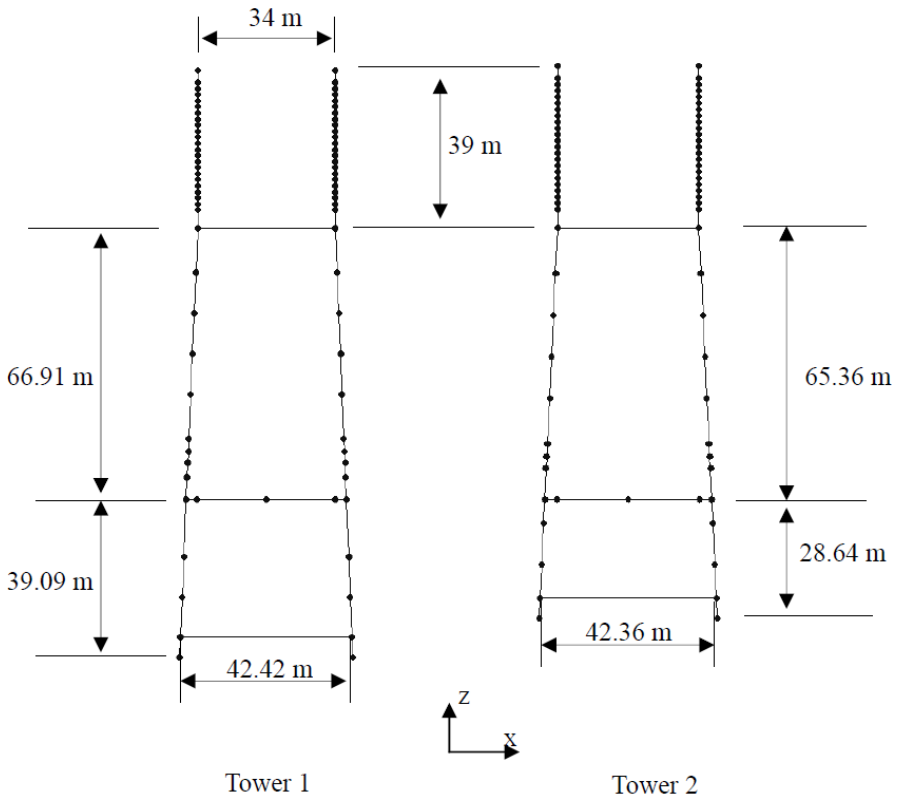

Figure 5-4 Modeling of two towers (Naderian et al. 2015)

5.2.2.3. MODELING THE STAY CABLES

The finite strip model developed by Naderian et al. (2015) was adopted for the 176 cables which were assumed to be linear elastic elements and were modeled by Cable Strip. Thermal loads were converted to equivalent tension forces at the two ends of each cable strip, to account for the pre-stresses in the cables, which are shown in detail in Figure 5-5 with the variable pre-stressed force for each cable. These pre-stressed cables are also modeled by FSM with same force bearing capacity. The highest pre-stressed cables are located at the bottom of the tower, connecting the left side-span to the tower; these are also the shortest cables for the left side-span. The detailed geometric distribution and elaborated descriptions of the pre-stress force for all the steel cables are presented in detail in Appendix B.

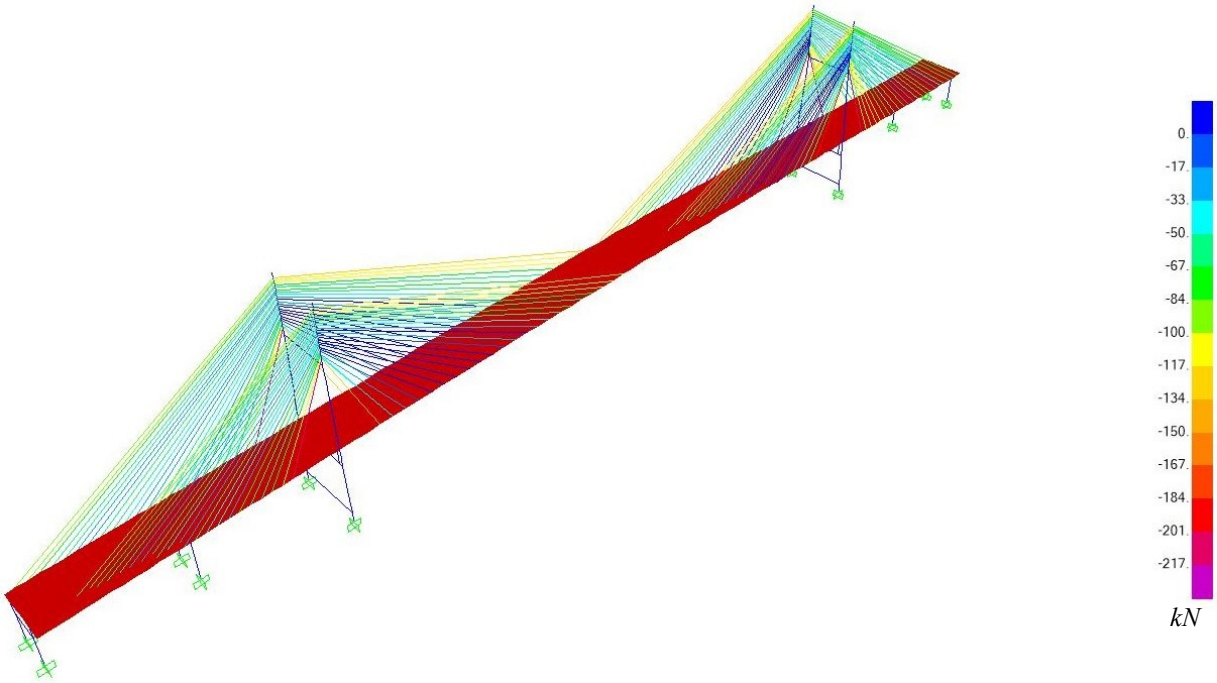

Figure 5-5 Pre-stressed forces of 176 cables modeled by SAP 2000 software

5.2.2.4. BOUNDARY CONDITIONS

For both the FEM and the LFSM models of the KSM Bridge, the boundary conditions of a continuous bridge deck were employed, and the simply support conditions were used for the two towers on each side of the deck. Also, the four piers support the deck that had two simply support conditions for each top of the pier connecting to the deck. The towers and the piers were restrained only at their base. Pre-stressed cables were connected between the deck and the tower at each end, which was modeled with the Cable Strip model within FSM. Transition sections between the deck, tower, and pier were modeled by the integrated FSM developed by Naderian et al. (2015).

5.2.3. COMPOSITE MODELING ASSUMPTIONS

To derive the laminate properties of the FRP materials and the numerical simulation results from the computing programs, several relevant assumptions were made to introduce the static analysis in this research. Table 5-1 compiles the detailed assumptions and the difference between LFSM and FEM assumptions employed in the current research, in conformity with the theoretical concept presented by Gibson (1994). It should be mentioned that the FEM model was built by SAP 2000 software, version 15.0.0. Since most of the results were derived by these two numerical simulation methods, it was assumed that the FEM always holds and obtains the most accurate values, which are regarded as reliable results used for validating the LFSM model results.

Table 5-1 Summary of modeling concepts and the definitions between LFSM and FEM

ASSUMPTIONS	LAMINATE FSM	FEM (SAP 2000)
Orthotropic Laminae	The plate consists of orthotropic laminae bonded together, with the principal material axes of the orthotropic laminae oriented along arbitrary directions with respect to the *xy* axes.	
Material Property	1) Extensional stiffnesses A_{ij} 2) Coupling stiffnesses B_{ij} 3) Bending stiffnesses D_{ij}	$E_2=E_3$, $G_{12}=G_{13}$, $\upsilon_{12}=\upsilon_{13}=\upsilon_{23}$, $G_{23}=4GPa$
Thickness	The thickness of the plate, *t*, is constant and much smaller that the lengths along the plate edges, *a* and *b*.	
Displacement	The displacements *u*, *v*, and *w* are small compared with the plate thickness.	
In-plane Strain	ε_x, ε_y, and γ_{xy} are small compared with unity.	
Transverse Shear Strain	γ_{xz} and γ_{yz} are negligible	The material component $S_{22} \neq 0, S_{23} = \infty$
Tangential displacement	*u* and *v* are linear functions of the *z* coordinate.	
Transverse Normal Strain	ε_z is negligible.	
Transverse Shear Stress	τ_{xz} and τ_{yz} vanish on the plate surfaces defined by $z = \pm t/2$	
Deck types	Top bottom shell strip	Shell-layered/nonlinear
Principals	Each ply obeys Hooke's law	Property/Stiffness modification factors are all set as 1, since they are inoperative when modeling layered shell area sections (e.g., Membrane *f* modifier, Bending *m* modifier, Shear *v* modifier, Mass modifier, Weight modifier)

5.2.4. MATERIAL PROPERTIES AND CONFIGURATIONS OF LAMINATE DECK

5.2.4.1. MATERIAL PROPERTIES

As the composite material, CFRP (IM6G/3501-6) have been verified in the previous chapter for the FRP Slab-girder Bridge model; it is intended to extend the application for modeling the deck

of the KSM long-span cable-stayed bridge. Except for the conventional concrete material for the towers and piers, as well as the pre-stressed steel for the cables, the laminate FRPs are used to model the deck of Kap Shui Mun Bridge, which has detailed properties of the CFRP material recommended by Chan et al. (2013), as introduced in Table 5-2 below.

Table 5-2 Basic material properties of FRP materials adopted in the design

Material	ρ / $kg{\cdot}m^{-3}$	E_{11}/GPa	E_{22}/GPa	G_{12}/GPa	v_{12}
CFRP (IM6G/3501-6)	1600	147	10	7	0.25
Concrete Deck (Main span) (Naderian et al. 2015)	3880	30	30	12.5	0.3
Concrete Deck (Side span) (Naderian et al. 2015)	3630	200	200	76.9	0.2

5.2.4.2. CONFIGURATIONS OF LAYOUT FOR LAMINATES

The $[0/90/0/90/0]_s$ orientations laminates configuration was used because, as pointed out by Chan et al. (2013) because these have a better behavior both in static and dynamic analyses, and they have the highest stiffness based on the analysis results obtained in the previous chapter. The deck with the $[0/45/90/-45/0]_s$ laminates orientation failed to verify the overall stability, because of the higher bending moment, vertical deflection, higher natural frequencies, and larger power spectrum density recorded. Moreover, the isotropic laminates with symmetric cross-ply $[0/90/0/90/0]_s$ were preferred when modeling the bridge deck than had been approved by the composite slab-girder bridge in the last chapter. Instead of the non-symmetric laminates with arbitrarily oriented plies to avoid potential coupling effects, it could lead to complex combinations of longitudinal, vertical, and torsional deformations, as mentioned by the laminate plate model developed by Naderian et al. (2014). In this case, the orientation component [0/90/0/0/90/0] was introduced and was applied as core cells for the deck of the long-span cable-stayed bridge. Initially concentrated loads and live loads were applied, which were considered as per the reference to the design of the bridge deck design codes.

Overall, three configurations for the FRP laminates layout were modelled for the deck of Kap Shui Mun Bridge; as the most effective difference among these laminas properties is the thickness of each lamina several values were investigated: (1) 0.38m, (2) 0.76m, as recommended by Naderian (2017) and (3) 1.02m. Typically, the definition of the lamina thickness is based on the experimental studies available in the literature, since currently there is no engineering application on a real bridge deck. For instance, Chan et al. (2013) assigned the cross-section of the concrete box girder as 12.7 m^2, which is equivalent to the lamina thickness of 12.7/34.2 = 0.3713 m. Therefore in the

current research, the laminated deck of 0.38 m thickness was investigated. However, it was found that the lateral static results for the static strain-stress behavior were beyond the acceptable limits. This is due to the high bending or shear capacity of box girders, as well as the high number (9 tubes for each edge of box girder) used by Chan et al. (2013) for modeling the FRP bridge deck. Based on the section properties calculated and presented in Table 2-17, 0.76 m thickness was selected as the proposed thickness of the laminated FRP deck. However, to meet the critical requirements of the bridge codes and design standards, especially for the deflection under live load, a new deck thickness of 1.02 m was finally determined as the lamina thickness for the composite KSM bridge model.

The detailed configurations of the laminates layout are described in Table 5-3 and Table 5-4. A schematic representation of the entire assembly is presented in Figure 5-6.

Table 5-3 Two types of thickness and configurations of layout: 0.38m, 0.76m

LAMINA	**LAMINA (1): 0.38(m)**		**LAMINA (2): 0.76(m)**		
Cell Number	***Laminate Alignment***	***Thickness***	***Cell Number***	***Laminate Alignment***	***Thickness***
Top-Bottom	**Deg.**	**mm**	**Top-Bottom**	**Deg.**	**mm**
1	[0/90/0/0/90/0]	60	**1**	[0/90/0/0/90/0]	60
			2	[0/90/0/0/90/0]	60
2	[0/90/0/0/90/0]	60	**3**	[0/90/0/0/90/0]	60
			4	[0/90/0/0/90/0]	60
3	[0/90/0/0/90/0/90]	70	**5**	[0/90/0/0/90/0]	60
			6	[0/90/0/0/90/0/0/90]	80
4	[90/0/90/0/0/90/0]	70	**7**	[90/0/0/90/0/0/90/0]	80
			8	[0/90/0/0/90/0]	60
5	[0/90/0/0/90/0]	60	**9**	[0/90/0/0/90/0]	60
			10	[0/90/0/0/90/0]	60
6	[0/90/0/0/90/0]	60	**11**	[0/90/0/0/90/0]	60
			12	[0/90/0/0/90/0]	60
Total		380			760

Table 5-4 Configurations of layout for lamina (3): 1.02m

LAMINA (3): 1.02(m)		Cell Number																
		Top-Bottom																
Ply Number	***Thickness***	***Laminate Alignment* (Deg.)**																
Top-Bottom	**mm**	**1**	**2**	**3**	**4**	**5**	**6**	**7**	**8**	**9**	**10**	**11**	**12**	**13**	**14**	**15**	**16**	**17**
①	**10**	90	0	0	0	0	0	0	0	0	0	0	0	0	0	0	0	0
②	**10**	90	90	90	90	90	90	90	90	90	90	90	90	90	90	90	90	90
③	**10**	90	0	0	0	0	0	0	0	0	0	0	0	0	0	0	0	0
④	**10**	0	0	0	0	0	0	0	0	0	0	0	0	0	0	0	0	90
⑤	**10**	90	90	90	90	90	90	90	90	90	90	90	90	90	90	90	90	90
⑥	**10**	0	0	0	0	0	0	0	0	0	0	0	0	0	0	0	0	90
Total	**1020**	**60**	**60**	**60**	**60**	**60**	**60**	**60**	**60**	**60**	**60**	**60**	**60**	**60**	**60**	**60**	**60**	**60**

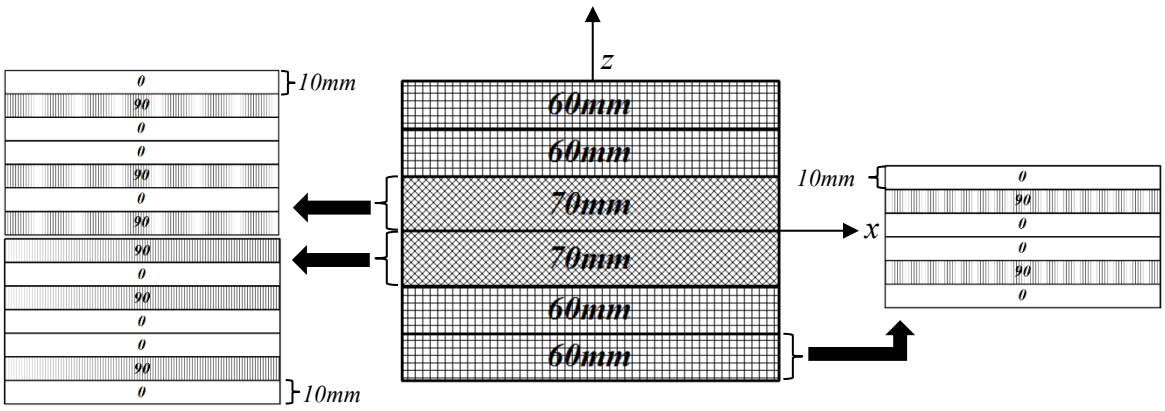

a) Lamina (1): 0.38m thickness configuration layout

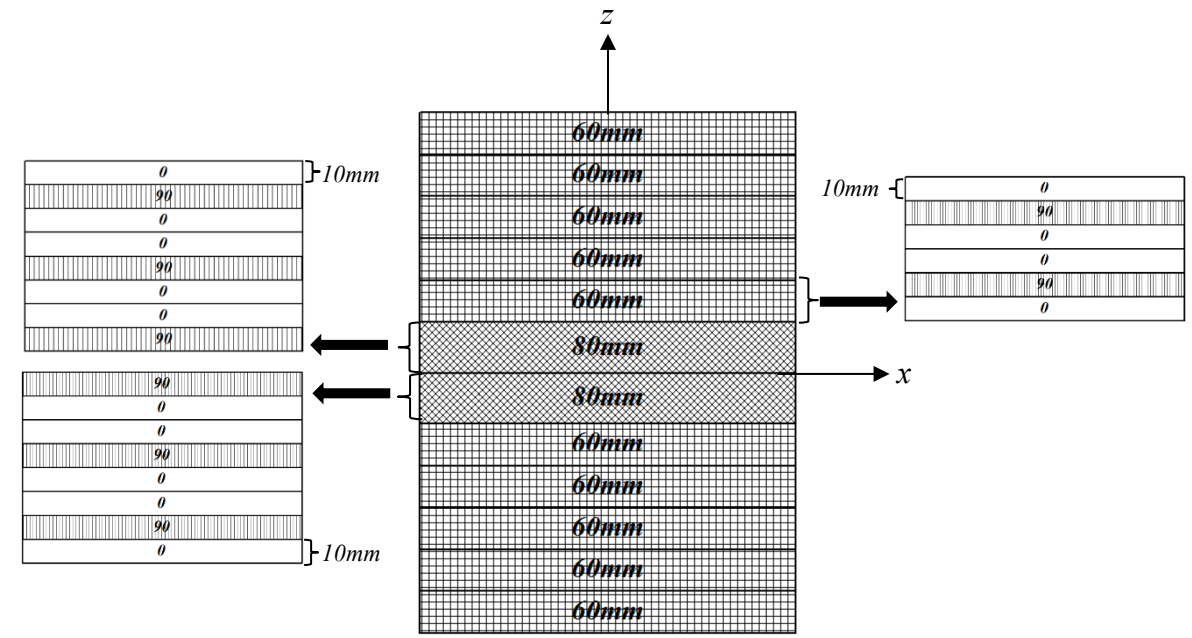

b) Lamina (2): 0.76m thickness configuration layout

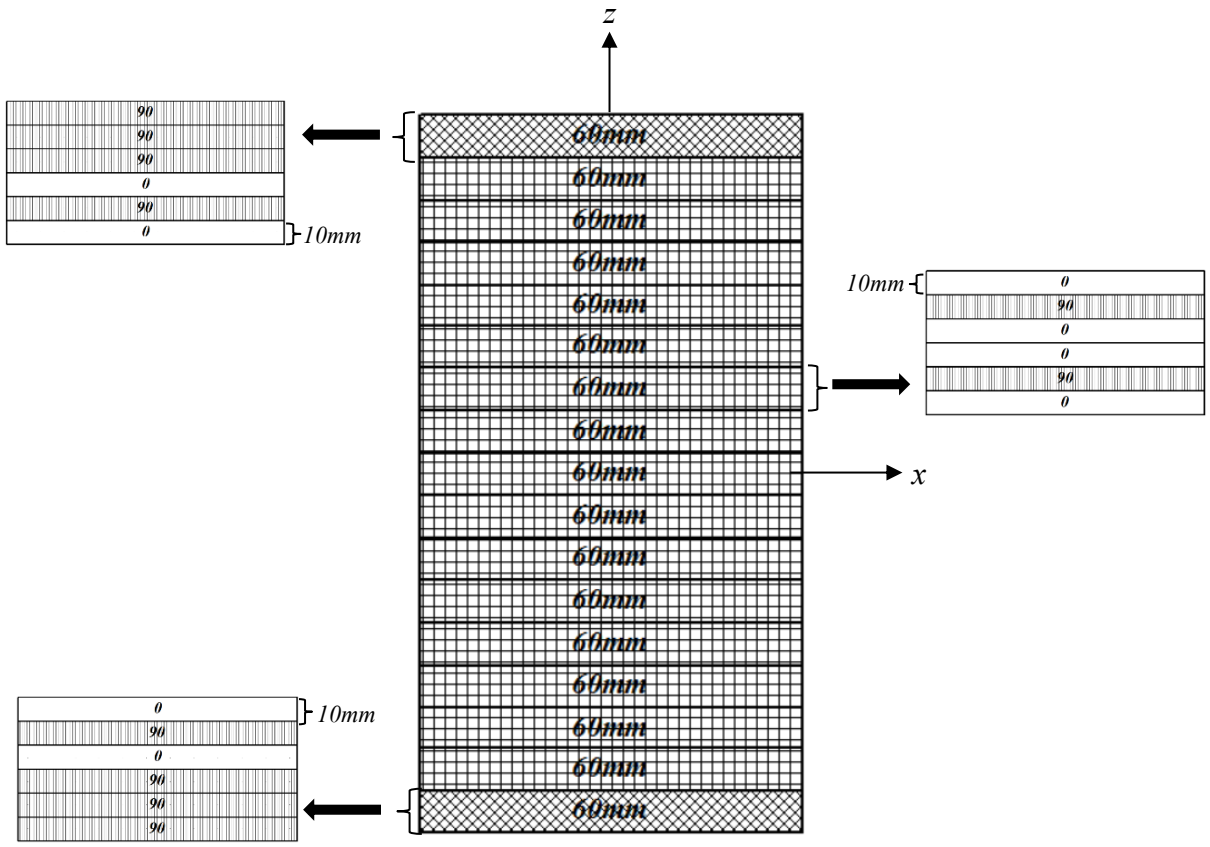

c) Lamina (3): 1.02m thickness configuration layout

Figure 5-6 Configurations of layout for the three laminas models

5.2.4.3. SECTION PROPERTIES

The bridge deck cross-section properties with the applied FRPs of different laminae thickness were calculated and are presented in Table 5-5.

Table 5-5 Section properties of the FRP deck system

Property Value	Lamina (1): 0.38m	Lamina (2): 0.76m	Lamina (3): 1.02m
Cross section area/m^2	12.996	25.992	34.884
Torsional constant/m^4	0.6215	4.9373	11.878
Moment of Inertia about 3 axis/m^4	0.1564	1.2511	3.0244
Moment of Inertia about 2 axis/m^4	1266.7201	2533.4402	3400.1435
Shear area in 2 direction/m^2	10.8844	21.7688	29.2161
Shear area in 3 direction/m^2	10.8844	21.7688	29.2161

The corresponding laminae stiffnesses were calculated by the aid of a MATLAB code that was built by Naderian (2013) and was modified by the current author in 2016 to integrate higher thicknesses of the lamina plates, which were later adopted for the Kap Shui Mun Bridge model. The FRP material properties for the three layouts above can be written as follows:

a) Lamina (1): 0.38m

The laminate extensional stiffnesses A_{ij} (i, j=1, 2, or 6) are:

$$[A] = 10^7 \times \begin{bmatrix} 3.6837 & 0.0954 & 0 \\ 0.0954 & 2.3078 & 0 \\ 0 & 0 & 0.2660 \end{bmatrix} kPa \cdot m \tag{5-1}$$

The laminate coupling stiffnesses B_{ij} (i, j=1, 2, or 6) are:

$$[B] = 10^{-8} \times \begin{bmatrix} 0.1490 & 0.0056 & 0 \\ 0.0056 & 0.1688 & 0 \\ 0 & 0 & 0.0078 \end{bmatrix} kPa \cdot m^2 \tag{5-2}$$

The laminate bending stiffnesses D_{ij} (i, j=1, 2, or 6) are:

$$[D] = 10^5 \times \begin{bmatrix} 4.6638 & 0.1148 & 0 \\ 0.1148 & 2.5459 & 0 \\ 0 & 0 & 0.3201 \end{bmatrix} kPa \cdot m^3 \tag{5-3}$$

b) Lamina (2): 0.76m

The laminate extensional stiffnesses A_{ij} (i, j=1, 2, or 6) are:

$$[A] = 10^7 \times \begin{bmatrix} 7.6425 & 0.1908 & 0 \\ 0.1908 & 4.3405 & 0 \\ 0 & 0 & 0.5320 \end{bmatrix} kPa \cdot m \tag{5-4}$$

The laminate coupling stiffnesses B_{ij} (i, j=1, 2, or 6) are:

$$[B] = 10^{-8} \times \begin{bmatrix} 0.4649 & -0.0004 & 0 \\ -0.0004 & -0.0581 & 0 \\ 0 & 0 & 0.0101 \end{bmatrix} kPa \cdot m^2 \tag{5-5}$$

The laminate bending stiffnesses D_{ij} (i, j=1, 2, or 6) are:

$$[D] = 10^5 \times \begin{bmatrix} 3.7251 & 0.0918 & 0 \\ 0.0918 & 2.0427 & 0 \\ 0 & 0 & 0.2561 \end{bmatrix} kPa \cdot m^3 \tag{5-6}$$

c) Lamina (3): 1.02m

The laminate extensional stiffnesses A_{ij} (i, j=1, 2, or 6) are:

$$[A] = 10^7 \times \begin{bmatrix} 9.8298 & 0.2561 & 0 \\ 0.2561 & 6.2526 & 0 \\ 0 & 0 & 0.7140 \end{bmatrix} kPa \cdot m \tag{5-7}$$

The laminate coupling stiffnesses B_{ij} (i, j=1, 2, or 6) are:

$$[B] = 10^{-8} \times \begin{bmatrix} 0.3517 & -0.0045 & 0 \\ -0.0045 & 0.4649 & 0 \\ 0 & 0 & 0.0253 \end{bmatrix} kPa \cdot m^2 \tag{5-8}$$

The laminate bending stiffnesses D_{ij} (i, j=1, 2, or 6) are:

$$[D] = 10^6 \times \begin{bmatrix} 7.6536 & 0.2220 & 0 \\ 0.2220 & 6.2898 & 0 \\ 0 & 0 & 0.6190 \end{bmatrix} kPa \cdot m^3 \tag{5-9}$$

As indicated in Chapter 3, a symmetric laminate has both geometric and material property symmetry about the middle surface, which can also be observed in the matrices above. All the three laminae have the symmetric cross-ply laminates as shown in Figure 5-6 a), b) and c) and the main difference between them are the lamina thickness of the deck. The three modeled layouts have the symmetric condition fulfilled, according to the definition of Eq. (3-14) and the numerical

results of the laminate coupling stiffness $[B]_{ij}$ above, which leads to the major simplification that all terms $B_{ij} = 0$.

There are in total 18 components of stiffness necessary to describe the material properties for each lamina and to substitute the elastic modulus, shear strength modulus, and the passion ratio, among other equivalent properties of the FRP materials. After that, these components are assembled into the laminate FSM programs to calculate the strain and stress magnitude.

5.3. STATIC ANALYSIS

The FRP Kap Shui Mun Bridge modeled by the laminated finite strip model with interactions sections between different structural elements of the bridge is statically analyzed under the effect of several external loads. Some of these loads are mainly acting on the bridge deck, while some are acting on the sub-structure, as detailed in the sections below. For the same reason, two groups of external loads were assigned to the deck and towers in the present study. The location and magnitude of the static loads described below were chosen as per the description provided in the IFSM study performed by Shen et al. (2009) and Naderian et al. (2015) for the same bridge, in order to compare and validate the results obtained by the current LFSM model of the Kap Shui Mun Bridge. The pre-stress conditions in the cables were also considered in the current analysis.

To determine the lamina configuration which describes better the bridge deck structural response, different combinations of concentrated loads, as well as the distributed live loads, were applied to the hybrid composite cable-stayed bridges modeled with the three thicknesses detailed in Figure 5-6 and Table 5-5 above. The results were compared with the IFSM model results with original materials reported by Naderian et al. (2015).

5.3.1. LOADING MODELING AND RESULTS

5.3.1.1. CONCENTRATED LOADS

For the static analysis, five load cases with a constant value of 15000 kN concentrated forces acting on different components of the structure and in different directions, were employed as shown in Figure 5-7.

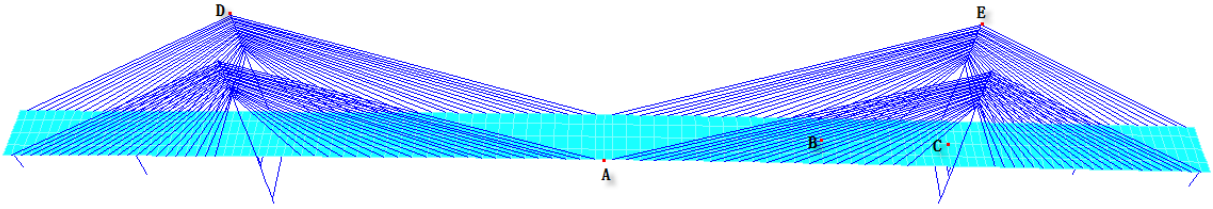

a) Critical locations for the bridge model

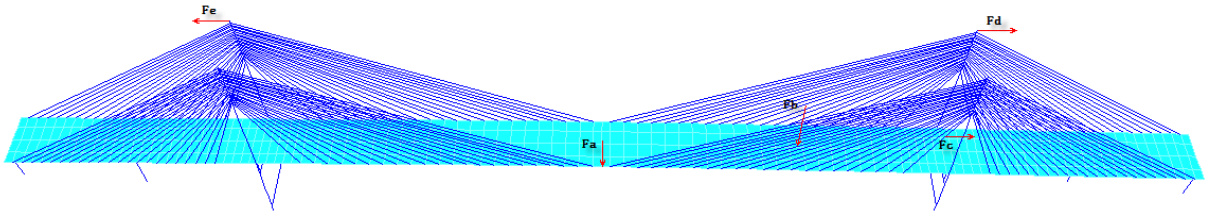

b) Concentrated loads applied on the bridge model

Figure 5-7 Load cases and critical locations distribution (Naderian et al. 2015)

Table 5-6 summarizes the applied concentrated loads, their location and the direction they were applied.

Table 5-6 Load cases definition

CONCENTRATED LOADS	LOCATION	NODAL LINES	DIRECTION
Load Fa	Deck: x=375 m	Deck nodal line 5	Transverse (-y)
Load Fb	Deck: x=493.5 m	Deck nodal line 3	Vertical (-z)
Load Fc	Deck: x=590 m	Deck nodal line 2	Longitudinal (+x)
Load Fd	Tower 2: left top	Tower 2 nodal line 1	Longitudinal (+x)
Load Fe	Tower 1: left top	Tower 1 nodal line 1	Longitudinal (-x)

5.3.1.2. LIVE LOADS

The application of a 550 kN/m live load, according to the traffic loading recommended by the Canadian Highway Bridge Design Code (2012) and as estimated by the IFSM model developed by Chan et al. (2013) with the new developed composite decks, was applied with uniform distribution along the FRP Kap Shui Mun Bridge, as shown in Figure 5-8.

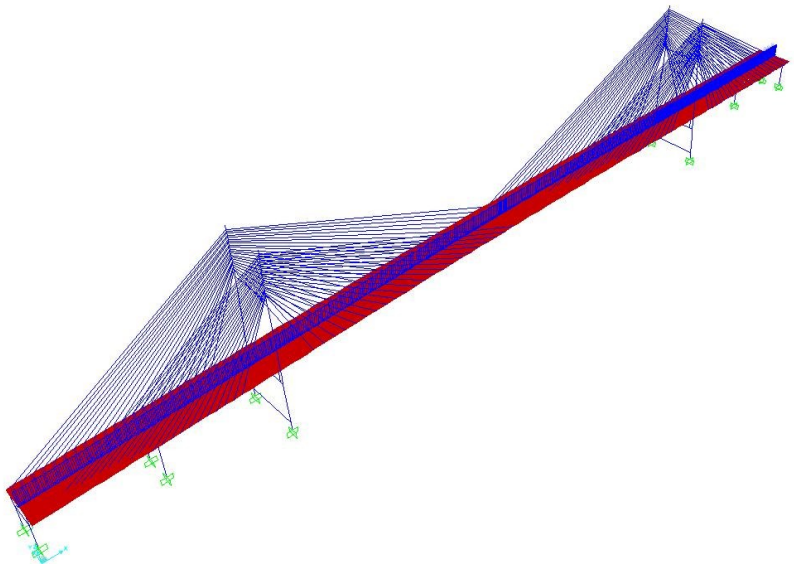

Figure 5-8 Live load distribution on the FRP-KSM Bridge

5.3.2. STATIC RESULTS

The deflection of the FRP Kap Shui Mun Bridge was very close to null under the effect of the dead load and the initial pre-stressing in the stay-cables, which is same to the results reported by Naderian et al. (2015) on the IFSM concrete deck KSM bridge model. The deflections registered for different combinations of static loads applied at the critical locations of the bridge were determined and were illustrated below for different lamina thicknesses. Figure 5-9 presents the deflections under live load for lamina (1) of thickness 0.38 m, and Figure 5-10 refers to the lamina (2) of 0.76 m, while Table 5-9 to Table 5-11 and Figure 5-11 to Figure 5-13 depict the results for lamina (3) of 1.02 m. Moreover, the numerical finite strip results were compared with those obtained by finite element method of the FRP-KSM Bridge and were also summarized in these tables and figures. In general, the deflection calculated by the LFSM approach agrees well with the FEM results for all loading conditions, especially for the lamina (3), which indicates that the proposed approach can successfully model a full hybrid composite bridge structure using the finite strip method with the integrated tower and pier bearing deck interaction sections. Due to space limitations, the static results under concentrated loads for lamina (1) and lamina (2) were each

demonstrated in a calculation example, and the results are put into Figure 5-15 to Figure 5-19. Therefore, only the live load deflections were presented more details. The static results corresponding to lamina (3) are mainly showed as follows.

5.3.2.1. LAMINA (1): 0.38M

1) Concentrated loads:

For lamina (1), the deflections corresponding to different combinations of concentrated static loads applied at the critical locations of the FRP-KSM Bridge model determined by the LFSM method were in relatively acceptable agreement with the FEM model of the FRP-KSM Bridge. Table 5-7 summarizes the deflection conditions developed by both FEM and LFSM for the corresponding critical locations under load Fa+Fb+Fc+Fd. These detailed static results produced by LFSM according to each loading case were illustrated and presented in Figure 5-15 to Figure 5-19 as a comparison.

Table 5-7 Deflection under static load: Fa+Fb+Fc+Fd for lamina (1)

		Location	A (375m)	B (493.4m)	C (590m)	D (Tower 1 left-top)	E (Tower 2 left-top)
Load Fa+Fb+ Fc+Fd	u (mm)	LFSM	191.12	101.45	20.45	159.86	86.31
		FEM	206.16	108.35	20.31	156.29	87.46
	v (mm)	LFSM	7.07	9.03	5.30	96.93	375.19
		FEM	7.46	8.29	5.67	95.60	375.30
	w (mm)	LFSM	689.29	1084.45	0.28	4.31	3.31
		FEM	682.54	1117.10	0.29	4.13	3.35

2) Live load:

The deflections recorded under a uniformly distributed live load of 550 kN/m were higher for the main span of the FRP-KSM Bridge model when estimated by the LFSM method, when compared with the results obtained for the FE model, as it can be noticed in Figure 5-9. Also for the last side span the FEM registered higher deflections than the LFSM model.

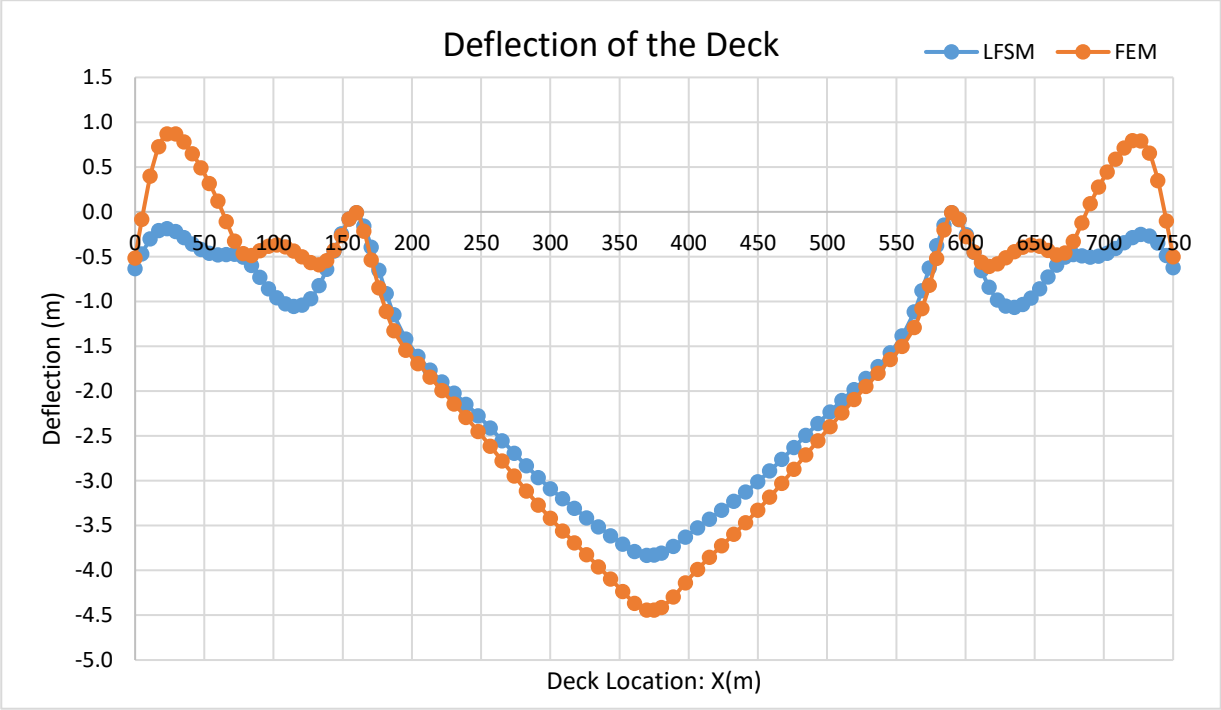

Figure 5-9 Deflection in nodal line 3 under live load for lamina (1)

5.3.2.2. LAMINA (2): 0.76M

1) Concentrated load:

For lamina (2), as also pointed out by Naderian, the deflection corresponding to different combinations of concentrated static loads applied at the critical locations of the FRP-KSM Bridge model determined by the LFSM method, were in relatively acceptable agreement with the FEM model of the FRP-KSM Bridge. Table 5-8 shows the deflection results developed both by FEM and LFSM, as an example for the corresponding critical locations under load Fa+Fb+Fc. These detailed static results produced by LFSM according to each loading case were illustrated and presented in Figure 5-15 to Figure 5-19 as a comparison.

Table 5-8 Deflection under static load: Fa+Fb+Fc for lamina (2)

		Location	A (375m)	B (493.4m)	C (590m)	D (Tower 1 left-top)	E (Tower 2 left-top)
Load Fa+Fb+Fc	u (mm)	LFSM	129.26	77.62	23.23	146.82	111.91
		FEM	134.04	80.68	23.56	142.55	116.25
	v (mm)	LFSM	2.21	4.72	0.51	93.69	8.59
		FEM	2.02	4.80	0.48	92.22	3.48
	w (mm)	LFSM	792.65	309.31	0.34	4.31	5.19
		FEM	778.15	327.84	0.36	4.11	5.31

2) Live load:

For lamina (2), the deflections recorded under a uniformly distributed live load of 550 kN/m were found to be in better agreement with the FEM results, however these were still slightly higher for the main span, when compared with the results obtained for the LFSM model, as it can be noticed in Figure 5-10. Also for the side spans the FEM registered higher deflections than the LFSM model.

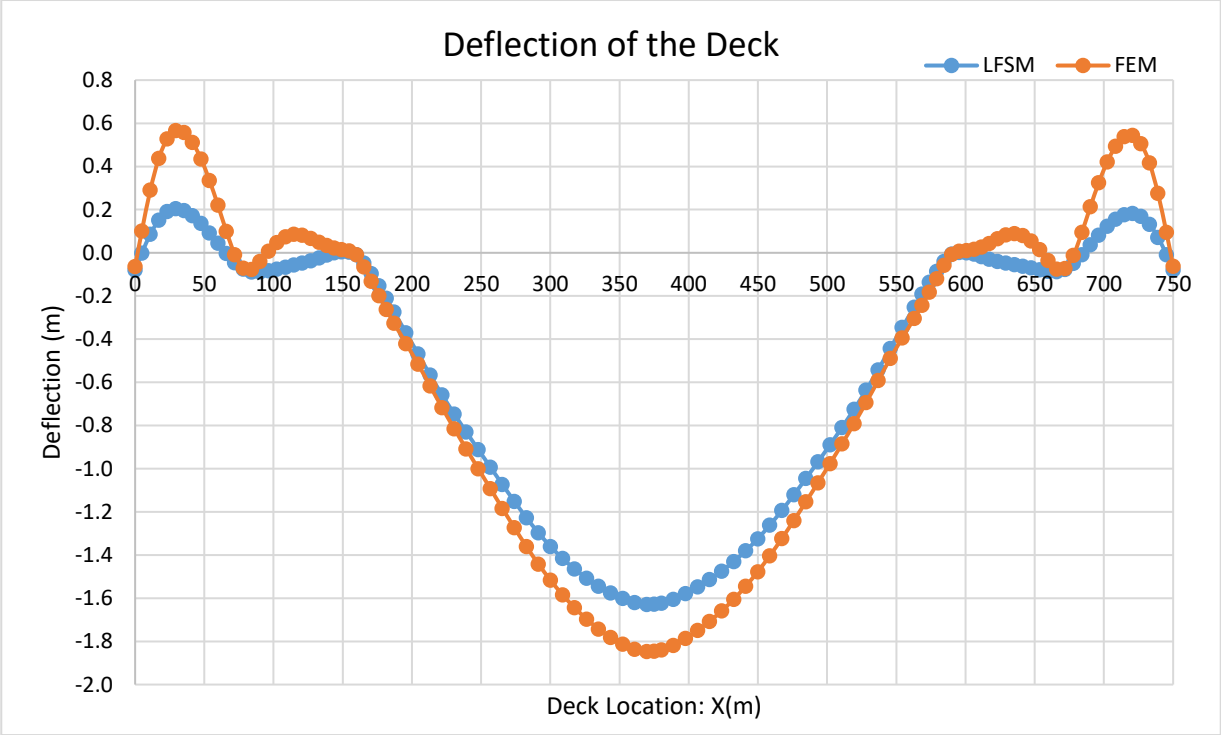

Figure 5-10 Deflection on nodal line 3 under live load for lamina (2)

5.3.2.3. LAMINA (3): 1.02M

The deflection response for lamina (3) under live load and concentrated loads were investigated in detail and are presented in the following subsection. Since it has been shown that the strain-stress difference can be determined under the same load cases from the deflections contribution plots by both approaches; five loading conditions with the corresponding deflection responses and the deflection under uniform live load for lamina (3) are presented as follows.

1) Concentrated Load: Fa

Regarding load Fa, both approaches have proved to be compatible with each other, regarding the deflections in each direction: transverse *u*, longitudinal *v*, and vertical *w*. All the deflections monitored at the defined critical points along the bridge are collected in Table 5-9. It is obvious that the maximum deflection occurred on nodal line 5 which is situated on the edge of the bridge deck.

Table 5-9 Deflection under static load: Fa for lamina (3)

		Location	A (375m)	B (493.4m)	C (590m)	D (Tower 1 left-top)	E (Tower 2 left-top)
Load Fa	u (mm)	LFSM	104.17	65.54	21.79	130.60	104.79
		FEM	107.25	67.64	22.05	127.45	108.47
	v (mm)	LFSM	3.19	0.85	1.67	112.68	115.18
		FEM	3.02	0.88	1.60	112.49	114.49
	w (mm)	LFSM	840.73	119.30	0.28	3.90	3.69
		FEM	840.35	117.05	0.27	3.73	3.79

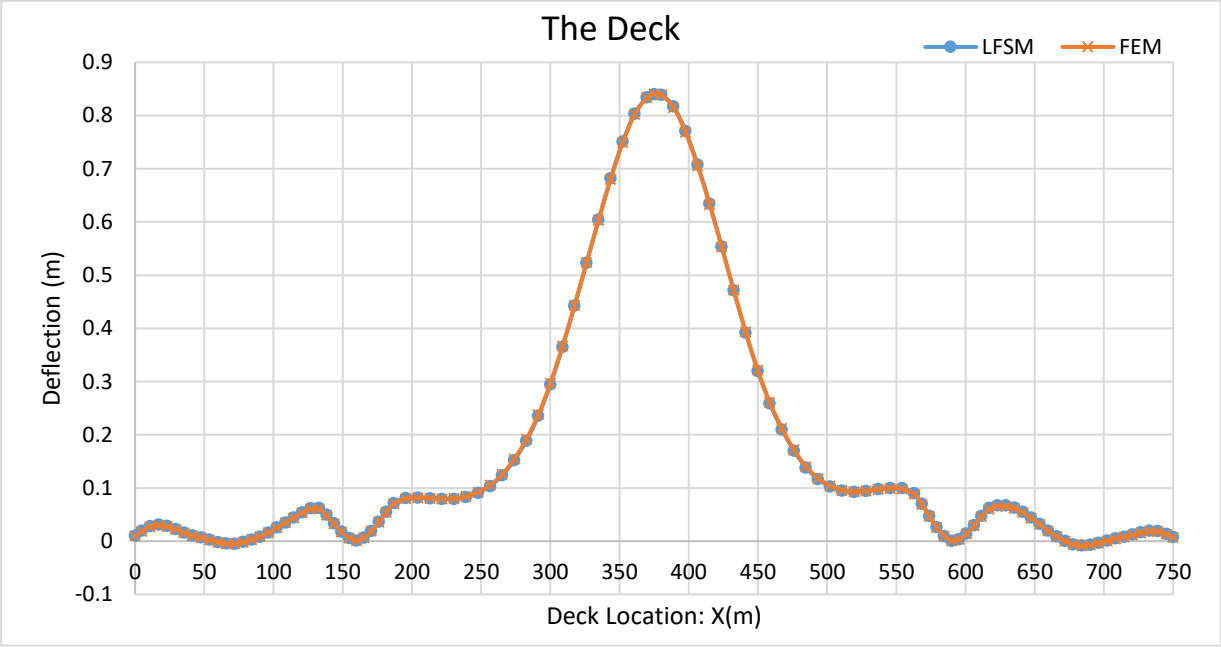

a) Deflection *w* on the deck: Nodal line 5.

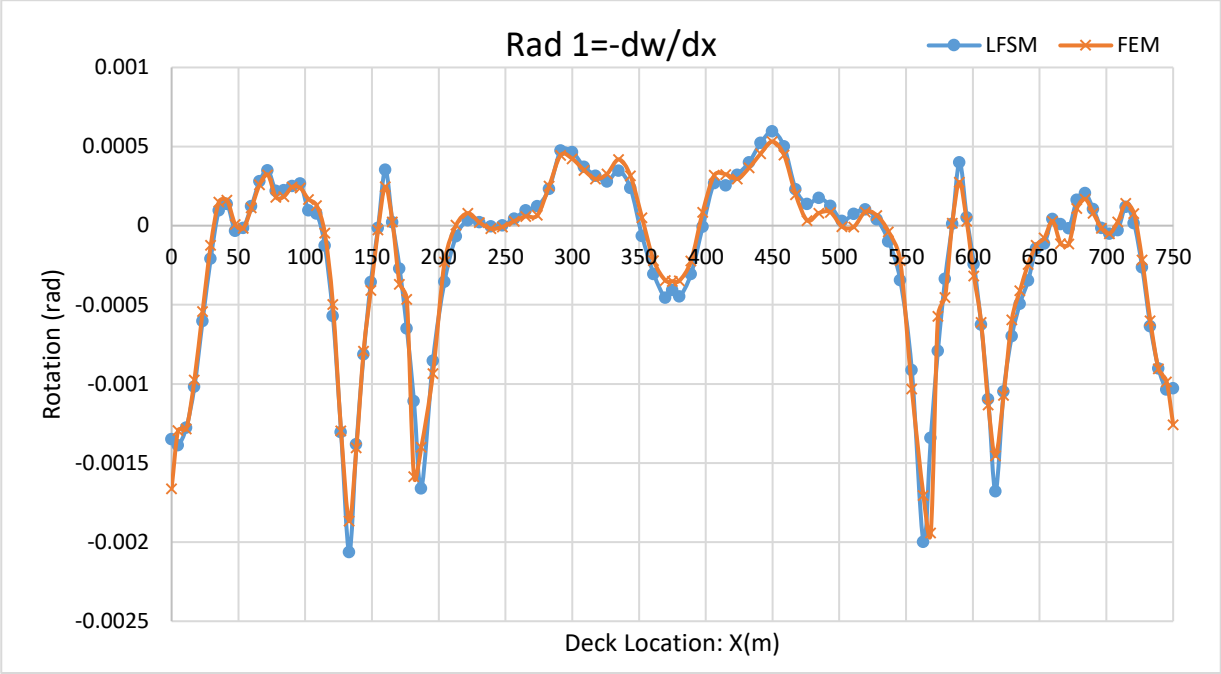

b) Rotation on the deck (Rad 1): Nodal line 5.

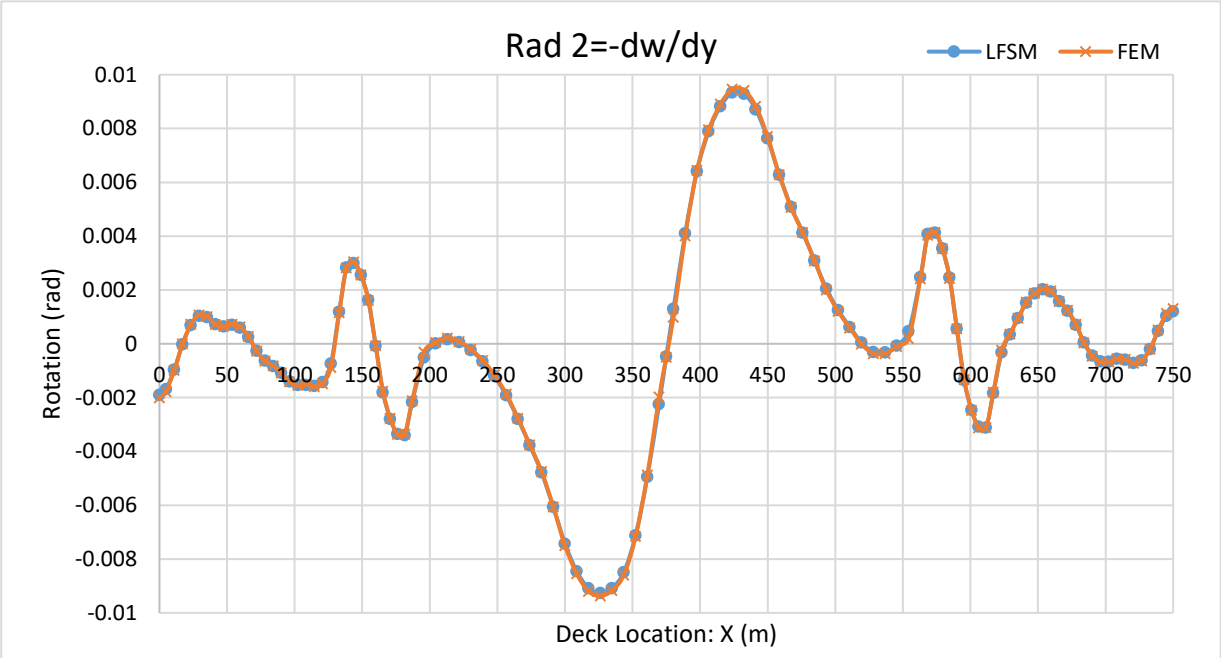

c) Rotation on the deck (Rad 2): Nodal line 5.

Figure 5-11 Deflections and rotations under load Fa for lamina (3)

The deflection obtained for the FRP-KSM Bridge model by the LFSM were in acceptable agreement with the FEM results, as it can be noticed in Figure 5-11 above. Also the rotations around the transverse and longitudinal axes *x* (Rad 1) and *y* (Rad 2) are performed respectively,

induced by the Fa load along the same nodal line 5, were found to be in very acceptable agreement between the two investigated models as it can be noticed in Figure 5-11a), b), and c). It should be noticed that both the vertical deflection and the rotation 1 develops a symmetric shape because of the relatively symmetrical features of the bridge. However, the rotation 2 has an anti-symmetric shape.

2) Load: Fa+Fb

When the loading combination Fa+Fb was applied, the static deflections were found to be in acceptable agreement, especially for the longitudinal *v* direction along the deck, while some differences were noticed for the transverse *u* and vertical *w* deflections, especially along the deck, as shown in Table 5-10.

Table 5-10 Deflection under static load: Fa+Fb for lamina (3)

		Location	A (375m)	B (493.4m)	C (590m)	D (Tower 1 left-top)	E (Tower 2 left-top)
Load Fa+Fb	u (mm)	LFSM	104.17	65.54	21.79	130.59	104.64
		FEM	107.25	67.64	22.05	127.45	108.34
	v (mm)	LFSM	0.35	5.53	3.22	108.69	43.11
		FEM	0.18	5.65	3.21	107.97	40.09
	w (mm)	LFSM	771.21	165.78	0.20	3.99	5.28
		FEM	767.75	179.42	0.23	3.82	5.37

The vertical deflection on nodal line 5 is still large but reduced when applying one more load Fb which is applied on nodal line 3. In this case, the nodal line 3 (middle line of the deck) is selected and shown in Figure 5-12 to investigate the effects of the additional load, when there is already acceptable difference comparing the results between FEM and LFSM. There is a gap in the point B because of the applied vertical concentrated load that affects the equilibrium of the vertical deflections. Rotation 1 has an obvious difference between the two approaches from 200 m to the middle of the span, which shows that these two methods have a different estimation for smaller orders of magnitude ranges. Moreover, the rotation 2 still has an anti-symmetric shape for nodal line 3 as shown in Figure 5-12 c).

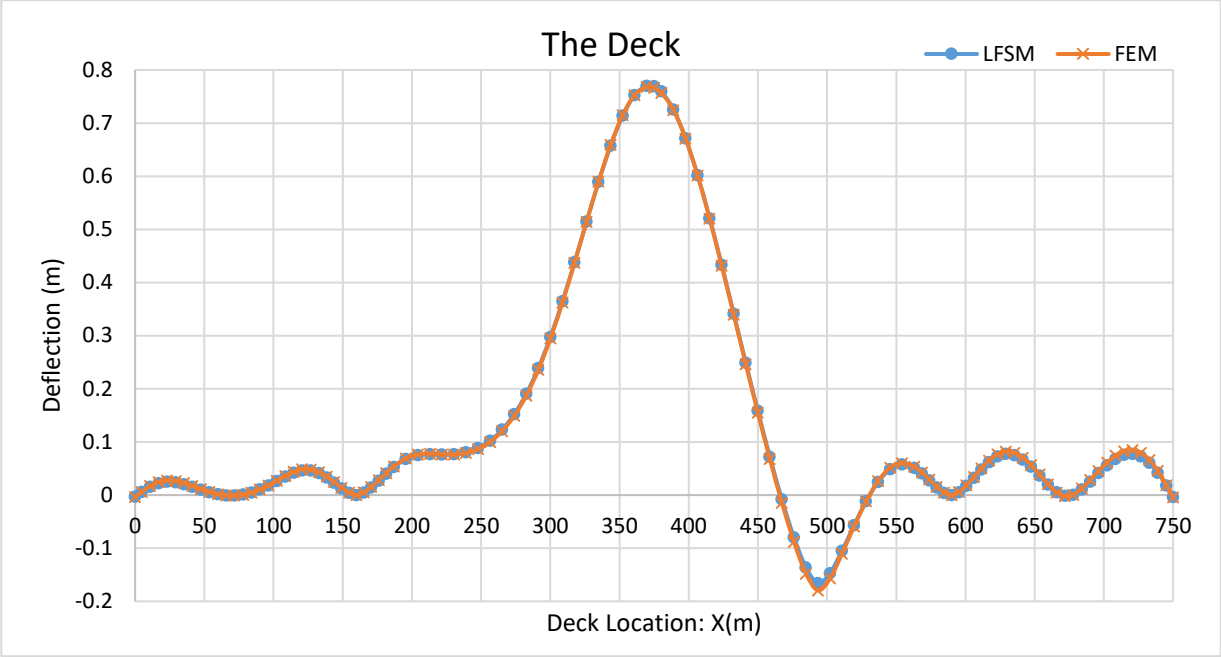

a) Deflection *w* on the deck: Nodal line 3.

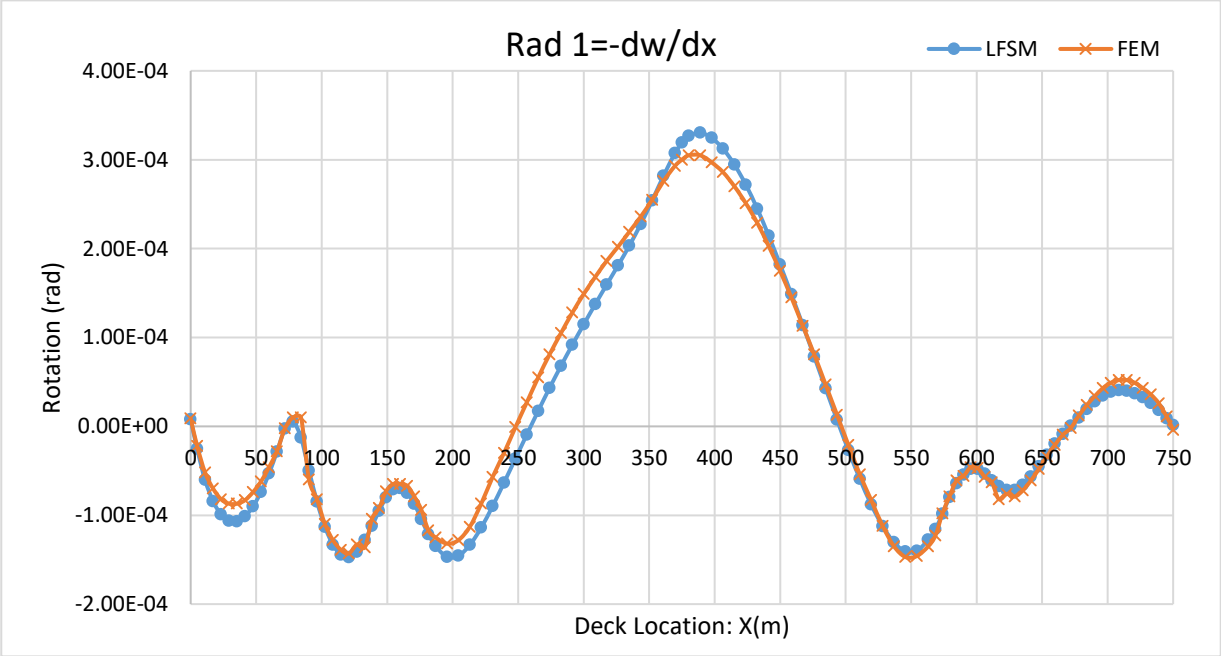

b) Rotation on the deck (Rad 1): Nodal line 3.

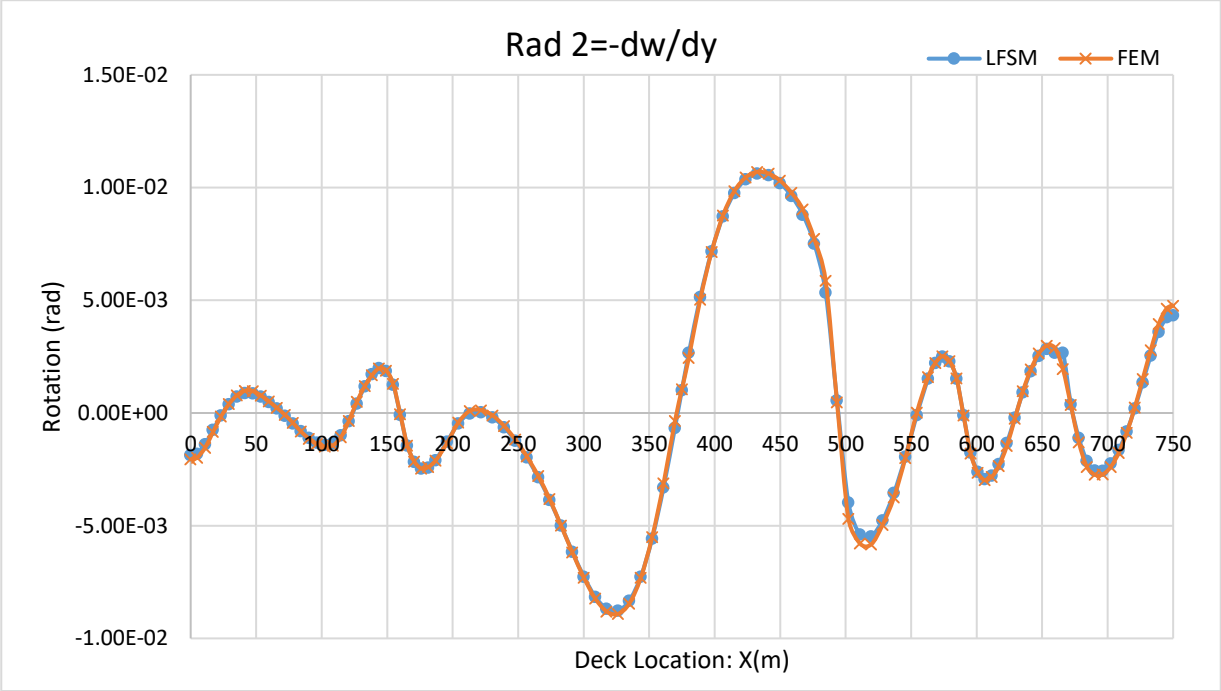

c) Rotation on the deck (Rad 2): Nodal line 3.

Figure 5-12 Deflections and rotations under load Fa+Fb for lamina (3)

3) Load: Fa+Fb+Fc

One additional load, Fc, is applied on the deck in the longitudinal *v* direction to determine deflections. In this case, it is harder to distinguish the differences in the longitudinal direction. However, there are almost no changes happened in the critical locations that can be observed in Table 5-11.

Table 5-11 Deflection under static load: Fa+Fb+Fc for lamina (3)

		Location	A (375m)	B (493.4m)	C (590m)	D (Tower 1 left-top)	E (Tower 2 left-top)
Load Fa+Fb+Fc	u (mm)	LFSM	100.86	62.37	20.50	127.17	98.42
		FEM	103.81	64.29	20.70	124.14	101.66
	v (mm)	LFSM	2.97	2.79	0.39	105.86	46.57
		FEM	2.82	2.89	0.35	105.20	43.64
	w (mm)	LFSM	770.58	164.22	0.19	3.92	5.08
		FEM	767.17	177.79	0.21	3.76	5.16

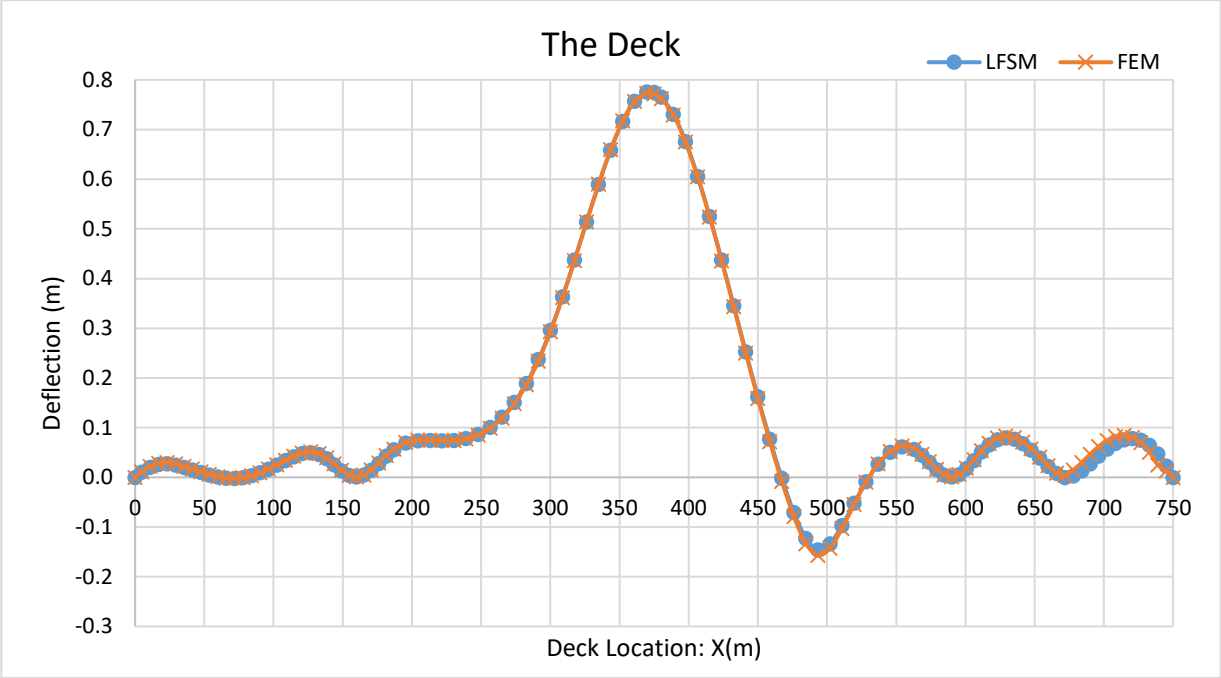

a) Deflection *w* on the deck: Nodal line 2.

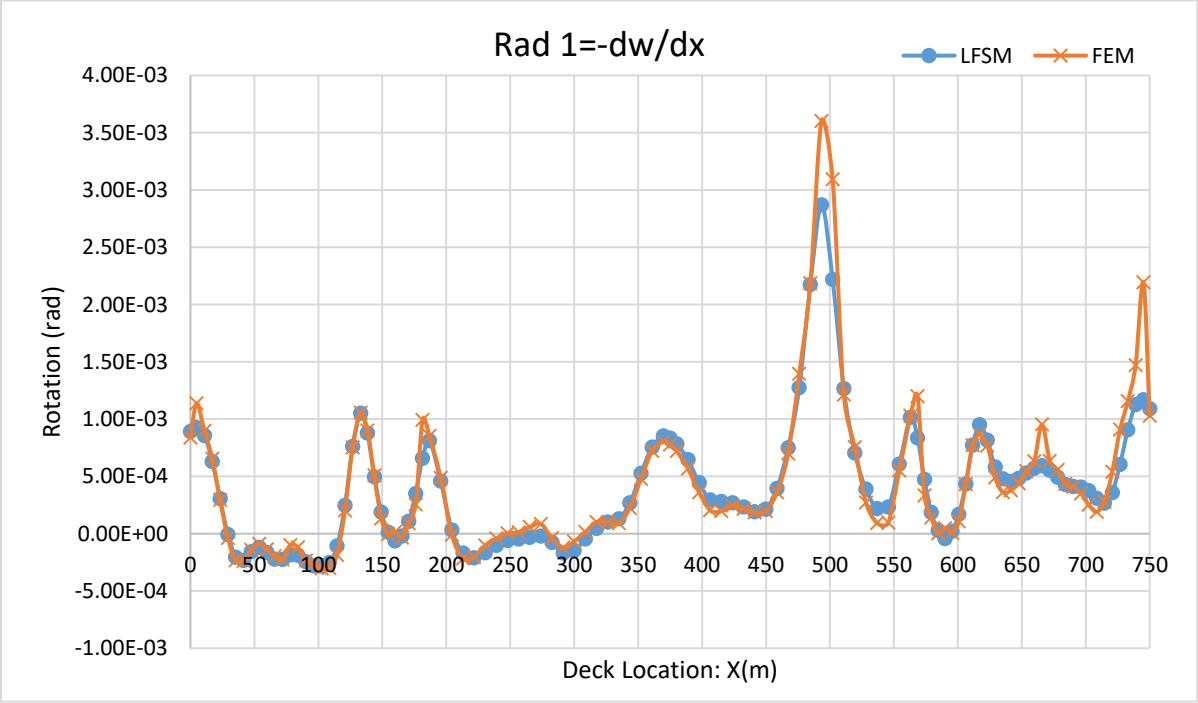

b) Rotation on the deck (Rad 1): Nodal line 2.

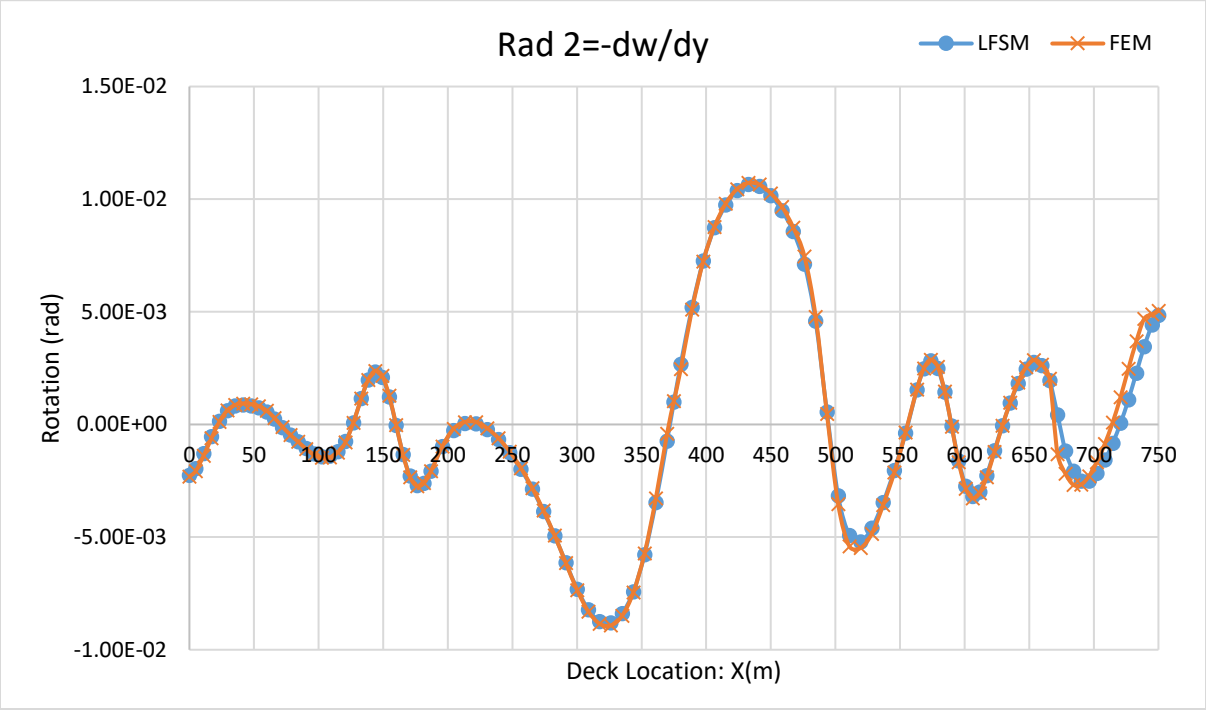

c) Rotation on the deck (Rad 2): Nodal line 2.

Figure 5-13 Deflections and rotations under load Fa+Fb+Fc for lamina (3)

Since small difference occurred in this case, thus the vertical deflections on the deck, as well as the rotation 1 and 2 on nodal line 2 (9.66 m from nodal line 3), are selected to investigate the validity of the static results, as shown in Figure 5-13. It is obvious that results from the two methods meet an acceptable agreement, except for the rotation 1 where the vertical concentrated load was applied. This is because of the sensitive characteristics for rotations around the *x*-axis.

Since the load Fd and Fe are applied on the deck that intends to determine the displacements effects of towers, therefore, they are not selected to analyze the influence on the FRP deck. However, they are performed by the author and attached in Appendix C.

4) Live load

For lamina (3), the deflections recorded under a uniformly distributed live load of 550 kN/m had the best agreement among the laminae investigated, however slightly smaller deflections were noticed again for the main span for the LFSM method, when compared with the results obtained for the FE model, as it can be noticed in Figure 5-14 a). Also for the side spans the FEM registered higher deflections than the LFSM model especially for the two side spans. A similar trend was noticed for the rotation distribution plots. However, an excellent agreement was met for the middle span rotation.

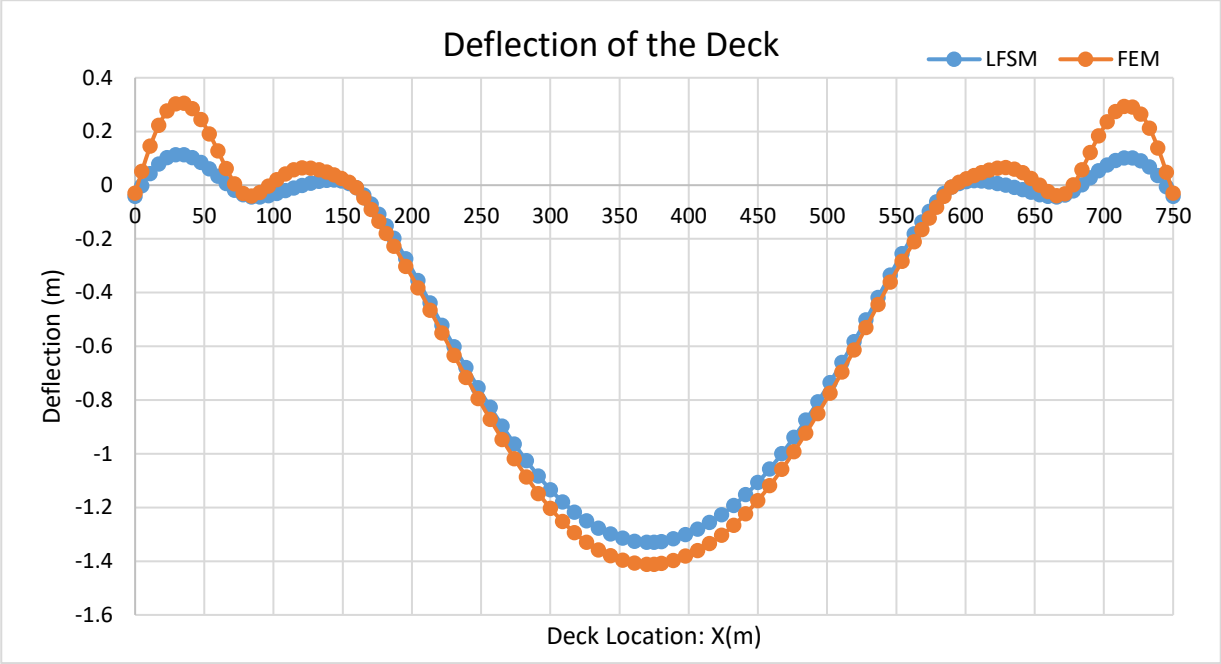

a) Deflection on the deck: Nodal line 3.

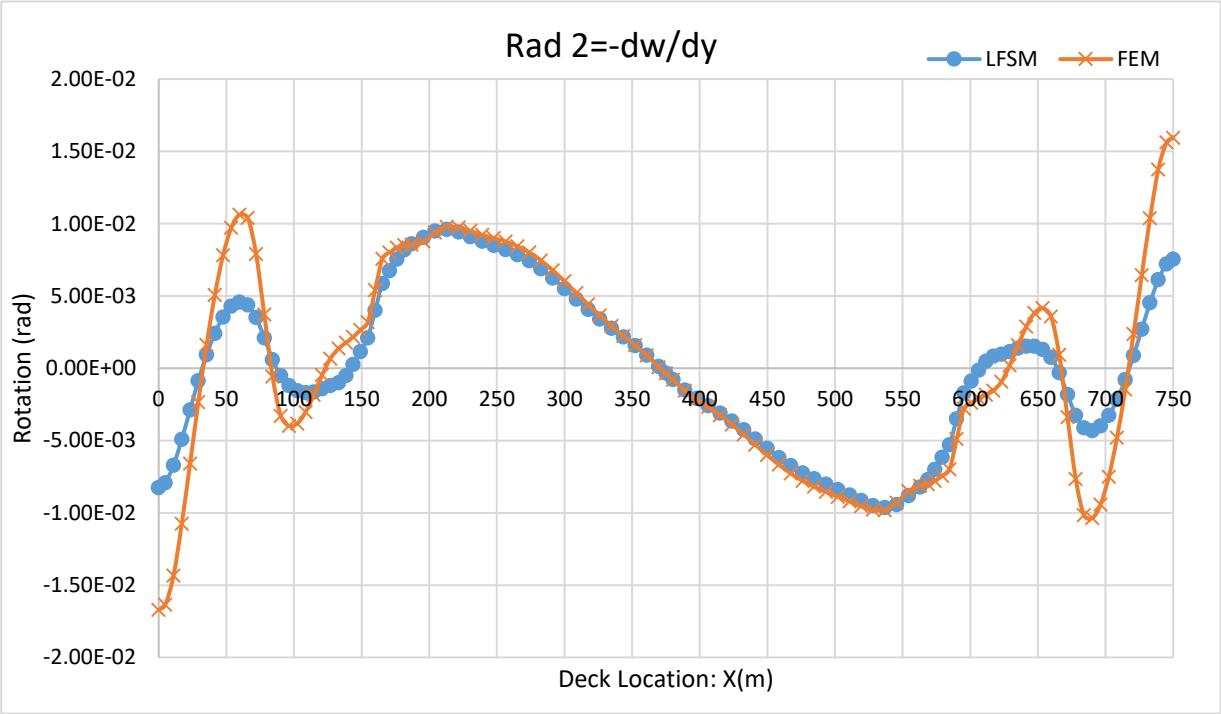

b) Rotation on the deck (Rad 2): Nodal line 3.

Figure 5-14 Deflections and rotations under live load for lamina (3)

5.3.3. ANALYSIS OF THE STATIC RESULTS

The three laminae of thicknesses 0.38 m, 0.78 m and 1.02 m as defined above, were investigated under the effect of the concentrated loads applied at the critical locations along the deck and the tip of the tower, and under the effect of the uniformly distributed live load. It is concluded that the higher thickness for the FRP bridge deck, the stronger stiffness the deck will have. Moreover, these meet the critical deflection requirements stipulated in the Canadian Highway Bridge Design Code (2012) as well as the other standards, such as Design of FRP Bridges and Highway Structures within the standard Highway Structures: Approval Procedures and General Design (2005). It should be mentioned that the serviceability requirements may govern the design of the FRP components, due to the relatively low values of the elastic modulus. The deflection of the structure, should not be such as to affect its appearance or serviceability adversely. This can be achieved by limiting the deflection of the FRP components under the effect of the live load, to L/300, where L is the length of the main span, including the shear-induced deformation. The deflection limit should be applied locally and globally, in both longitudinal and transverse directions of the deck.

In this case, lamina (3) with the thickness of 1.02 m is selected with the proposed FRP deck applied for the KSM cable-stayed bridge, and the maximum deflection under live load is described as (Design of FRP Bridges and Highway Structures, 2005):

$$1.33\ m\left(LFSM\right) \le 1.41\ m\left(FEM\right) \le span/300 = 1.43\ m \tag{5-10}$$

The FRP decks modeled with lamina (1) and lamina (2) showed deflections under the live load beyond this critical maximum deflection. Obviously, the static results for the three laminas were considered as accurate when meeting an acceptable agreement for both the concentrated loads and the uniformly distributed live load for the two methods: LFSM and FEM. Also, the deflection at the critical locations of each component, especially the deflection and rotation of the deck laminated shell strips, were proved to be the be accurate, because the results from the two methods agree well with each other. It is assumed that the FEM always has the most accurate results values between these two methods, and comparison with other practical studies was not possible, due to the lack of the experimental data or actual site measurements conducted on FRP bridge decks. In this case, a parametric study was carried out for the three laminae models, to compare the static results; also, the results from the original Kap Shui Mun Bridge were compared in the following section and were considered to meet the requirement of critical deflection. Thus the results obtained in the current research were verified for the static results.

5.3.3.1. CONCENTRATED LOAD RESULTS COMPARISON

After reviewing the deflections registered at the critical locations for each lamina, it was noticed that lamina (3) had the smallest deflection under concentrated loads since both concrete bridge and hybrid composite bridge meet a very acceptable agreement between the two methods. Also, the most efficient critical locations are A, B on the deck and D, E on each tower, since the deflections of location C are always very small because of the supporting pier at this location. Figure 5-15 to 5-19 compare the static results obtained from the applied concentrated loads derived by FSM for both concrete KSM Bridge (Naderian et al. 2015) and the current three hybrid composite Kap Shui Mun Bridge models with lamina (1), lamina (2), and lamina (3). All the values represent the effective deflection magnitudes under each load cases for the specific nodal line.

It is obviously that the smallest deflection of the deck was registered for the transverse and longitudinal deflections, while for the towers maximum deflections occurred mainly in the vertical direction when compared with the original concrete deck model. It can be easily observed that the actual deflection for the deck and towers approached each other for the two investigated methods LFSM and FEM from above figures. Therefore, these deflection and displacement values for both the concrete bridge (by IFSM) and the three-different laminated composite bridges (by LFSM) were collected in Figure 5-15 to 5-19 below.

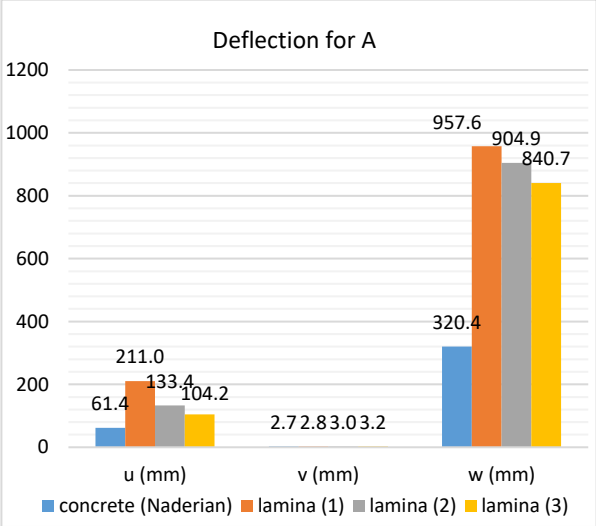

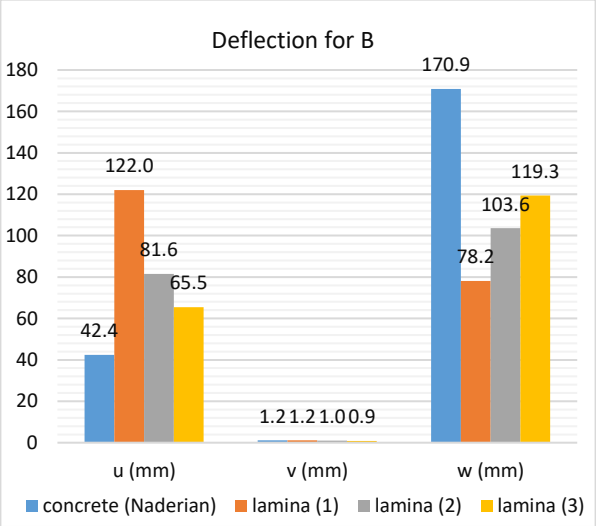

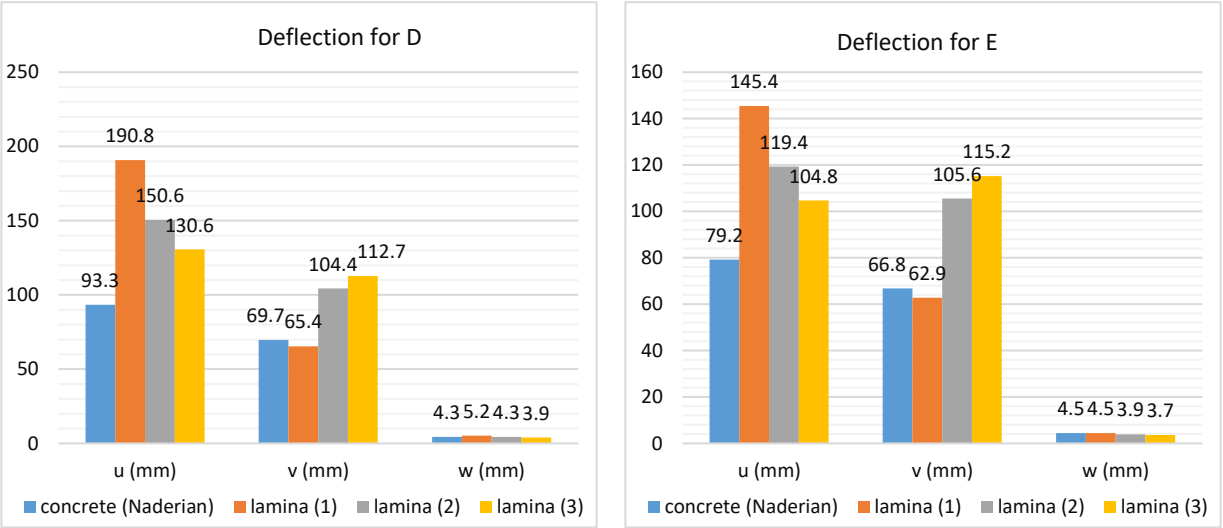

Figure 5-15 Deflections comparison under concentrated load Fa

Obviously, the concrete deck has the best deflection behavior among these decks under the load Fa as shown in Figure 5-15, except for the vertical deflection for point B.

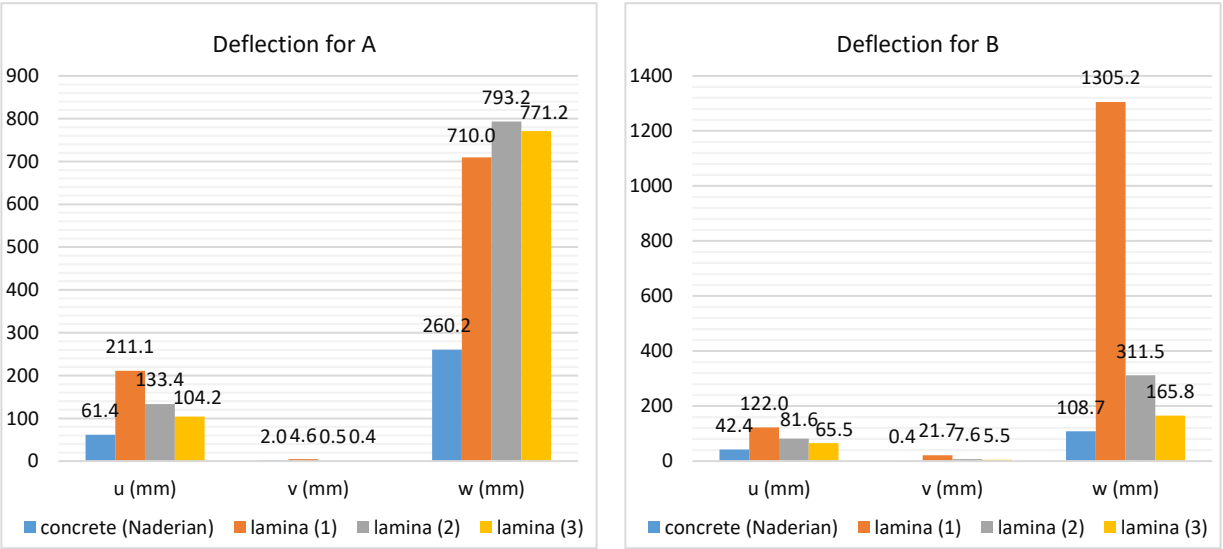

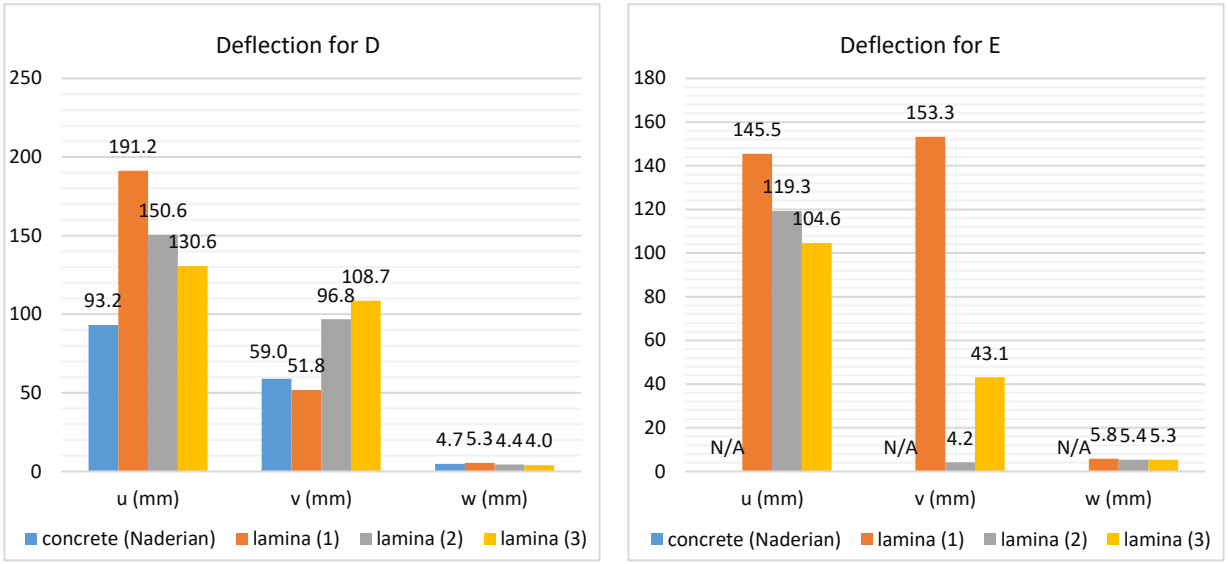

Figure 5-16 Deflections comparison under concentrated load Fa+Fb

There is no obvious maximum deflection behavior among the three laminated decks investigated under load Fa and Fb, as shown in Figure 5-16, except for the lamina (1) that has a large vertical deflection on point B. Otherwise, the other three types of decks showed acceptable deflection results when the load Fb was applied.

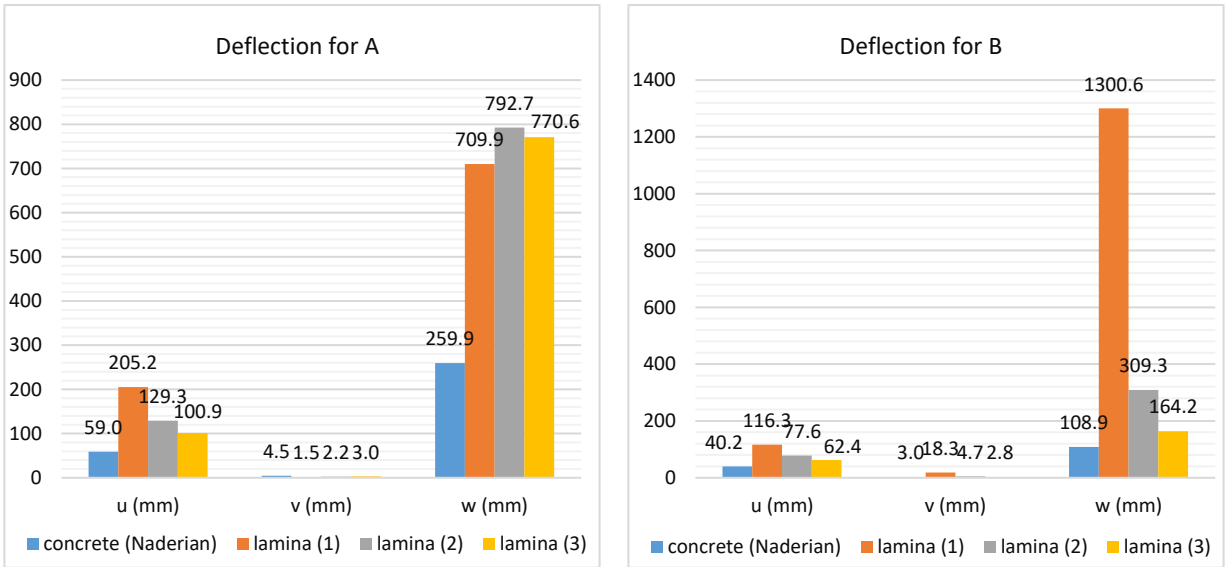

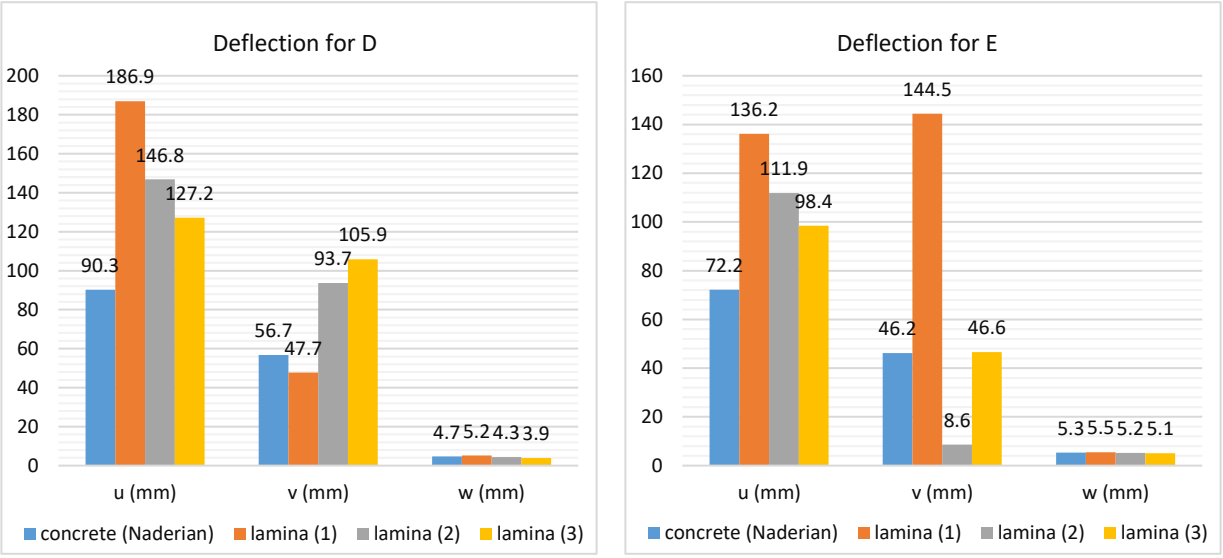

Figure 5-17 Deflections comparison under concentrated load Fa+Fb+Fc

Similar trends were noticed for the deflections obtained under loading combination Fa+Fb+Fc as shown in Figure 5-17. The deflection behavior among these decks showed a gradually increasing trend with the decrease of the lamina thickness, except for the lamina (1), that has a large vertical deflection at point B. On the other hand, lamina (2) is the best choice for undertaking the effects of these three loads.

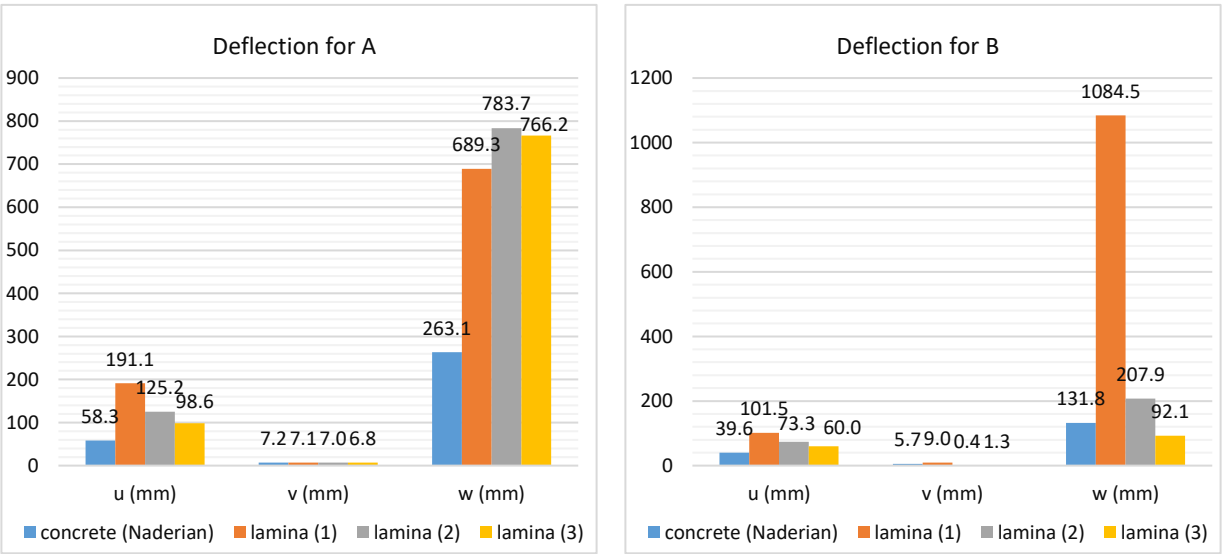

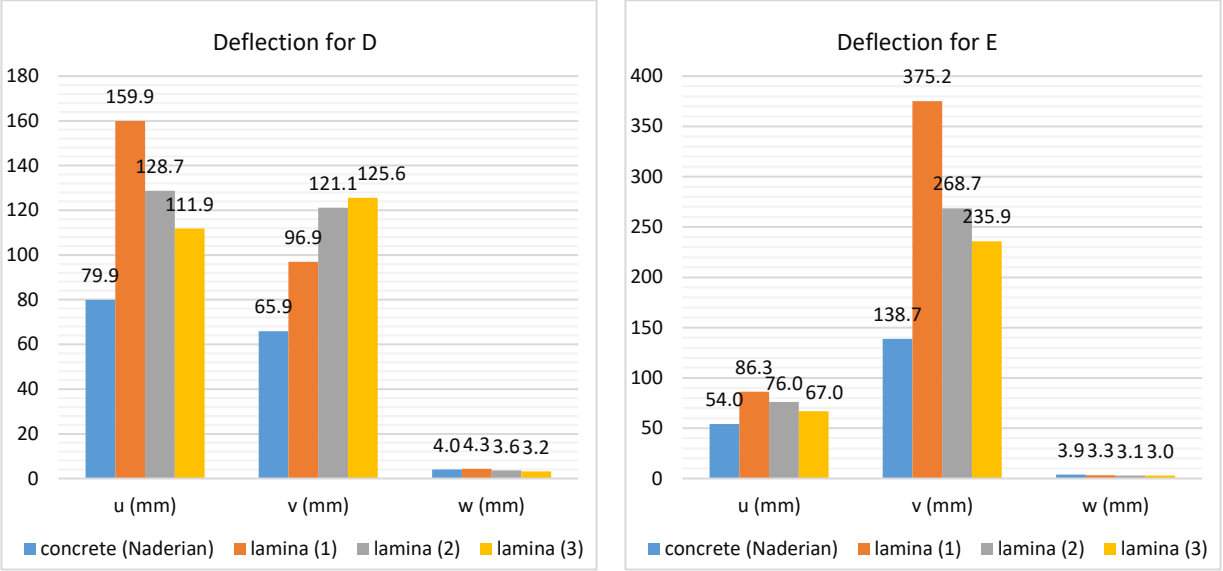

Figure 5-18 Deflections comparison under concentrated load Fa+Fb+Fc+Fd

For the load case 4, when the concentrated loads Fa+Fb+Fc+Fd were used, obviously, the original concrete deck showed the minimum deflection distributions among all the investigated decks as shown in Figure 5-18. As a result, concrete is suggested to model the deck when applying these four concentrated loads, but if the use of FRP materials is sought for the bridge deck, then the lamina (3) model is recommended.

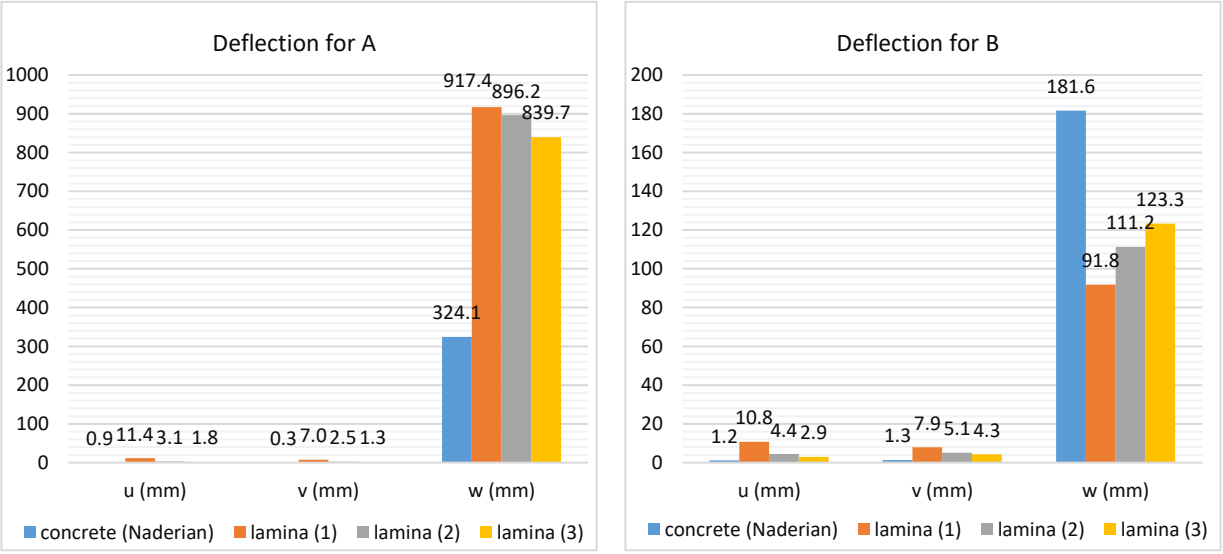

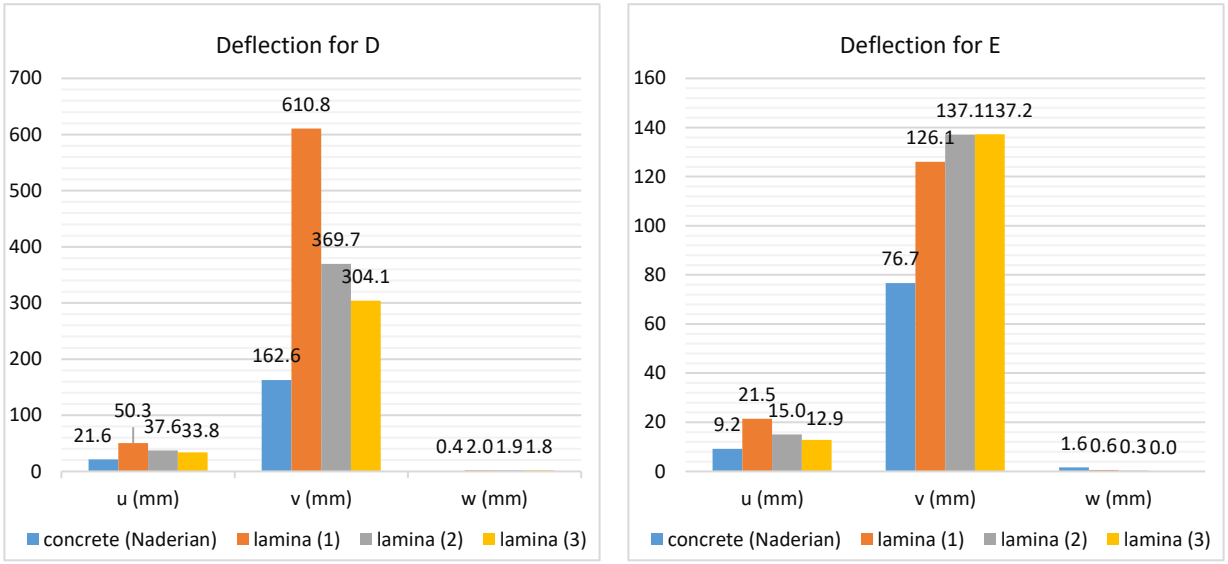

Figure 5-19 Deflections comparison under concentrated load Fe

For the last concentrated loading case 5, where the Fe load is applied on the tower, again the original concrete deck registered the minimum deflection magnitude among all the investigated bridge decks, as it can be noticed in Figure 5-19. For the FRP bridge decks, the minimum deflection was noticed for the lamina (3) model, except for the vertical deflection at point B, where lamina (1) had a better result.

5.3.3.2. LIVE LOAD RESULTS COMPARISON

Since the deflections under the concentrated loads are not critical for the standard design loads combinations, such as dead load, live load, wind load, etc., the uniformly distributed live load was considered as the most efficient loads for investigating the bridge deck deflection, as defined in Figure 5-8. After comparing the live load deflections for the three laminae models applied for the deck (Figure 5-20), it was noticed that the deflection curves are very similar to the lamina (2) and lamina (3) decks, however, a very big difference was recorded for the lamina (1) model, estimated by LFSM. This proves that the lamina (2) and (3) would be the appropriate models for designing the FRP bridge decks when applying distributed loads.

Obviously, except for the critical maximum deflection calculated in Eq. 5-10 for lamina (3), the other two laminas do not meet the requirements. When it comes to the deflection curves under live load, lamina (1) with the thickness of 0.38 m has the largest deflection curve that almost every point has the biggest deflection in the vertical direction. Also, there is a sharp decrease for the deflection in the middle of the span, which means the deflections changed significantly because of the limit shear strength for lamina (1). Regarding lamina (2), the deflection is closer to the lamina

(3) but still exceeds the critical requirements. Consequently, the composite FRP cable-stayed bridge with the deck of the lamina (3) is the most capable one for satisfying the static deflection criteria.

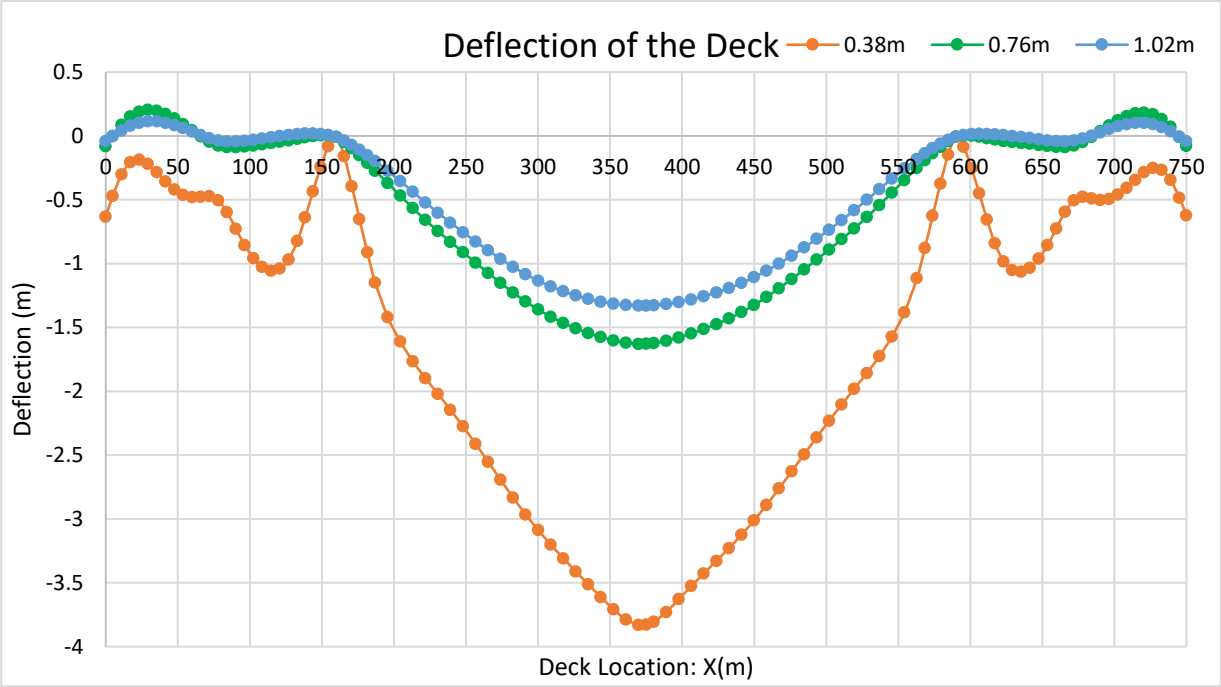

Figure 5-20 Comparison of deflection under live load for three laminas

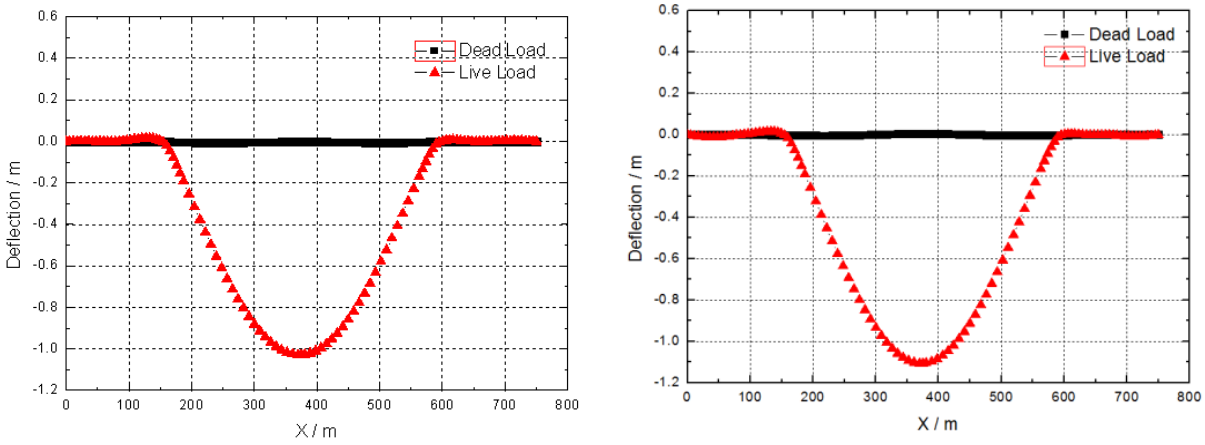

(a) Original Kap Shui Mun Bridge (b) The proposed new FRP design

Figure 5-21 Deck deflection under dead load and live load conditions (Chan et al. 2013)

As mentioned in Chapter 2, Chan et al. (2013) also investigated the FRPs materials for modeling the deck of the Kap Shui Mun Bridge. It is necessary to compare the results obtained in the current research by applying the LFSM model for the deck and the results reported by Chan et al. (2013), as shown in Figure 5-20 and Figure 5-21. It can be noticed that there is an increasing trend of the deflections under the effect of the uniform live load when comparing the original Kap Shui Mun Bridge, FRP box-girder bridge with the laminated FRP bridge using lamina (3) model. The reason might be the lower stiffness of the FRP materials and the smaller cross section area of the FRP box-girder used by Chan et al. (2013), even though, the laminated FRP deck has the lowest stiffness compared with the two other laminated deck models. There is no doubt that the FRP decks have their advantages, such as lower self-weight, which will improve the time required for construction and the associated cost; reasonable FRP strain-stress behavior that has no fatigue characteristics; more durability than the concrete and steel or hybrid decks, etc. Usually, the FRP materials are in the form of box or sandwich (laminated FRP). Considering the FRPs weak capacity of resisting the loads in the transverse direction, when designing, it is necessary to arrange this material normal to the bridge longitudinal axis. Thus, the effective area is much smaller than the normal area of the FRP materials. The absolute deflection of the FRP designed bridge deck is larger because of the low stiffness, where the section properties for both concrete bridge and FRP bridge can be found in Table 2-17 and Table 5-5. Moreover, when experiments are performed or when the full-scale FRP bridge deck is constructed, it is suggested to increase the stiffness of the FRP deck such that two to four stiffening beams can be included in the FRP deck.

5.4. FREE VIBRATION ANALYSIS

5.4.1. NATURAL FREQUENCIES

It has been discussed in the previous chapter that the accuracy of the frequency domain analysis depends very much on the free vibration analysis and the natural frequencies of the model. The visualization of the vibration mode shapes reported below was determined by using the modal analysis in FEM in SAP 2000. Also, it was shown that the improved LFSM approach could capture the free vibration characteristics of a girder bridge and both methods yielded similar frequency domain response, because of the good agreement of the natural frequencies, especially for lamina (3). For cable-stayed bridges, for which lower natural frequencies are predicted, good frequency domain responses can be achieved by both LFSM and FEM, with only minor differences, as detailed in the sections below.

Consequently, the three laminae models have very similar natural frequencies, according to the Figure 5-22, in particular for the lamina (2) with a thickness of 0.76 m and lamina (3) with a thickness of 1.02 m. This means that these two laminae have a very similar frequency domain response when applying the seismic excitations. However, the lamina (3) has a better static behavior; in this case, it is selected to proceed further with the detailed investigation of the lamina (3) modeled Kap Shui Mun Bridge model, for both LFSM and FEM frequency domain analyses.

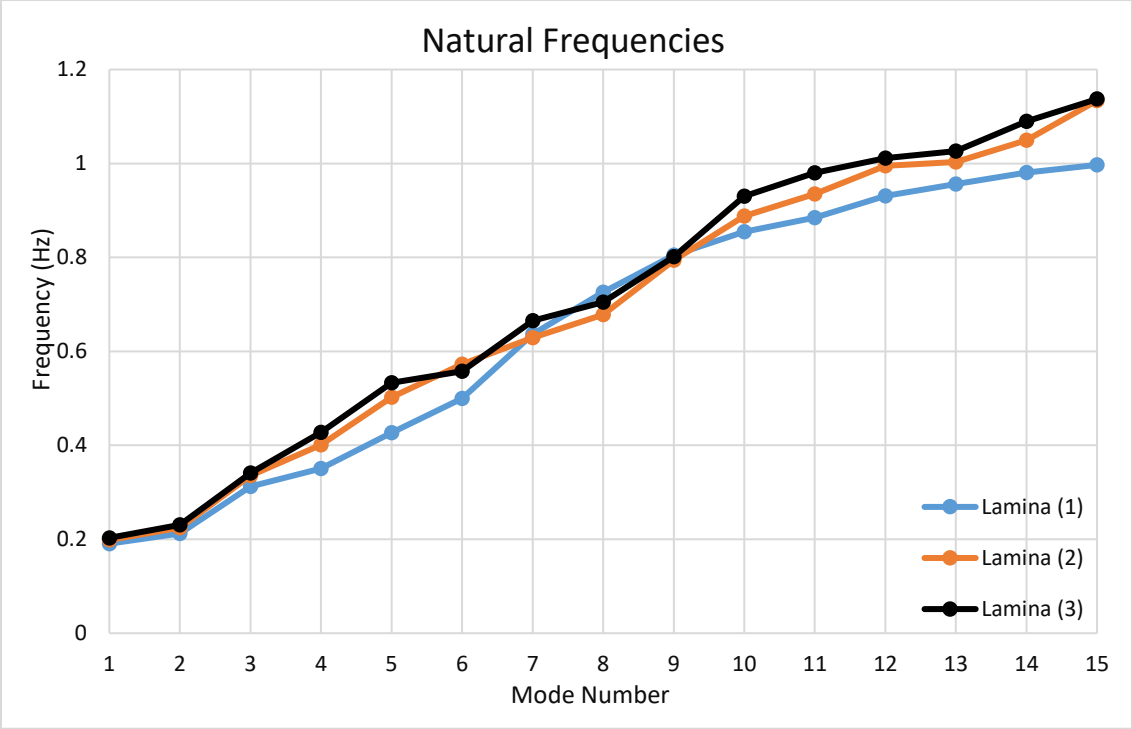

Figure 5-22 Comparisons of natural frequencies for the KSM bridge modeled with three laminas

In terms of free vibrations analysis, Figure 5-23 compares the first fifteen natural frequencies of the KSM bridge models, for the proposed lamina (3), which are derived from the SAP 2000 model for the FEM, and from the MATLAB codes for the LFSM method as adapted from Naderian et al. (2013). The shell element was used for modeling the laminated deck for Kap Shui Mun Bridge for both methods because this element showed a better agreement than the Slab-girder Bridge. Also, the structural damping value was set as 0.02 within both approaches. It can be easily found that the two numerical methods result in a very acceptable agreement for the natural frequencies.

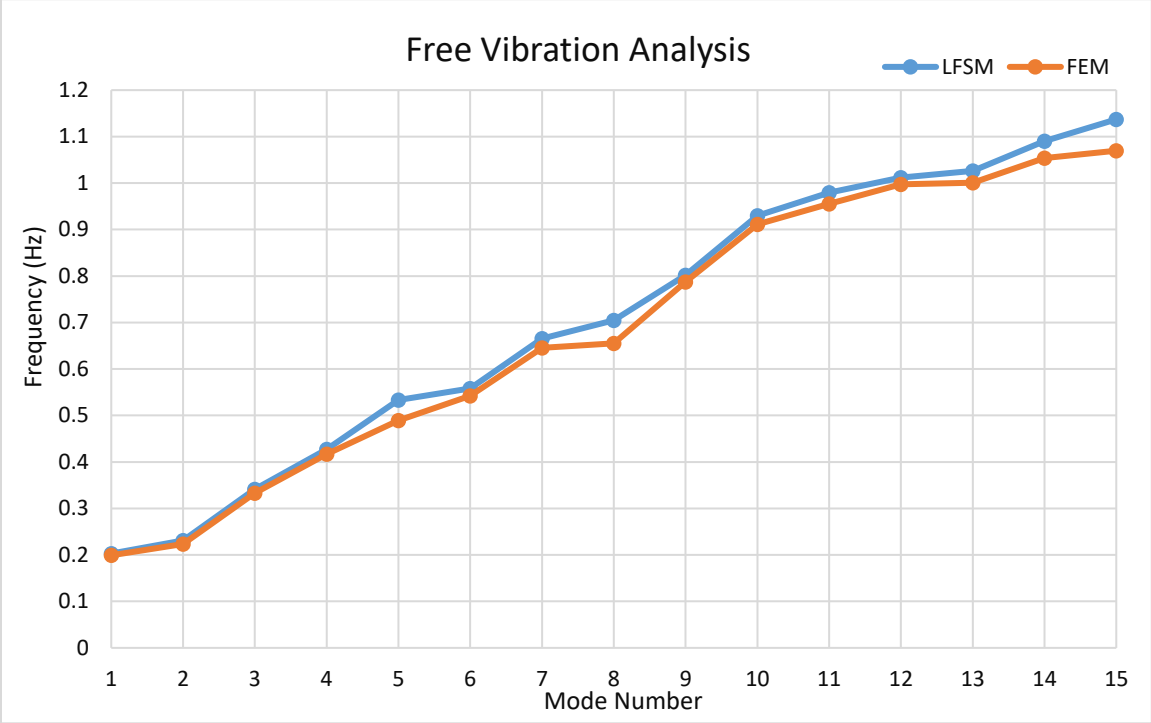

Figure 5-23 Natural frequencies for the first fifteen mode shapes of the FEM and LFSM KSM Bridge Lamina (3) models

Within the first 15 vibration modes of the FRP-KSM Bridge model, there are two swaying modes for the pylon, eight bending modes of the deck, three torsion modes of the deck, and two lateral bending modes of the deck. It is obvious that the differences of frequencies between LFSM and FEM are variable in the first 15 models especially for the modes 5, 8 and 14, and 15, otherwise the natural frequency obtained by LFSM were slightly higher than the FEM obtained frequencies. Again, it could be noticed that that the deck torsion modes have the largest difference between the natural frequencies of these two methods, which means that currently, the LFSM is not approaching to deck torsion modes as estimated by the FEM model. This is also because of the laminate coupling stiffnesses terms B_{ij} that were used to define the interactions between the layers of the laminates, which is almost equal to zero, because of the symmetric distribution of the laminates as explained above. Also, it might be due to the partial modeling of the laminates that do not take into consideration various coupling effects, influencing the natural frequencies which may lead to complex combinations of extensional, flexible, and torsional deformations.

Figure 5-24 shows the detailed comparison, for each type of natural frequency modes registered in the first five modes of the two methods: LFSM and FEM. It was noticed that in general a very acceptable agreement was obtained for the first or the first two vibration modes, of each type; however, with the increase of the mode number, the LFSM slightly overestimated the natural

frequencies associated with each mode, especially for the pylon sway and the deck torsional modes. The discrepancies are smaller than 0.06 Hz. Therefore it can be considered that overall, a very acceptable agreement was achieved for the natural frequencies obtained by LFSM and FEM.

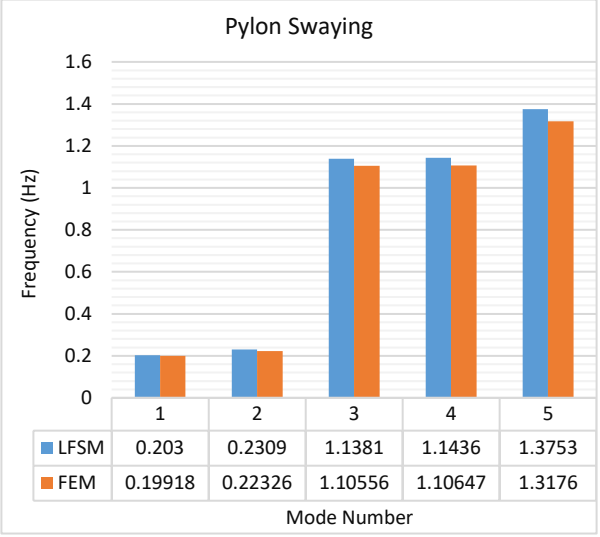

(a) Pylon swaying: First five modes

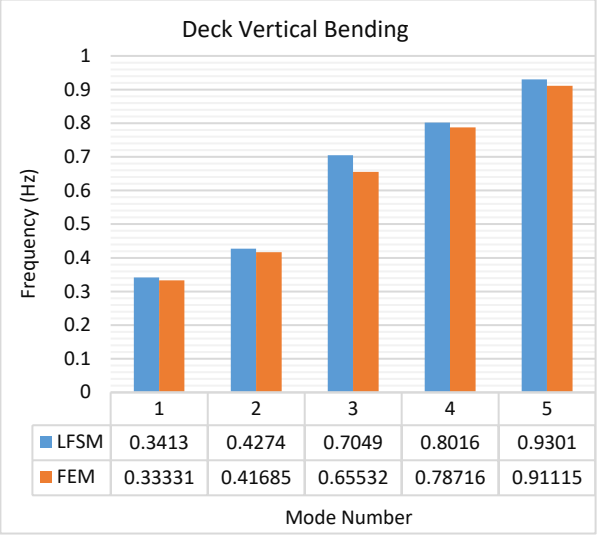

(b) Deck vertical bending: First five modes

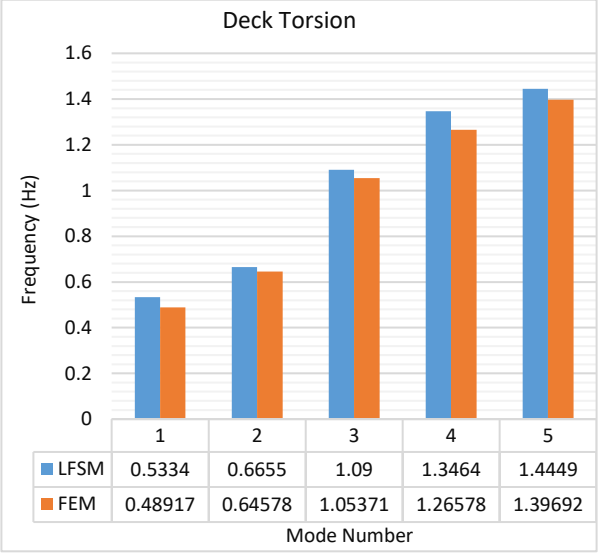

(c) Deck torsion: First five modes

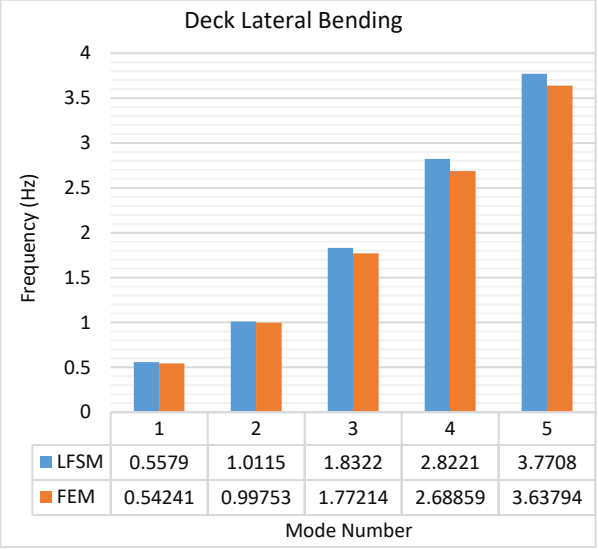

(d) Deck lateral bending: First five modes

Figure 5-24 Natural frequencies for the first five modes of different modes for composite KSM Bridge with lamina (3)

The detailed first two deformed shapes calculated by LFSM from each type of vibration modes, as identified by SAP 2000 in Figure 5-24 above, were illustrated for the KSM bridge model in Figure 5-25 to Figure 5-28.

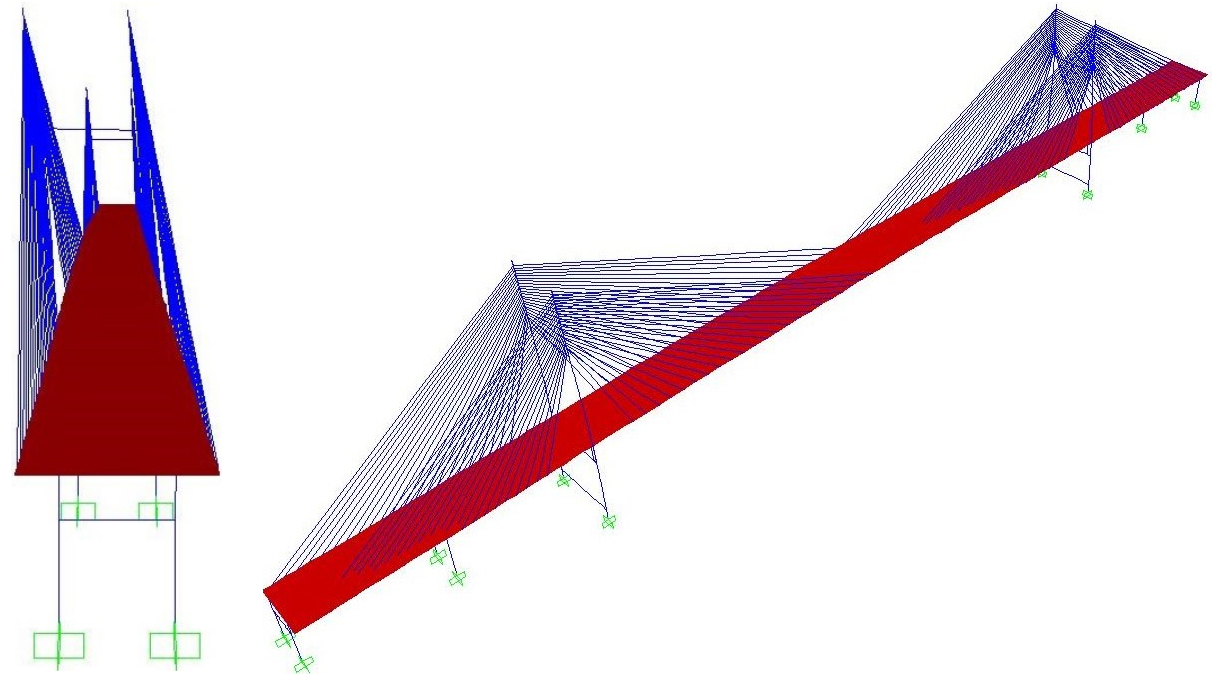

a) Mode shape 1: first pylon swaying mode (0.203 Hz)

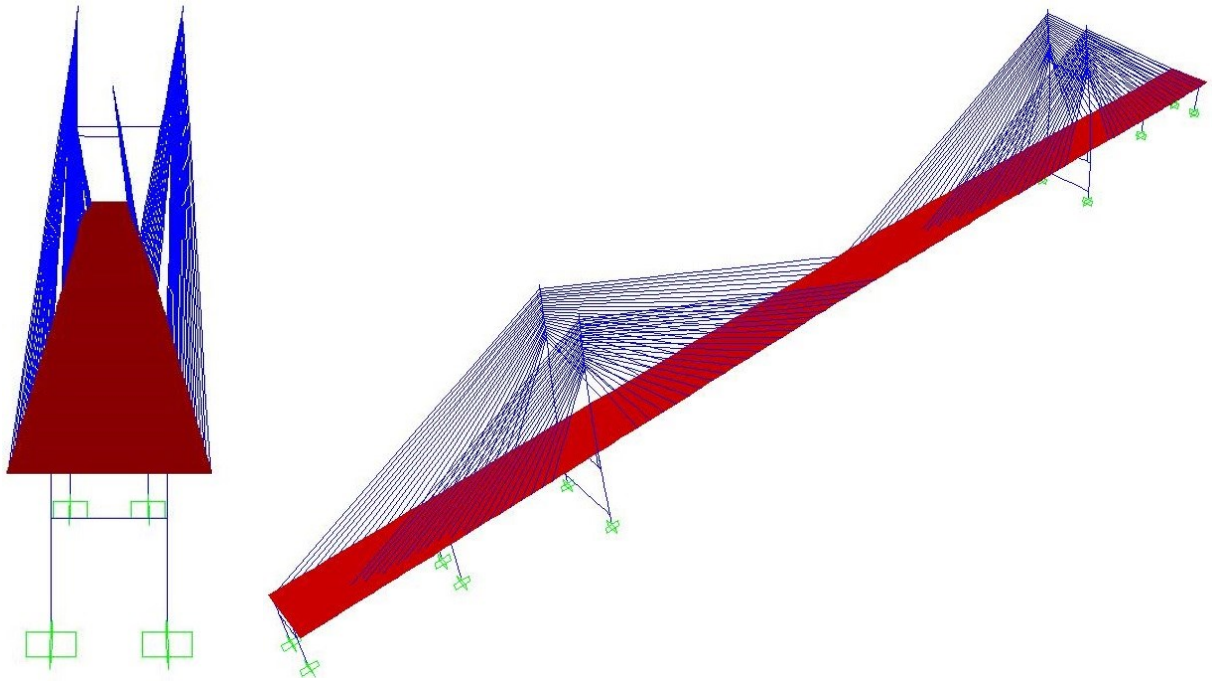

b) Mode shape 2: second pylon swaying mode (0.2309 Hz)

Figure 5-25 The deformed shapes for first two pylon swaying modes for composite KSM Bridge with lamina (3)

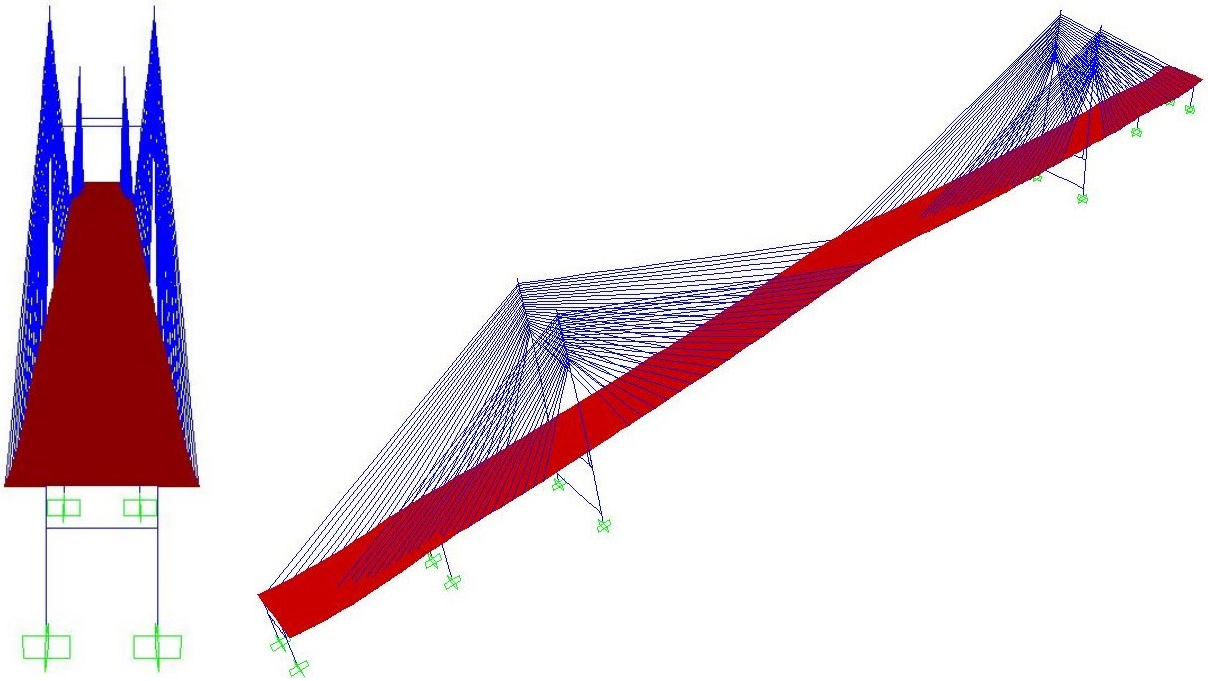

a) Mode shape 1: first deck vertical bending mode (0.3413 Hz)

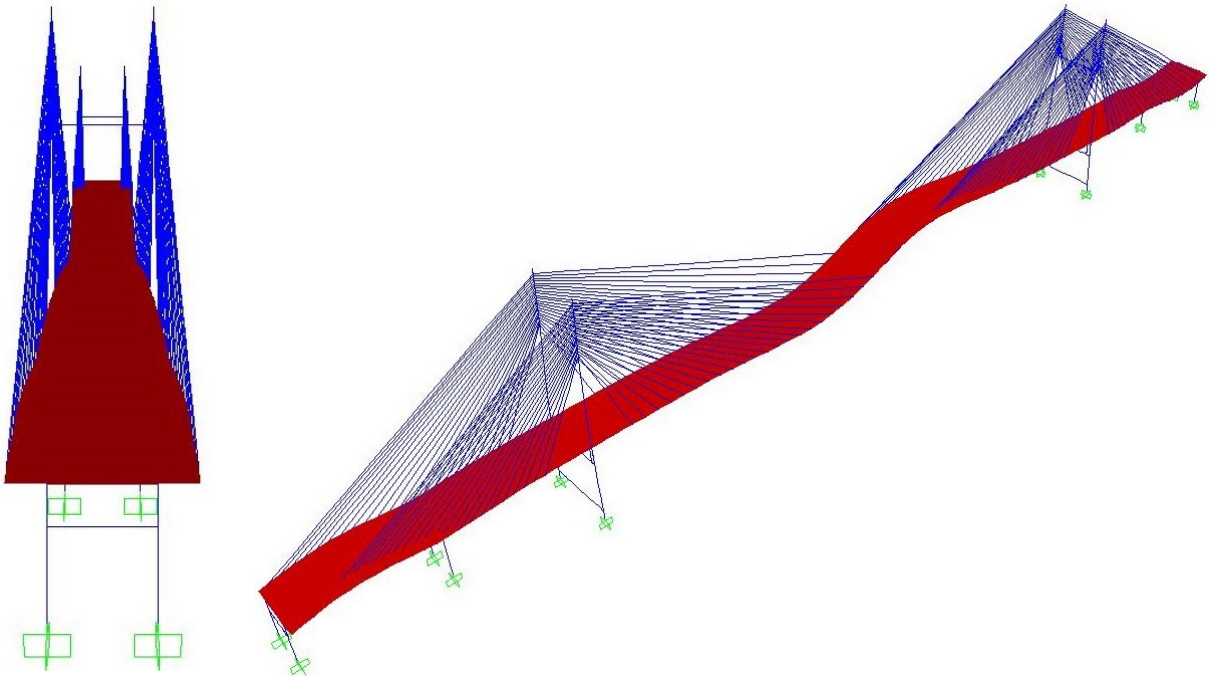

b) Mode shape 2: second deck vertical bending mode (0.4274 Hz)

Figure 5-26 The deformed shapes for first two deck vertical bending modes for composite KSM Bridge with lamina (3)

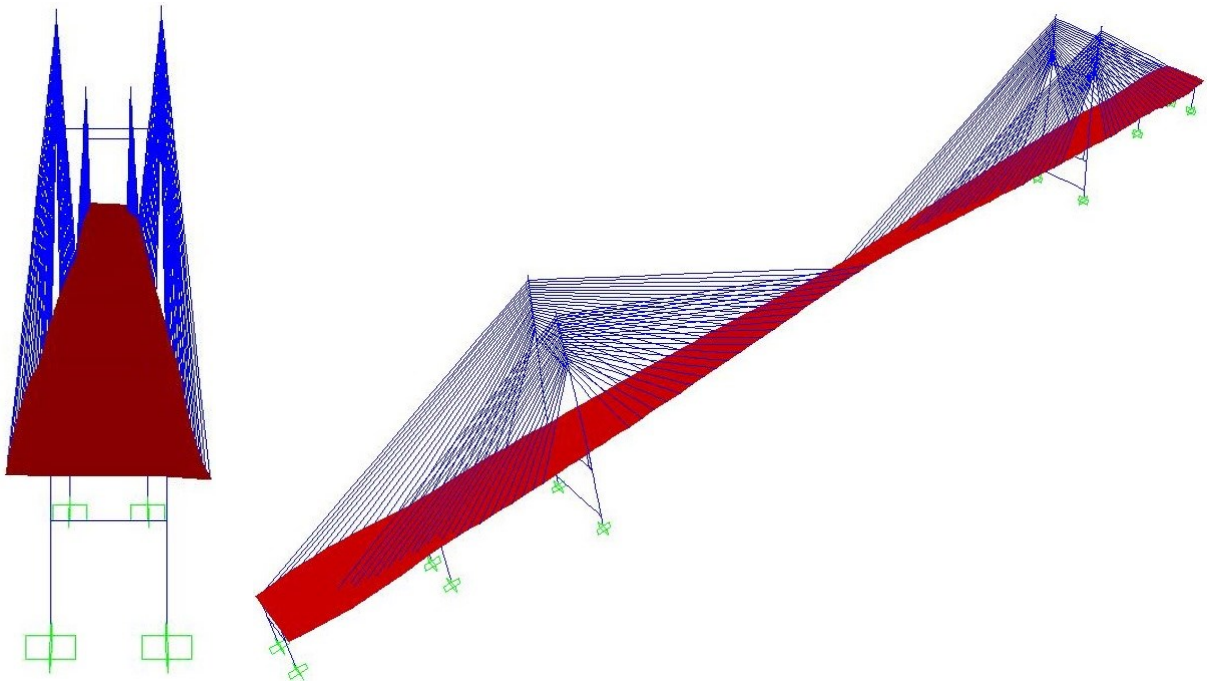

a) Mode shape 1: first deck torsional mode (0.5334 Hz)

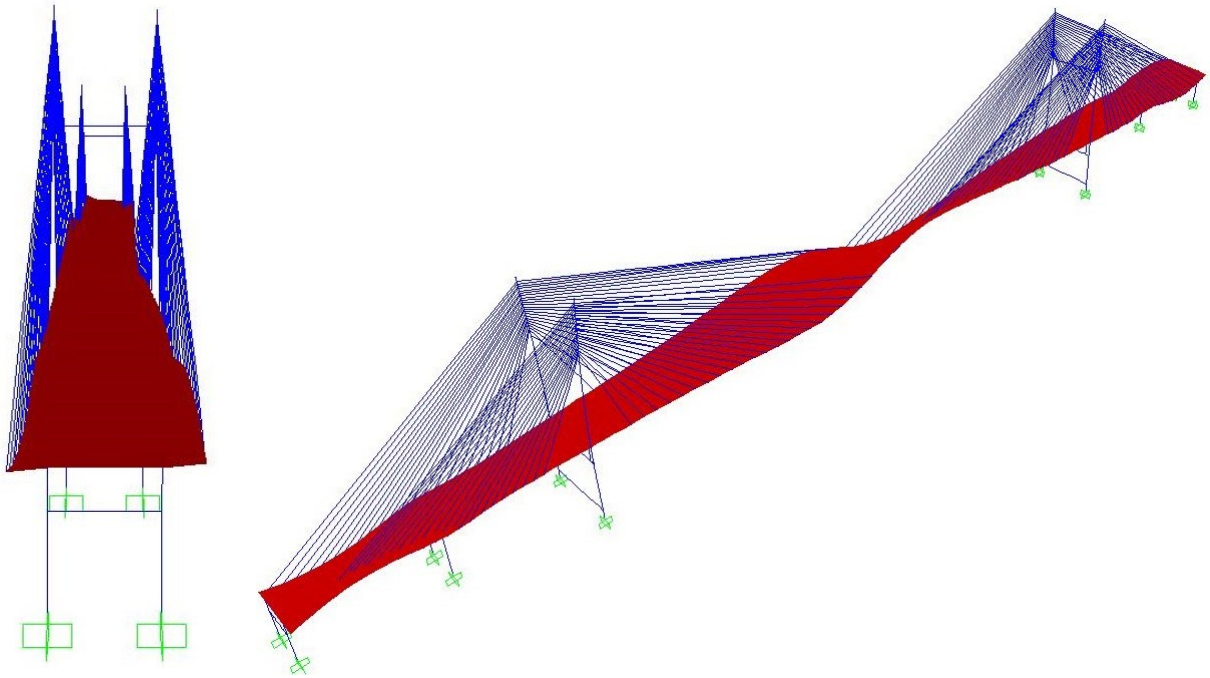

b) Mode shape 2: second deck torsion mode (0.6655 Hz)

Figure 5-27 The deformed shapes for first two deck torsion modes for composite KSM Bridge with lamina (3)

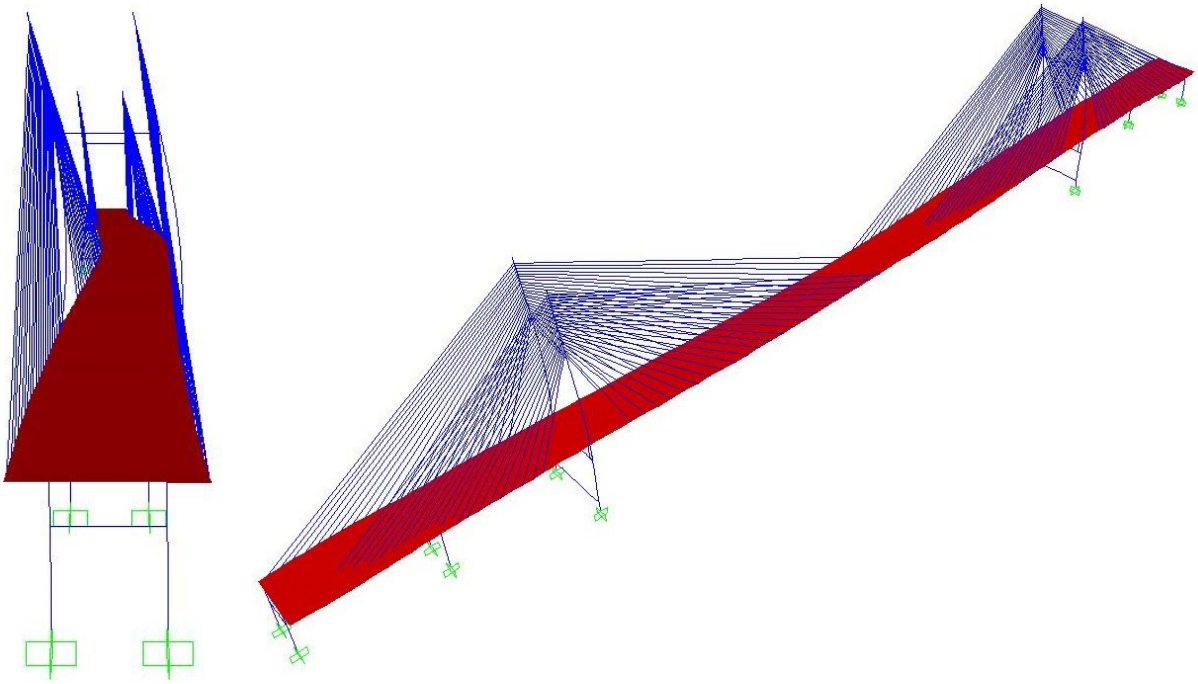

a) Mode shape 1: first deck lateral bending mode (0.5579 Hz)

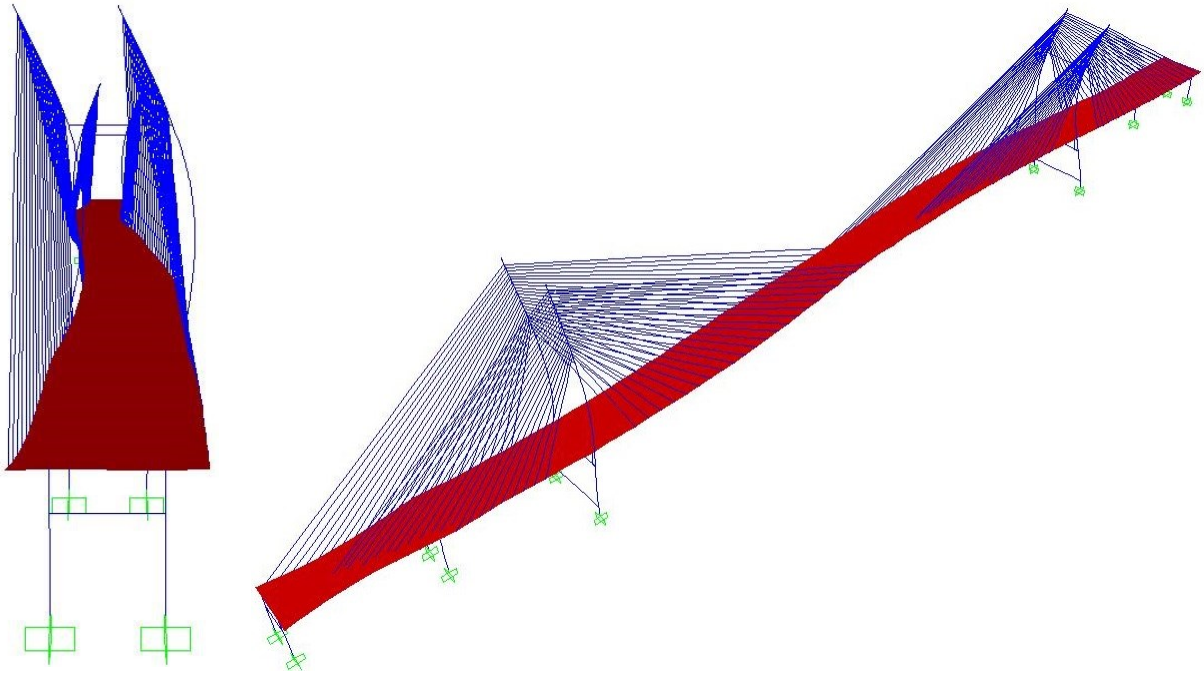

b) Mode shape 2: second deck lateral bending mode (1.0115 Hz)

Figure 5-28 The deformed shapes for first two deck lateral bending modes for composite KSM Bridge with lamina (3)

5.4.2. COMPARISON OF NATURAL FREQUENCIES

A brief comparison of the natural frequencies developed by Chan et al. (2013) for the original concrete deck model is included in Table 2-18. Also, a comparison with the original concrete FSM model reported by Naderian et al. (2015) as well as the laminated FRP deck model was taken into consideration. In this case, Table 5-12 compares the natural frequencies for all these four models into comparison. It is mentioned from the beginning that any small change in the modeling assumptions can significantly influence the natural frequencies or the order of occurrence of the vibration mode shapes. In Table 5-12, P stands for pylon swaying mode, B stands for bending mode, T stands for torsional mode, and L stands for the lateral mode of vibration.

Table 5-12 Comparison of natural frequencies between concrete bridge and hybrid FRP bridge

Mode No.	Original model (Hz) (Chan et al. 2013)	Mode Shape	FRP box girder model (Hz) (Chan et al. 2013)	Mode Shape	Original model (Hz) by IFSM (Naderian et al. 2015)	Mode Shape	Laminated FRP deck model (Hz) by LFSM	Mode Shape
1	0.40902	B	0.46053	B	0.2101	P	0.203	P
2	0.49862	P	0.50152	P	0.2406	P	0.2309	P
3	0.59413	B	0.65015	P	0.425	B	0.3413	B
4	0.659	P	0.69357	L	0.5184	L	0.4274	B
5	0.72181	L	0.73535	B	0.7524	T	0.5334	T
6	0.83962	T	1.0222	B	0.8516	B	0.5579	L
7	0.93887	B	1.1387	T	0.9258	L	0.6655	T
8	1.2509	P	1.2646	B	1.0018	B	0.7049	B
9	1.2527	L	1.3466	L	1.1381	P	0.8016	B
10	1.3673	P	1.3789	P	1.1391	P	0.9301	B
11	1.3771	P	1.3867	P	1.3409	T	0.9797	B
12	1.5224	T	1.5205	T	1.3532	L	1.0115	L
13	1.7022	T	1.6882	B	1.6523	B	1.026	B
14	1.7305	B	1.8154	L	1.7362	P	1.09	T
15	1.809	P	1.9654	T	1.8928	T	1.1371	B

To perform a more visualized comparison, these four models have been plotted in Figure 5-29. It is clear that they all have an increasing trend, however, the two frequencies magnitudes observed for the first two modes, which are about 0.4 Hz (Mode 1), 0.5 Hz (Mode 2) for the original and the FRP box girder models are almost double than those of the IFSM and the LFSM models which are 0.2 Hz (Mode 1), and 0.25 Hz (Mode 2) respectively. However, except for the first two modes, the

three types of bridges: Original Model, FPR Box-girder Model, and Original Mode by FSM have a very similar tendency and growth rate in the magnitudes of frequencies. The laminated FRP deck has a lower growth in the frequencies trend, recording much lower natural frequencies than the other bridge models.

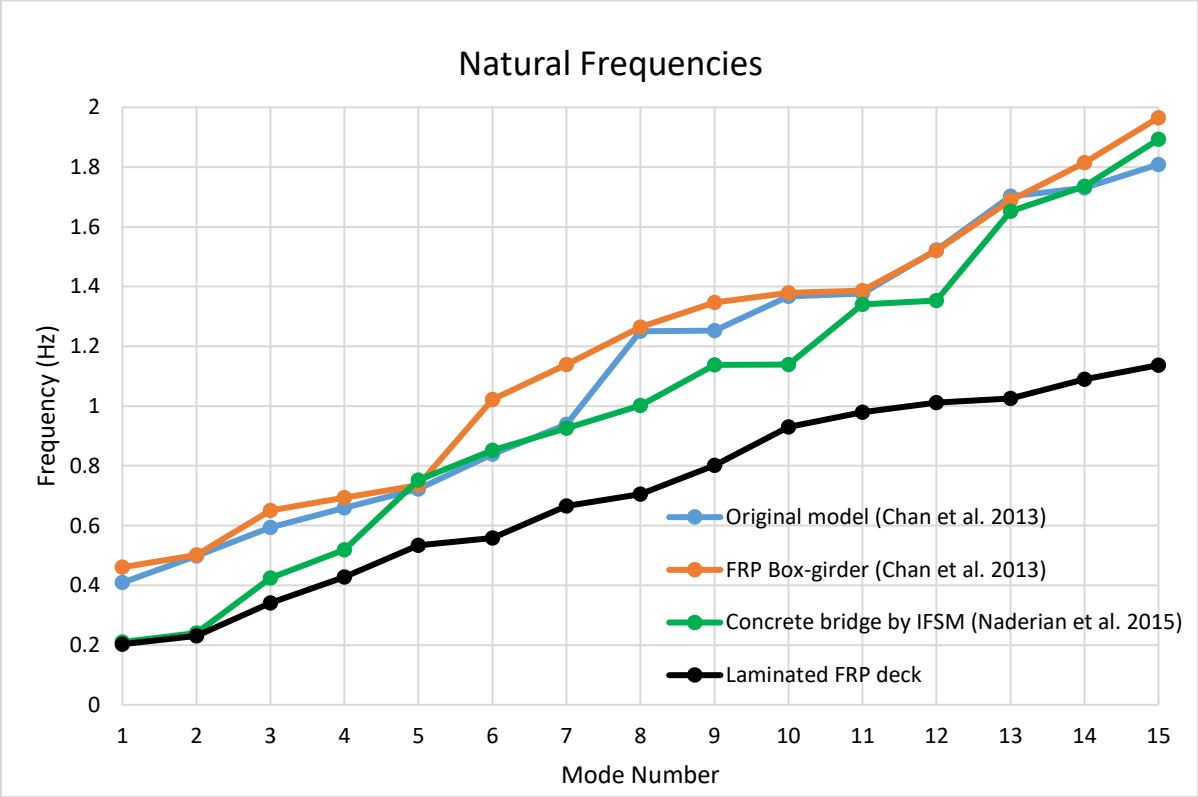

Figure 5-29 Comparison of natural frequencies for four types of bridges

Regardless of the magnitude of the natural frequencies, the concrete bridge has a similarly deformed shape compared with the LFSM-FRP bridge. Also, the specific mode shapes have a similar distribution of the natural frequencies, which can be found in Table 5-12. Therefore, Figure 5-30 gives a detailed comparison of the natural frequencies, depending on the four types of mode shapes encountered, between the original concrete Kap Shui Mun Bridge (Naderian et al. 2015) and the Laminated FRP bridge as shown in Figure 5-24. It should be noted that the Laminated FRP model above used the lamina (3) layout, which had a thickness of 1.02 m. This lamina model was selected because it was the single one who verified the maximum static deflection requirement as described by the bridge design codes. Other laminae models could have had a better agreement for the natural frequency of the entire bridge, as reported by Naderian (2017) who will perform a detailed study on the lamina (2) deck model, with 0.76 m thickness.

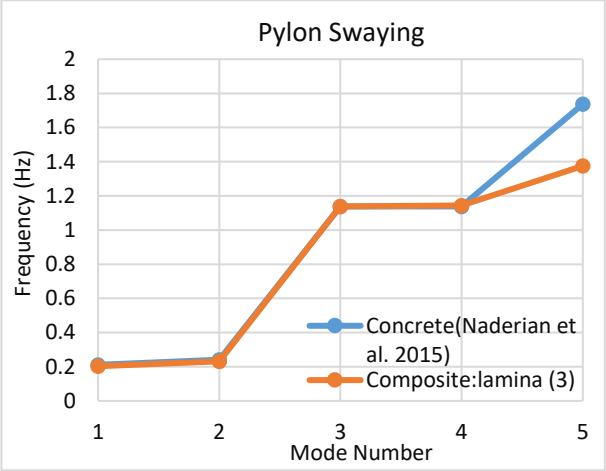

(a) Pylon swaying: First five modes

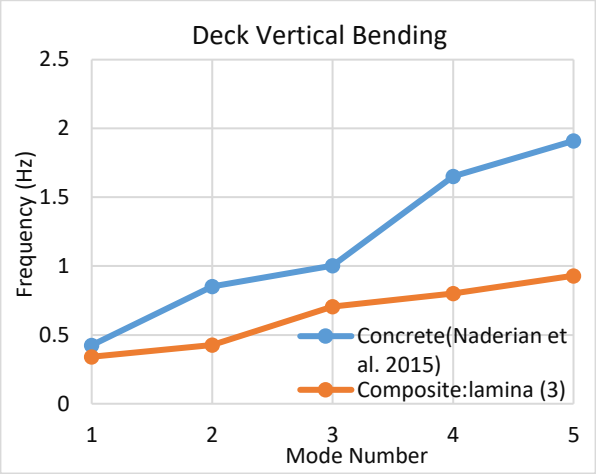

(b) Deck vertical bending: First five modes

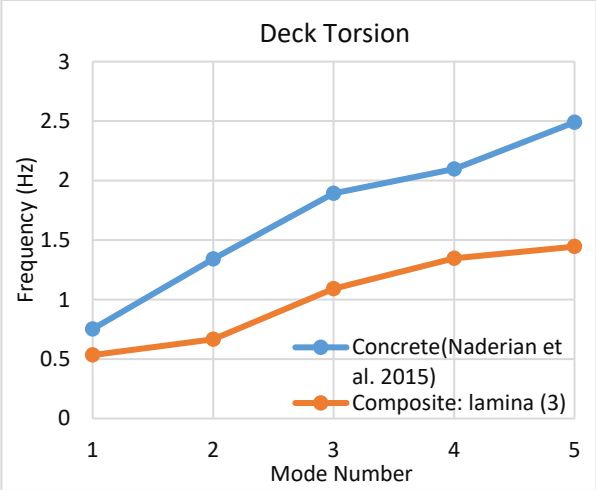

(c) Deck torsion: First five modes

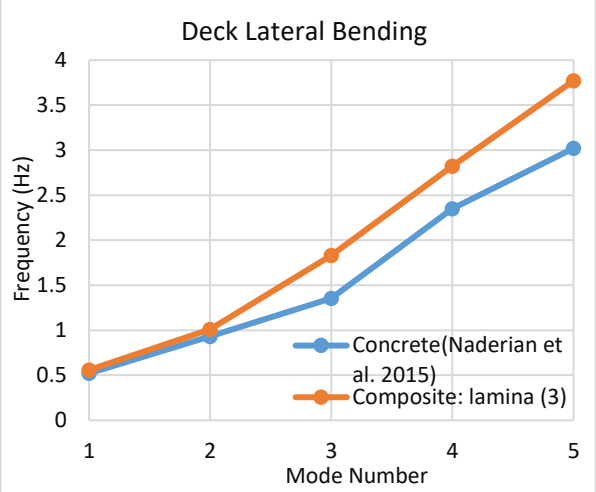

(d) Deck lateral bending: First five modes

Figure 5-30 Natural frequencies comparisons between concrete bridge and FRP bridge

It is noticed that the original Kap Shui Mun Bridge model always has larger natural frequencies for the vertical deck mode as well as the deck torsion modes, which proves that the laminated FRP bridge model has the lowest natural frequencies. As for the pylon swaying modes, they all have very similar frequencies for the first five modes. Furthermore, the deck lateral bending modes meet a different trend that the laminated FRP bridge is showing larger natural frequencies than the concrete one.

However, it had been proved in Chapter 3 that the FRP-Slab-girder Bridge model has a larger natural frequency than the FEM model because the total weight is reduced and the stiffness is increased with the adoption of the FRP materials. Thus, it was not expected that the laminated FRP

Cable-stayed bridge model would have the lowest natural frequencies. This means that the FRP bridge has large different dynamic behavior from the concrete bridge. When it comes to the long-span cable-stayed bridge, the original Kap Shui Mun Bridge has the largest total weight, the laminated FRP bridge has the total middle weight, and the FPR box-girder bridge has the smallest self-weight compared with them.

If the stiffness maintains a constant value, then the natural frequency increase with the decreasing of the total weight. Thus, it can be determined from the LFSM model, as well as from the comparison of the static deflection results, that the laminated FRP bridge has the lowest stiffness, after the FRP box-girder bridge, and the original Kap Shui Mun Bridge has the largest stiffness. In this case, it cannot be solved that because of the lowest stiffness as well as the medium self-weight, the laminated FRP bridge has a lower natural frequency. However, it does not mean that it has a bad dynamic behavior or it is not capable enough to sustain the seismic excitations even the aerodynamic excitations. In this case, time history domain and frequency domain analyses would provide more details. Since all the frequency domain analyses are transformed from the time domain, time domain analyses have been completed, and figures are plotted in Appendix D. Moreover, to determine the dynamic behavior for the laminated FRP bridge, frequency domain analysis is strongly suggested to apply different seismic excitations, with differing frequency characteristics, as it will be demonstrated in the next Chapter. Both the time history domain and frequency domain analyses are all developed for the composite Kap Shui Mun Bridge with the laminated FRP deck: lamina (3), 1.02m.

CHAPTER 6. FREQUENCY DOMAIN ANALYSIS FOR COMPOSITE LONG-SPAN CABLE-STAYED BRIDGES

Similar to the time history analysis, the frequency domain analysis is extremely depending on the accuracy of the natural frequency. It had been approved that the LFSM is exactly capable of developing the dynamic analysis including the free vibrations and time history that meet a wonderful agreement with FEM results. In Chapter 4, it had been approved that LFSM can produce the frequency domain analysis directly by using the PEM that was firstly used within the FS environment by Shen et al. (2013) for a Slab-girder Bridge and extended by the current author for the long-span cable-stayed bridge. This is because it can reduce the noise influence and errors efficiently than the Fourier Transform (FT) or Fast Fourier Transform (FFT).

However, in this chapter, Welch's Method was used to develop the frequency domain analysis in another approach that is transformed from the time domain analysis both for LFSM and FEM. This approach was selected because the calculation time required by the FEM is too long, especially for the wide frequency domain. Thus, this chapter introduces a new alternative for the numerical method employed in the LFSM environment, compared with FEM realized in SAP 2000 for the frequency domain analysis. The damping magnitude is still set as 0.02 which keep the natural frequency the same that can improve the results meet a great agreement between these two methods.

The current frequency domain analysis has concentrated on the response to uniform and nonuniform seismic excitations which were developed from the time domain analysis by using the Welch's Method, and the test signal was also selected as sinus wave. The basic time history MATLAB programs are built by Shen (2009) and Naderian et al. (2016) and were employed by the current author for the FRP bridge. Some case studies are performed for seismic analysis of FRP Kap Shui Mun Bridge using the time history domain method introduced in Chapter 3 within the LFSM environment and were included in Appendix D. The main objective of the current research is to establish a procedure for estimating the frequency domain analysis for the Laminated FRP bridge model, investigated by LFSM method.

Consequently, the LFSM can reduce the analytical time efficiently compared with FEM, especially for the same accuracy of the results. The unit of acceleration response for the time history is *g* which is equal to 9.81 m/s^2 for both input seismic excitations and time domain analysis results is detailed in Appendix D. In this case, the magnitude of time history acceleration response is proposed to be reduced by the factor 1/9.81. Therefore, the unit becomes $(m/s^2)/Hz$ for the PSD acceleration response. Otherwise, the units for the PSD would be g^2/Hz instead.

Similarly, the unit for the Log (PSD) figures is dB/Hz in Eq. (6-1) for the power expression.

$$PSD\left(dB/Hz\right)=10\log\left(PSD\left(g^2/Hz\right)\right) \tag{6-1}$$

The unit of displacement response is m^2/Hz for PSD and dB/Hz for Log (PSD).

To investigate the seismic response of FRP KSM bridge, some critical points as shown in Figure 6-1 which are different from the critical locations selected for the static analysis, are selected, and the frequency domain results are plotted for these locations. Since the cable-stayed bridge can be regarded as symmetric in both geometric and properties, point G on the deck, which is symmetric to point E is considered only once. Also, points C and D which are on the deck with vertical supports are also considered once because of the limit seismic response due to the supports on piers and tower.

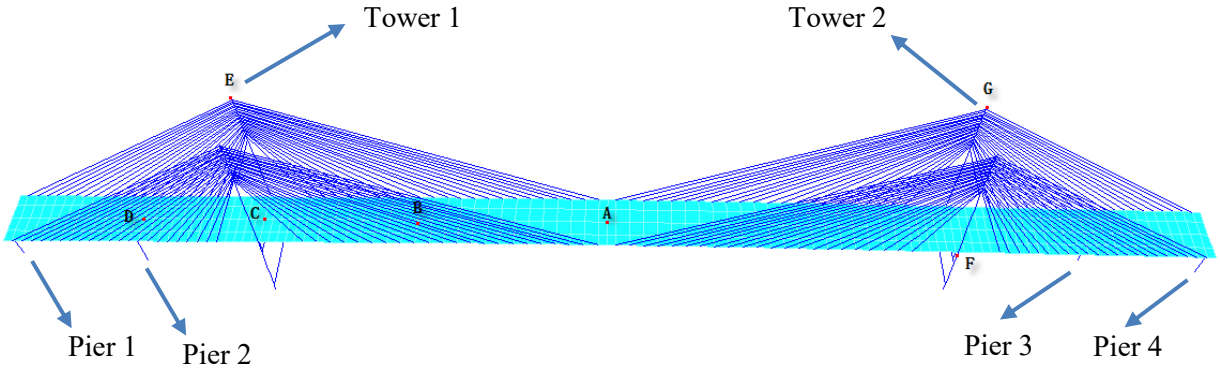

Figure 6-1 Critical points for seismic response investigation (Adapted from Naderian et al. 2016)

6.1. UNIFORM EXCITATION

As the simplest case, all the degrees of freedom in the corresponding direction vibrate under the same ground motion. An artificial sine wave and a real seismic wave are applied to the FRP Kap Shui Mun Bridge. Moreover, for the uniform excitation, not only the LFSM results are investigated, but also FEM model developed by the SAP 2000 is also studied as a validating reference for the currently reported results. The power spectrum density (PSD) plots are used to analyze the powers and the frequencies of the proposed bridges, and the Log (PSD) is used to determine the accuracy of the results when comparing the outcomes from the two methods, FEM and LFSM.

6.1.1. UNIFORM SINE WAVE EXCITATION

Firstly, a uniform ground motion sine wave acceleration is applied, and the acceleration and displacement acceleration output results at points A, D on the deck and F on the towers, are shown in Figure 6-2 to Figure 6-3. Only the first 50 vibration modes out of the 300 models investigated were plotted for improving the data visibility reported in these graphs.

In terms of the PSD of the longitudinal response at point F on the tower, as shown in Figure 6-2, the two methods LFSM and FEM yielded the same dominant frequency of 1.025 Hz, for both acceleration and displacement responses, corresponding to the mode 13 of the natural frequencies, which is a deck bending mode. The FEM had the natural frequency of 1.01 Hz for the mode 13. However, the PSD results for the displacement and acceleration have locked on the same frequency as the LFSM model, thus showing an acceptable agreement between these two methods. As it is clearly shown, the PSD energy content estimated by LFSM has a larger power, compared with the FEM (about 1.5 times of FEM), which can also be noticed for Log (PSD).

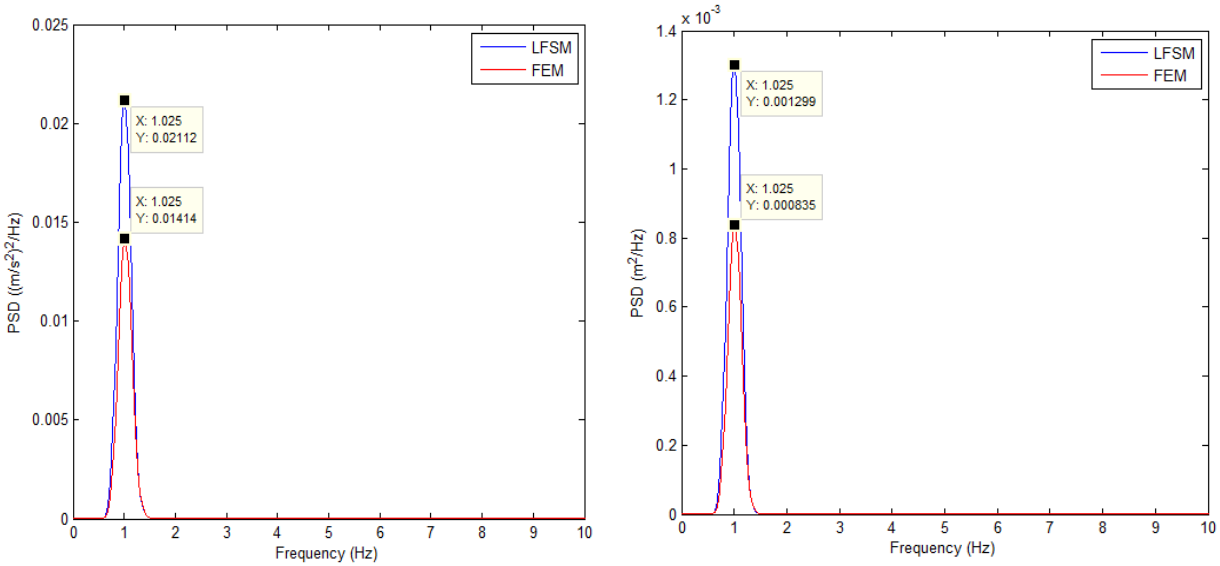

a) Longitudinal Acceleration Responses at Point F (PSD)

b) Longitudinal Displacement Responses at Point F (PSD)

Figure 6-2 PSD of the longitudinal acceleration and displacement response at point F under the uniform sine wave excitation ground motion

Also, it can be found that the two methods meet a very acceptable agreement for the Log (PSD) responses as shown in Figure 6-3, especially in the smaller frequency range. As expected the application of the artificial sine wipes multiple frequencies, as noticed after the dominant frequency in Figure 6-3, but none of these have a dominant energy content. Thus these cannot determine large dynamic responses for this branch.

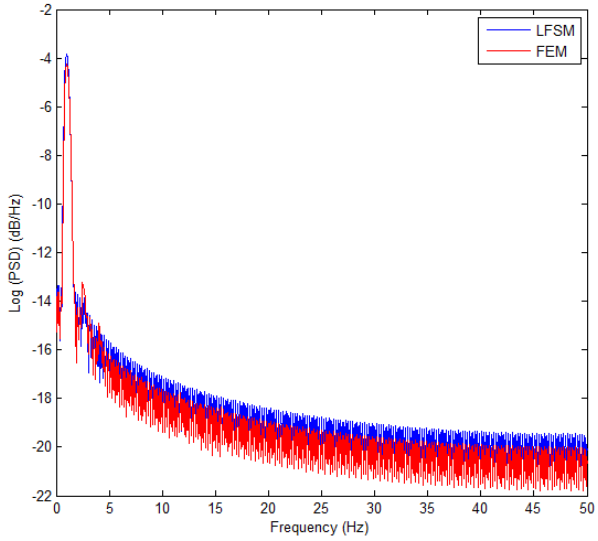

a) Longitudinal Acceleration Responses at Point F (Log PSD)

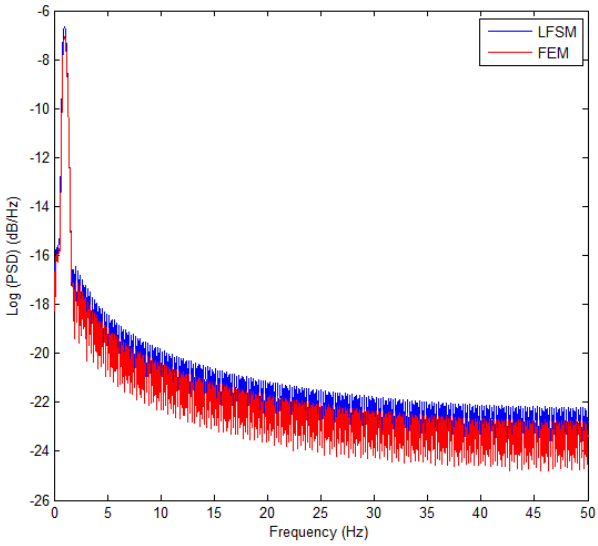

b) Longitudinal Displacement Responses at Point F (Log PSD)

Figure 6-3 Log (PSD) of the longitudinal acceleration and displacement response at point F under the uniform sine wave excitation ground motion

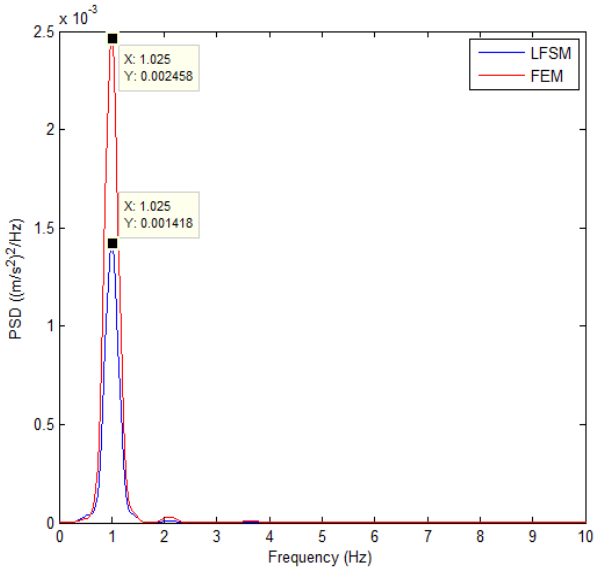

a) Transverse Acceleration Responses at Point D (PSD)

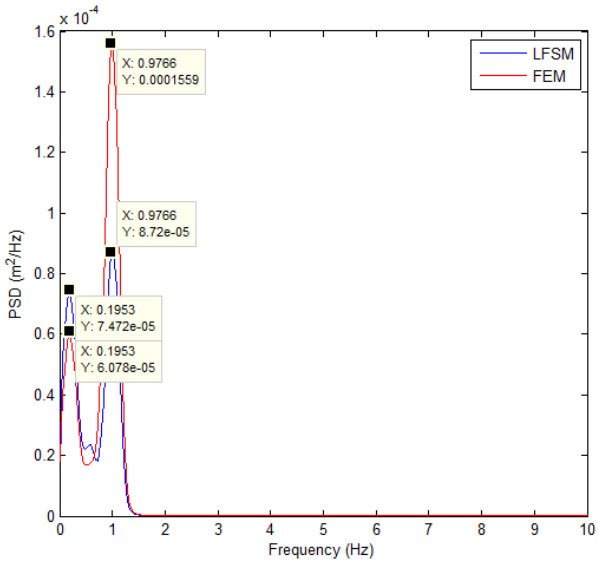

b) Transverse Displacement Responses at Point D (PSD)

Figure 6-4 PSD of the transverse acceleration and displacement response at point D under the uniform sine wave excitation ground motion

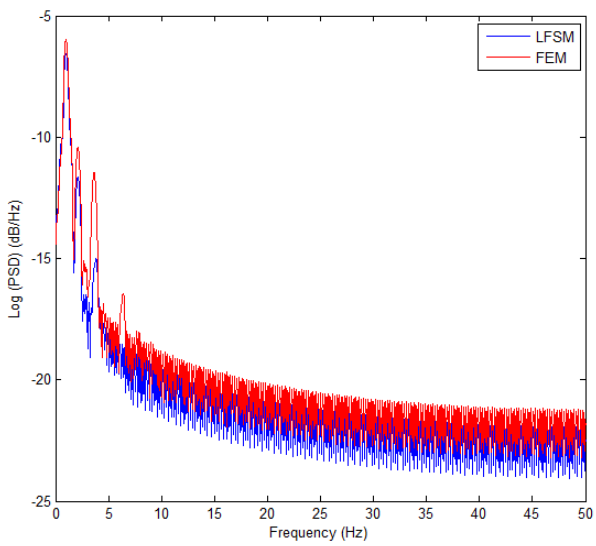

a) Transverse Acceleration Responses at Point D (Log PSD)

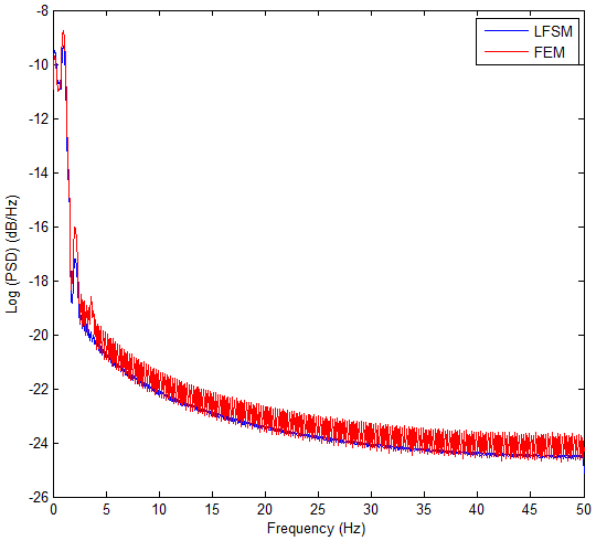

b) Transverse Displacement Responses at Point D (Log PSD)

Figure 6-5 Log (PSD) of the transverse acceleration and displacement response at point D under the uniform sine wave excitation ground motion

When considering the PSD of the transverse response at point D on the deck (Figure 6-4) where the pier supported is located, the acceleration response had only one dominant frequency at 1.025 Hz that corresponds to the same mode 13 from the natural frequency modes. However, the displacement response has a more complicated pattern registering two peaks, one at a minimum frequency of 0.1953 Hz and the second one at the maximum frequency of 0.9766 Hz, which are mode 1, as the sway mode of the tower and mode 12, as the bending mode of the deck, of the free vibration analysis, respectively. This means that the two models, with the proposed deformed shapes, can significantly affect the response to point D when the transverse uniform sine wave excitations are applied. Moreover, FEM always had a larger energy power magnitude for both the acceleration and displacement responses. Regarding the Log (PSD) represented in Figure 6-5, the displacement response seems to have smaller and fewer frequency windows, when compared with the acceleration response, which means the LFSM model is more reliable for the displacement response. In the corresponding time history response for point D, the maximum acceleration is 0.5 g that reached by FEM at about 1.5s, and for the displacement response, the maximum displacement is 0.018m at 14s both for LFSM and FEM.

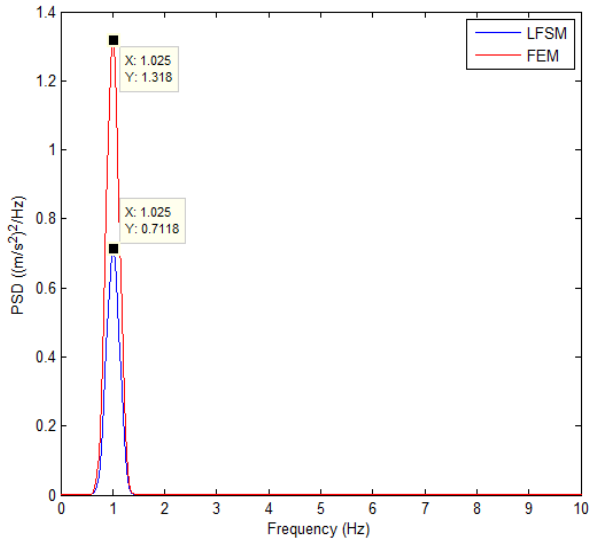

a) Vertical Acceleration Responses at Point A (PSD)

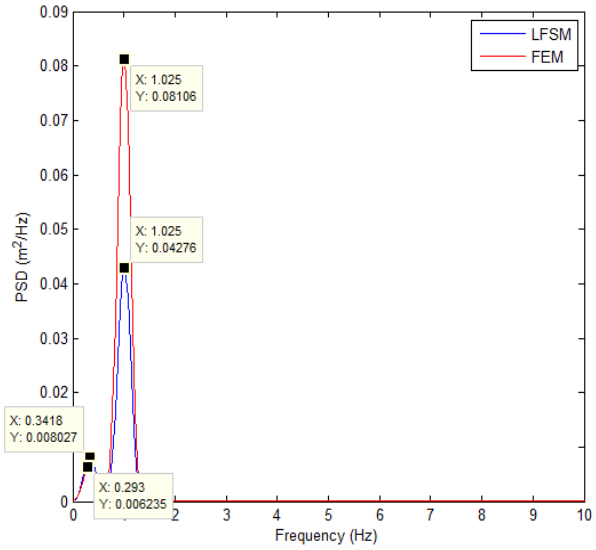

b) Vertical Displacement Responses at Point A (PSD)

Figure 6-6 PSD of the vertical acceleration and displacement response at point A under the uniform sine wave excitation ground motion

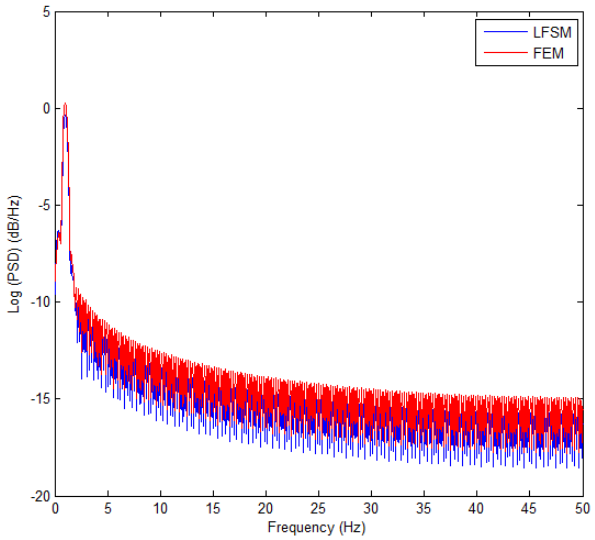

a) Vertical Acceleration Responses at Point A (Log PSD)

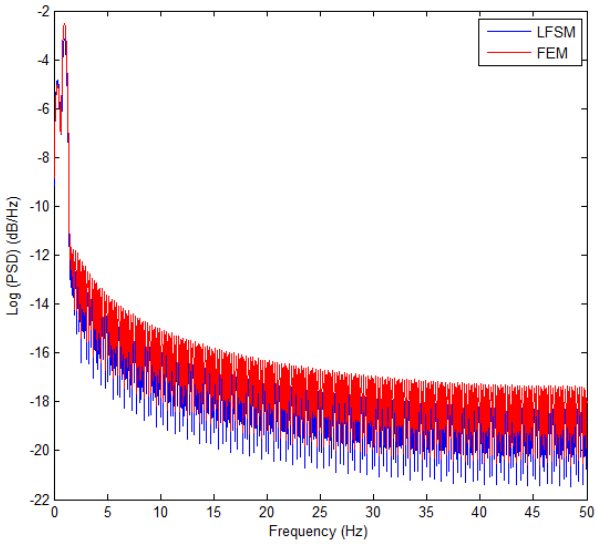

b) Vertical Displacement Responses at Point A (Log PSD)

Figure 6-7 Log (PSD) of the vertical acceleration and displacement response at point A under the uniform sine wave excitation ground motion

Point A which is situated in the middle of the main span of the deck, can be considered as a critical point and is very important to be investigated. Similarly to the longitudinal response of point F, for point A, 1.025 Hz is the only dominant frequency that can be identified in the PSD of Figure

6-6. Regarding the displacement PSD response, smaller frequencies of 0.293 Hz for FEM, and 0.3418 Hz for LFSM were identified, which correspond to the mode 3, which is a deck bending mode, in the natural frequency analysis. This means the PSD of the displacement under vertical uniform sine wave excitation can cause higher dynamic responses at the smaller frequencies. Regarding Log (PSD) response (Figure 6-7), it seems that both methods the LFSM and the FEM are estimating very reasonable results, especially within the first 2.0 Hz.

6.1.2. UNIFORM CHICHI EARTHQUAKE EXCITATION

The sine wave is not an existing earthquake but is just a theoretical signal used to simulate the real ground excitations. Therefore, the uniform ground motion as an applied acceleration. The Chichi earthquake that is a real earthquake wave happened in Taiwan had applied to the Slab-girder Bridge as shown in Figure 4-34 is assigned to all degrees of freedom of the bridge in a certain direction. Furthermore, the PSD of Chichi earthquake ground motion (Figure 4-34 b)) were assigned to all the degrees of freedom of the bridge in a transverse direction. Typically, the acceleration of Chichi earthquake represents the input to the LFSM model that was adapted based on the FSM algorithm coded in MATLAB, and the PSD of the Chichi earthquake was applied on the FRP bridge in the FEM model created in SAP 2000. However, because the same theoretical basis called Welch's Method was used by the FE method, the same analysis approach was adopted for the LFSM model. The responses from three points: B, C on the deck, and E on the tower, are shown in Figure 6-8 to Figure 6-13.

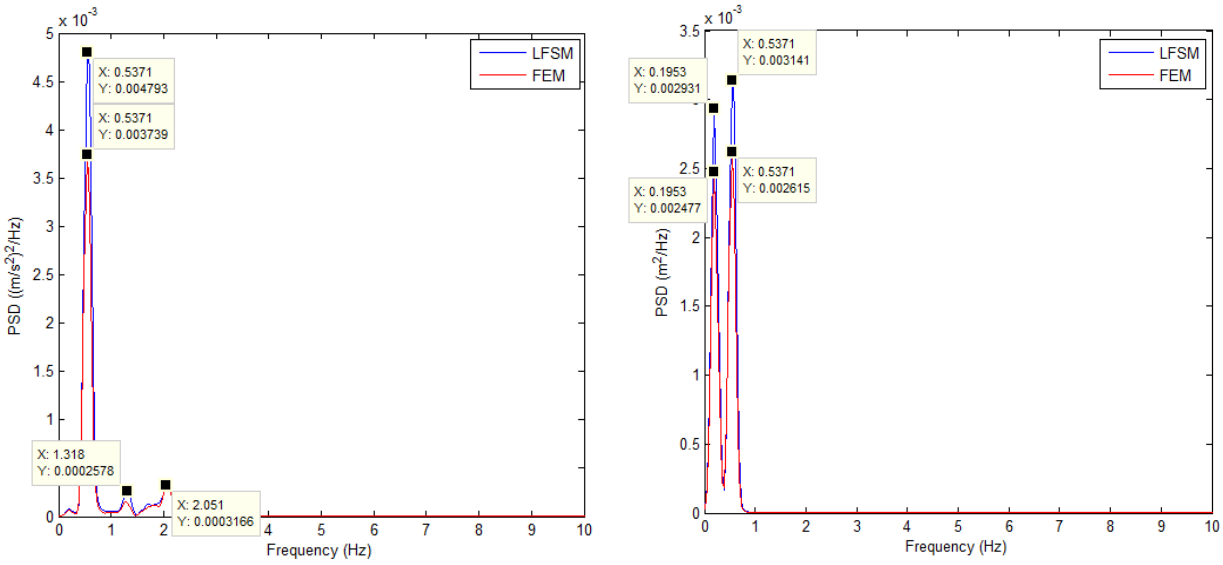

a) Transverse Acceleration Responses at Point B (PSD)

b) Transverse Displacement Responses at Point B (PSD)

Figure 6-8 PSD of the transverse acceleration and displacement response at point B under the uniform Chichi earthquake excitation ground motion

Three transverse acceleration frequency peaks of 0.5371 Hz (model 5), 1.318 Hz (model 20), and 2.051 Hz (model 41) were selected and were found to be the first three effective frequencies in the PSD plot (Figure 6-8). However, the displacement response has shown only two dominant frequencies 0.1953 Hz (model 1), and 0.5371 Hz (model 5) which are considered as the two most effective frequencies caused by the transverse uniform Chichi earthquake excitations.

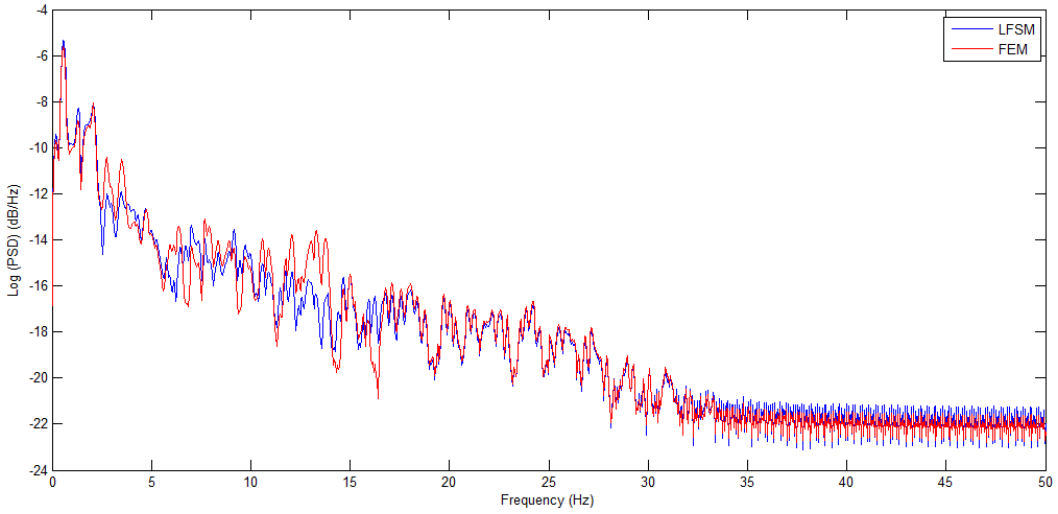

a) Transverse Acceleration Responses at Point B (Log PSD)

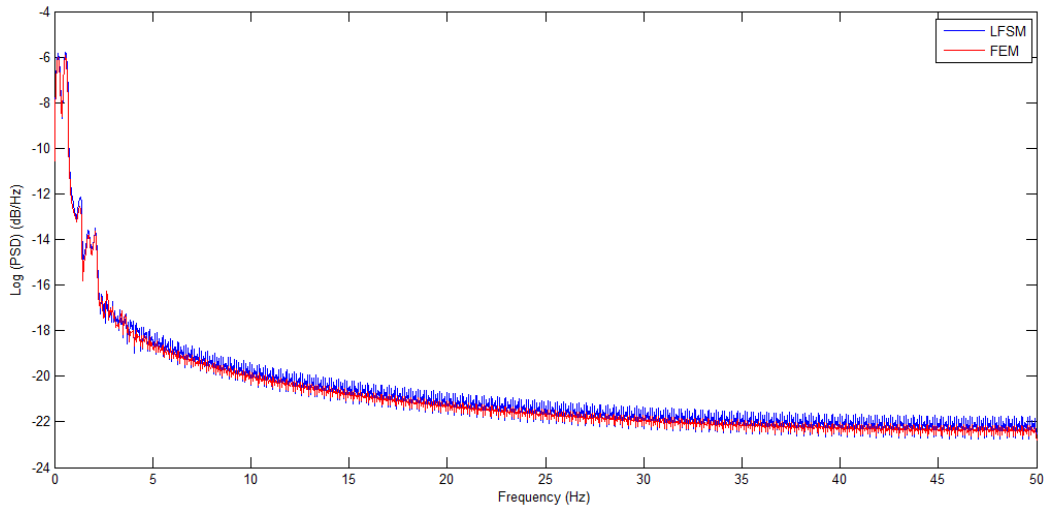

b) Transverse Displacement Responses at Point B (Log PSD)

Figure 6-9 Log (PSD) of the transverse acceleration and displacement response at point B under the uniform Chichi earthquake excitation ground motion

Regarding the Log (PSD) plots (Figure 6-9), the acceleration and displacement frequency responses meet a very acceptable agreement between the two approaches LFSM and the FEM,

except for the slight difference noticed in the first 17 Hz of the acceleration response where the FEM has higher energy content response. However, a very similar trend was noticed when compared with the LFSM response, regarding the frequencies loops.

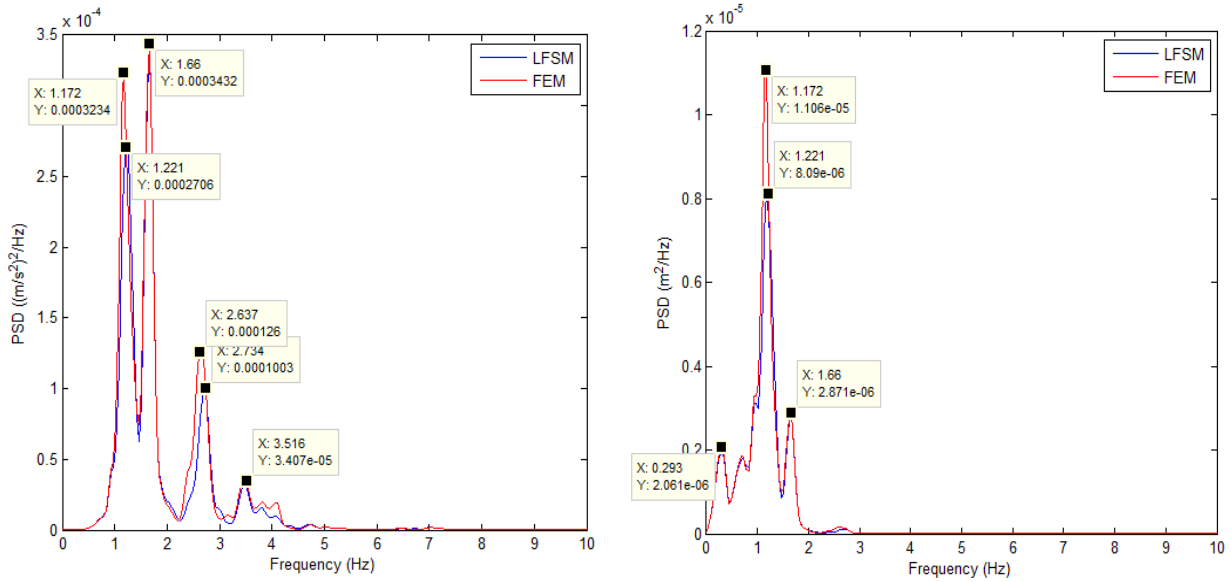

a) Longitudinal Acceleration Responses at Point C (PSD)

b) Longitudinal Displacement Responses at Point C (PSD)

Figure 6-10 PSD of the longitudinal acceleration and displacement response at point C under the uniform Chichi earthquake excitation ground motion

A total of four dominant frequencies 1.172 Hz, 1.66 Hz, 2.637 Hz, and 3.516 Hz are dominant frequencies for FEM. As for LFSM, 1.211 Hz (model 19), 1.66 Hz (model 27), 2.734 Hz (model 44), and 3.516 Hz (model 61) are regarded as the dominant frequencies in the PSD (Figure 6-10 a)) for the acceleration response. In terms of displacement PSD response, only three dominant frequencies were found in the PSD of the longitudinal displacement response, which are 0.293 Hz, 1.172 Hz, and 1.66 Hz (model 27) for FEM, and 1.172 Hz, 1.221 Hz (model 19), and the same third peak at 1.66 Hz (model 27) for LFSM. The last two dominant frequencies are equal to the first two frequencies in the acceleration PSD response which means a stronger dynamic response could be associated with these frequencies.

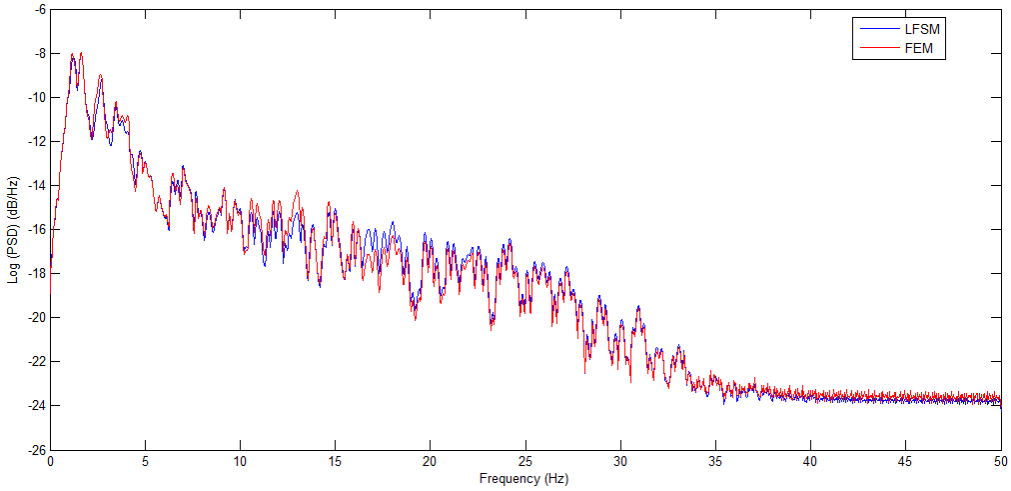

a) Longitudinal Acceleration Responses at Point C (Log PSD)

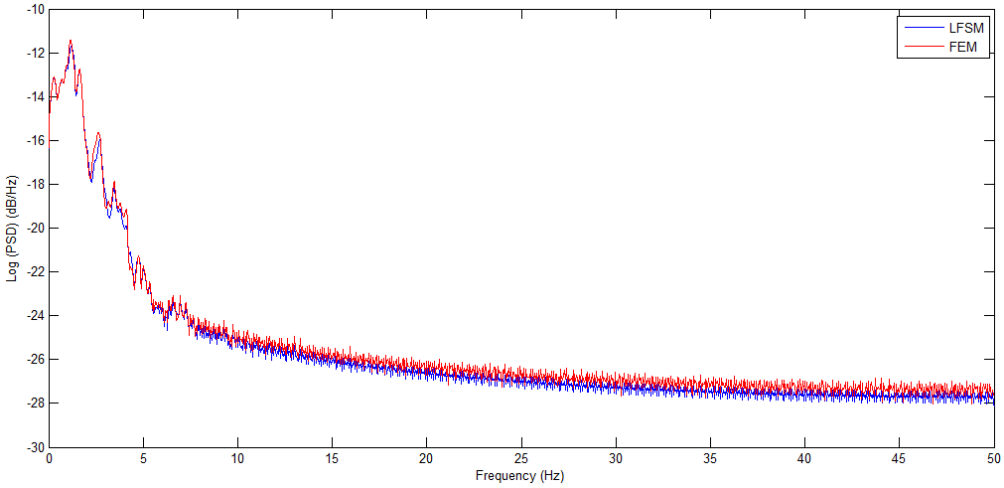

b) Longitudinal Displacement Responses at Point C (Log PSD)

Figure 6-11 Log (PSD) of the longitudinal acceleration and displacement response at point C under the uniform Chichi earthquake excitation ground motion

When considering the Log (PSD) for both LFSM and FEM, it can be noticed that they have no difference regardless of the range of the frequencies target, for small frequency domain but also for larger frequency domain up to 50 Hz as shown in Figure 6-11. The frequency peaks identified in the PSD acceleration and displacement frequency responses are also registered in the Log (PSD) responses as dominant frequencies, as expected.

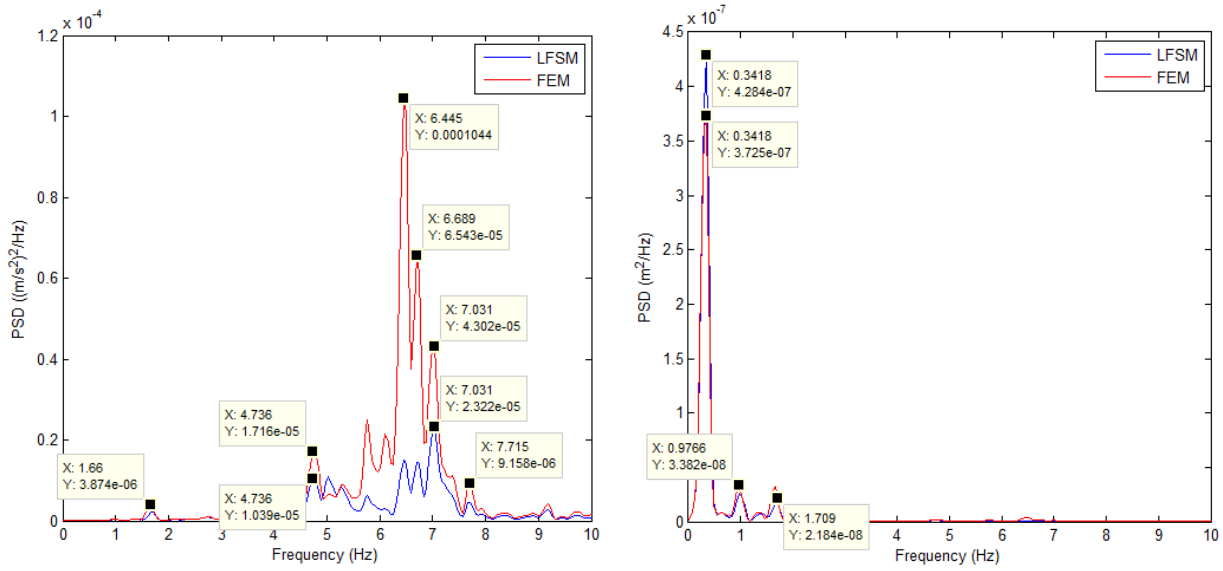

a) Vertical Acceleration Responses at Point E (PSD) b) Vertical Displacement Responses at Point E (PSD)

Figure 6-12 PSD of the vertical acceleration and displacement response at point E under the uniform Chichi earthquake excitation ground motion

The performance of LFSM for the vertical acceleration and displacement responses, as shown in the PSD plot in Figure 6-12 seems to have a bigger difference when compared with the FEM estimated responses. However, they have the similar tendency. Also, the large difference in response magnitudes can be found in the time history response for accelerations and displacements registered at point E, that can be found in Appendix D. This discrepancy could be due to the noise data which was not filtered out and some errors induced by the vertical modes of the bridge. Since the critical point, E is located on top of the tower and not on the deck, the recorded signal is much more sensitive to both vertical vibration of the deck and swaying vibration of the tower that may contain different frequency components. Also in the Log (PSD) of acceleration shown in Figure 6-13, it can be noticed that the last 10 Hz had a bigger difference between the LFSM and FEM methods. However, the PSD of the displacement response had a very acceptable agreement, for both methods, extending beyond the three dominant frequencies of 0.3418 Hz (model 3), 0.9766 Hz (model 11), and 1.709 Hz (model 28) that can be significantly affected when applying the vertical earthquake excitations.

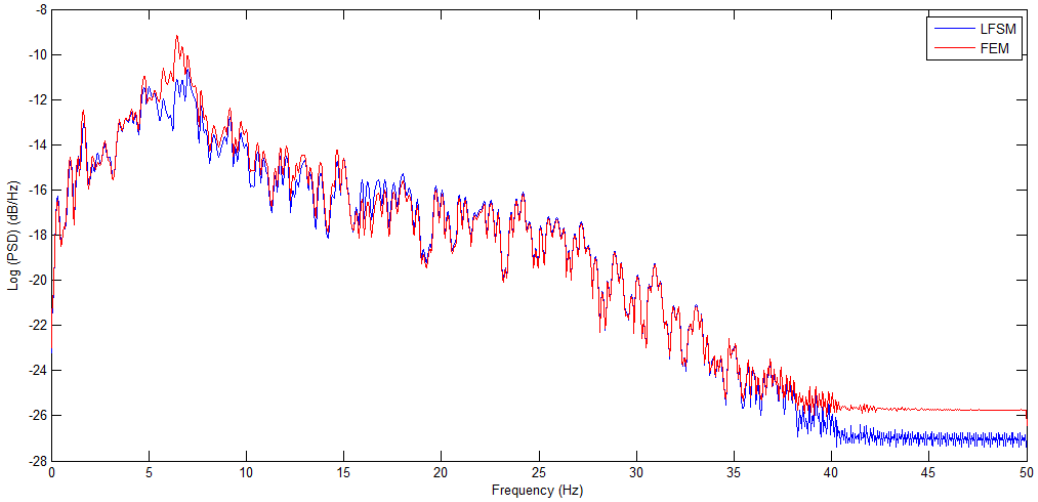

a) Vertical Acceleration Responses at Point E (Log PSD)

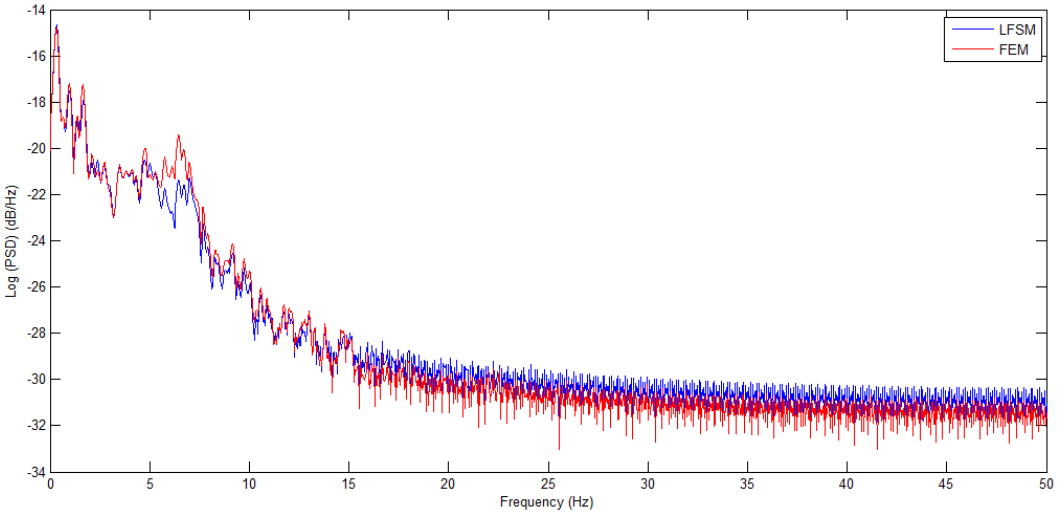

b) Vertical Displacement Responses at Point E (Log PSD)

Figure 6-13 Log (PSD) of the vertical acceleration and displacement response at point E under the uniform Chichi earthquake excitation ground motion

6.2. NONUNIFORM EXCITATION

When considering the application of the nonuniform excitation as a seismic loading for the FRP KSM cable-stayed bridge, different motions should be prescribed at different points, which are discussed in the following sub-sections. The advantages of using the frequency domain analysis stand out as the difficulty to perform the time history domain analysis for the long-span cable-stayed bridges because of the complicated modeling assumptions of the structure and the definition of the boundary conditions. Moreover, the computing time required for the SAP 2000 software is extremely long for simpler smooth frequency domain loading signals. Also, it has been determined

that the LFSM can perform the frequency domain analysis for uniform excitation loadings, with much shorter computation times, as previous results have shown. Therefore, LFSM is selected as the only and most capable approach to developing the time domain analysis under nonuniform excitations, as most of the cases tried in FEM did not achieve the convergence.

6.2.1. WAVE PASSAGE EFFECT

The Chichi earthquake wave is adopted as the input source, and the velocities of the earthquake waves are assumed to be 500 m/s and 1000 m/s in the longitudinal direction. The earthquake wave is assumed to be transmitted to Pier one first, and the ground motion will then be transmitted to the following towers and piers one by one. In the finite strip model, this is achieved by inputting the seismic waves with different time lags at the various supports. An earthquake wave with infinite velocity is also adopted, which means that there is no time lag when transmitting the seismic wave between different supports which is equivalent to uniform excitation.

The acceleration responses and the displacement responses at Point E located at the half of the middle span on the deck are presented in Figure 6-14 for different wave velocities. In the second case, the excitation is applied in the longitudinal direction, and the responses of point B on the tower are investigated. The results are shown in Figure 6-15.

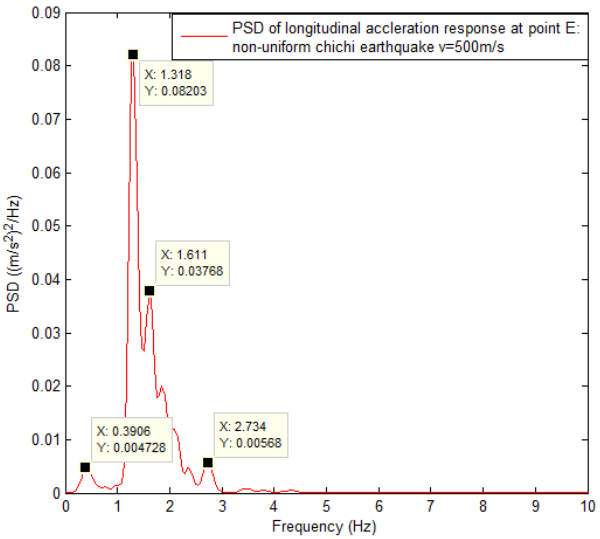

a) Longitudinal Acceleration Response at point E for velocity = 500 m/s (PSD)

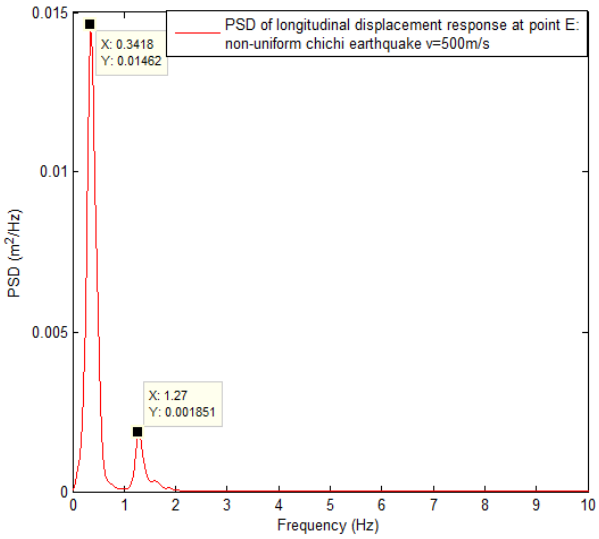

b) Longitudinal Displacement Response at point E for velocity = 500 m/s (PSD)

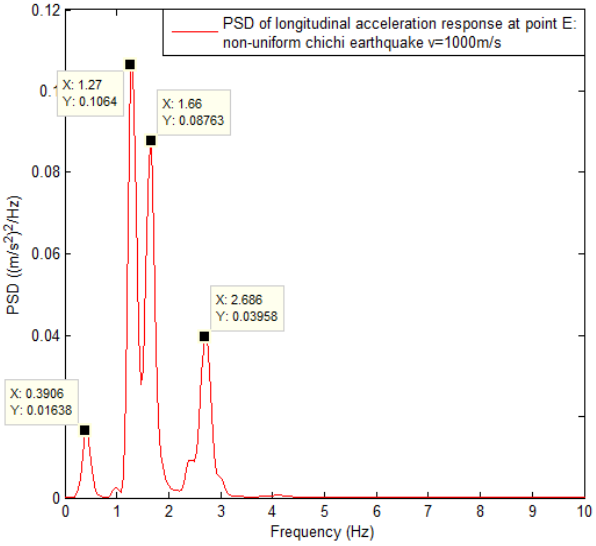

c) Longitudinal Acceleration Response at point E for velocity = 1000 m/s (PSD)

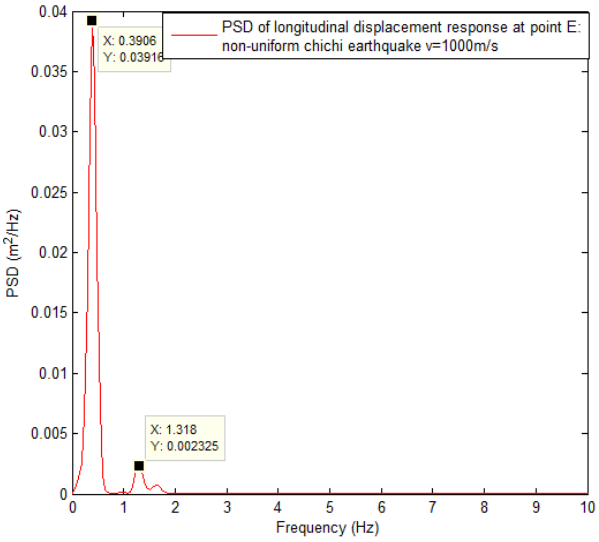

d) Longitudinal Displacement Response at point E for velocity = 1000 m/s (PSD)

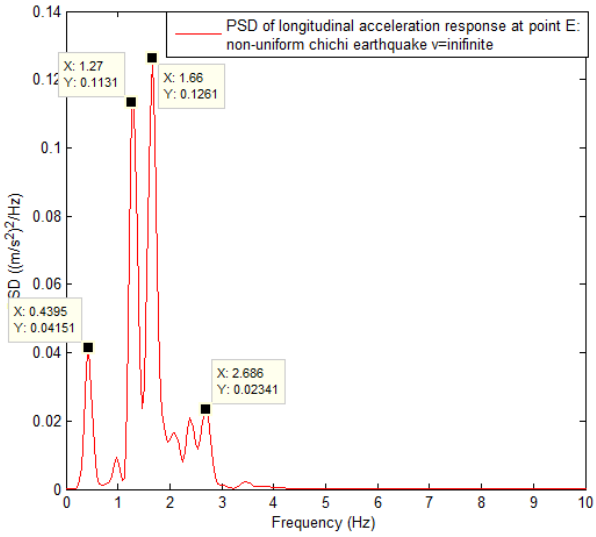

e) Longitudinal Acceleration Response at point E for velocity = infinite (PSD)

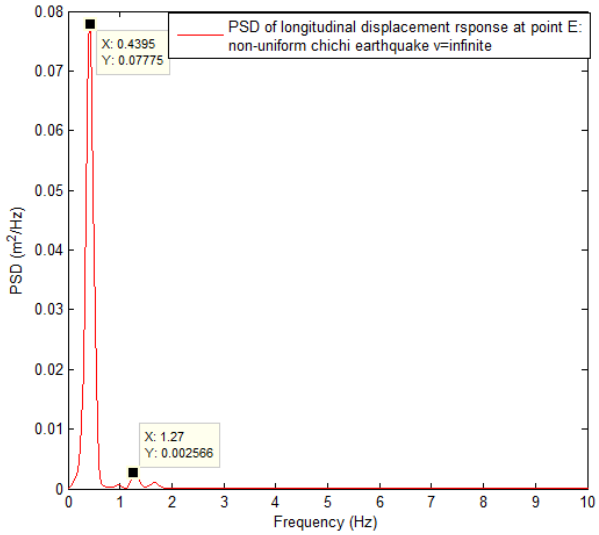

f) Longitudinal Displacement Response at point E for velocity = infinite (PSD)

Figure 6-14 PSD of the longitudinal acceleration and displacement response at point E under the nonuniform Chichi earthquake for wave passage effects

For the PSD of longitudinal acceleration response at point E (Figure 6-14), four dominant frequencies can be found in each case. The dominant frequencies are 0.3906 Hz, 1.318 Hz, 1.611 Hz, and 2.734 Hz for v=500 m/s; 0.3906 Hz, 1.27 Hz, 1.66 Hz, and 2.868 Hz for v=1000 m/s; 0.4395 Hz, 1.27 Hz, 1.66 Hz, and 2.686 Hz. All these dominant frequencies are not considered as corresponding to the natural frequencies because of the variable velocity of the seismic waves. However, 0.3906 Hz, 1.27 Hz, 1.66 Hz, and 2.686 Hz are the natural frequencies of the FRP-KSM

Bridge, which are the closest to the ones in PSD with the higher energy content. Regarding the displacement PSD response, the following three cases have the tendency of the response consistent with that of the first peak of vibration reached a very high energy content level and the second one which reached a much smaller energy value in PSD (Figure 6-14 b)). With the increase of the velocity, the minimum dominant frequencies start from 0.3418 Hz, 0.3906 Hz, to 0.4395 Hz and the maximum frequencies are 1.27 Hz for the velocities of the wave of v = 500 m/s and infinite (Figure 6-14 d)), while 1.318 Hz was registered for v = 1000 m/s (Figure 6-14 f)).

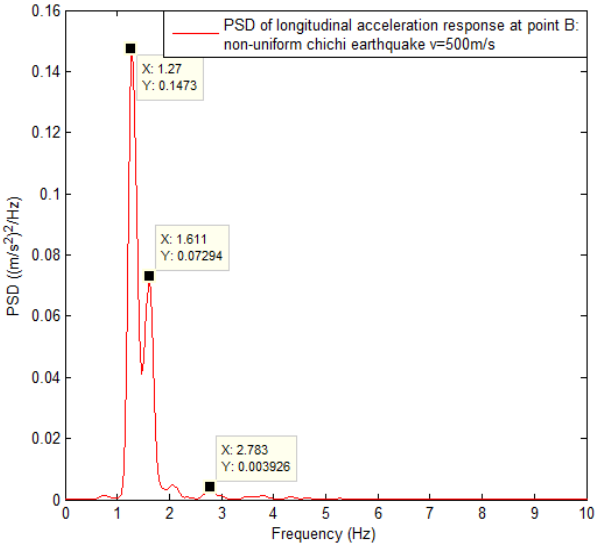

a) Longitudinal Acceleration Response at point B for velocity = 500 m/s (PSD)

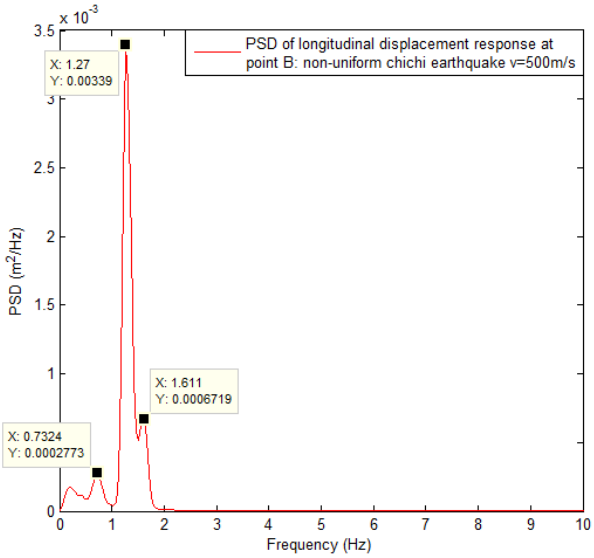

b) Longitudinal Displacement Response at point B for velocity = 500 m/s (PSD)

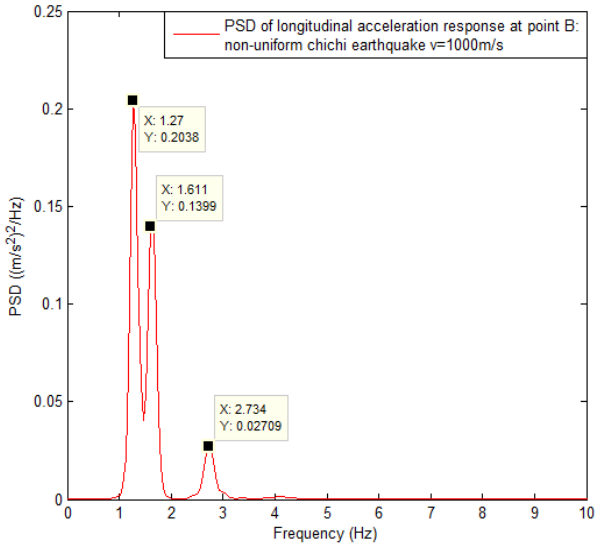

c) Longitudinal Acceleration Response at point B for velocity = 1000 m/s (PSD)

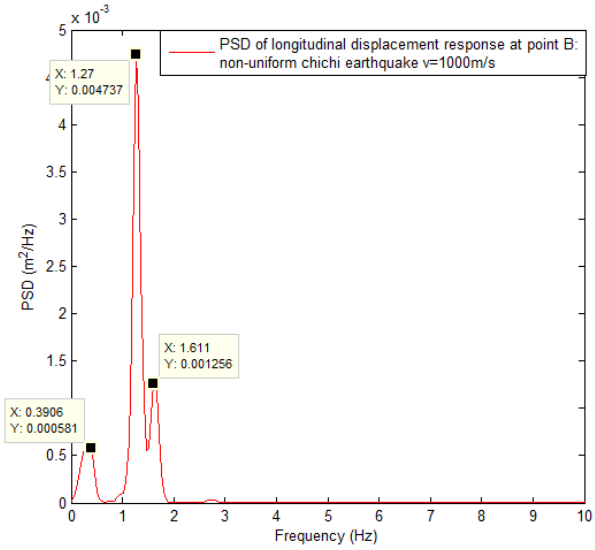

d) Longitudinal Displacement Response at point B for velocity = 1000 m/s (PSD)

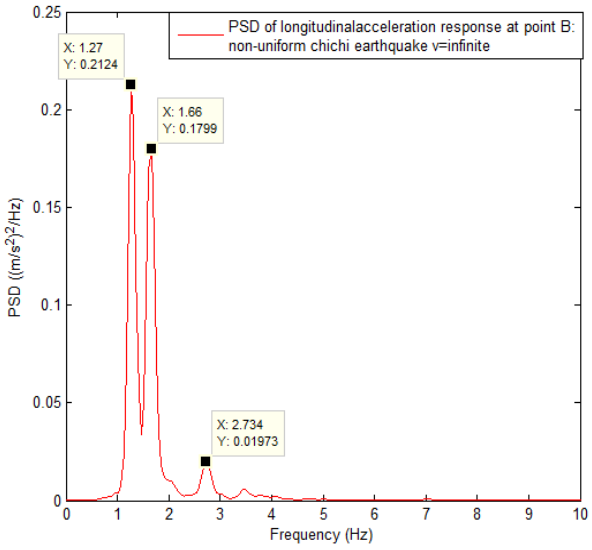

e) Longitudinal Acceleration Response at point B for velocity = infinite (PSD)

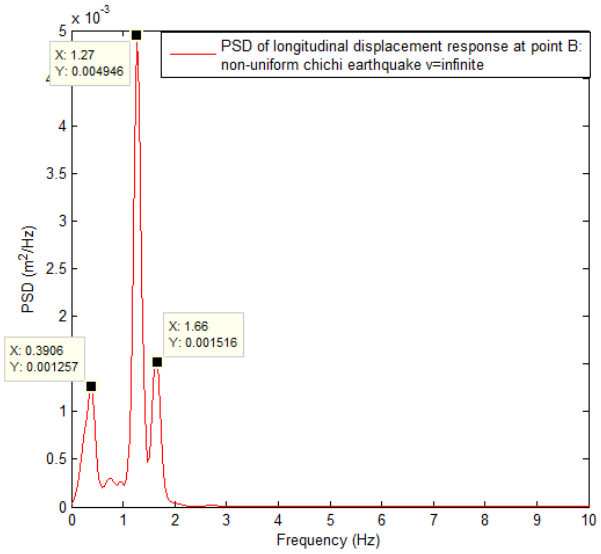

f) Longitudinal Displacement Response at point B for velocity = infinite (PSD)

Figure 6-15 PSD of the longitudinal acceleration and displacement response at point B under the nonuniform Chichi earthquake for wave passage effects

It is clear that for the PSD of the longitudinal acceleration response at point B (Figure 6-15), there are three dominant frequencies that are 1.27 Hz, 1.611 Hz, and 2.783 Hz for v = 500 m/s; 1.27 Hz, 1.611 Hz, and 2.734 Hz for v = 1000 m/s; 1.27 Hz, 1.66 Hz, and 2.734 Hz for v = infinite. These corresponding frequencies are very close to each other for different seismic wave velocities, and eventually, the PSD spikes show a compatible trend. Similarly, there are also three corresponding displacement PSD response dominant frequencies that are 0.7324 Hz, 1.27 Hz, and 1.611 Hz for v= 500 m/s; 0.3906 Hz, 1.27 Hz, and 1.611 Hz for v = 1000 m/s; 0.3906 Hz, 1.27 Hz, and 1.66 Hz for v = infinite. It is obvious that the last two frequencies correspond to the first two frequencies registered for the acceleration PSD, which gives more sensitive effects in the lower frequencies range when applying the earthquake excitations with variable wave velocities.

6.2.2. VARYING SEISMIC EXCITATION

In the time history method, the numerical results are highly dependent on the selected ground acceleration sample records. To investigate the dynamic behavior of a long span bridge under varying seismic excitation at the supports, the earthquake records from SMART-1 is used. The earthquake records in SMART-1 are the raw data observed at different places during the earthquake. Therefore, the records have already included the influences of the incoherence effect, attenuation effect and site effect. Two acceleration records observed at two places, at a distance 1000 m apart, are used. The first record components are applied to the vertical direction named vertically Input-1, and Input-2 as shown in Figure 6-16 (a) and (b). Identically, the second record

components are applied to the longitudinal direction named longitudinally Input-1, and Input-2 as shown Figure 6-16 (c) and (d).

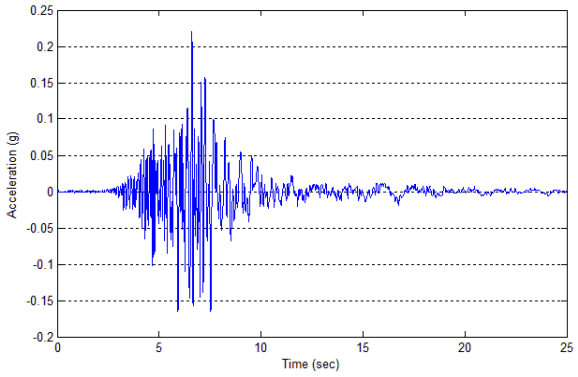

a) Vertical components of Seismic Wave: Input-1

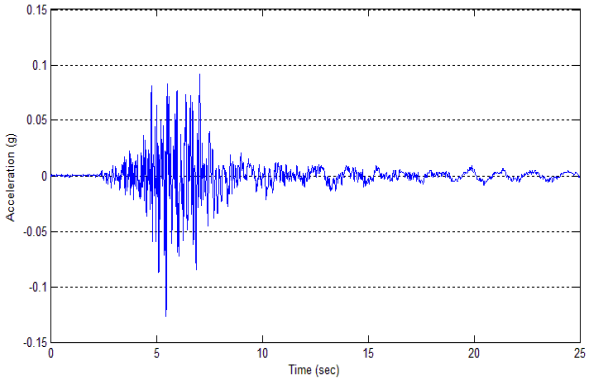

b) Vertical components of Seismic Wave: Input-2

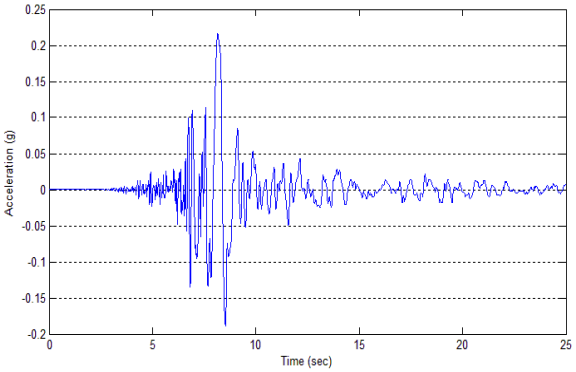

c) Longitudinal components of Seismic Wave: Input-1

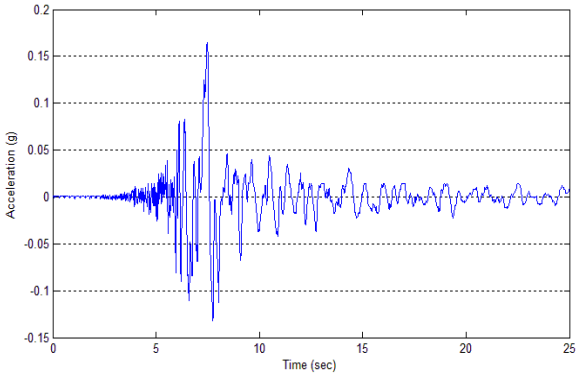

d) Longitudinal components of Seismic Wave: Input-2

Figure 6-16 The two directional components of Seismic Wave (Naderian et al. 2016)

Typically, three analysis cases are undertaken. In the first modes, Input-1 is assigned to all the bridge supports. Secondly, the Input-2 is assigned to all of the bridge's supports, respectively. In the third case, Input-1 is added to Pier 1, Pier 2 and Tower 1, while Input-2 is added to Pier 3, Pier 4 and Tower 2, and all the situations are uniform excitation, but they come to nonuniform excitations when mixed.

When it comes to the frequency domain analysis that transformed from the time domain, these acceleration signals can also be transformed to the PSD record by the Welch's Method. The first PSD of record components are applied to the vertical direction named vertically Input-1, and Input-2 as shown in Figure 6-17 (a) and (b). Identically, the second PSD of record components are

applied to the longitudinal direction named longitudinally Input-1, and Input-2 as shown in Figure 6-17(c) and (d).

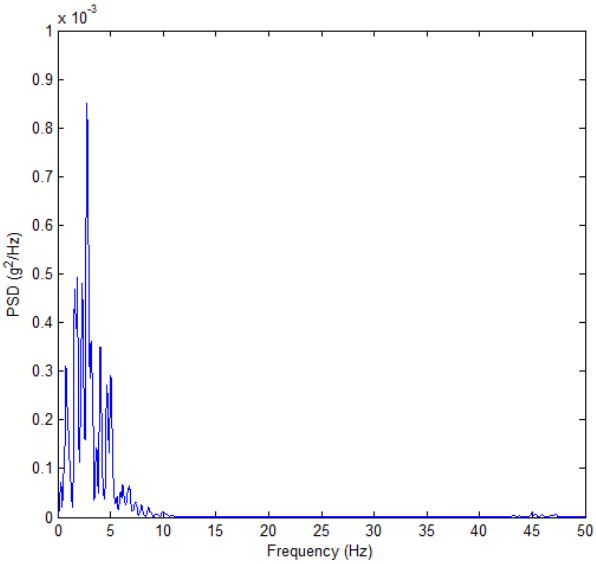

a) Vertical components of Seismic Wave: Input-1

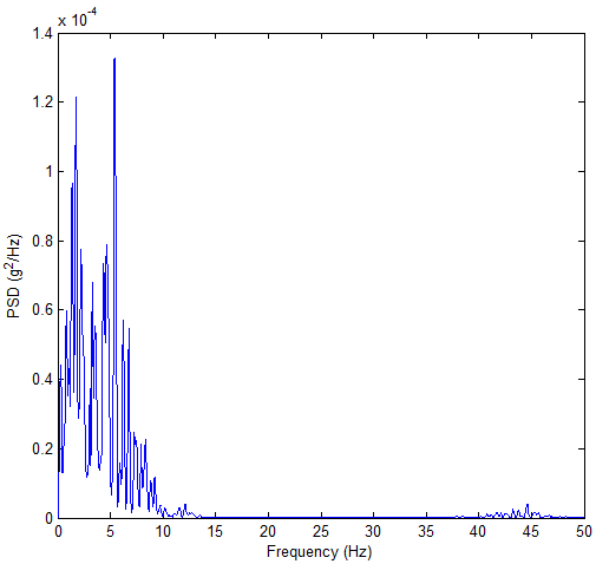

b) Vertical components of Seismic Wave: Input-2

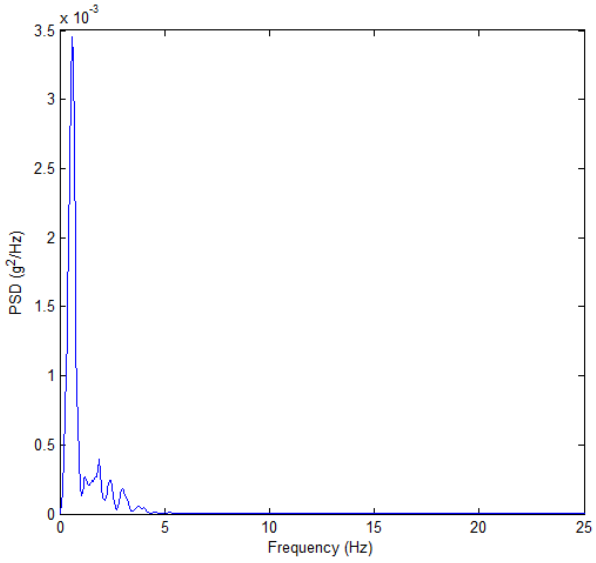

c) Longitudinal components of Seismic Wave: Input-1

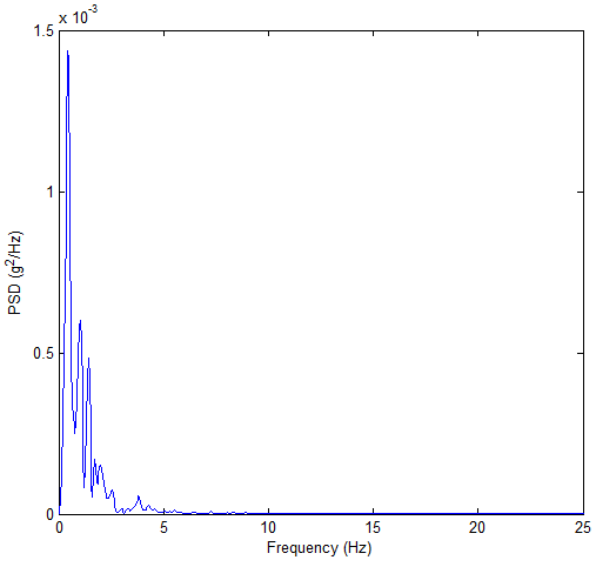

d) Longitudinal components of Seismic Wave: Input-2

Figure 6-17 PSD of the two directional components of Seismic waves

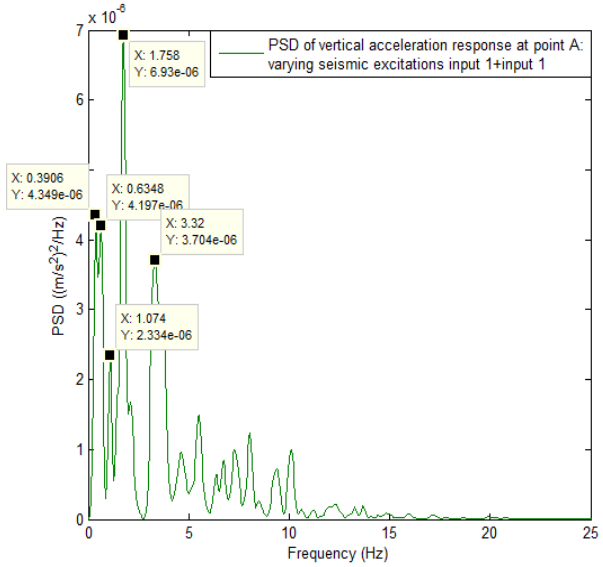

a) Vertical Acceleration Reponses at Point A: Input-1 + Input-1 (PSD)

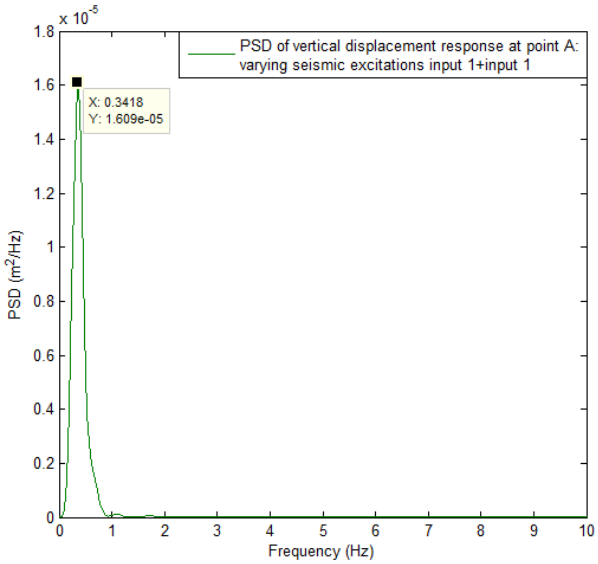

b) Vertical Displacement Reponses at Point A: Input-1 + Input-1 (PSD)

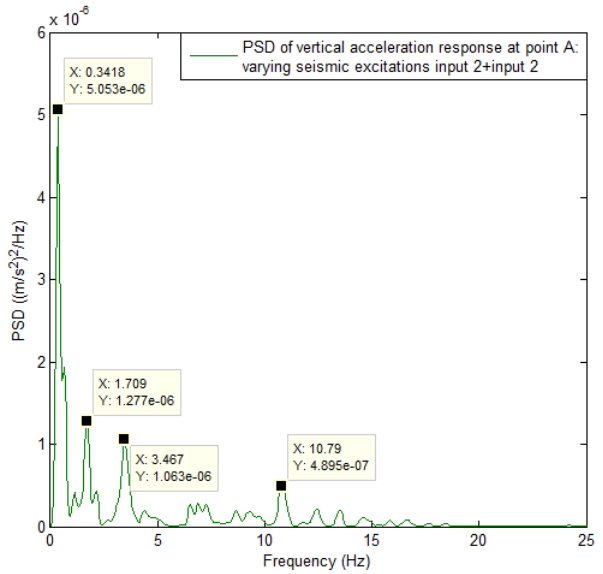

c) Vertical Acceleration Reponses at Point A: Input-2 + Input-2 (PSD)

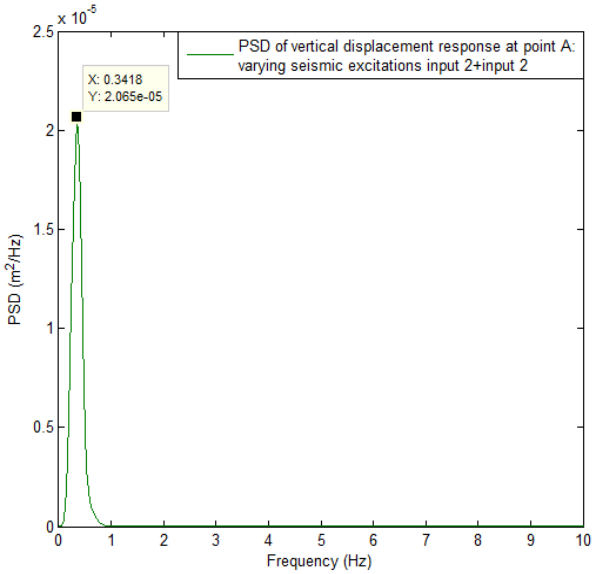

d) Vertical Displacement Reponses at Point A: Input-2 + Input-2 (PSD)

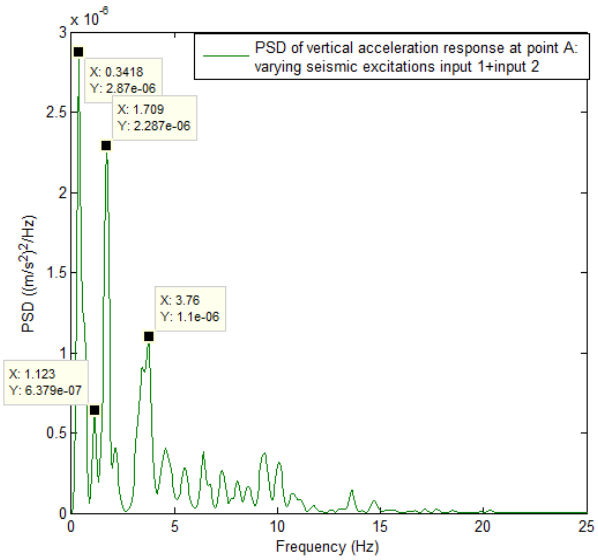

e) Vertical Acceleration Reponses at Point A: Input-1 + Input-2 (PSD)

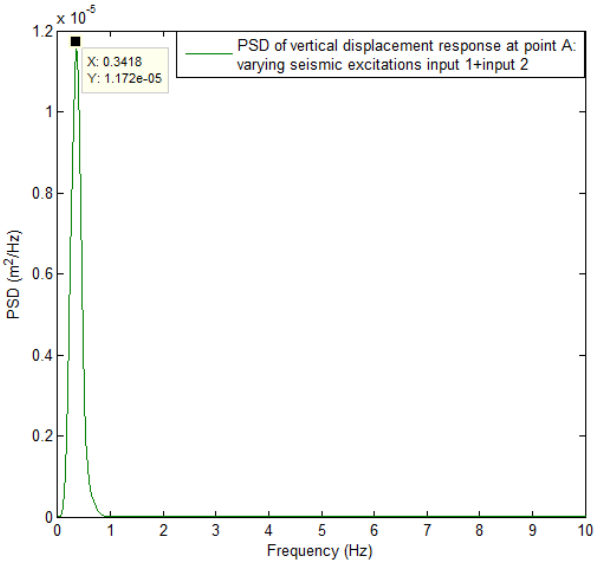

f) Vertical Displacement Reponses at Point A: Input-1 + Input-2 (PSD)

Figure 6-18 PSD of the vertical acceleration and displacement response at point A under the nonuniform Chichi earthquake for varying seismic excitations

It can be noticed that, besides the predominant vertical frequency, which is 1.758 Hz for the case 1, about seven additional spikes also appear in the same PSD graph (Figure 6-18). According to the free-vibration analysis, the corresponding bridge deck natural frequency is 1.7041 Hz (model 28) which is vertical vibration mode. Clearly, the spikes generated at more than 3.32 Hz, do not represent the natural frequency of the bridge deck model and should not have a significant effect on the overall response of the bridge. These can be ignored when a better estimation of the bridge vibration frequency response is sought, but also for the loading data preparation when extracting the seismic wave derivatives. An analogous situation was encountered for the cases 2 and 3 when the dominant frequencies were 0.3418 Hz, and the frequencies which do not have significant effect were 3.467 Hz and 3.76 Hz respectively.

Regarding the PSD of the vertical displacement response, for all three cases, one dominant frequency was 0.3418 Hz corresponding to mode 3 of the natural frequencies modes. This means that the displacement PSD response reaches the largest value at 0.3418 Hz regardless of the investigated input cases.

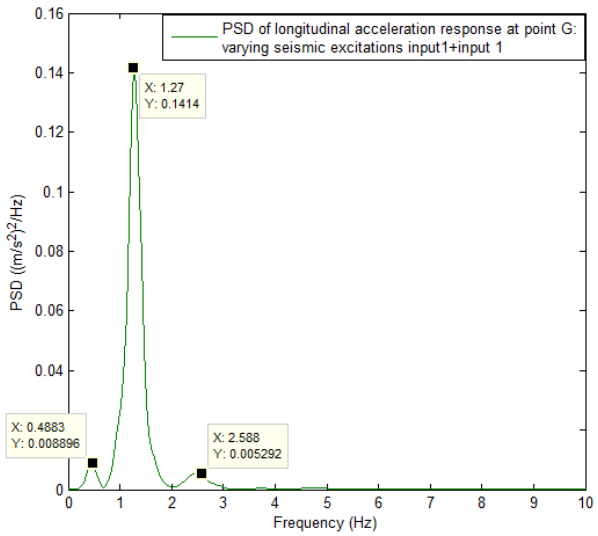

a) Longitudinal Acceleration Reponses at Point G: Input-1 + Input-1 (PSD)

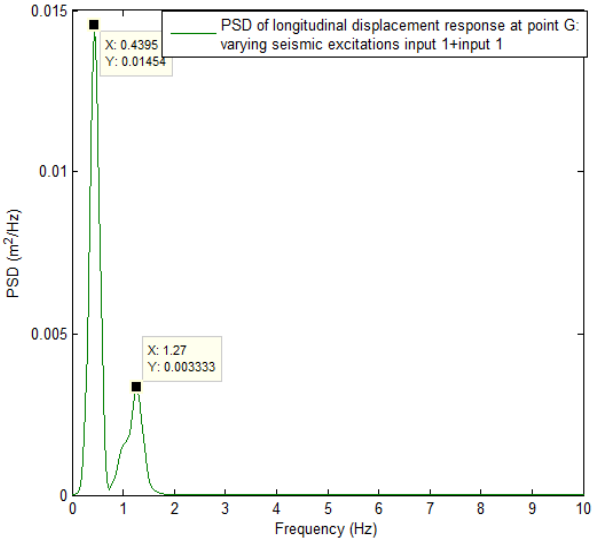

b) Longitudinal Displacement Reponses at Point G: Input-1 + Input-1 (PSD)

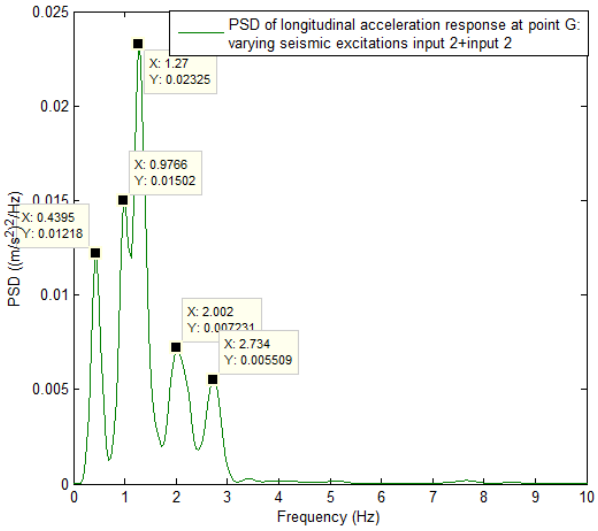

c) Longitudinal Acceleration Reponses at Point G: Input-2 + Input-2 (PSD)

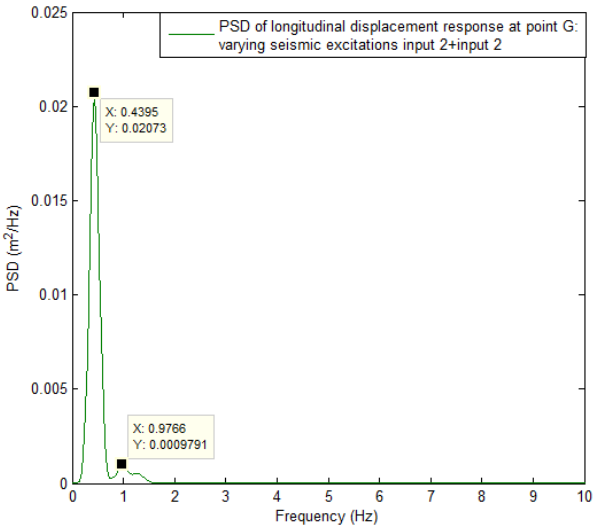

d) Longitudinal Displacement Reponses at Point G: Input-2 + Input-2 (PSD)

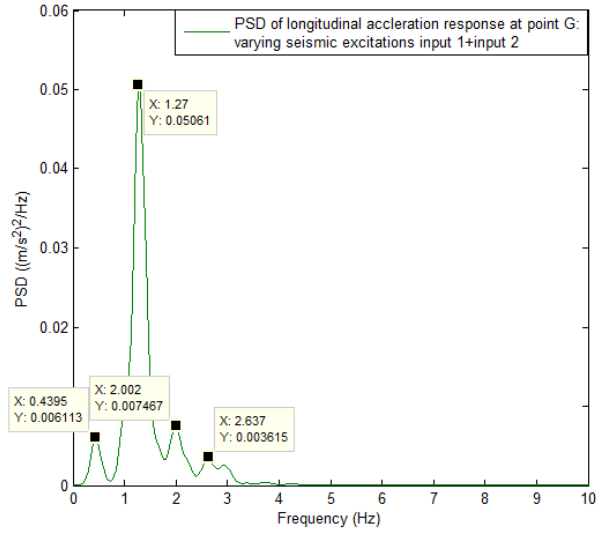

e) Longitudinal Acceleration Reponses at Point G: Input-1 + Input-2 (PSD)

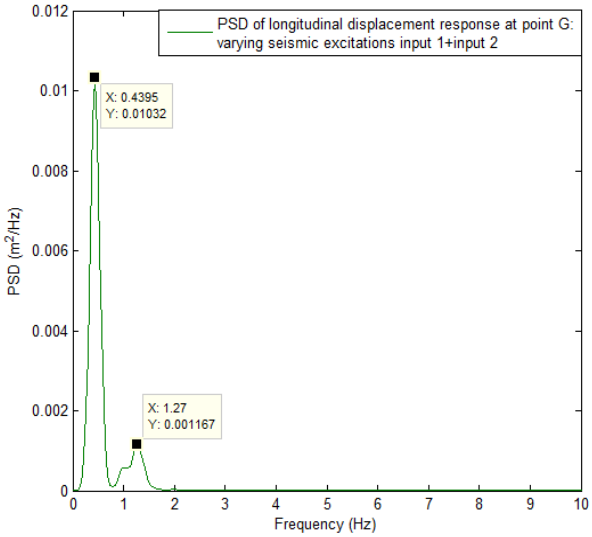

f) Longitudinal Displacement Reponses at Point G: Input-1 + Input-2 (PSD)

Figure 6-19 PSD of the longitudinal acceleration and displacement response at point G under the nonuniform Chichi earthquake for varying seismic excitations

Different from the cases discussed above, the dominant frequency for the acceleration PSD of a response of point G was 1.27 Hz (Figure 6-19). However, the occurrence of other spikes, such as 0.4935 Hz and even beyond 2.002 Hz cannot be neglected in this case. The causes of these spikes were partly from the motions of the supports, which were transferred to the top of the tower. Another possible cause might be the interaction effects between these two applied signals. However, 0.4395 Hz, 0.9766 Hz as well as 1.27 Hz are the most dominant frequencies corresponding to the PSD graph of displacement response, where it can be determined that 0.4395 Hz is the first effective longitudinal modes for the tower vibration.

6.3. COMPUTATIONAL TIME

Finite strip method has been widely recognized for its efficiency in numerical analysis. The previous research had shown the efficiency of the integrated finite strip method for the concrete slab-girder bridge (Shen et al. 2013). Similarly, the currently proposed laminated finite strip solution also shows its advantage in computational time-saving. The frequency domain computations were executed on a personal computer with an Intel Core i7 4710 HQ CPU and 8GB physical memory with a 512 G solid state disk, where the SAP 2000 with a version of 15.0.0 was used for the FEM analysis as well. Regarding the laminated finite strip method, the static analysis was implemented by several C++ programs, while the dynamic frequency domain analysis was developed by the MATLAB programs, which transform the 3D problems into a 2D mathematic problem.

However, even though the LFSM model for the FRP Kap Shui Mun Bridge has a larger number of DOF than the FEM model, the time for computation could still be reduced without losing accuracy. This is because the FS environment can separate the C++ programs (static analysis) and MATLAB programs (dynamic analysis) into several independent parts, which can use the stiffness matrix and the mass matrix directly after the static process, when applying the frequency domain analysis. The efficiency of the proposed laminated finite strip solution is more obvious when comparing both methods, as shown in Table 6-1 for some of the most complex computations conducted in the current research.

Table 6-1 Computational times comparison

Method	LFSM	FEM
Uniform Sinewave	19.08 s	1470 s
Uniform Chichi Earthquake	20.54 s	1678 s
Nonuniform Chichi Earthquake	35.75 s	Failed (Overflow)
Varying seismic excitations	41.86 s	Failed (Overflow)

6.4. VALIDATION OF FREQUENCY DOMAIN RESULTS

To better understand the effect of the various seismic excitations on the acceleration and displacement responses of the FRP-KSM Cable-stayed Bridge, a total of seven critical points along the bridge were studied by determining the time histories as detailed in Appendix D as well as the processed results for the frequency domain responses as shown in Figure 6-2 to Figure 6-19.

These PSD results tend to yield peaks at dominant frequencies, some of them with higher energy content than the others, and most of them pointing to a correspondent in the natural frequency mode shapes. The first feature is anticipated, because they are all obtained based on the Welch's Method, but differ regarding input directions and frequency of the seismic excitations. As outlined above, we are looking for the peak frequency values that are in common for the xx, yy, and zz directions. For each direction, we have data from a total of seven critical points which initially appeared as a sorting and clustering problem; however, we cannot simply select the frequency values following the rank of the energy power. This is because the forcing signal was applied in the longitudinal and vertical directions (i.e., yy, zz), which led to the most significant vibration and

the most outstanding power of the PSD level both in the longitudinal and vertical directions. Following the frequencies indicated by the rank of the power, might lead to misinterpreting the forced response of the laminated FRP deck system of the bridge span in xx direction. This challenge needs to be addressed by finding a rational comparison of the vibration in yy, and zz with those in x, that can be carried out consistently and systematically.

Therefore, the objective of this research is to propose a so-called normalized PSD (Peng et al. 2012), abbreviated as NPSD, and to apply it to each investigated case, for each direction before extracting the actual frequencies of the peaks and their energy power. The NPSD estimation is obtained by setting the maximum power value one in the PSD estimation for each case along each direction. An NPSD graph is similar, and it corresponds to the PSD plot, except that the absolute power is replaced by a relative power ranging from zero to one. Thus, the frequency of any peak in the energy power is not altered, which serves the comparison purpose.

For convenience, Table 6-2 to Table 6-5 gives the relevant power for the seven points, along with their responses along the three directions, *xx*, *yy,* and *zz*. However, the unnecessary PSD should be neglected when considering the dominant frequencies. In this table, the peaks with a relative power more than 10% were further highlighted. The relative power (PSD) is equal to or greater than 10% of all four types of responses in all three directions. Clustering techniques could be further detailed; however, an alternative path to condense the information in Table 6-2 to Table 6-5.

Table 6-2 Peak frequencies with their normalized power (PSD) corresponding to the transverse direction

Transverse Direction	Locations	Response	Transverse Direction (x)	
			Freq. (Hz)	Relative PSD
Uniform Sine wave	D	Acceleration	**1.025**	1
		Displacement	**0.1953**	0.7
			0.9766	1
Uniform Chichi earthquake	B	Acceleration	**0.5371**	1
		Displacement	1.318	0.05
			2.051	0.07
			0.1953	0.93
			0.5371	1

Table 6-3 Peak frequencies with their normalized power (PSD) corresponding to the longitudinal direction (1)

Longitudinal direction	Locations	Response	Longitudinal Direction (y)	
			Freq. (Hz)	Relative PSD
Uniform Sin wave	F	Acceleration	**1.025**	1
		Displacement	**1.025**	1
Uniform Chichi earthquake	C	Acceleration	**1.221**	0.79
			1.66	1
			2.734	0.29
			3.516	0.1
		Displacement	0.293	0.25
			1.221	1
			1.66	0.35
Varying excitations	G	Acceleration	0.4883	0.063
			1.27	1
			2.588	0.04
			0.4395	0.52
			0.9766	0.65
			1.27	1
			2.002	0.31
			2.734	0.24
			0.4395	0.12
			1.27	1
			2.002	0.15
			2.637	0.71
		Displacement	**0.4395**	1
			1.27	0.23
			0.4395	1
			0.9766	0.05
			0.4395	1
			1.27	0.11

Table 6-4 Peak frequencies with their normalized power (PSD) corresponding to the longitudinal direction (2)

Longitudinal direction	Locations	Response	Longitudinal Direction (y)	
			Freq. (Hz)	Relative PSD
Wave passage effects	B	Acceleration	**1.27**	1
			1.611	0.5
			2.783	0.03
			1.27	1
			1.611	0.69
			2.734	0.13
			1.27	1
			1.66	0.85
			2.734	0.93
		Displacement	0.7324	0.08
			1.27	1
			1.611	0.2
			0.3906	0.17
			1.27	1
			1.611	0.27
			0.3906	0.27
			1.27	1
			1.66	0.31
	E	Acceleration	0.3906	0.06
			1.318	1
			1.611	0.46
			2.734	0.03
			0.3906	0.15
			1.27	1
			1.66	0.82
			2.686	0.37
			0.4395	0.33
			1.27	0.9
			1.66	1
			2.686	0.19
		Displacement	**0.3418**	0.1
			1.27	1
			0.3906	1
			1.318	0.06
			0.4395	1
			1.27	0.03

Table 6-5 Peak frequencies with their normalized power (PSD) corresponding to the vertical direction

Vertical direction	Locations	Response	Vertical Direction (z)	
			Freq. (Hz)	Relative PSD
Uniform Sine wave	A	Acceleration	**1.025**	1
		Displacement	**1.025**	1
Uniform Chichi earthquake	E	Acceleration	**1.66**	0.17
			4.376	0.45
			7.031	1
			7.715	0.39
		Displacement	**0.3418**	1
			0.9766	0.08
			1.709	0.05
Varying excitations	A	Acceleration	**0.3906**	0.63
			0.6348	0.61
			1.074	0.34
			1.758	1
			3.32	0.53
			0.3418	1
			1.709	0.25
			3.467	0.21
			10.79	0.38
			0.3418	1
			1.123	0.22
			1.709	0.8
			10.79	0.35
		Displacement	**0.3418**	1
			0.3418	1
			0.3418	1

The following guidelines were employed to extract the most significant concluding remarks:

(1) Each direction was treated separately.

(2) Low-frequency vibrations in the three directions were of particular interest.

(3) Within each direction, a total of four cases with equal weight were considered. The NPSD values were added up for all the four cases and then were divided by four. The added-up results in each direction are presented as one consolidated NPSD in each direction, the peak frequencies in common for all the four cases and the seven critical locations investigated are listed as follows:

***xx*:** 0.1953 Hz, 0.5371, **1.025 Hz**.

***yy*: 0.3418 Hz**, **0.3906 Hz**, 0.4395 Hz, 0.9766 Hz, **1.025 Hz**, 1.221 Hz, 1.27 Hz, 1.318 Hz, 1.611 Hz, 1.66 Hz, 2.002 Hz, 2.686 Hz, 2.734 Hz.

***zz*: 0.3418 Hz**, **0.3906 Hz**, **1.025 Hz**, 1.66 Hz, 1.709 Hz, 10.79 Hz.

In general, it is easier to identify the peak frequencies in common for all three directions based on the above summary. The frequency of 1.025 Hz appeared the most often. Thus it is possible to determine significant responses for the higher modal frequencies, as they are shared in all three directions. The narrow frequency band from 0.3418 Hz to 0.3906 Hz marks the range for the fundamental frequency because the band is valid for both longitudinal and vertical directions. A range rather than a collection of discrete values is specified, given the influence of the window length to the PSD estimation. The other frequencies such as 1.221 Hz, 1.27 Hz, and so on need to be further investigated, as significant characteristics in dynamic responses in the future. The clustering of frequencies beyond 50 Hz will not be discussed further, given the fact that this frequency response exceeds the earthquake excitations.

CHAPTER 7. CONCLUSIONS AND FUTURE WORK

7.1. CONCLUSIONS

This thesis presented a numerical simulation study which investigated the static and dynamic performance of a typical Slab-girder Bridge and a representative Long-span Cable-stayed Bridge, which they are produced with composite materials fibre-reinforced polymer (FRP). Chapter 2 provided a general literature review of the pertinent research and studies. Also, the theoretical basis had been calculated and presented in Chapter 3, which is fundamental for the following work for the finite strip analysis. The concepts and modeling assumptions for the laminated finite strip method, which is the extension of the integrated finite strip method, were introduced, and the numerical simulation was achieved by modifying the basic C++ and MATLAB codes to realize the requirements for the change of the concrete materials to composite materials and the associated bridge configurations.

The investigations performed in the current research included the adaptation of the laminated finite strip method, finite element method, composite materials properties, configurations of the layout of FRP deck, static analysis, free vibrations analysis, time domain analysis, and the frequency domain analysis. A reasonable agreement could be noticed between the numerical results of the laminated finite strip method with those obtained by using the finite element method employed by the aid of SAP 2000 software.

In total, two types of bridges were tested, the Continuous Slab-girder Bridge with the concrete pier and laminated FRP deck that has a reduced the thickness as well as the self-weight efficiently determined, and the Kap Shui Mun Cable-stayed Bridge with the laminated FRP deck, with three thickness configurations. [0/90/0/0/90/0] is considered as the most efficient distribution of the core cells of laminated FRP decks. However, only based on a detailed parametric study and the static deflection and natural frequencies validations, only one bridge deck was selected to be applied in the practical application in the future.

In general, the reduced computational time and efficiency of the laminated finite strip method were much better than the finite element method. When it comes to the dynamic analysis and frequency domain analysis of the cable-stayed bridges for which the FEM model has a very high number of degrees of freedom, the finite strip method becomes more efficient. For the simulations involving a nonuniform seismic excitation, the FEM model of the KSM Bridge could not achieve convergence. The current comprehensive study performed on static and seismic responses of long-span bridges provides the opportunity for modeling the laminate deck cable-stayed bridges using

the finite strip method. This will lead to optimization of the long-span cable-stayed bridges based on their performances.

The overall Slab-girder Bridge, that is regarded as a case study and application before the long-span cable-stayed bridge, maximum and residual displacements, bending moment, free vibrations, deformed shapes for the proposed model, frequency domain analysis and Log (PSD) were considered as the main criteria to judge the behavior of the FRP bridge. The conclusions from the current research program can be summarized below:

- For the static simulations, the main criteria included the maximum displacement and deflection in each direction which had shown that the FRP bridge could withstand similar static loading displacement behavior and dynamic behavior when reducing the deck thickness efficiently. It also provides a most efficient configuration of the lamina layout for the laminated FRP deck that is very useful in the practical application.
- For the free vibrations analysis, the FRP bridge has a higher natural frequency, which means it will not be very affected by the ground motion when the seismic waves are applied.
- Regarding the frequency domain analysis, the Pseudo Excitation Method (PEM), which is a frequency domain method was used. It had been observed that the computation time had been significantly reduced which makes this method more efficient than before with the same high accuracy, especially, that is more versatile for performing the real seismic excitation analysis. Therefore, for massive and complex structures like long-span cable-stayed bridges with thousands of degrees of freedoms and dozens of support conditions, the frequency domain analysis can be performed more rapidly and accurately on a personal computer.

Regarding the Long-span Cable-stayed Bridge model investigation, following almost the same analytical process but employing different C++ and MATLAB codes, as studied and explored in Chapter 4 and Chapter 5 also representing the main distribution of the current research. As it had been proved, the LFSM has an acceptable response agreement for any types of loadings. In other words, there is almost no difference for the static results between the two approaches FEM and LFSM:

- The configurations of the lamina layout, as well as the thickness, can influence the structural behavior of the long-span cable-stayed bridge. Since there are totally three types of laminated FRP decks modeled by the current author who aims to find the most efficient lamina model that has the optimum static and dynamic capacities. Moreover, except for the displacement at critical points, deflection lines on each nodal line on the deck, as well as

the rotation around the x and y-axes, had been displayed and plotted, which greatly improved the simulation of strain-stress characteristics for the hybrid long-span cable-stayed bridges. Even though the FRP bridge always has larger static deflection responses under the concentrated load, the overall stiffness of the deck is still strong enough to fulfill the minimum deflection requirements stipulated in the design bridge codes.

- Moreover, the line load, which is defined as the live load in this research, is applied to the laminated cable-stayed bridge through the finite strip method which has been realized in previous studies. This has provided an alternative approach for examining the static behavior for the composite bridges rather than the finite element approach (FEA). Even though the stiffness of the entire FRP bridge is lower than the original cable-stayed bridge, with the reduction of the overall deck mass, it is still capable of performing very well and to satisfy the critical structural response criteria.
- Despite the low natural frequencies of the FRP-KSM Bridge, the composite bridge has very reasonable acceleration and displacement responses under seismic effects. Regarding the acceptance of FRP materials when constructing a long-span bridge, the high strength-to-weight ratio, better durability, corrosion resistance, and fatigue resistance are considered as superior properties that have more advantages over steel and concrete materials. Furthermore, the composite components with the hybrid bridge, like FRP decks, have much more significantly different from those of the traditional concrete and steel decks such as mass, stiffness, and damping. As a result, significant but reasonable different performance happens to composite bridges with FRP decks.
- Regarding the frequency domain analysis, the dynamic analysis procedure in the laminated finite strip method environment can be performed with the same approach as the one used in the finite element method. After solving an eigenvalue problem, the natural frequencies of the bridge structures can be obtained. Furthermore, the power spectrum response can be realized directly. An additional extension is that LFS environment can now perform the frequency domain analysis by converting the time domain results, while the computing time can be reduced significantly when compared with the same procedure applied through the FEM. Since it was observed that with the use of finite strip method in the design and analysis of long-span bridges the results would converge rapidly and the computational costs will be much lower in comparison with other numerical methods like finite element method (FEM). Moreover, a normalized power spectrum density entitled NPSD is introduced and applied during the frequency domain analysis, for providing a unique perspective for the interpretation of the frequency domain analysis results.

7.2. RECOMMENDATIONS AND FUTURE WORK

The following recommendations for future research are suggested:

- One of the important objectives of future work is to investigate whether using the new composite FRP materials for the main span of cable-stayed bridges that exceed 1000 m, can open the new field of composite super long-span bridges. To be able to can construct the new super long-span bridges by the new composite materials in the future, the laminated FRP deck model is expected to be extended to the laminated box girders. On the other hand, it can also be implemented by the FRP "I" girders supporting the laminated decks.
- The natural frequencies obtained for the composite KSM Bridge modeled by LFSM were much lower than the other models created for the same bridge. In the current study focused on determining the effect of changing the concrete deck to a laminated deck model, however, to achieve better agreement for the natural frequencies of this bridge, the stay-cables pre-tensions should be re-evaluated, and a new laminate bridge model should be assessed based on these new parameters.
- Although the use of composite FRP materials for the bridge structural components induces a reduction of the overall weight of the bridges, and thus longer spans can be constructed, special attention should be paid to the other critical instabilities reported for such long-span bridges, like the aerodynamic instability, the general aerodynamic behavior of hybrid composite bridges and the coupled vibrations of wind–vehicle–bridge (WVB).
- Furthermore, a new generation of long-span bridges with of twin and multiple decks are under investigation or some of them are already constructed. The finite strip method could be the optimum tool for modeling and analysing bridges such as, Megane Multi-Box Bridge as well as the Stonecutters Bridge, thus a frequency domain analysis for both seismic effects and aerodynamic contributions, which are necessary due to their distinctive design and requirements of meeting higher engineering technical solutions, could be easily conducted.

REFERENCES

A.C. Manalo, T. A. (2012). Composite Behaviour of a Hybrid FRP Bridge Girder and Concrete Deck. *Advances in Structural Engineering Vol. 15 No. 4*.

Ada´ny S, S. B. (2006). Buckling mode decomposition of single-branched open cross-section members via finite strip method: derivation. *Thin-Wall Struct*.

Almansour, H., & Cheung, M. S. (2010, July). Structural performance of laminated FRP box girder bridge deck compared to slab on prestressed concrete girder bridge. *The 8th Canada Japan Joint Workshop on Composites, Montreal, Canada*, pp. 1-32.

Aly S. Nazmy, A. M.-G. (1992). Effects of Ground Motion Spatial Variability on the Response of Cable-stayed Bridges. *Earthquake Engineering and Structural Dynamics, VOL. 21*, pp. 1-20.

Au Ftk, C. Y. (1993). Isoparametric spline finite strip for plane structures. *Computers and Structures; 48(1)*, pp. 23-32.

Ben Y.B. Chan, M. M. (2013). Nonlinear dynamic analysis of fiber reinforced ultra-long span cable stayed bridges. *Bridge Structures 9*, pp. 3-19.

Bradford M.A, A. M. (1995). Buckling of plates with different end conditions using the finite strip method. *J Comput Struct; 56(1)*, pp. 75-83.

Brown, T. G. (1972). Finite strip analysis of skew slabs. *McGill-EIC Conference in Finite Element Method in Civil Engineering*, pp. 1141-1151.

Brown, T. G. (1975). Semi-analytic solution of skew box girder bridges. *Proc. Inst. Civ. Eng., part 2, 59*, pp. 487-500.

Bun, C. Y. (2008). *Vehicle-Wind-Long Span Bridges Interaction and Its Effect on Speed Limit and Vehicle Stability.* Civil and Environmental Engineering Department, HKUST: PhD thesis.

Caprani, C. C. (2013, November 4). Application of the pseudo-excitation method to assessment of walking variability on footbridge vibration. *Computers and Structures 132 (2014) 43–54*.

Carassale, L., Wu, T., & Kareem, a. A. (2014, 140(8): 04014051). Nonlinear Aerodynamic and Aeroelastic Analysis of Bridges: Frequency Domain Approach. *J. Eng. Mech.*

Chang, C. C. (2004). *Earthquake Engineering Lecture Notes.* Department of Civil Engineering Hong Kong University of Science and Technology.

Chao, W. (2015). *Damage Modelling of FRP Composite Bridge Decks.* The Hong Kong University of Science and Technology: ph. D Thesis.

Chen CJ, G. R. (1991). B-Spline compound strip analysis of stiffened plates under transverse loading. *Computers and Structures; 34(2)*, pp. 337-347.

Chen CJ, G. R. (1991). Spline compound strip analysis of folded plate structures with intermediate supports. *Computers and Structures; 39(3/4)*, pp. 369–379.

Chen, M. J. (1984). Analysis of thin parallelogram plates' bending by spline- finite-strip method. *Applied mathematics and mechanics, 5(6)*, p. 1727.

Cheng, S. H. (2003). Comparison of numerical techniques for 3D flutter analysis of cable-stayed bridges. *Computers and Structures (81)*, pp. 2811–2822.

Cheng-Yu Yang, M. M. (2011). Shake Table Test of Cable-Stayed Bridge Subjected to Non-Uniform Excitation. *Procedia Engineering 14*, pp. 931–938.

Cheung Y. K., T. L. (1998). *The finite strip method.* USA: CRC Press.

Cheung, M. L. (1990). Analysis of haunched, continuous bridges by spline finite strips. *Comput. Struct;36(2)*, pp. 287-300.

Cheung, M. L. (1992). Spline finite strip analysis of continuous haunched box- girder bridges. *Can. J. Civil Eng.;(19)*, pp. 724-728.

Cheung, M. S. (1970). Analysis of slab and girder bridges by the finite strip method. *Build. Sci., 5 (2)*, pp. 95-105.

Cheung, M. S. (1971). Natural vibrations of thin flat-walled structures with different boundary conditions. *Journal of Sound Vibrations*.

Cheung, M. S. (1988). Analysis of continuous haunched box-girder bridges by the finite strips. *Journal of Structural Engineering, 115 (5)*, pp. 1076-1087.

Cheung, M. S. (1988). Analysis of haunched bridges by finite strip method. *Computers and Structures, 28 (5)*, pp. 621-626.

Cheung, M. S. (1992). Spline finite strip analysis of continuous haunched box-girder bridges. *Canadian Journal of Civil Engineering*.

Cheung, M. S. (1994, March). Combined boundary element, finite strip analysis of bridges, Journal of Structural Engineering. *Journal of Structural Engineering, Vol. 120, No. 3*.

Cheung, Y. F. (1982). Spline finite strip in structural analysis. (pp. 704-709). Shanghai: Proc. Int. Conf. Fin. Elem. Meth.

Cheung, Y. K. (1968). The finite strip method in the analysis of elastic plates with two opposite simply supported ends. *Proc. Inst. Civ. Eng., 40*, pp. 1-7.

Cheung, Y. K. (1969). Analysis of curved box girder bridges by finite strip method. *IABSE publications, 31/I*, pp. 1-19.

Cheung, Y. K. (1969). The analysis of cylindrical orthotropic curved bridge decks. *IABSE publications, 29-II*, pp. 41-52.

Cheung, Y. K. (1971). Analysis of simply supported thick layered plates. *ASCE, 97(EM3)*, pp. 1039-1044.

Cheung, Y. K. (1976). *Finite Strip Method in Structural Analysis.* University of Calgary.

Cheung, Y. K. (1987). Large deflection analysis of arbitrary shaped thin plates. *Computers & Structures, 26(5)*, pp. 811-814.

Cheung, Y. K. (1988). Free vibration and static analysis of general plate by spline finite strip. *Computational Mechanics, 3(3),*, pp. 187-197.

Cheung, Y. K. (1989). Postbuckling analysis of circular cylindrical shells under external pressure. *Thin-Walled Structures, 7(3-4)*.

Computers and Structures, Inc. (2004, August). *Lin ear and Non linear Static and Dynamic Analysis and Design of Three-Dimensional Structures BA SIC ANALYSIS REFERENCE MANUAL.* Berkeley, Califor nia, USA.

CSA-S6-12. (2012). *Canadian Highway Bridge Design Code, Canadian.*

Dawe, D. J. (2002). Use of the finite strip method in predicting the behaviour of composite laminated structures. *Composite Structures*, pp. 11-36.

Dey, S. S. (1980, June). Finite strip method of analysis for orthotropic curved bridge decks,. *Proc. Instn Ciu. Engrs, Part 2*, pp. 69, 511-519.

Duan Lian, C. W.-F. (2015, Feburary 3). Longest Bridges and Bridge Spans. *Handbook of International Bridge Engineering*.

Fan, S. C. (1982). *Spline finite strip in structural analysis.* PhD thesis, Department of Civil Engineering, the University of Hong Kong.

Fan, S. C. (1982). *Spline finite strip in structural analysis.* University of Hong Kong.

Fang Zhi, G. C. (2009). Nonlinear behavior of concrete beams with hybrid FRP and stainless steel reinforcements. *J. Cent. South Univ. Technol.*, p. 0495−0502.

Gibson, R. F. (1994). *Principles of Composite Material Mechanics.* Department of Mechanical Engineering Wayne State University Detroit, Michigan.

Hamidreza Naderian, M. M. (2015). Integrated finite strip analysis for long-span cable-stayed bridges. *Computers and Structures 158*, pp. 82-97.

Hetland, R. (2015). *Operational modal analysis of the Dolmsundet Bridge during construction.* Norwegian University of Science and Technology Department of Structural Engineering.

Ilker Fatih Kara, A. F. (2015). Flexural behavior of hybrid FRP/steel reinforced concrete beams. *Composite Structures 129*, pp. 111–121.

J. M. Ko, Z. G. (n.d.). *Modal Analysis of Cable-Stayed Kap Shui Mun Bridge Taking Cable Local Vibration into Consideration.* Department of Civil and Structural Engineering, The Hong Kong Polytechnic University, Kowloon, Hong Kong.

JS., P. (1973). Finite element structural analysis of local instability. *AIAA J;11:33–9*.

Karim, M. R. (2005). *Constitutive Modeling and Failure Criteria of Carbon-fiber Reinforced Polymers Under High Strain Rates.* The Graduate Faculty of The University of Akron.

Kong, J. a. (1995). Generalized spline finite strip for the analysis of plates. *Thin-Walled Structures, 22(3)*, pp. 181-202.

Lau, D. T. (2000, October). 3D Flutter analysis of bridges by spline finite strip method, Journal of Structural Engineering. *Journal of Structural Engineering, Vol. 126, No. 10*.

Lau, S. C. (1986). Buckling of thin flat-walled structures by a spline finite strip method. *Thin-Walled Structures, 4(4),*, pp. 269-294.

Lau, S. C. (1989). Inelastic buckling analyses of beams, columns and plates using the spline finite strip method. *Thin-Walled Structures, 7(3-4)*, pp. 213-238.

LG., T. (1990). Application of spline finite strip method in the analysis of space structures. *Thin-Walled Structures; 10*, pp. 235-246.

Li, W. (1991). *Linear and Nonlinear Finite Strip Analysis of Bridges.* School of Graduate Studies and Reasearch, University of Ottawa.

Li, W. Y. (1988). *Spline finite strip analysis of arbitrarily shaped plates and shells.* PhD thesis, Univ. of Hong Kong.

Li, W. Y. (n.d.). Spline Finite Strip Analysis of General Plates. *Journal of Engineering Mechanics, 112(1)*, pp. 43-54.

Li, Z. S. (2013). Constrained finite strip method for thin-walled members with general end boundary conditions. *Journal of Engineering Mechanics*.

Logan, D. L. (2007). *A First Course in the Finite Element Method.* Fourth Edition, Thomson.

Loo, Y. C. (1975). The finite strip analysis of multispan box-girder bridges with intermediate stiffening members. *British Steel Corporation Fellowship Final Report, University of Dundee*.

M. S. Cheung, W. G. (1991). Spline finite strip analysis of continuous haunched box-girder bridges. *Can. J. Civ. Eng. 19*, pp. 724-728.

M. S. Cheung, W. L. (1989, May). Analysis of continuous, haunched box-girder bridges by finite strips. *Journal of Structural Engineering*, p. 115.

Martin Noël and Amir Fam, M. (2016). Design Equations for Concrete Bridge Decks with FRP Stay-in-Place Structural Forms. *J. Compos. Constr., 04016024*.

Michael Ch Hui, D. Y. (2011, September 28). Major bridge development in Hong Kong, China—past, present and future. *Front. Archit. Civ. Eng. China 2011, 5(4)*, pp. 405–414.

Moe M. S. Cheung, Z. S. (2009). Integrated Finite Strip Solution for Box Girder Bridges and Slab-on-girder Bridges. *Journal of Computer Modeling in Engineering and Science, vol.45, no.2*, pp. 155-177.

Mohammed Ettouney, A. H. (2001, December). Frequency-domain Analysis of Long-span Bridges Subjected to Nonuniform Seismic Motions. *Journal of Bridge Engineering*, pp. 577-586.

Mohammed R. Karim, M. S. (2006). Rate-Dependent Constitutive Equations for Carbon Fiber-Reinforced Epoxy. *POLYMER COMPOSITES*.

Naderian, H. (2014). *Finite Strip Modeling of Long-span Cable-stayed Bridges.* phD Proposal.

Naderian, H. (2017). *Advanced numerical techniques for dynamic and aerodynamic analysis of bridges.* University of Ottawa.

Naderian, H. R. (2010). Distortional Buckling of Stiffened Cold-Formed Steel Channel Sections. *Proceedings of the 10th International Conference on Computational Structures Technology*.

Naderian, H. R. (2010). Stability of Unstiffened and Stiffened Cold Formed Steel I- Sections by the Bubble Finite Strip Method. *Proceedings 135 of the 10th International Conference on Computational Structures Technology, Valencia, Spain*.

Naderian, H. R. (2011, Sept.). Torsional and Flexural Buckling of Composite FRP Columns with Cruciform Sections Considering Local Instabilities. *Journal of Composite Structures, Volume 93, Issue 10*, pp. 2575-2586.

Naderian, H. R. (2013, July). *Finite Strip Analysis of Bridges User Manual.* Hong Kong/Ottawa: Hong Kong University of Science and Technology/University of Ottawa.

Naderian, H. R. (22 – 25 May 2012). Global Buckling Behavior of Composite FRP Cruciform Section Columns by Complex Finite Strip Method. *Proceedings of the 6th International Conference on Advanced Composite Materials in Bridges and Structures, Kingston.* Kingston, ON, Canada.

Naderian, H., Cheung, M. M., Shen, Z., & Dragomirescu, E. (2016). Seismic Analysis of Long-Span Cable-Stayed Bridges by an Integrated Finite Strip Method. *J. Bridge Eng.*

P. D. Soden, M. J. (1998). Lamina Properties, Lay-up Configurations and loading Conditions for a Range of Fibre-reinforced Composite Laminates. *Composites Science and Technology (58)*, pp. 1011-1022.

Pálsson, G. P. (2012). *Finite Element Modelling and Updating of Medium Span Road Bridges.* Brovej, Building 118, 2800 Kgs. Lyngby, Denmark: Department of Civil Engineering, Technical University of Denmark.

Peng F. Tang, J.-s. P. (2012, August). A Structural Identification of Real-world Shear-critical Prestressed Concrete Highway Bridge. *Oklahoma Transportation Center*.

Plank R J, W. W. (1974). Buckling under combined loading of thin flat walled structures by a complex finite strip method. *Int J Numer Methods Eng*.

Powell, G. H. (1969). Analysis of orthotropic steel plate bridge decks. (pp. 909-922). Proc. ASCE, 95 (ST5).

Prenter, P. M. (1975). *Splines and Variational Methods.* New York: Wiley.

Q. W. Zhang, T. Y. (n.d.). Finite-element Model Updating for the Kap Shui Mun Cable-stayed Bridge. *J. Bridge Eng., 2001, 6(4)*, pp. 285-293.

S. C. Fan, Y. K. (1983, October). Analysis of shallow shells by spline finite strip method. *Eng. Struct., Vol. 5*.

Shen, Z. (2009). *An Integrated Finite Strip Solution for Long Span BridgesShen, Z.* Department of Civil and Environmental Engineering, Hong Kong University of Science and Technology: MPhill thesis.

Soudki, M. N. (2013). Effect of Prestressing on the Performance of GFRP-Reinforced Concrete Slab Bridge Strips. *JOURNAL OF COMPOSITES FOR CONSTRUCTION © ASCE*, pp. 188-196.

Soudki, M. N. (2014). Fatigue Behavior of GFRP Reinforcing Bars in Air and in Concrete. *J. Compos. Constr.*

Soudki, M. N. (2015). Fatigue Behavior of Full-Scale Slab Bridge Strips with FRP Reinforcement. *J. Compos. Constr.*

The Highways Agency, Scottish Executive, Welsh Assembly Goverment Llywodraeth Cynulliad Cymru, The Department for Regional Development Northern Ireland. (2005, May). Design of FRP Bridges and Highway Structures.

Timoshenko, S. G. (1970). *Theory of Elasticity.* 3rd edition, McGraw-Hill, New York.

Timoshenko, S. W.-K. (1959). *Theory of Plates and Shells.* 2nd edition, McGrew-Hill, New York.

W.H., W. (1968). A unified approach to the initial buckling of stiffened panels in compression. *Aeronaut Quart*.

Wang, S. Z. (2004). Vibration analysis of rectangular composite laminated plates using layerwise B-spline finite strip method. *Composite structures structures, (68)*, pp. 349-358.

Welch, P. D. (1967, June). The Use of Fast Fourier Transform for the Estimation of Power Spectra: A Method Based on Time Aver-aging Over Short, Modified Periodograms. *IEEE Transactions on Audio and Electroacoustics, VOL. Au-15, NO. 2*.

Wrobel, L. C., & Aliabadi, M. H. (2002). *The Boundary Element Method.* New Jersey: Wiley.

Y. K. Cheung, S. C. (1983, June). Static analysis of right box girder bridges by spline finite strip method. *Proc. Instn Ciu. Engrs, Part 2, 75*, pp. 311-323.

Yao, Z. R. (2010). *Material and geometric non- linear isoparametric spline finite strip analysis of perforated thin-walled steel structures.* School of Civil Engineering, University of Sydney: Research report R910.

Zhao Peng, X. L.-z. (2015). Analysis and design procedure of hybrid long-span cable-stayed bridge using advanced composite material. *Journal of Reinforced Plastics*.

Zhenyuan Shen, C. K. (2009). *The Integrated Finite Strip Solution Computer Programs User Manual.* Department of Civil and Environmental Engineering The Hong Kong University of Science and Technology.

Zhenyuan Shen, M. M. (2013). An Integrated Finite Strip Solution for Dynamic Analysis of Continuous Multi-span Bridges. *CSCE 2013 General Conference*.

Zhong, W. C. (1998). The precise finite strip method. *Comput.*, pp. 773-783.

Zhu, D. S. (1988). *Nonlinear static and dynamic analysis of plates and shells by spline finite strip method.* PhD thesis, Univ. of Hong Kong.

Zhu, D. S. (1989). Postbuckling analysis of shells by spline finite strip method. *Computers and Structures, 31(3)*, pp. 357-364.

Zhu, D. S. (1996). Postbuckling analysis of circular cylindrical shell under combined loads. *Computers & Structures, 58(1)*, pp. 21-26.

Zienkiewicz, O. C. (1972). he finite prism in analysis of thick simply supported bridge boxes, Proc. *Proc,. Inst. Civ. Eng. 53*, pp. 147-172.

APPENDIX A

Welch's Method Transform MATLAB program:

```
n=4001;                                          %Number of input time domain signal
dt=0.01;                                         %Time interval
nfft=4096;      %Number of discrete Fourier transform (DFT) points to use in the PSD estimate
fs=1/dt;                                         %Sampling frequency
[Pxx,f]=pwelch((x),[],[],nfft,fs);               %x=S/9.81 for the acceleration PSD
                                                 %x=S for the displacement PSD
plot(f,(Pxx),'b');          % Plot the PSD vs frequency plot developed by FSM in blue line
plot(f,log(Pxx),'b');  % Plot the Log (PSD) vs frequency plot developed by FEM in blue line
hold on;                                         %Plot PSD plots for both methods in one figure
[Pxx,f]=pwelch((x),[],[],nfft,fs);               %x=SS/9.81 for the acceleration PSD
                                                 %x=SS for the displacement PSD
plot(f,(Pxx),'r');          % Plot the PSD vs frequency plot developed by FEM in red line
plot(f,log(Pxx),'r');  % Plot the Log (PSD) vs frequency plot developed by FEM in red line
xlabel('Frequency(Hz)')
ylabel('PSD(g^2/Hz)')
ylabel('Log(PSD)(dB/Hz)')
```

APPENDIX B

Explanations (Naderian, 2013):

1: No.: number of cable elements

2. AY: length of strip,

3. Radius: radius of cable section,

4. dx: x component of the cable element

5. dy: y component of the cable element

6. dz: z component of the cable element

7. Elastic modulus

8. Poisson ratio

9. FP: magnitude of load (this is equivalent pre-stressed load – thermal load) in the first end

10. NFP: the direction of the concentrated load: 1 x, 2 y, 3 z (local coordinate) in the second end

11. YFP: Y coordinate of concentrated load in the second end

12. Temp: corresponding temperature of the pre-stress force

No.	AY	Radius	dx	dy	dz	EE	UU	FP	NFP	YFP	Temp
1	182.4869758	0.07	-0.1	155.1	-96.1534	150000000	0.3	3321.982103	2	182.4869758	92.2222
2	176.4736891	0.07	-0.1	149	-94.5619	150000000	0.3	3321.982103	2	176.4736891	92.2222
3	170.4814221	0.07	-0.1	142.9	-92.9704	150000000	0.3	2961.76709	2	170.4814221	82.2222
4	164.5124718	0.07	-0.1	136.8	-91.3789	150000000	0.3	2241.337062	2	164.5124718	62.2222
5	158.5694712	0.07	-0.1	130.7	-89.7874	150000000	0.3	1881.122049	2	158.5694712	52.2222
6	152.6554512	0.07	-0.1	124.6	-88.1959	150000000	0.3	1160.692021	2	152.6554512	32.2222
7	146.7739149	0.07	-0.1	118.5	-86.6044	150000000	0.3	1160.692021	2	146.7739149	32.2222
8	140.9289295	0.065	-0.1	112.4	-85.0129	150000000	0.3	1932.581447	2	140.9289295	62.2222
9	135.1252381	0.065	-0.1	106.3	-83.4214	150000000	0.3	1621.987889	2	135.1252381	52.2222
10	129.3683985	0.065	-0.1	100.2	-81.8299	150000000	0.3	1311.394331	2	129.3683985	42.2222
11	123.6649539	0.065	-0.1	94.1	-80.2384	150000000	0.3	1000.800773	2	123.6649539	32.2222
12	118.0226456	0.065	-0.1	88	-78.6469	150000000	0.3	690.2072158	2	118.0226456	22.2222
13	112.4506766	0.06	-0.1	81.9	-77.0554	150000000	0.3	1382.048852	2	112.4506766	52.2222
14	106.9647674	0.06	-0.1	75.8	-75.4706	150000000	0.3	1117.401087	2	106.9647674	42.2222
15	101.5688014	0.06	-0.1	69.7	-73.8791	150000000	0.3	1117.401087	2	101.5688014	42.2222
16	96.28326497	0.06	-0.1	63.6	-72.2876	150000000	0.3	852.7533218	2	96.28326497	32.2222
17	91.12737544	0.055	-0.1	57.5	-70.6961	150000000	0.3	1606.06021	2	91.12737544	72.2222
18	86.12442012	0.055	-0.1	51.4	-69.1046	150000000	0.3	1161.304938	2	86.12442012	52.2222
19	81.30263631	0.055	-0.1	45.3	-67.5131	150000000	0.3	1383.682574	2	81.30263631	62.2222
20	76.69620164	0.055	-0.1	39.2	-65.9216	150000000	0.3	1606.06021	2	76.69620164	72.2222
21	72.34626297	0.06	-0.1	33.1	-64.3301	150000000	0.3	2705.287678	2	72.34626297	102.2222
22	68.30184426	0.06	-0.1	27	-62.7386	150000000	0.3	5748.736977	2	68.30184426	217.2222
23	182.4869758	0.07	0.1	155.1	-96.1534	150000000	0.3	3321.982103	2	182.4869758	92.2222
24	176.4736891	0.07	0.1	149	-94.5619	150000000	0.3	3321.982103	2	176.4736891	92.2222
25	170.4814221	0.07	0.1	142.9	-92.9704	150000000	0.3	2961.76709	2	170.4814221	82.2222
26	164.5124718	0.07	0.1	136.8	-91.3789	150000000	0.3	2241.337062	2	164.5124718	62.2222
27	158.5694712	0.07	0.1	130.7	-89.7874	150000000	0.3	1881.122049	2	158.5694712	52.2222
28	152.6554512	0.07	0.1	124.6	-88.1959	150000000	0.3	1160.692021	2	152.6554512	32.2222
29	146.7739149	0.07	0.1	118.5	-86.6044	150000000	0.3	1160.692021	2	146.7739149	32.2222
30	140.9289295	0.065	0.1	112.4	-85.0129	150000000	0.3	1932.581447	2	140.9289295	62.2222
31	135.1252381	0.065	0.1	106.3	-83.4214	150000000	0.3	1621.987889	2	135.1252381	52.2222
32	129.3683985	0.065	0.1	100.2	-81.8299	150000000	0.3	1311.394331	2	129.3683985	42.2222
33	123.6649539	0.065	0.1	94.1	-80.2384	150000000	0.3	1000.800773	2	123.6649539	32.2222
34	118.0226456	0.065	0.1	88	-78.6469	150000000	0.3	690.2072158	2	118.0226456	22.2222
35	112.4506766	0.06	0.1	81.9	-77.0554	150000000	0.3	1382.048852	2	112.4506766	52.2222
36	106.9647674	0.06	0.1	75.8	-75.4706	150000000	0.3	1117.401087	2	106.9647674	42.2222
37	101.5688014	0.06	0.1	69.7	-73.8791	150000000	0.3	1117.401087	2	101.5688014	42.2222
38	96.28326497	0.06	0.1	63.6	-72.2876	150000000	0.3	852.7533218	2	96.28326497	32.2222
39	91.12737544	0.055	0.1	57.5	-70.6961	150000000	0.3	1606.06021	2	91.12737544	72.2222
40	86.12442012	0.055	0.1	51.4	-69.1046	150000000	0.3	1161.304938	2	86.12442012	52.2222
41	81.30263631	0.055	0.1	45.3	-67.5131	150000000	0.3	1383.682574	2	81.30263631	62.2222
42	76.69620164	0.055	0.1	39.2	-65.9216	150000000	0.3	1606.06021	2	76.69620164	72.2222

No.	AY	Radius	dx	dy	dz	EE	UU	FP	NFP	YFP	Temp
43	72.34626297	0.06	0.1	33.1	-64.3301	150000000	0.3	2705.287678	2	72.34626297	102.2222
44	68.30184426	0.06	0.1	27	-62.7386	150000000	0.3	5748.736977	2	68.30184426	217.2222
45	228.8944254	0.07	0.1	209.7	91.7527	150000000	0.3	4402.627144	2	228.8944254	122.2222
46	220.3366484	0.07	0.1	201	90.262	150000000	0.3	4042.412131	2	220.3366484	112.2222
47	211.8040966	0.07	0.1	192.3	88.7788	150000000	0.3	3682.197117	2	211.8040966	102.2222
48	203.2997388	0.07	0.1	183.6	87.303	150000000	0.3	2601.552076	2	203.2997388	72.2222
49	194.8270991	0.07	0.1	174.9	85.8346	150000000	0.3	2241.337062	2	194.8270991	62.2222
50	186.3903733	0.065	0.1	166.2	84.3737	150000000	0.3	2243.175004	2	186.3903733	72.2222
51	177.9944369	0.065	0.1	157.5	82.9202	150000000	0.3	1621.987889	2	177.9944369	52.2222
52	169.645156	0.065	0.1	148.8	81.4741	150000000	0.3	1311.394331	2	169.645156	42.2222
53	161.3496243	0.065	0.1	140.1	80.0355	150000000	0.3	690.2072158	2	161.3496243	22.2222
54	153.1163152	0.065	0.1	131.4	78.6043	150000000	0.3	0	2	153.1163152	0
55	144.9556657	0.06	0.1	122.7	77.1806	150000000	0.3	588.1055566	2	144.9556657	22.2222
56	136.8803827	0.06	0.1	114	75.7643	150000000	0.3	323.4577915	2	136.8803827	12.2222
57	128.9062664	0.06	0.1	105.3	74.3554	150000000	0.3	0	2	128.9062664	0
58	121.0530525	0.06	0.1	96.6	72.9539	150000000	0.3	0	2	121.0530525	0
59	113.3456629	0.055	0.1	87.9	71.5599	150000000	0.3	0	2	113.3456629	0
60	105.8156702	0.055	0.1	79.2	70.1734	150000000	0.3	0	2	105.8156702	0
61	98.50330935	0.055	0.1	70.5	68.7942	150000000	0.3	0	2	98.50330935	0
62	91.46053806	0.05	0.1	61.8	67.4224	150000000	0.3	0	2	91.46053806	0
63	84.75025427	0.05	0.1	53.1	66.0529	150000000	0.3	224.6234663	2	84.75025427	12.2222
64	78.45579797	0.05	0.1	44.4	64.6834	150000000	0.3	592.1898068	2	78.45579797	32.2222
65	72.68528003	0.06	0.1	35.7	63.3139	150000000	0.3	1117.401087	2	72.68528003	42.2222
66	67.57306188	0.065	0.1	27	61.9444	150000000	0.3	4106.73635	2	67.57306188	132.2222
67	228.8944254	0.07	-0.1	209.7	91.7527	150000000	0.3	4402.627144	2	228.8944254	122.2222
68	220.3366484	0.07	-0.1	201	90.262	150000000	0.3	4042.412131	2	220.3366484	112.2222
69	211.8040966	0.07	-0.1	192.3	88.7788	150000000	0.3	3682.197117	2	211.8040966	102.2222
70	203.2997388	0.07	-0.1	183.6	87.303	150000000	0.3	2601.552076	2	203.2997388	72.2222
71	194.8270991	0.07	-0.1	174.9	85.8346	150000000	0.3	2241.337062	2	194.8270991	62.2222
72	186.3903733	0.065	-0.1	166.2	84.3737	150000000	0.3	2243.175004	2	186.3903733	72.2222
73	177.9944369	0.065	-0.1	157.5	82.9202	150000000	0.3	1621.987889	2	177.9944369	52.2222
74	169.645156	0.065	-0.1	148.8	81.4741	150000000	0.3	1311.394331	2	169.645156	42.2222
75	161.3496243	0.065	-0.1	140.1	80.0355	150000000	0.3	690.2072158	2	161.3496243	22.2222
76	153.1163152	0.065	-0.1	131.4	78.6043	150000000	0.3	0	2	153.1163152	0
77	144.9556657	0.06	-0.1	122.7	77.1806	150000000	0.3	588.1055566	2	144.9556657	22.2222
78	136.8803827	0.06	-0.1	114	75.7643	150000000	0.3	323.4577915	2	136.8803827	12.2222
79	128.9062664	0.06	-0.1	105.3	74.3554	150000000	0.3	0	2	128.9062664	0
80	121.0530525	0.06	-0.1	96.6	72.9539	150000000	0.3	0	2	121.0530525	0
81	113.3456629	0.055	-0.1	87.9	71.5599	150000000	0.3	0	2	113.3456629	0
82	105.8156702	0.055	-0.1	79.2	70.1734	150000000	0.3	0	2	105.8156702	0
83	98.50330935	0.055	-0.1	70.5	68.7942	150000000	0.3	0	2	98.50330935	0
84	91.46053806	0.05	-0.1	61.8	67.4224	150000000	0.3	0	2	91.46053806	0

No.	AY	Radius	dx	dy	dz	EE	UU	FP	NFP	YFP	Temp
85	84.75025427	0.05	-0.1	53.1	66.0529	150000000	0.3	224.6234663	2	84.75025427	12.2222
86	78.45579797	0.05	-0.1	44.4	64.6834	150000000	0.3	592.1898068	2	78.45579797	32.2222
87	72.68528003	0.06	-0.1	35.7	63.3139	150000000	0.3	1117.401087	2	72.68528003	42.2222
88	67.57306188	0.065	-0.1	27	61.9444	150000000	0.3	4106.73635	2	67.57306188	132.2222
89	228.8944254	0.07	-0.1	209.7	-91.7527	150000000	0.3	4402.627144	2	228.8944254	122.2222
90	220.3366484	0.07	-0.1	201	-90.262	150000000	0.3	4402.627144	2	220.3366484	122.2222
91	211.8040966	0.07	-0.1	192.3	-88.7788	150000000	0.3	3682.197117	2	211.8040966	102.2222
92	203.2997388	0.07	-0.1	183.6	-87.303	150000000	0.3	2601.552076	2	203.2997388	72.2222
93	194.8270991	0.065	-0.1	174.9	-85.8346	150000000	0.3	2864.36212	2	194.8270991	92.2222
94	186.3903733	0.065	-0.1	166.2	-84.3737	150000000	0.3	2243.175004	2	186.3903733	72.2222
95	177.9944369	0.065	-0.1	157.5	-82.9202	150000000	0.3	1932.581447	2	177.9944369	62.2222
96	169.645156	0.065	-0.1	148.8	-81.4741	150000000	0.3	1311.394331	2	169.645156	42.2222
97	161.3496243	0.065	-0.1	140.1	-80.0355	150000000	0.3	690.2072158	2	161.3496243	22.2222
98	153.1163152	0.065	-0.1	131.4	-78.6043	150000000	0.3	379.6136581	2	153.1163152	12.2222
99	144.9556657	0.06	-0.1	122.7	-77.1806	150000000	0.3	852.7533218	2	144.9556657	32.2222
100	136.8803827	0.06	-0.1	114	-75.7643	150000000	0.3	588.1055566	2	136.8803827	22.2222
101	128.9062664	0.06	-0.1	105.3	-74.3554	150000000	0.3	0	2	128.9062664	0
102	121.0530525	0.06	-0.1	96.6	-72.9539	150000000	0.3	0	2	121.0530525	0
103	113.3456629	0.055	-0.1	87.9	-71.5599	150000000	0.3	271.7943943	2	113.3456629	12.2222
104	105.8156702	0.055	-0.1	79.2	-70.1734	150000000	0.3	0	2	105.8156702	0
105	98.50330935	0.055	-0.1	70.5	-68.7942	150000000	0.3	0	2	98.50330935	0
106	91.46053806	0.05	-0.1	61.8	-67.4224	150000000	0.3	224.6234663	2	91.46053806	12.2222
107	84.75025427	0.05	-0.1	53.1	-66.0529	150000000	0.3	592.1898068	2	84.75025427	32.2222
108	78.45579797	0.05	-0.1	44.4	-64.6834	150000000	0.3	775.972977	2	78.45579797	42.2222
109	72.68528003	0.06	-0.1	35.7	-63.3139	150000000	0.3	1382.048852	2	72.68528003	52.2222
110	67.57306188	0.06	-0.1	27	-61.9444	150000000	0.3	5087.117564	2	67.57306188	192.2222
111	228.8944254	0.07	0.1	209.7	-91.7527	150000000	0.3	4402.627144	2	228.8944254	122.2222
112	220.3366484	0.07	0.1	201	-90.262	150000000	0.3	4402.627144	2	220.3366484	122.2222
113	211.8040966	0.07	0.1	192.3	-88.7788	150000000	0.3	3682.197117	2	211.8040966	102.2222
114	203.2997388	0.07	0.1	183.6	-87.303	150000000	0.3	2601.552076	2	203.2997388	72.2222
115	194.8270991	0.065	0.1	174.9	-85.8346	150000000	0.3	2864.36212	2	194.8270991	92.2222
116	186.3903733	0.065	0.1	166.2	-84.3737	150000000	0.3	2243.175004	2	186.3903733	72.2222
117	177.9944369	0.065	0.1	157.5	-82.9202	150000000	0.3	1932.581447	2	177.9944369	62.2222
118	169.645156	0.065	0.1	148.8	-81.4741	150000000	0.3	1311.394331	2	169.645156	42.2222
119	161.3496243	0.065	0.1	140.1	-80.0355	150000000	0.3	690.2072158	2	161.3496243	22.2222
120	153.1163152	0.065	0.1	131.4	-78.6043	150000000	0.3	379.6136581	2	153.1163152	12.2222
121	144.9556657	0.06	0.1	122.7	-77.1806	150000000	0.3	852.7533218	2	144.9556657	32.2222
122	136.8803827	0.06	0.1	114	-75.7643	150000000	0.3	588.1055566	2	136.8803827	22.2222
123	128.9062664	0.06	0.1	105.3	-74.3554	150000000	0.3	0	2	128.9062664	0
124	121.0530525	0.06	0.1	96.6	-72.9539	150000000	0.3	0	2	121.0530525	0
125	113.3456629	0.055	0.1	87.9	-71.5599	150000000	0.3	271.7943943	2	113.3456629	12.2222
126	105.8156702	0.055	0.1	79.2	-70.1734	150000000	0.3	0	2	105.8156702	0

No.	AY	Radius	dx	dy	dz	EE	UU	FP	NFP	YFP	Temp
127	98.50330935	0.055	0.1	70.5	-68.7942	150000000	0.3	0	2	98.50330935	0
128	91.46053806	0.05	0.1	61.8	-67.4224	150000000	0.3	224.6234663	2	91.46053806	12.2222
129	84.75025427	0.05	0.1	53.1	-66.0529	150000000	0.3	592.1898068	2	84.75025427	32.2222
130	78.45579797	0.05	0.1	44.4	-64.6834	150000000	0.3	775.972977	2	78.45579797	42.2222
131	72.68528003	0.06	0.1	35.7	-63.3139	150000000	0.3	1382.048852	2	72.68528003	52.2222
132	67.57306188	0.06	0.1	27	-61.9444	150000000	0.3	5087.117564	2	67.57306188	192.2222
133	182.4869758	0.07	0.1	155.1	96.1534	150000000	0.3	2961.76709	2	182.4869758	82.2222
134	176.4736891	0.07	0.1	149	94.5619	150000000	0.3	2961.76709	2	176.4736891	82.2222
135	170.4814221	0.07	0.1	142.9	92.9704	150000000	0.3	2601.552076	2	170.4814221	72.2222
136	164.5124718	0.07	0.1	136.8	91.3789	150000000	0.3	1881.122049	2	164.5124718	52.2222
137	158.5694712	0.07	0.1	130.7	89.7874	150000000	0.3	1520.907035	2	158.5694712	42.2222
138	152.6554512	0.07	0.1	124.6	88.1959	150000000	0.3	1160.692021	2	152.6554512	32.2222
139	146.7739149	0.065	0.1	118.5	86.6044	150000000	0.3	1932.581447	2	146.7739149	62.2222
140	140.9289295	0.065	0.1	112.4	85.0129	150000000	0.3	1621.987889	2	140.9289295	52.2222
141	135.1252381	0.065	0.1	106.3	83.4214	150000000	0.3	1621.987889	2	135.1252381	52.2222
142	129.3683985	0.065	0.1	100.2	81.8299	150000000	0.3	1311.394331	2	129.3683985	42.2222
143	123.6649539	0.065	0.1	94.1	80.2384	150000000	0.3	1000.800773	2	123.6649539	32.2222
144	118.0226456	0.065	0.1	88	78.6469	150000000	0.3	1000.800773	2	118.0226456	32.2222
145	112.4506766	0.06	0.1	81.9	77.0554	150000000	0.3	1646.696617	2	112.4506766	62.2222
146	106.9647674	0.06	0.1	75.8	75.4706	150000000	0.3	1382.048852	2	106.9647674	52.2222
147	101.5688014	0.06	0.1	69.7	73.8791	150000000	0.3	1117.401087	2	101.5688014	42.2222
148	96.28326497	0.055	0.1	63.6	72.2876	150000000	0.3	1828.437846	2	96.28326497	82.2222
149	91.12737544	0.055	0.1	57.5	70.6961	150000000	0.3	1383.682574	2	91.12737544	62.2222
150	86.12442012	0.05	0.1	51.4	69.1046	150000000	0.3	1878.671998	2	86.12442012	102.2222
151	81.30263631	0.05	0.1	45.3	67.5131	150000000	0.3	1878.671998	2	81.30263631	102.2222
152	76.69620164	0.05	0.1	39.2	65.9216	150000000	0.3	1878.671998	2	76.69620164	102.2222
153	72.34626297	0.06	0.1	33.1	64.3301	150000000	0.3	2440.639913	2	72.34626297	92.2222
154	68.30184426	0.06	0.1	27	62.7386	150000000	0.3	5351.765329	2	68.30184426	202.2222
155	182.4869758	0.07	-0.1	155.1	96.1534	150000000	0.3	2961.76709	2	182.4869758	82.2222
156	176.4736891	0.07	-0.1	149	94.5619	150000000	0.3	2961.76709	2	176.4736891	82.2222
157	170.4814221	0.07	-0.1	142.9	92.9704	150000000	0.3	2601.552076	2	170.4814221	72.2222
158	164.5124718	0.07	-0.1	136.8	91.3789	150000000	0.3	1881.122049	2	164.5124718	52.2222
159	158.5694712	0.07	-0.1	130.7	89.7874	150000000	0.3	1520.907035	2	158.5694712	42.2222
160	152.6554512	0.07	-0.1	124.6	88.1959	150000000	0.3	1160.692021	2	152.6554512	32.2222
161	146.7739149	0.065	-0.1	118.5	86.6044	150000000	0.3	1932.581447	2	146.7739149	62.2222
162	140.9289295	0.065	-0.1	112.4	85.0129	150000000	0.3	1621.987889	2	140.9289295	52.2222
163	135.1252381	0.065	-0.1	106.3	83.4214	150000000	0.3	1621.987889	2	135.1252381	52.2222
164	129.3683985	0.065	-0.1	100.2	81.8299	150000000	0.3	1311.394331	2	129.3683985	42.2222
165	123.6649539	0.065	-0.1	94.1	80.2384	150000000	0.3	1000.800773	2	123.6649539	32.2222
166	118.0226456	0.065	-0.1	88	78.6469	150000000	0.3	1000.800773	2	118.0226456	32.2222
167	112.4506766	0.06	-0.1	81.9	77.0554	150000000	0.3	1646.696617	2	112.4506766	62.2222
168	106.9647674	0.06	-0.1	75.8	75.4706	150000000	0.3	1382.048852	2	106.9647674	52.2222

No.	AY	Radius	dx	dy	dz	EE	UU	FP	NFP	YFP	Temp
169	101.5688014	0.06	-0.1	69.7	73.8791	150000000	0.3	1117.401087	2	101.5688014	42.2222
170	96.28326497	0.055	-0.1	63.6	72.2876	150000000	0.3	1828.437846	2	96.28326497	82.2222
171	91.12737544	0.055	-0.1	57.5	70.6961	150000000	0.3	1383.682574	2	91.12737544	62.2222
172	86.12442012	0.05	-0.1	51.4	69.1046	150000000	0.3	1878.671998	2	86.12442012	102.2222
173	81.30263631	0.05	-0.1	45.3	67.5131	150000000	0.3	1878.671998	2	81.30263631	102.2222
174	76.69620164	0.05	-0.1	39.2	65.9216	150000000	0.3	1878.671998	2	76.69620164	102.2222
175	72.34626297	0.06	-0.1	33.1	64.3301	150000000	0.3	2440.639913	2	72.34626297	92.2222
176	68.30184426	0.06	-0.1	27	62.7386	150000000	0.3	5351.765329	2	68.30184426	202.2222

APPENDIX C

1) Load: Fa+Fb+Fc+Fd

Table C-1 Deflection under static load: Fa+Fb+Fc+Fd for lamina (3)

		Location	A (375m)	B (493.4m)	C (590m)	D (Tower 1 left-top)	E (Tower 2 left-top)
Load Fa+Fb+ Fc+Fd	u (mm)	LFSM	98.64	60.02	17.82	111.86	66.99
		FEM	101.47	61.69	17.84	108.58	68.62
	v (mm)	LFSM	6.81	1.25	2.88	125.62	235.88
		FEM	6.72	1.22	2.99	126.11	238.79
	w (mm)	LFSM	766.16	92.14	0.02	3.22	2.98
		FEM	762.41	103.39	0.00	3.06	3.03

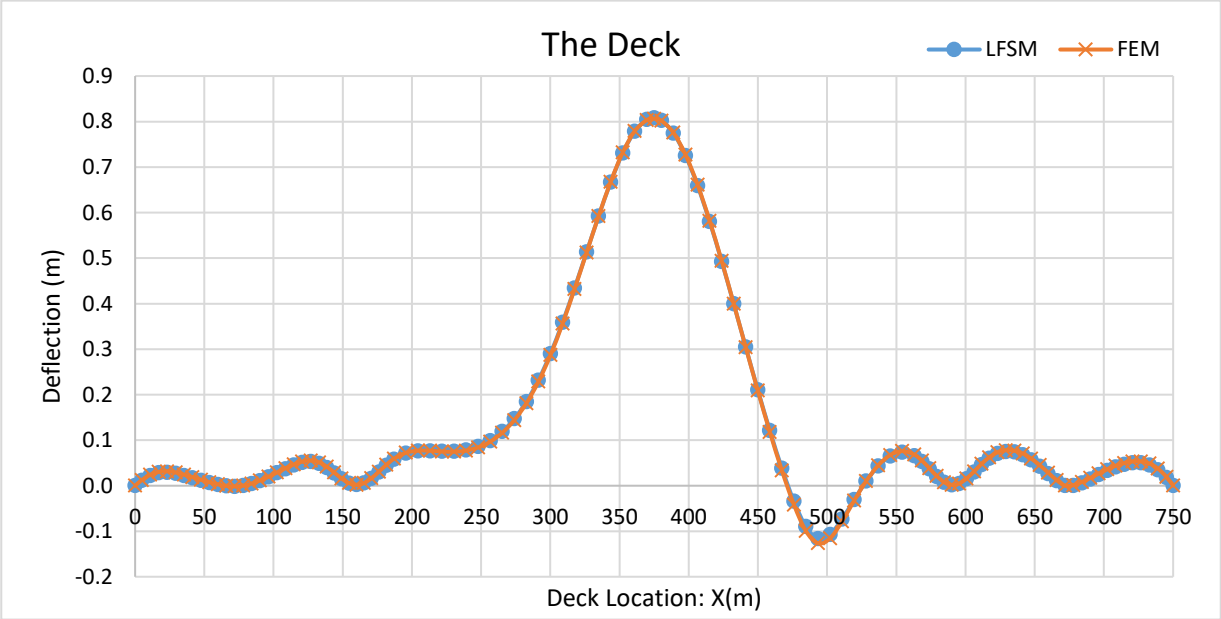

a) Deflection deflection *w* on the deck: Nodal line 4.

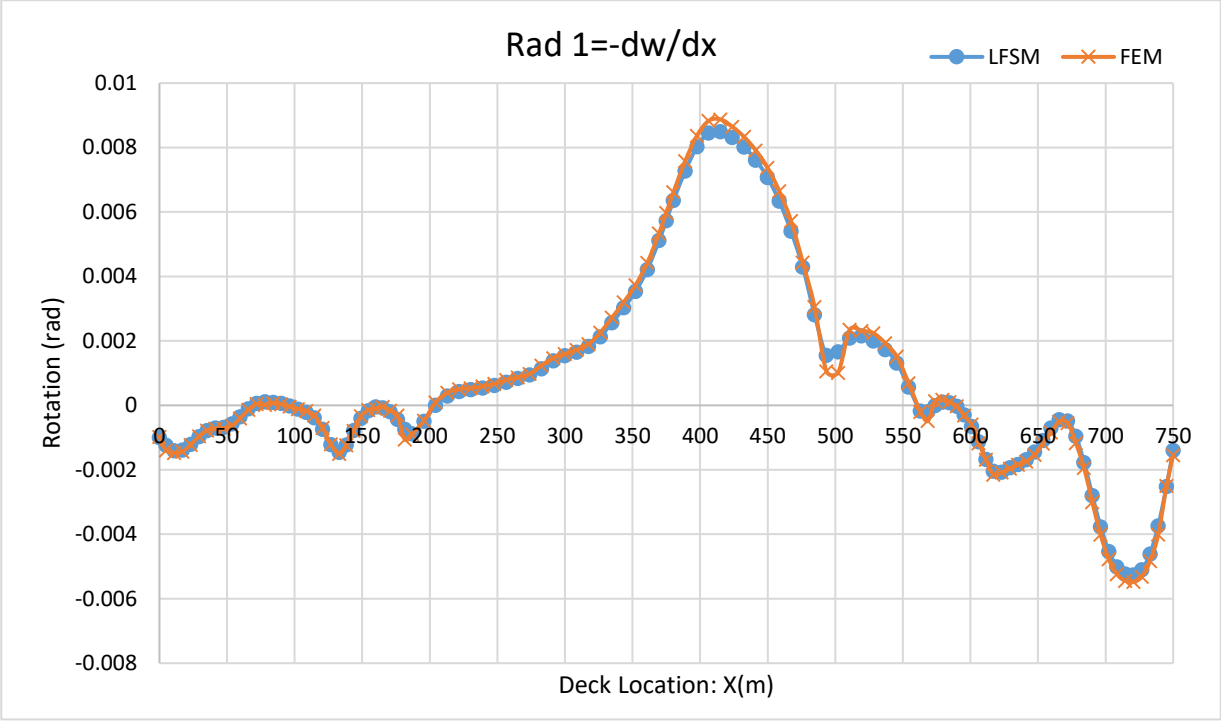

b) Rotation on the deck (Rad 1): Nodal line 4.

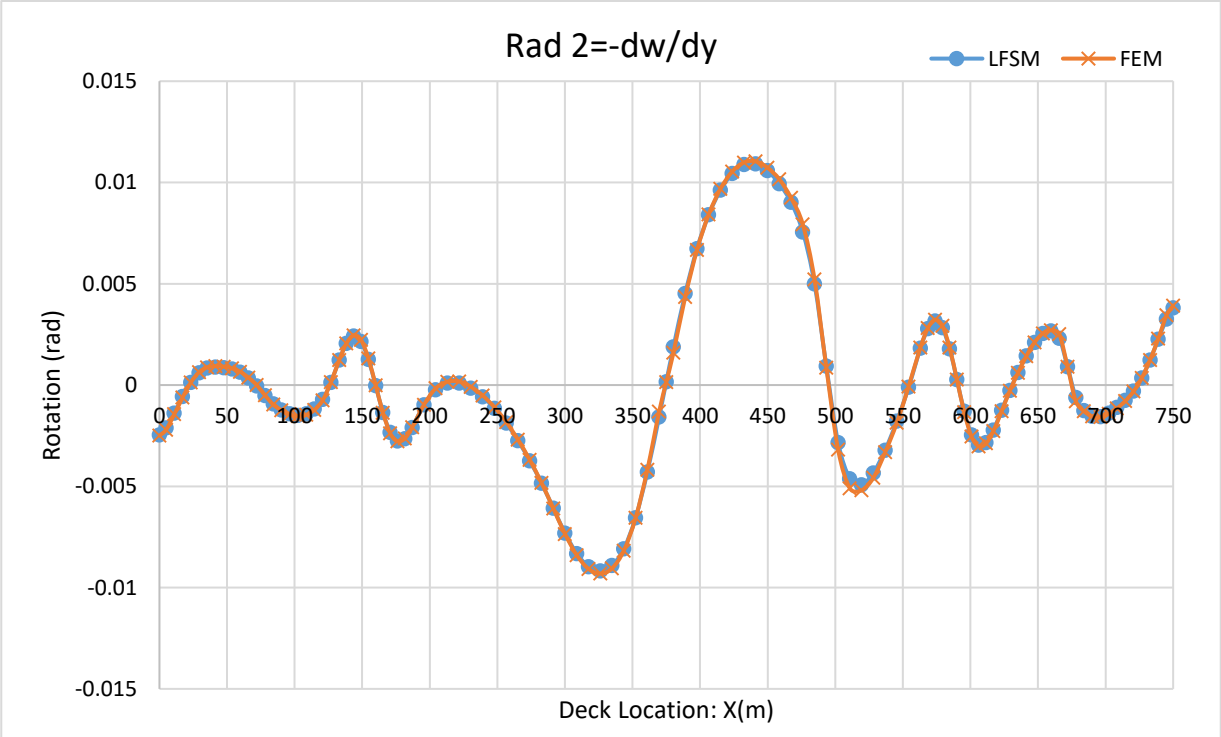

c) Rotation on the deck (Rad 2): Nodal line 4.

Figure C-1 Deflections and rotations under load Fa+Fb+Fc+Fd for lamina (3)

2) Load: Fe

Table C-2 Deflection under static load: Fe for lamina (3)

		Location	A (375m)	B (493.4m)	C (590m)	D (Tower 1 left-top)	E (Tower 2 left-top)
Load Fe	u (mm)	LFSM	1.77	2.93	1.62	33.78	12.91
		FEM	1.69	3.07	1.69	33.88	13.68
	v (mm)	LFSM	1.29	4.34	4.65	304.09	137.16
		FEM	1.44	4.41	4.55	309.76	137.74
	w (mm)	LFSM	839.67	123.31	0.31	1.75	0.03
		FEM	838.80	121.57	0.30	1.73	0.08

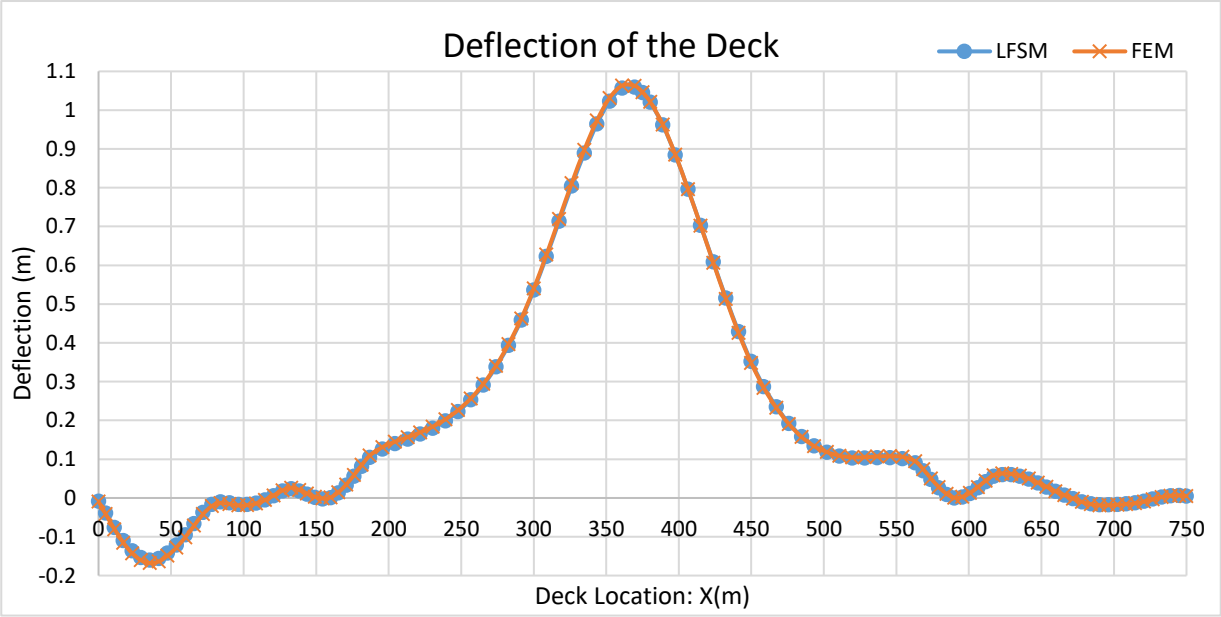

a) Deflection deflection *w* on the deck: Nodal line 1.

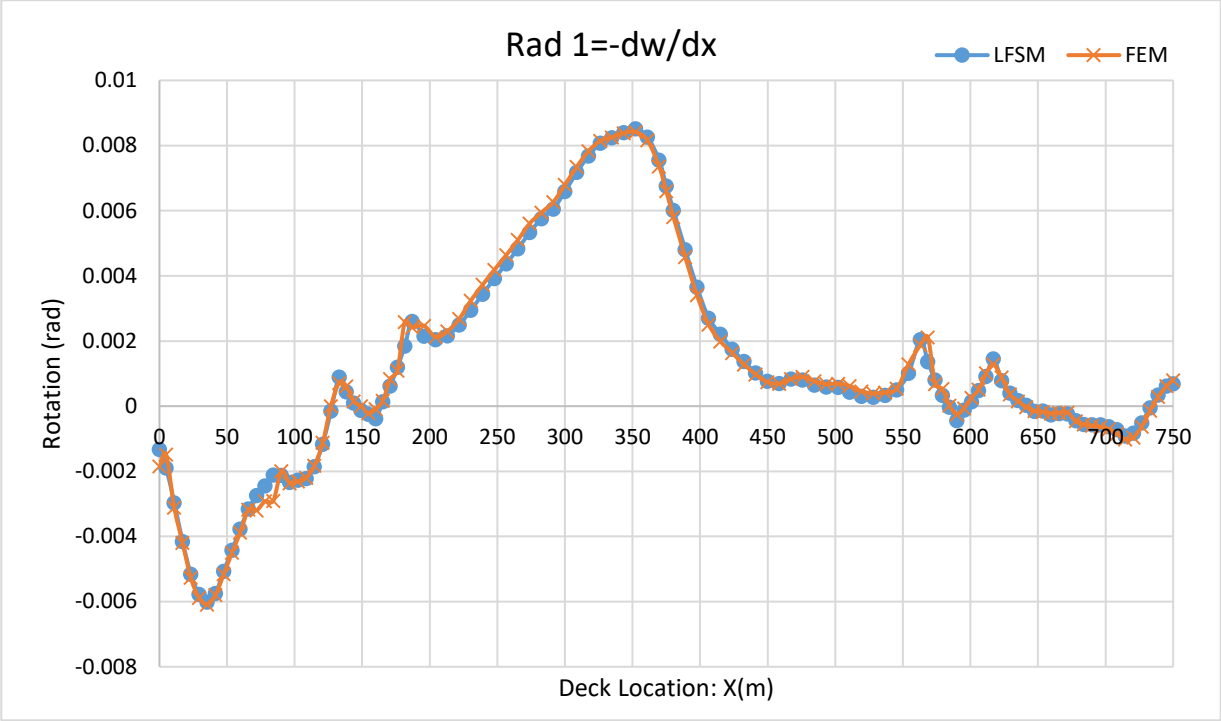

b) Rotation on the deck (Rad 1): Nodal line 1.

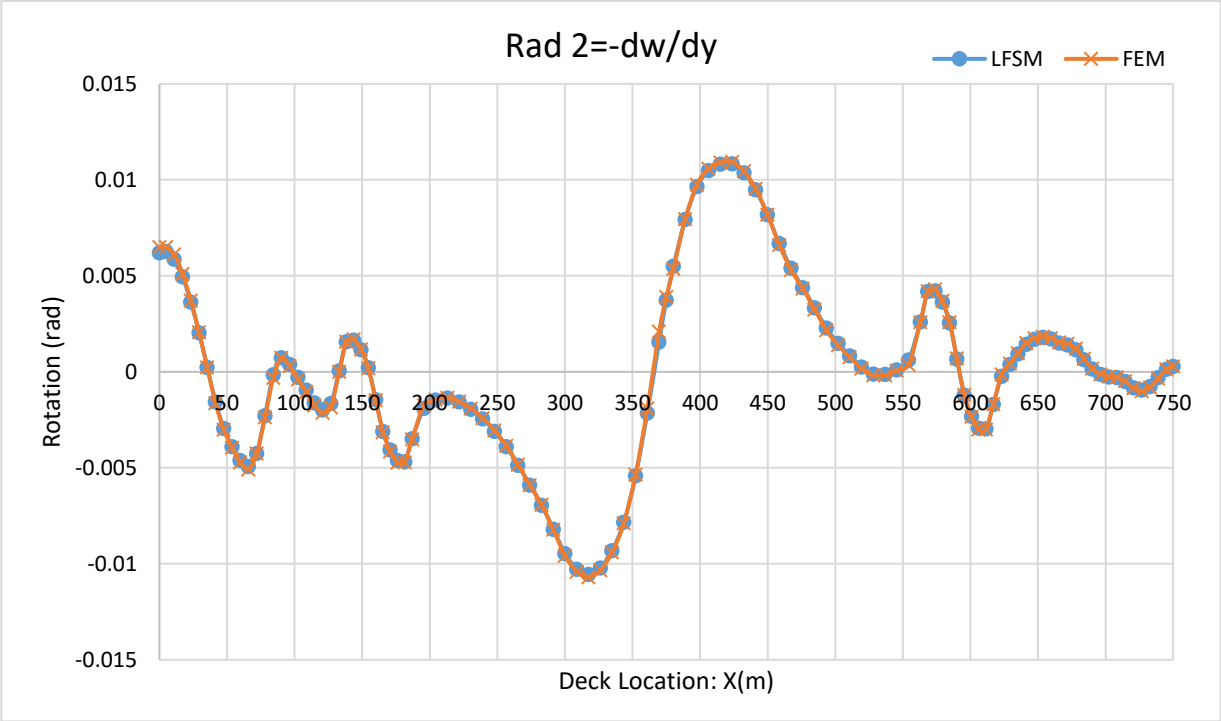

c) Rotation on the deck (Rad 2): Nodal line 1.

Figure C-2 Deflections and rotations under load Fe for lamina (3)

APPENDIX D

D-1 UNIFORM EXCITATION

1) UNIFORM SINE WAVE EXCITATION

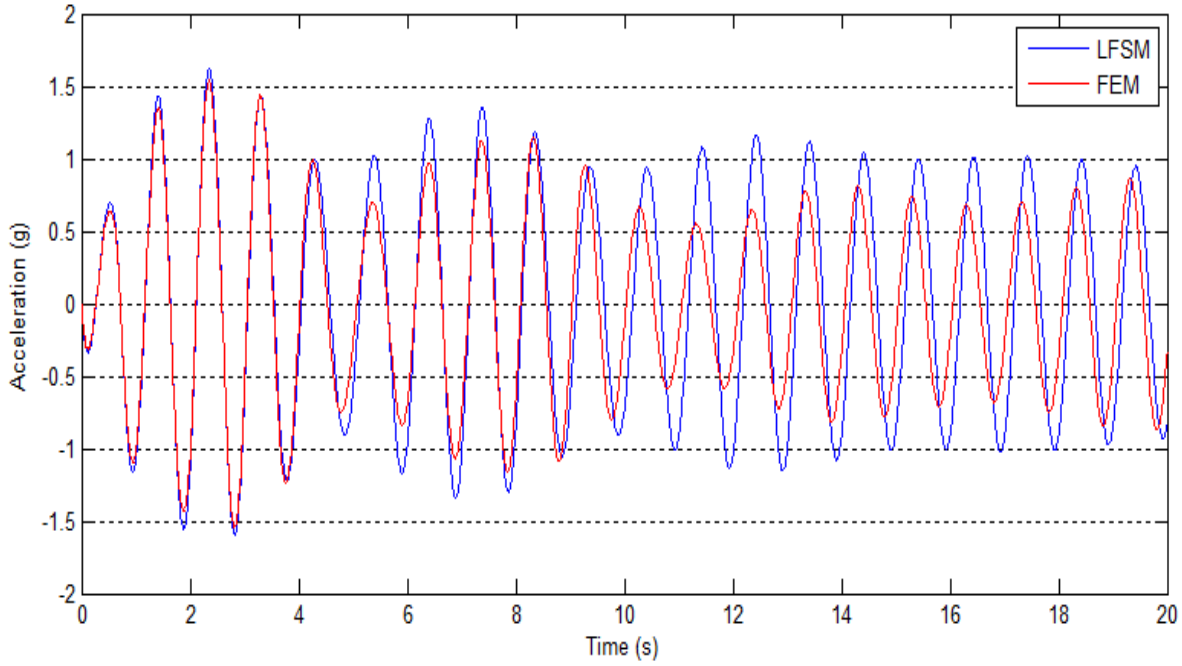

a) Longitudinal Acceleration Responses at Point F

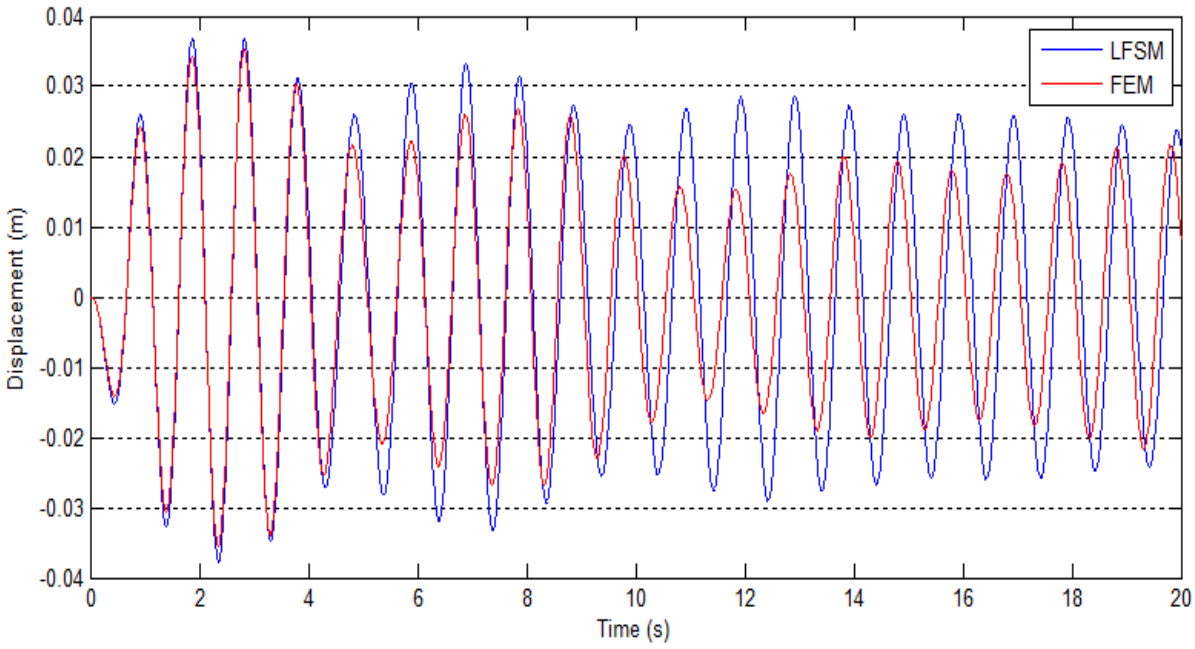

b) Longitudinal Acceleration Responses at Point F

Figure D-3 Longitudinal responses under uniform sine wave excitation at Point F

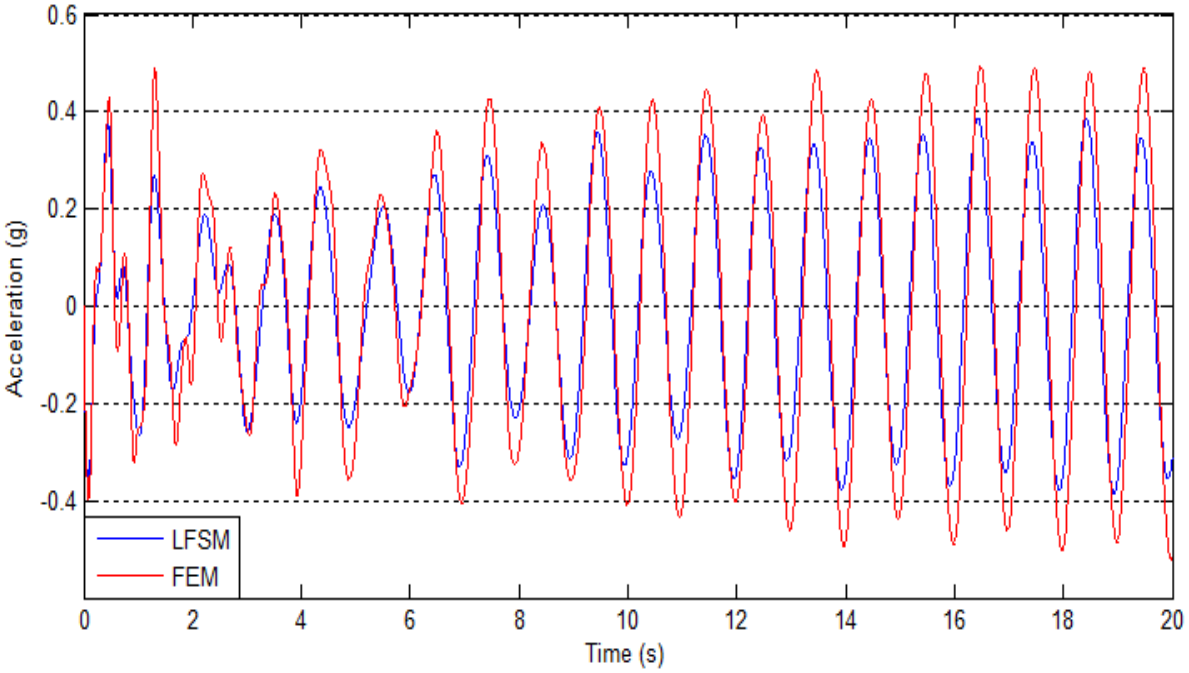

a) Transverse Acceleration Responses at Point D

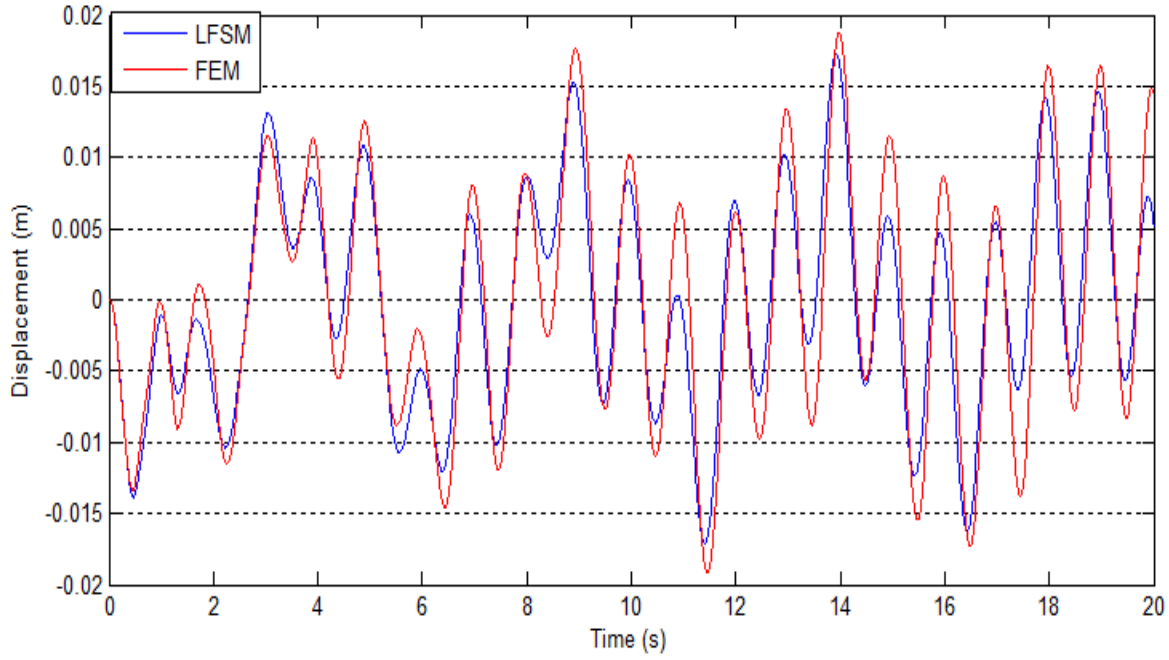

b) Transverse Displacement Responses at Point D

Figure D-4 Transverse responses under uniform sine wave excitation at Point D

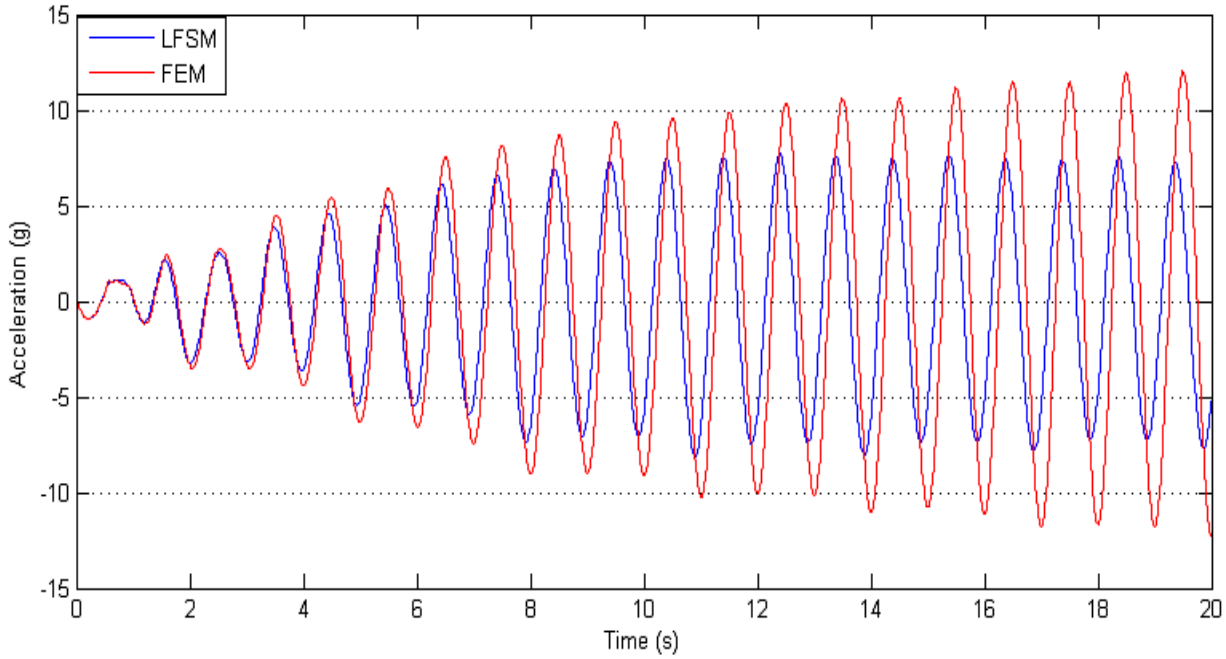

a) Vertical Acceleration Responses at Point A

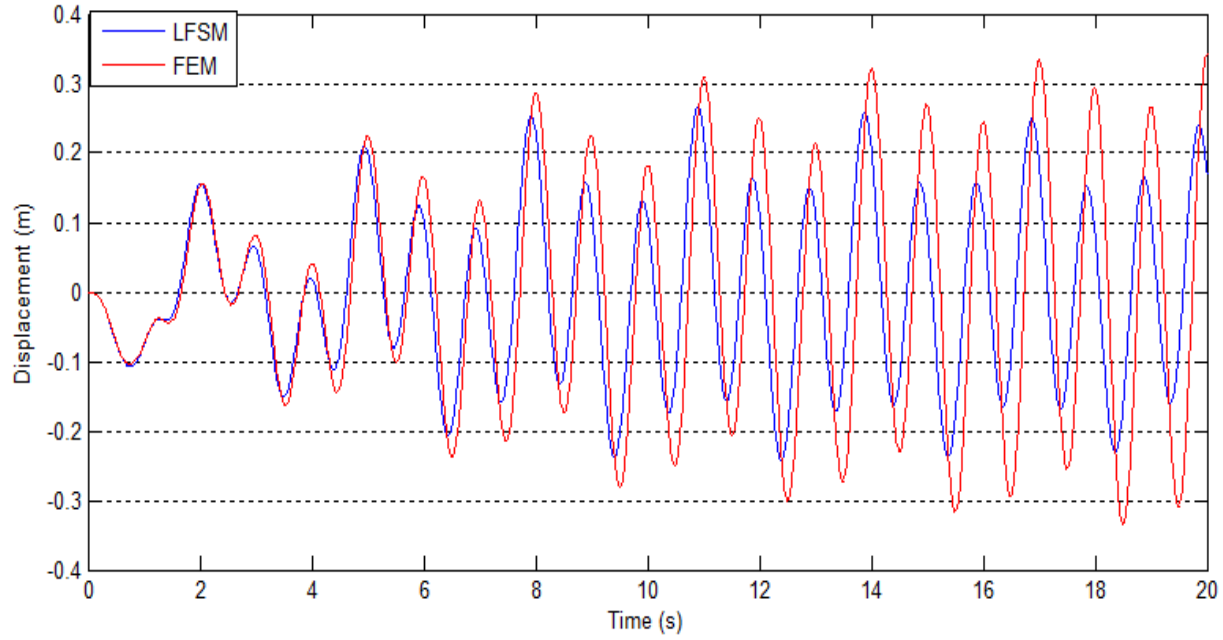

b) Vertical Displacement Responses at Point A

Figure D-5 Vertical responses under uniform sine wave excitation at Point A

2) UNIFORM CHICHI EARTHQUAKE EXCITATION

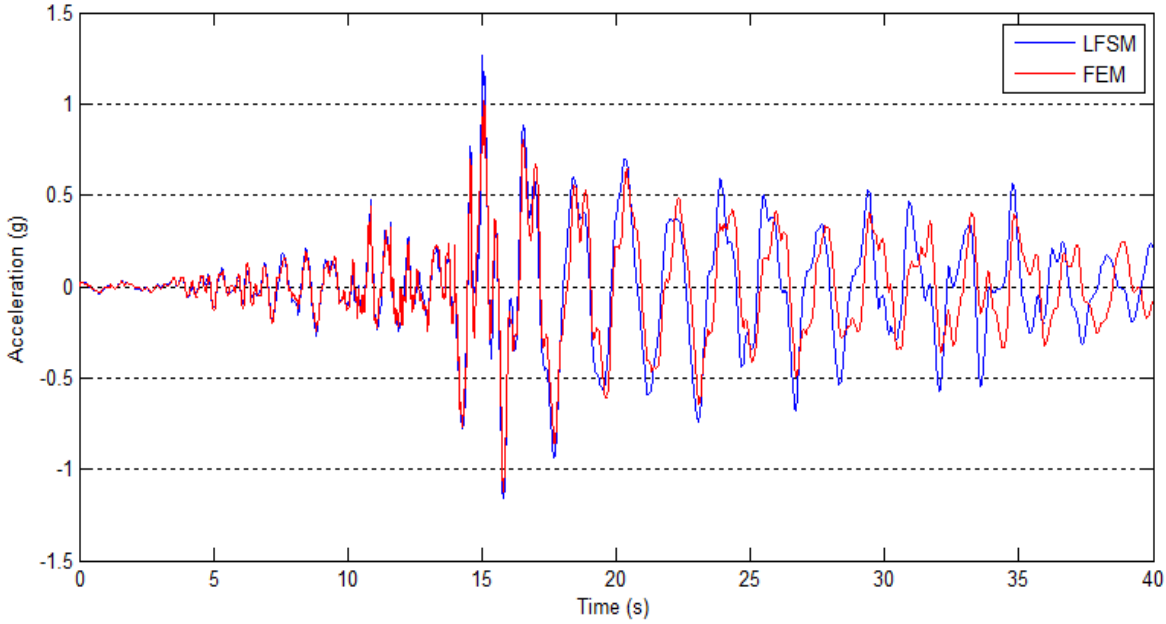

a) Transverse Acceleration Responses at Point B

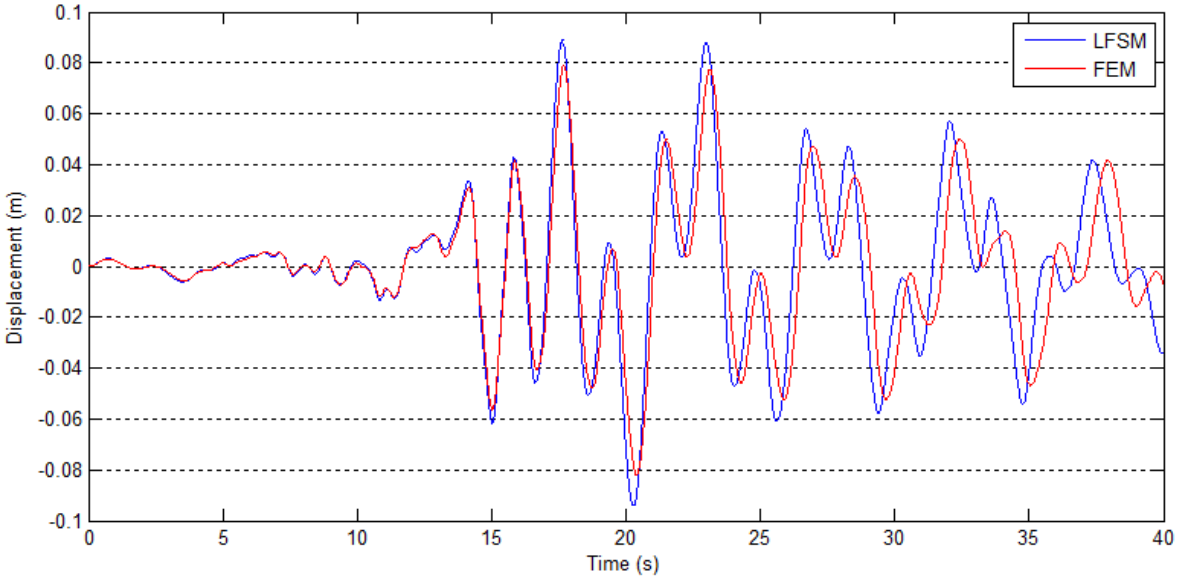

b) Transverse Displacement Responses at Point B

Figure D-6 Transverse responses under uniform Chichi earthquake excitation at Point B

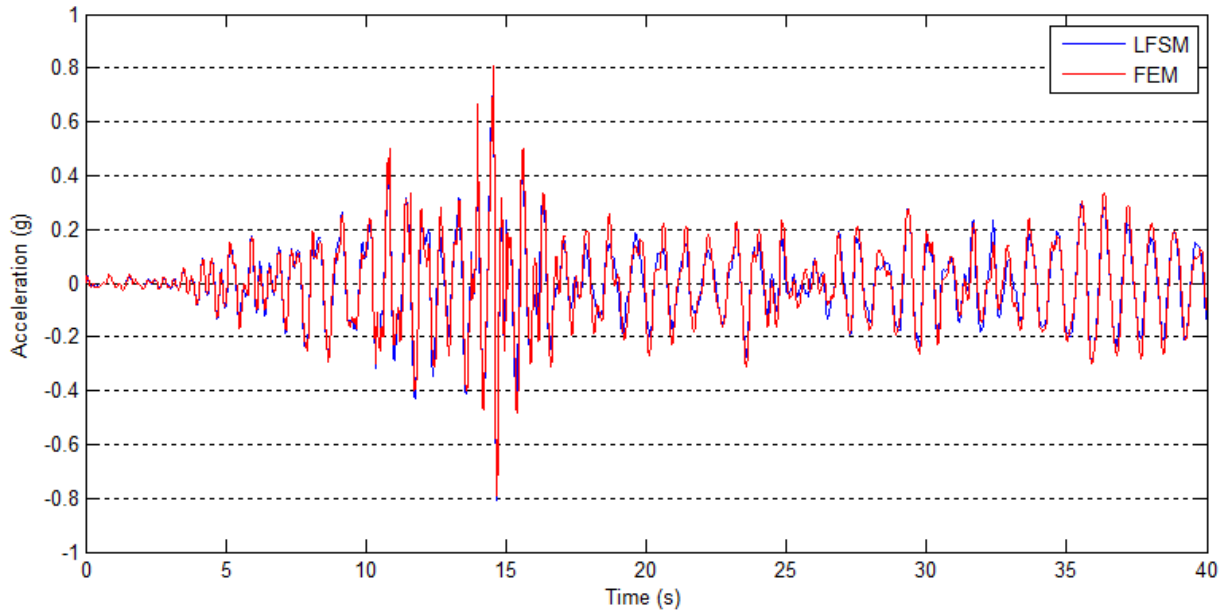

a) Longitudinal Acceleration Responses at Point C

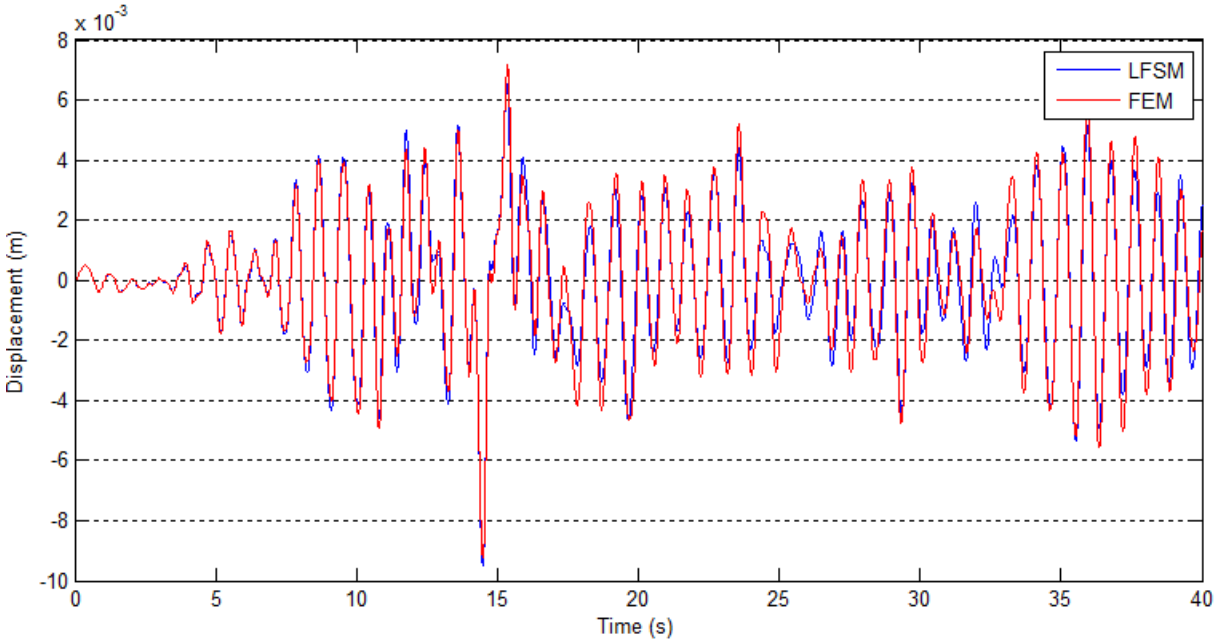

b) Longitudinal Displacement Responses at Point C

Figure D-7 Longitudinal responses under uniform Chichi earthquake excitation at Point C

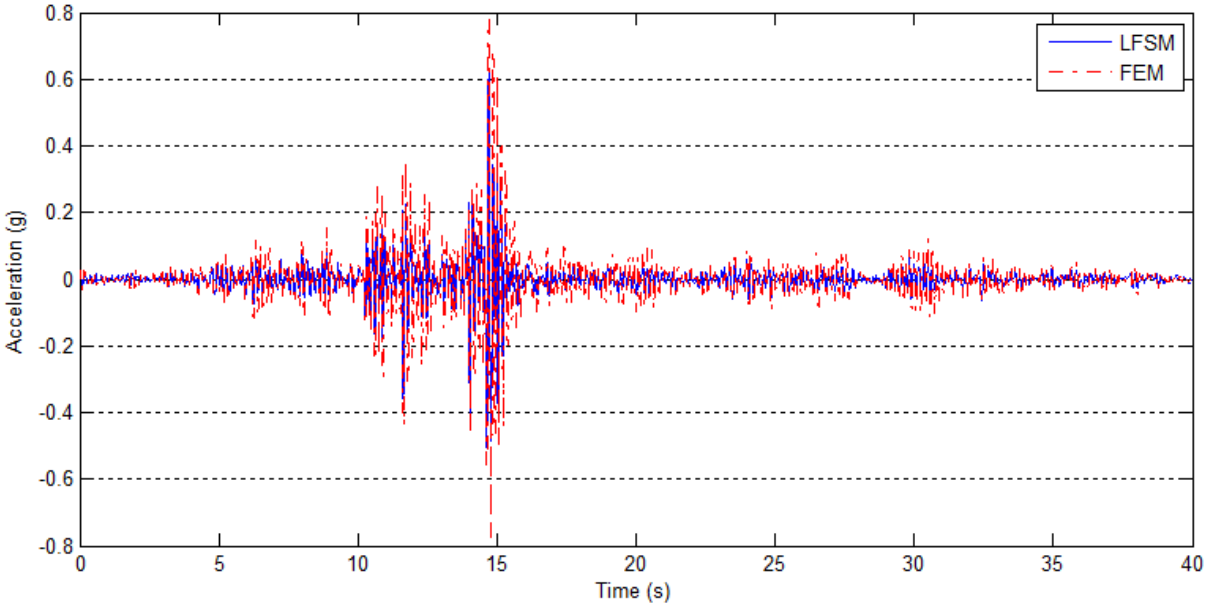

a) Vertical Acceleration Responses at Point E

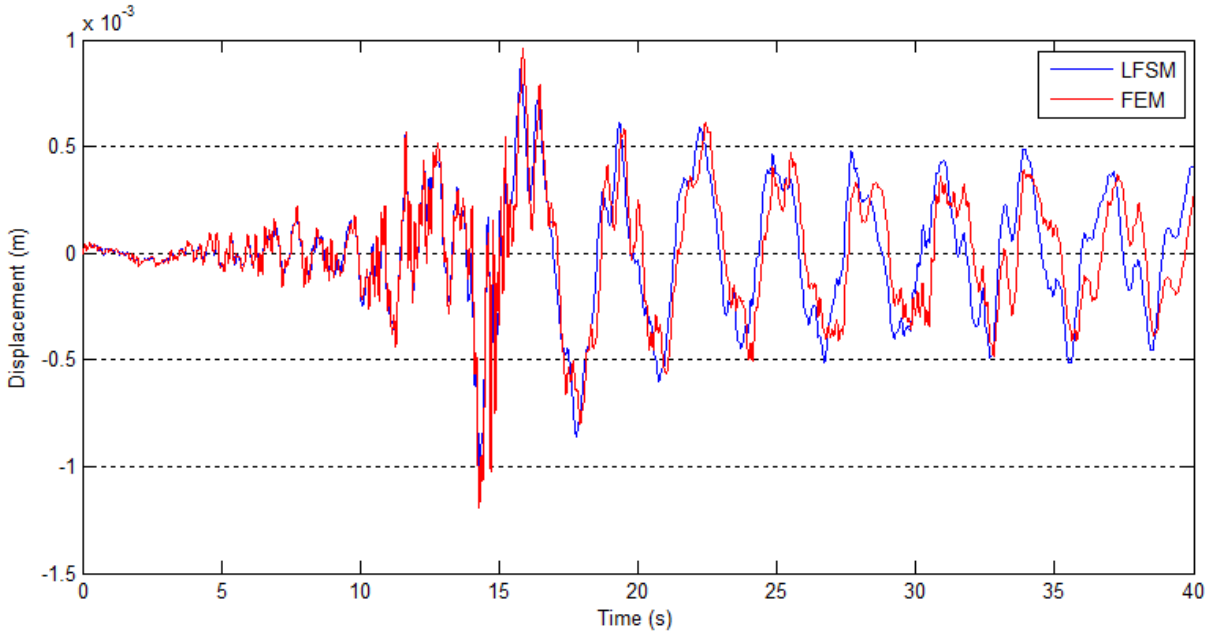

b) Vertical Displacement Responses at Point E

Figure D-8 Vertical responses under uniform Chichi earthquake excitation at Point E

D-2 NONUNIFORM EXCITATION

1) WAVE PASSAGE EFFECT

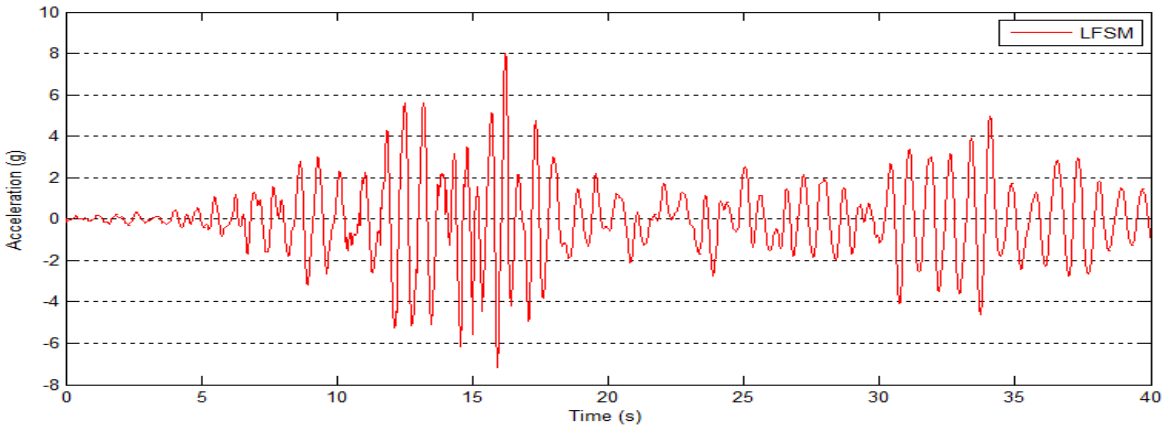

a) Longitudinal acceleration at Point E at the west tower for velocity = 500 m/s

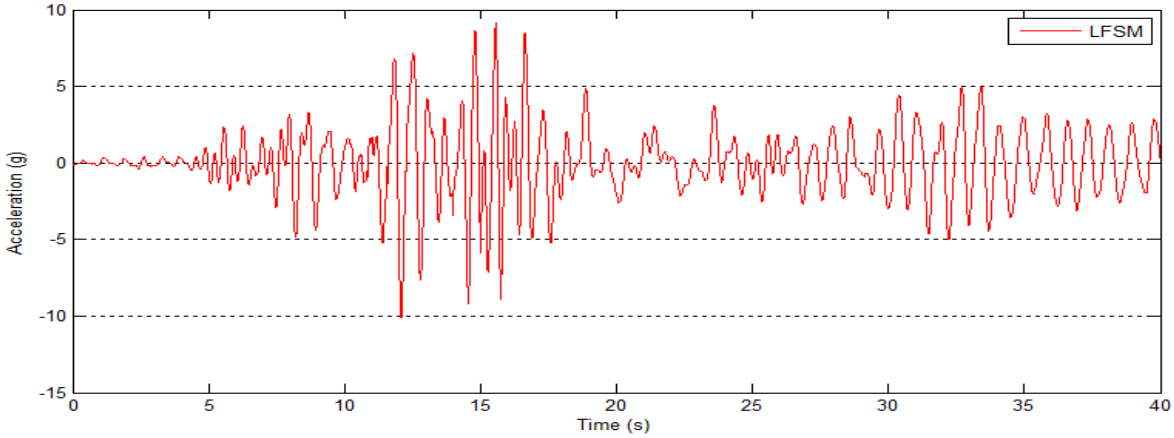

b) Longitudinal acceleration at Point E at the west tower for velocity = 1000 m/s

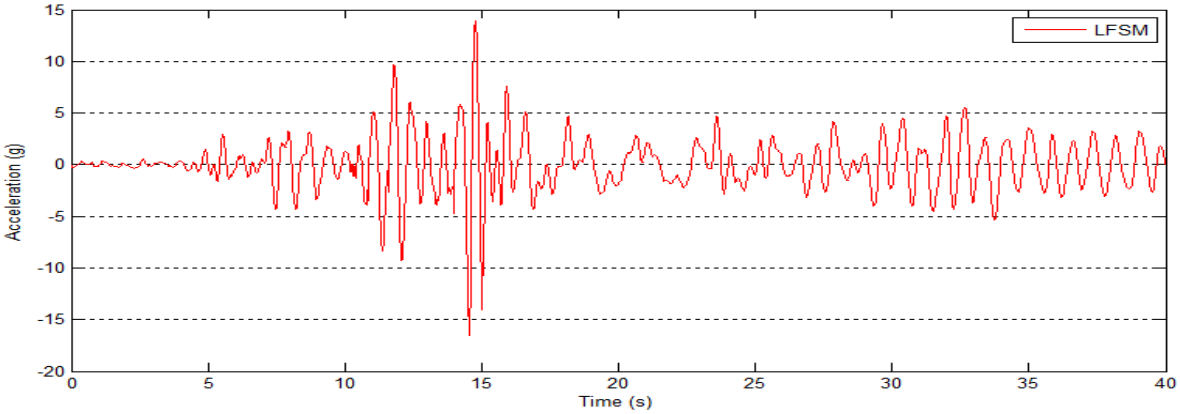

c) Longitudinal acceleration at Point E at the west tower for velocity = infinite

Figure D-9 Longitudinal acceleration response under nonuniform Chichi earthquake excitation for wave passage effects at Point E

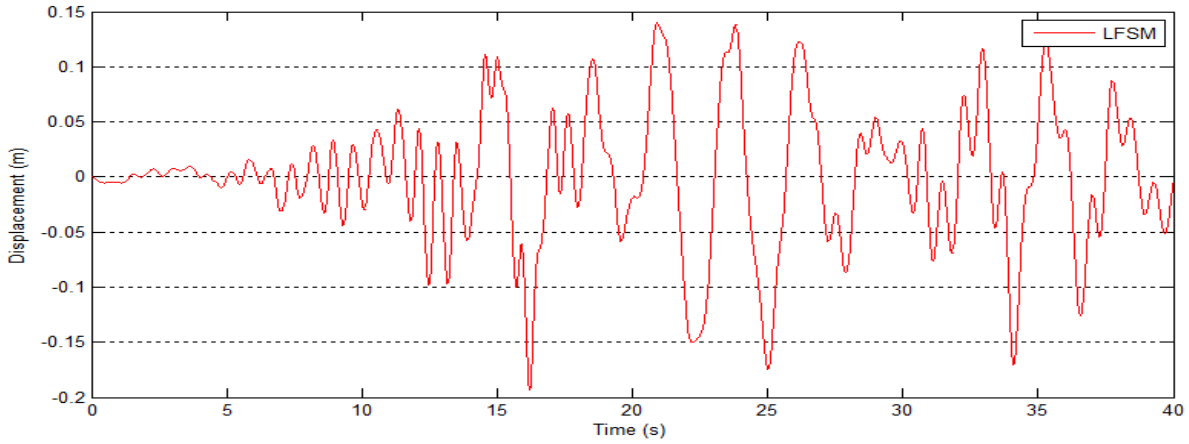

a) Longitudinal displacement at Point E at the west tower for velocity = 500 m/s

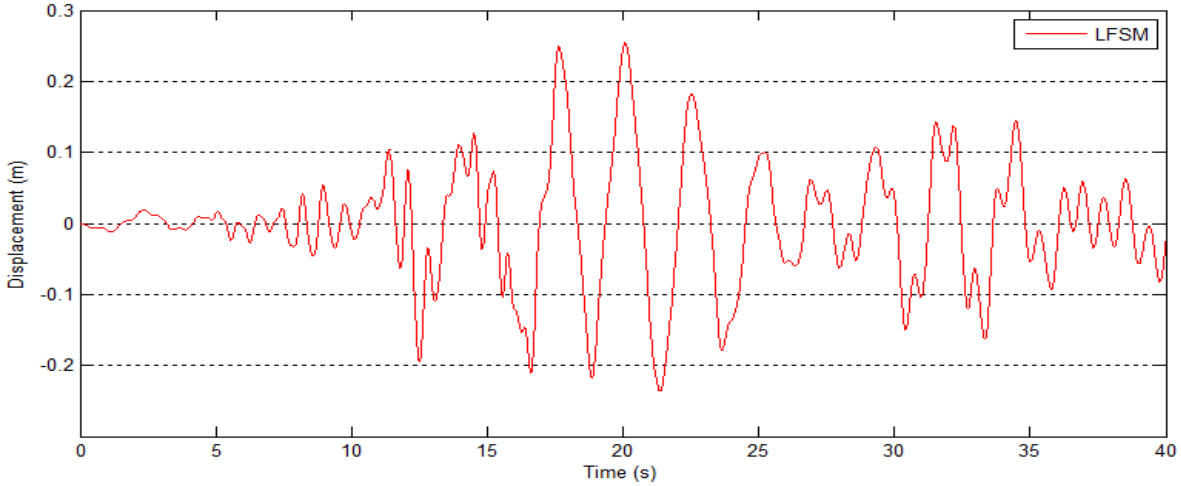

b) Longitudinal displacement at Point E at the west tower for velocity = 1000 m/s

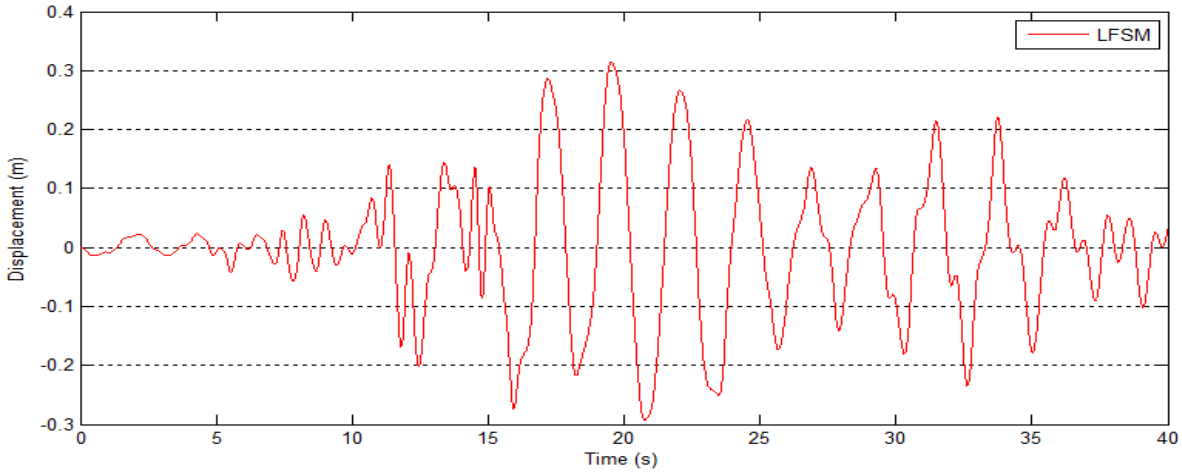

c) Longitudinal displacement at Point E at the west tower for velocity = infinite

Figure D-10 Longitudinal displacement response under nonuniform Chichi earthquake excitation for wave passage effects at Point E

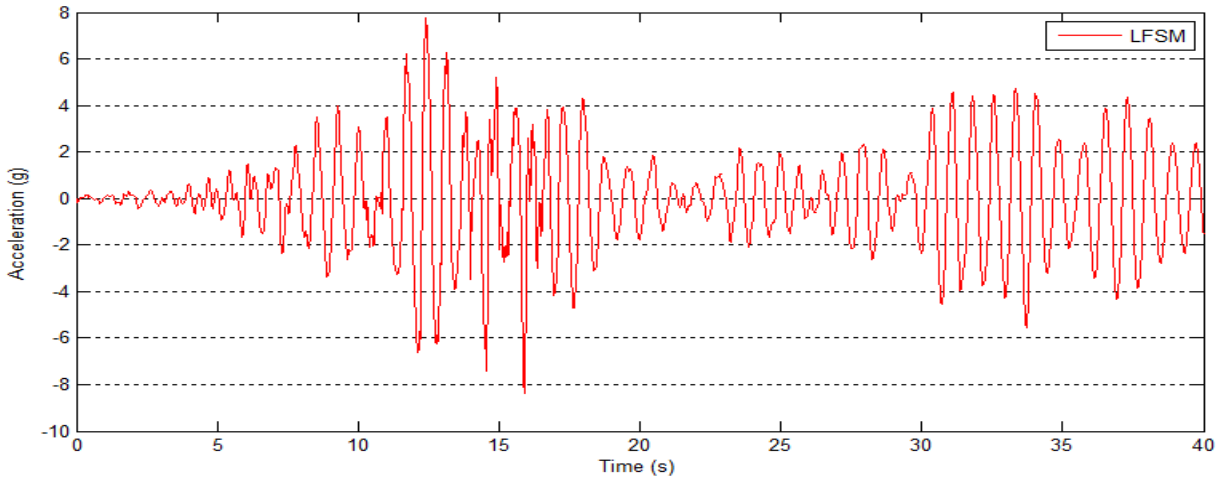

a) Longitudinal acceleration at Point B at the west tower for velocity = 500 m/s

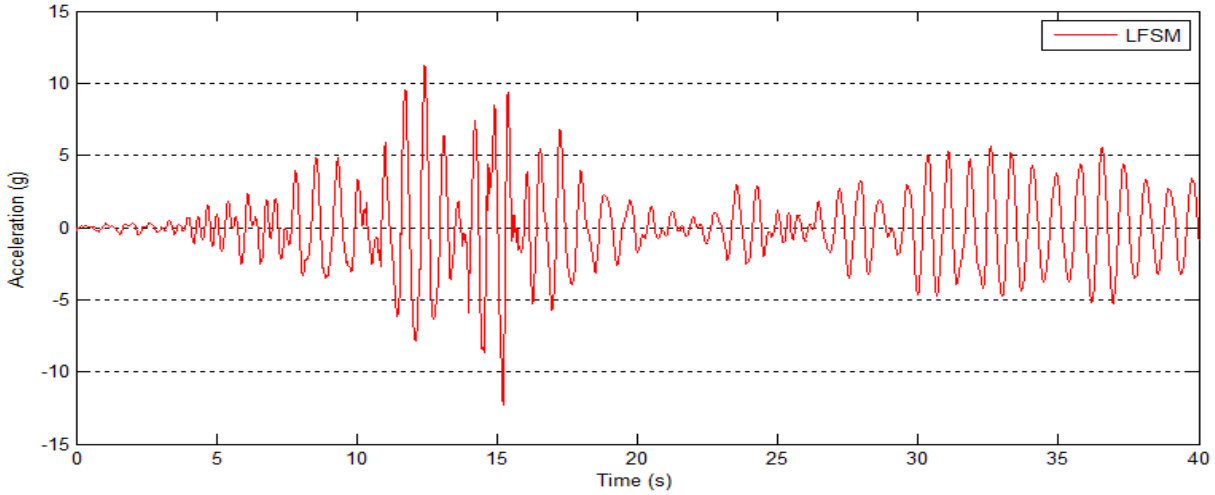

b) Longitudinal acceleration at Point B at the west tower for velocity = 1000 m/s

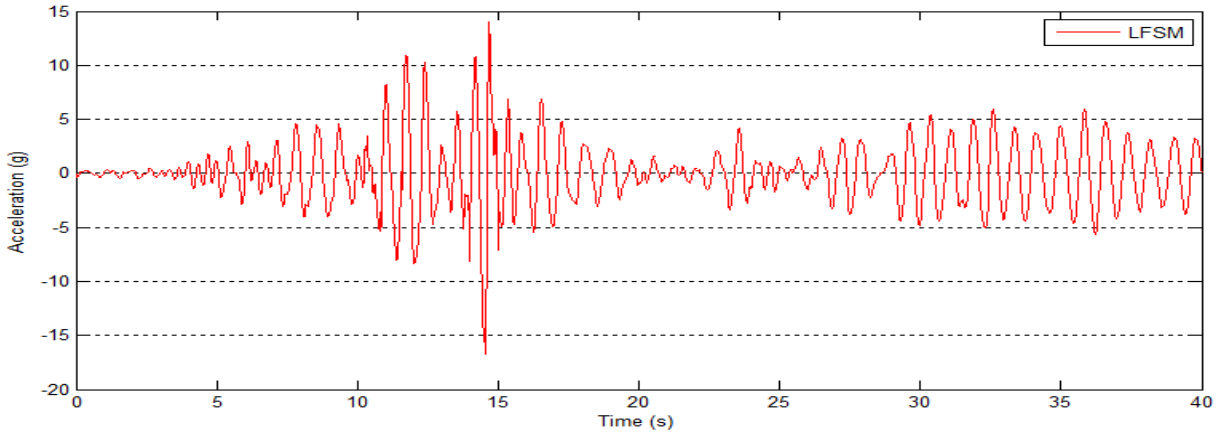

c) Longitudinal acceleration at Point B at the west tower for velocity = infinite

Figure D-11 Longitudinal acceleration response under nonuniform Chichi earthquake excitation for wave passage effects at Point B

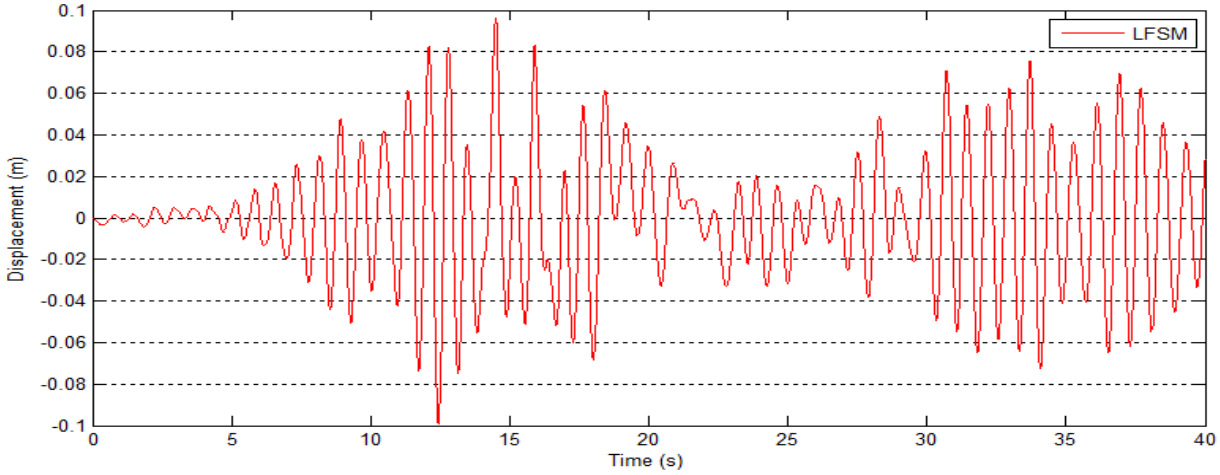

a) Longitudinal displacement at Point B at the west tower for velocity = 500 m/s

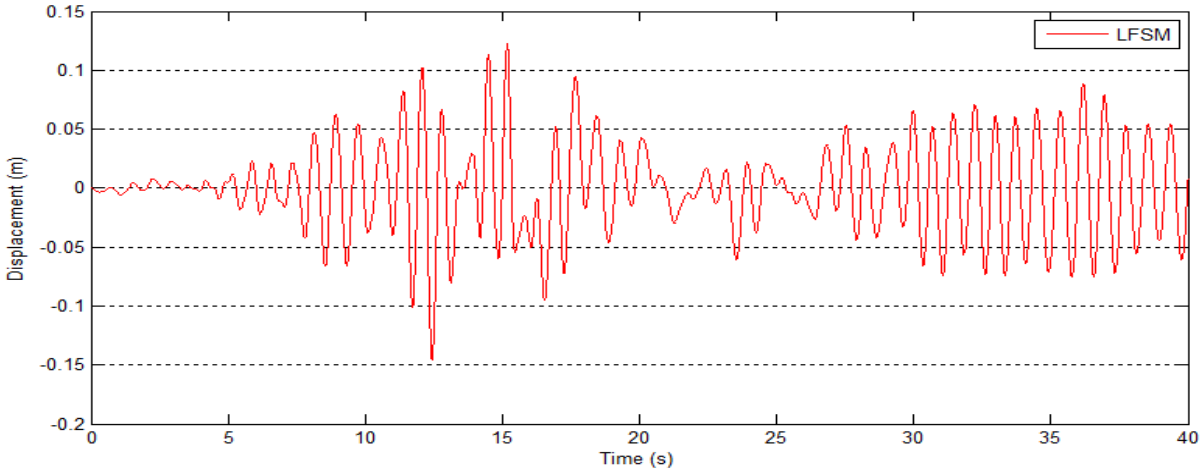

b) Longitudinal displacement at Point B at the west tower for velocity = 1000 m/s

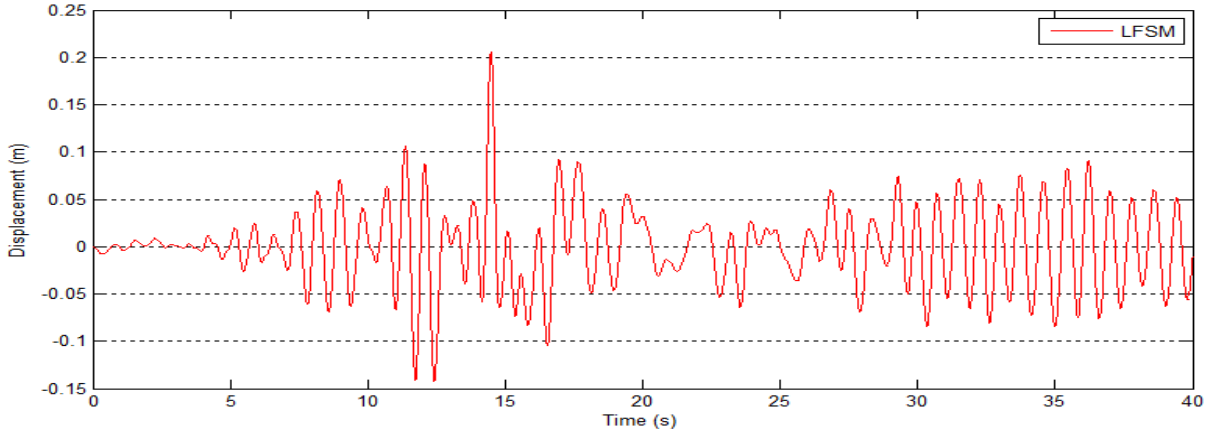

c) Longitudinal displacement at Point B at the west tower for velocity = infinite

Figure D-12 Longitudinal displacement response under nonuniform Chichi earthquake excitation for wave passage effects at Point B

2) VARYING SEISMIC EXCITATION

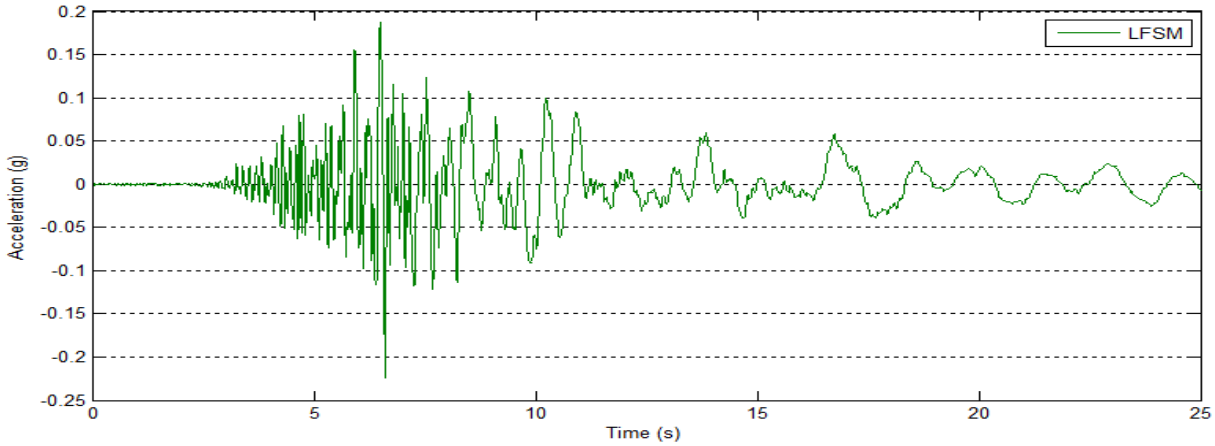

a) Vertical Acceleration Reponses at Point A: Input-1 + Input-1

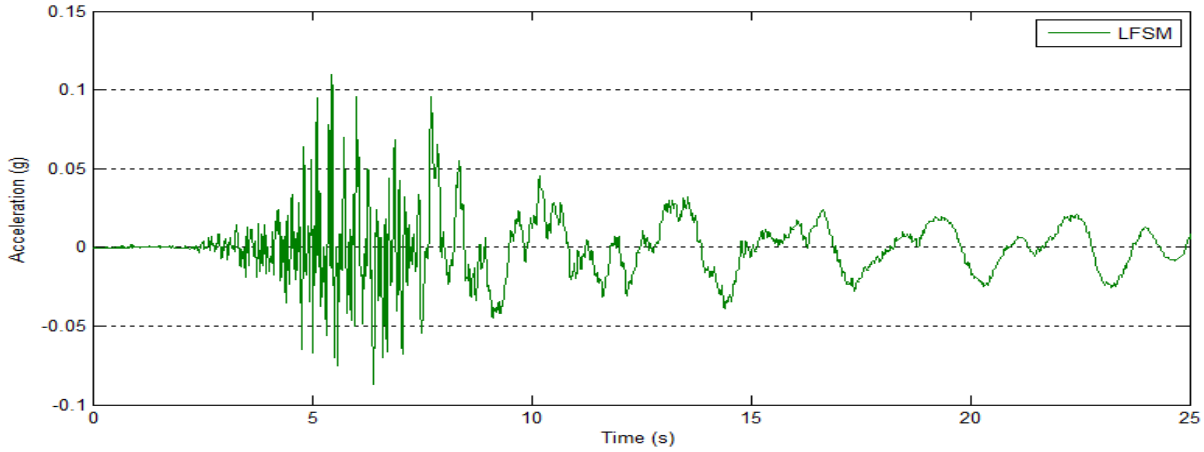

b) Vertical Acceleration Reponses at Point A: Input-2 + Input-2

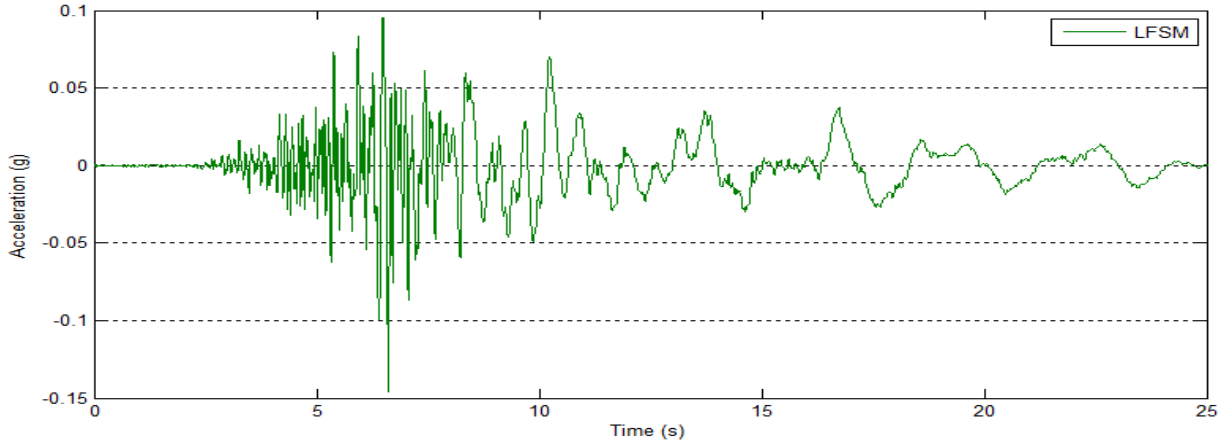

c) Vertical Acceleration Reponses at Point A: Input-1 + Input-2

Figure D-13 Vertical acceleration responses under varying seismic excitations at Point A on the deck

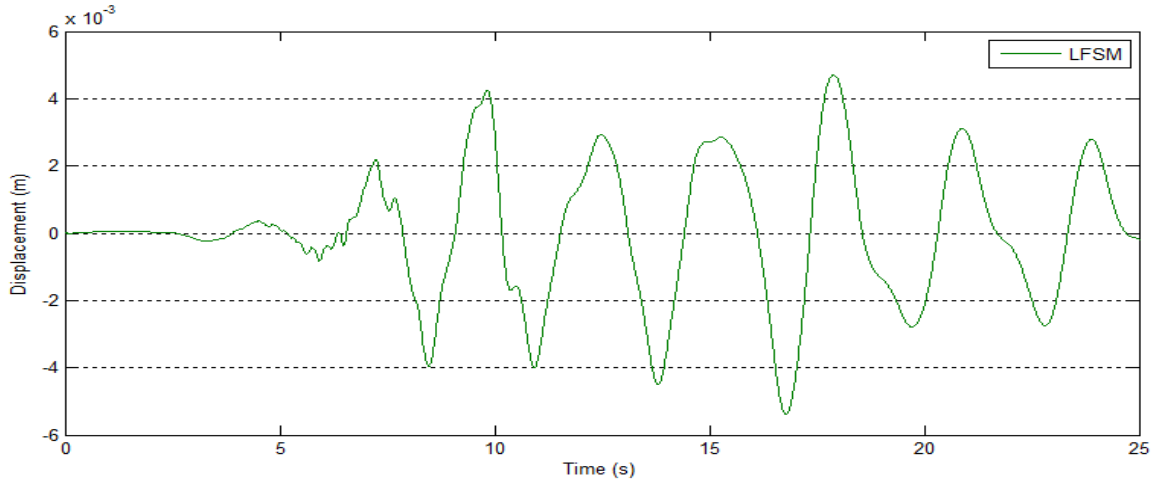

a) Vertical Displacement Reponses at Point A: Input-1 + Input-1

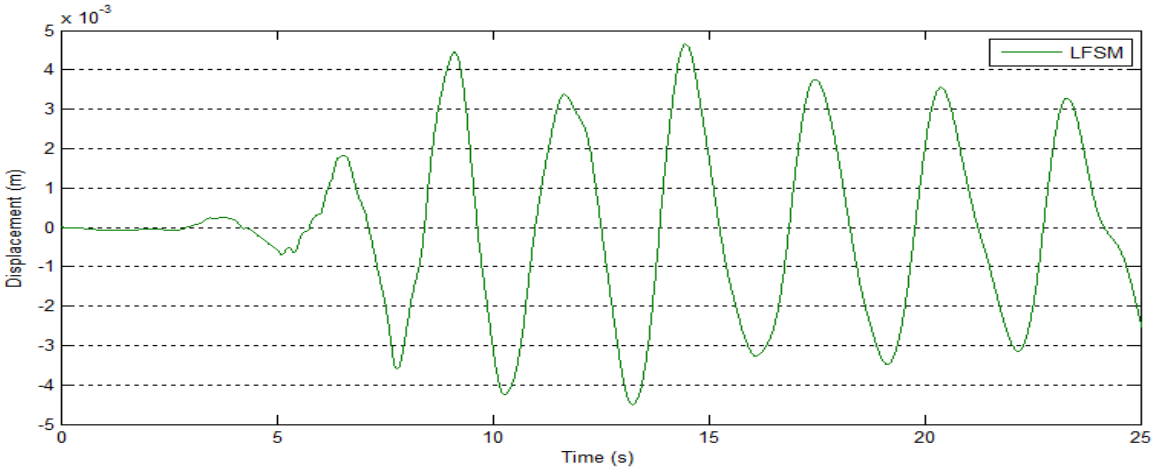

b) Vertical Displacement Reponses at Point A: Input-2 + Input-2

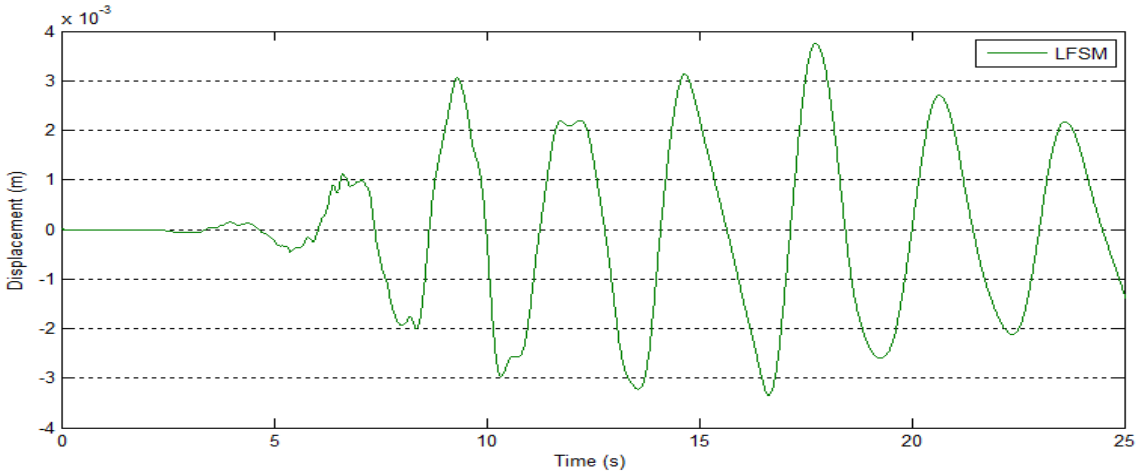

c) Vertical Displacement Reponses at Point A: Input-1 + Input-2

Figure D-14 Vertical displacement responses under varying seismic excitations at Point A on the deck

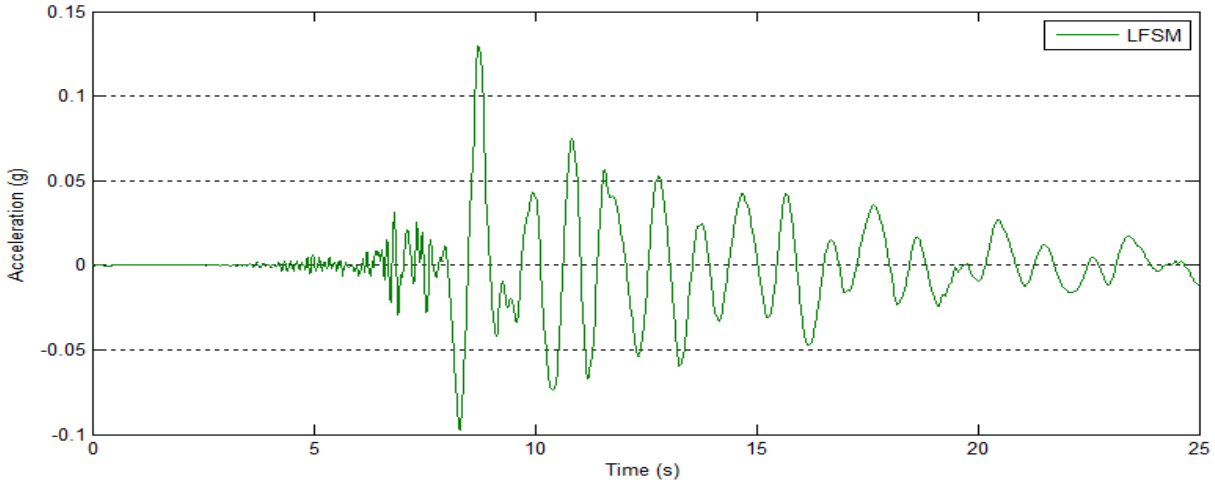

a) Longitudinal Displacement Reponses at Point G: Input-1 + Input-1

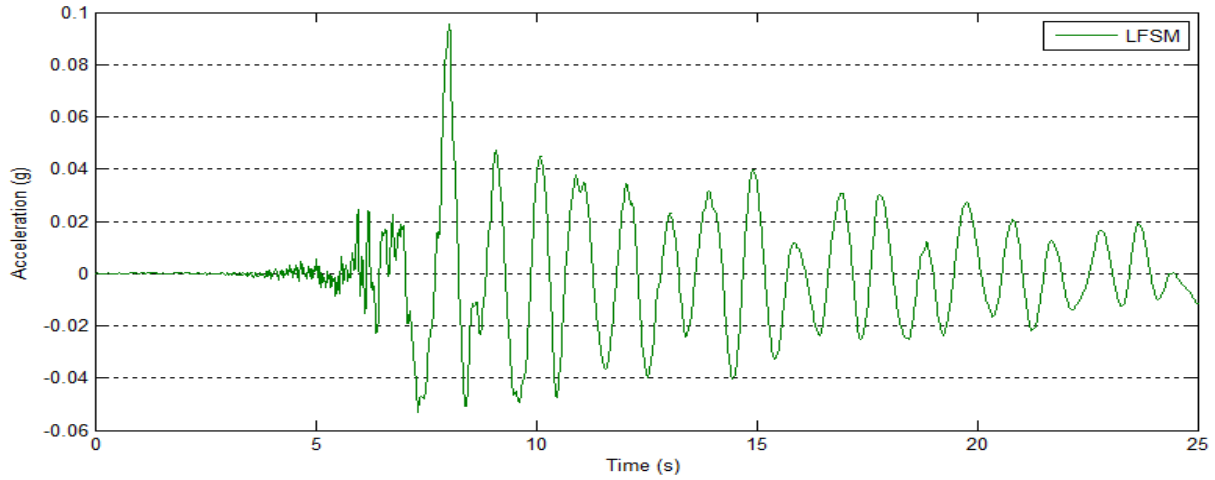

b) Longitudinal Displacement Reponses at Point G: Input-2 + Input-2

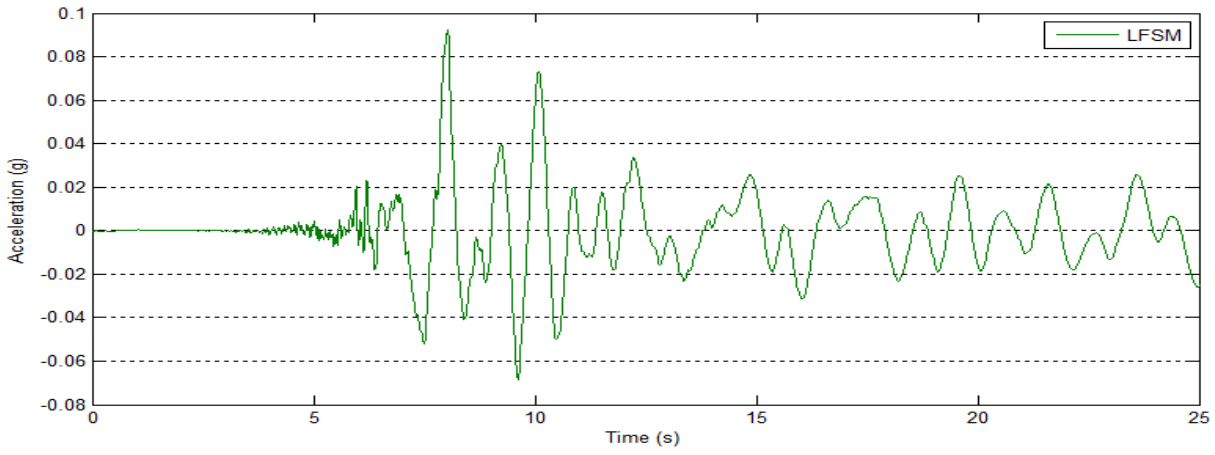

c) Longitudinal Displacement Reponses at Point G: Input-1 + Input-2

Figure D-15 Longitudinal acceleration responses under varying seismic excitations at Point G on the deck

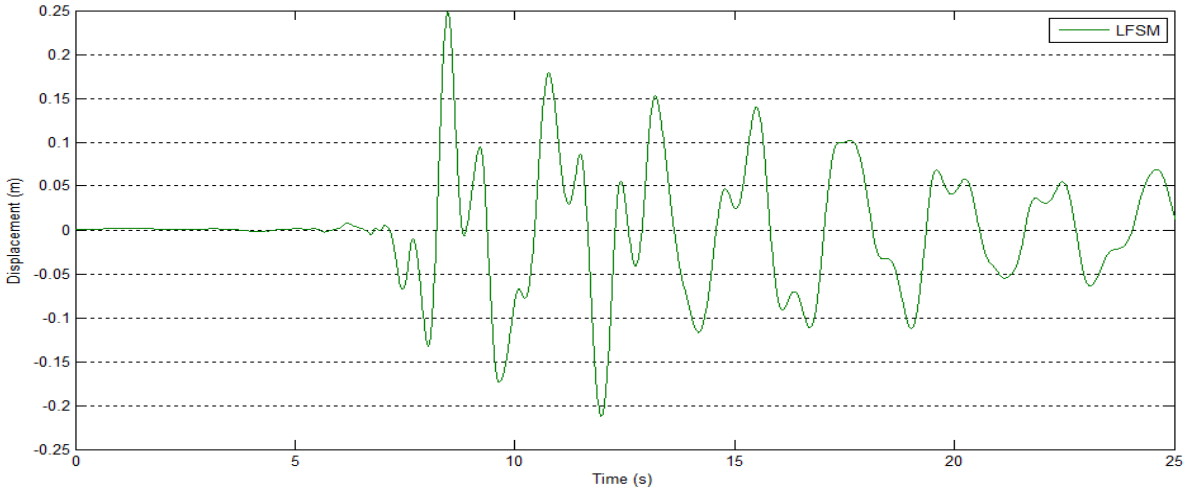

a) Longitudinal Displacement Reponses at Point G: Input-1 + Input-1

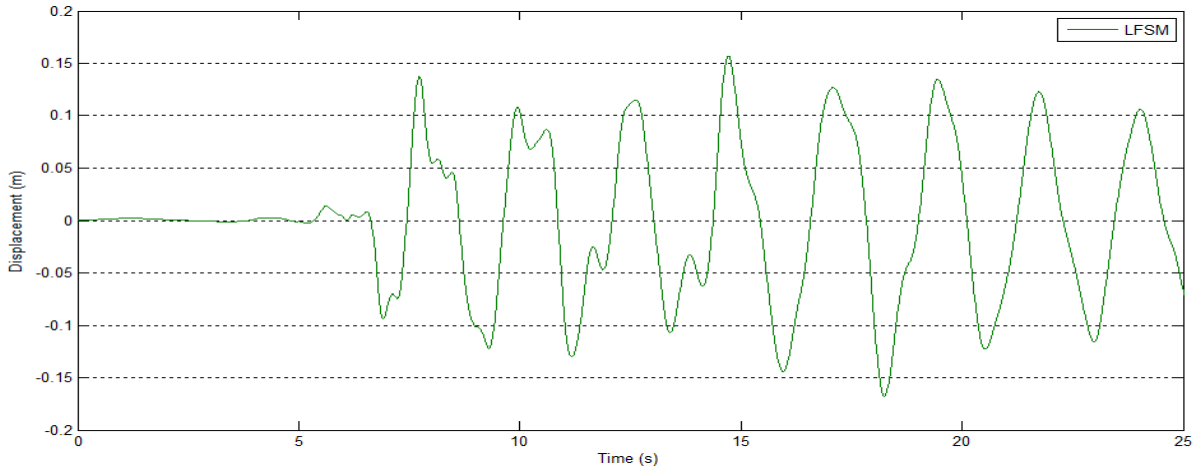

b) Longitudinal Displacement Reponses at Point G: Input-2 + Input-2

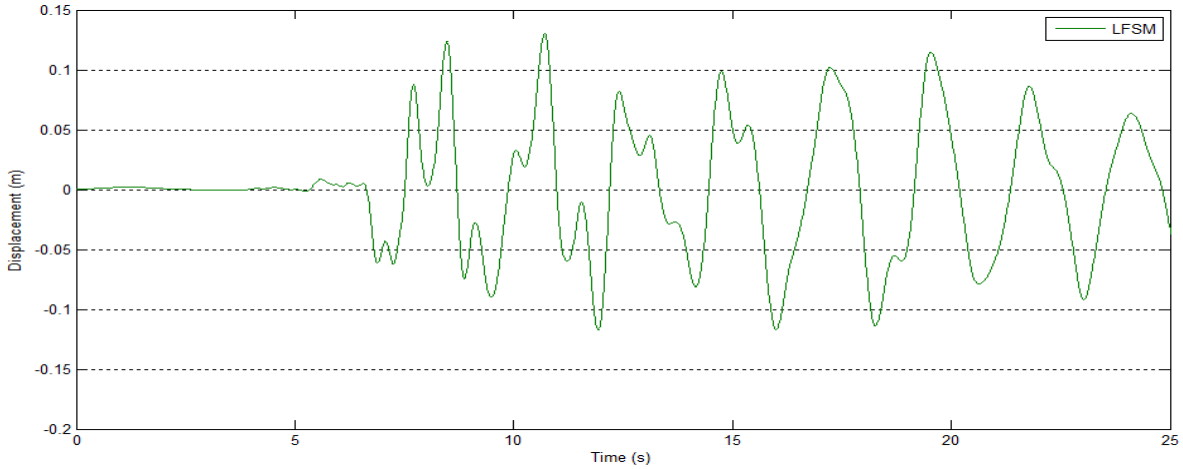

c) Longitudinal Displacement Reponses at Point G: Input-1 + Input-2

Figure D-16 Longitudinal displacement responses under varying seismic excitations at Point G on the deck